Luis Olivares-Quiroz
Osbaldo Resendis-Antonio *Editors*

Quantitative Models for Microscopic to Macroscopic Biological Macromolecules and Tissues

Springer

Quantitative Models for Microscopic to Macroscopic Biological Macromolecules and Tissues

Luis Olivares-Quiroz · Osbaldo Resendis-Antonio
Editors

Quantitative Models for Microscopic to Macroscopic Biological Macromolecules and Tissues

Springer

Editors
Luis Olivares-Quiroz
Universidad Autónoma de la Ciudad de México (UACM)
Mexico City, Mexico

Osbaldo Resendis-Antonio
Human Systems Biology Laboratory
Instituto Nacional de Medicina Genómica (INMEGEN)
México City, Mexico

Red de Apoyo a la Investigación-Coordinación de la Investigación, Científica- Universidad Nacional Autónoma de México (UNAM)
Mexico City, Mexico

Centro de Ciencias de la Complejidad-UNAM
México City, Mexico

ISBN 978-3-319-73974-8 ISBN 978-3-319-73975-5 (eBook)
https://doi.org/10.1007/978-3-319-73975-5

Library of Congress Control Number: 2018933456

Preface

New and recent advances in technology have opened a new era in our understanding of the fundamental principles that govern the evolution and dynamics of organic macromolecules, tissues, and cells under a large set of physical conditions and a wide range of time and length scales. In a successful assembly among cutting-edge experimental techniques, theoretical frameworks imported by physics and mathematics, and powerful and efficient computer algorithms, our current knowledge on the dynamics of biological phenomena has certainly witnessed a tremendous expansion in the last two decades. Now, it is possible to perform precise quantitative analysis of biological phenomena at different scales of times and space, ranging from picoseconds to weeks and from angstroms to meters for studying protein folding and peptide translocation to collective behavior in bird flocks and self-organization patterns in tissues. This vast knowledge has arisen only as an effective interdisciplinary research at the interface of physics, math, molecular biology, computer sciences, and systems biology.

Biological physics deals with the application of physical principles to accomplish computational simulations and analytical models in order to generate, analyze, and discuss mathematical and physical models for biological microscopic phenomena. A paradigmatic and classical example of this is the so-called protein folding problem, which refers to the passage of a one-dimensional primary structure of a protein into a three-dimensional quasicrystalline compact structure known as the native state. The first works of C. B. Anfinsen in 1960–1970 yielded the crucial observation that the native state, in fact, corresponded to a free energy minimum state for the intra- and intermolecular interactions of the protein and the solvent. This paramount observation opened up the door to physics in molecular biology. On another scale, systems biology associates the phenotype of a cell or tissues as a collective behavior. In this sense, emergent properties that result from the interaction of genes, proteins, and metabolites inside the cell and/or organism not present on single entities arise. Both areas have currently made relevant breakthroughs in natural sciences at different degrees of granularities involving fundamental question at microscopic, such as the structure of proteins, or macroscopic scales such as the computational modeling of genome scale metabolic networks to link the phenotype for precision

medicine. Such research fields are in the frontiers of science and, consequently, constantly evolving with the technological advances. To be a participant in this scientific revolution, there is an imperative need to discuss the direction and new trends in the field, identify potential developments in our specific context, and broadcast the knowledge to prepare the new generation of scientist with interest in these amazing and challenging areas.

With these purposes in mind, we organized the *Biological Physics Mexico City 2017 (BioPhys 2017),* which was held from 17 to 19 of May 2017 at the Center for Complexity Sciences, C3- UNAM, México (https://sites.google.com/site/biologicalphysicsmexico2017/). During this time, experts from the UK, Mexico, USA, Israel, and Europe discuss selected topics in physics, computer sciences, mathematics, and systems biology applied to numerous cutting-edge research problems at the interface of these disciplines. The meeting gathered a large number of audience including researchers, graduate and undergraduate students with a variety of backgrounds including biophysics, genomic sciences, physics, mathematics, and computational sciences. Our expectations and goals were satisfactorily reached. The outcome of this effort has had a two-fold positive result: On one side the establishment of collaboration between Mexican and international institutions, and on the other side, it has motivated young minds in the scientific community to pursue new research goals inspired by some of the lectures given. In this book, we have included a selection of these topics presented in the meeting, all these in the frontiers that embrace the fine modeling of protein folding to the computational interpretation of high-throughput technologies in cancer. In chapter one, Gumbart et al. present a detailed description of protein-folding pathways and function of beta-hairpins and beta-sheets. In second chapter, de la Rosa Perez et al. provide a description of microRNA, a short noncoding RNAs that regulate fine regulation in cancer. They present a study in prostate cancer. Then, the subdiffusive transport in heterogeneous environment is depicted by Fedorev et al. Afterwards, F. Sevilla discusses the nonequilibrium nature of the active motion. Then, two different and complementary chapters by Fussion et al. and Ana Leonor et al. describe some applications of the analysis of series analysis to describe the behavior of diseases through noninvasive methods of diagnostics in patients. The chapter "An Agent-Based Model to Study Selection of *Pseudomonas aeruginosa* Quorum Sensing by Pyocyanin: A Multidisciplinary Perspective on Bacterial Communication" describes a mathematical modeling of quorum sensing, one important phenomenon occurring in the population of bacteria. Subsequently, Torres-Romero et al. present a chapter titled "Zinc Efflux in *Trichomonas vaginalis*: In Silico Identification and Expression Analysis of CDF-Like Genes." Then, Armengol at al provide a summary of the state of the art in systems biology and metabolism of breast cancer with a special interest in clinical applications Finally, Victor Breña presents a dynamical analysis of the biochemical interaction in a plant root hair cell.

We are sure that this book will provide a guide to introduce some of the current topics of physics and systems biology. It is a pedagogic resource to motivate new talent in Mexico and stimulate the interdisciplinary research in biological sciences.

Finally, we express our gratitude to all the participants and the academic institutions that provided financial and/or administrative support during the event: Universidad Autonoma de la Ciudad de Mexico (UACM), Universidad Autónoma Metropolitana-Iztapalapa (UAM-Iztapalapa), Center for Complexity Science-UNAM, Instituto Nacional de Medicina Genómica, and Red de Apoyo a la Investigación-CIC-UNAM. Particularly we would like to express our gratitude to Dr. Orlando Guzmán Lopez of UAM-Iztapalapa for his academic, scientific support as well as logistic efforts as a co-organizer of the BioPhys 2017 Conference.

Mexico City, Mexico

Luis Olivares-Quiroz
Osbaldo Resendis-Antonio

Contents

Contributors

María Elizbeth Alvarez-Sánchez Posgrado en Ciencias Genómicas, Universidad Autónoma de la Ciudad de México (UACM), Ciudad de México, Mexico

L. C. Alvarez-Sánchez Laboratorio de Virología, Centro de Investigaciones Regionales "Dr. Hideyo Noguchi" de la Universidad Autónoma de Yucatán, Mérida, Yucatán, Mexico

Raúl Aragón-Franco Hospital Central Militar, Dirección General de Sanidad SEDENA, Ciudad de México, Mexico

V. Arana-Argáez Laboratorio de Farmacología, Facultad de Química de la Universidad Autónoma de Yucatán, Mérida, Yucatán, Mexico

Alejandra Armengol-Alonso Hematology and Oncology Department, Instituto Nacional de Ciencias Médicas y Nutrición Salvador Zubirán, México City, Mexico

Curtis Balusek School of Physics, Georgia Institute of Technology, Atlanta, GA, USA

Víctor F. Breña-Medina Department of Mathematics, ITAMRío Hondo 1, Ciudad de México, Mexico

Minerva Camacho-Nuez Posgrado en Ciencias Genómicas, Universidad Autónoma de la Ciudad de México (UACM), Ciudad de México, Mexico

Jose Gadú Campos-Saucedo Hospital Central Militar, Dirección General de Sanidad SEDENA, Ciudad de México, Mexico

David Alejandro de la Rosa Pérez Posgrado en Ciencias Genómicas, Universidad Autónoma de la Ciudad de México (UACM), Ciudad de México, Mexico

Bruno Estañol Centro de Ciencias de la Complejidad (C3), Universidad Nacional Autónoma de México, Mexico City, Mexico

Laboratorio de Neurofisiología Clínica, Departamento de Neurología y Psiquiatría, Instituto Nacional de Ciencias Médicas y Nutrición "Salvador Zubirán", Mexico City, Mexico

Sergei Fedotov School of Mathematics, The University of Manchester, Manchester, UK

K. Fernández-Martín Laboratorio de Bioquímica y Genética Molecular, Facultad de Química de la Universidad Autónoma de Yucatán, Mérida, Yucatán, Mexico

Alejandro Frank Instituto de Ciencias Nucleares, Universidad Nacional Autónoma de México, Mexico City, Mexico

Centro de Ciencias de la Complejidad, Universidad Nacional Autónoma de México, Mexico City, Mexico

Colegio Nacional, Mexico City, Mexico

Jean Pierre J. Fossion Belgian Association of Medical Acupuncture (ABMA-BVGA), Brussels, Belgium

Ruben Fossion Instituto de Ciencias Nucleares, Universidad Nacional Autónoma de México, Mexico City, Mexico

Centro de Ciencias de la Complejidad (C3), Universidad Nacional Autónoma de México, Mexico City, Mexico

Rodolfo García-Contreras Department of Microbiology and Parasitology, Faculty of Medicine, UNAM, Mexico City, Mexico

Lorena García-Iglesias Posgrado en Ciencias Físicas, Universidad Nacional Autónoma de México, Mexico City, Mexico

Karla P. García-Pelagio Facultad de Ciencias, Universidad Nacional Autónoma de México, Mexico City, Mexico

Carlos Omar Germán-Garrido Escuela Militar de Graduados de Sanidad, Ciudad de México, Mexico

James C. Gumbart School of Physics, Georgia Institute of Technology, Atlanta, GA, USA

Anthony Hazel School of Physics, Georgia Institute of Technology, Atlanta, GA, USA

Hyea Hwang School of Materials Science and Engineering, Georgia Institute of Technology, Atlanta, GA, USA

Ammar Jalalimanesh Technical University of Munich, Zentrum Mathematik, Garching, Germany

Iranian Research Institute for Information Science and Technology (IRANDOC), Tehran, Iran

Christina Kuttler Technical University of Munich, Zentrum Mathematik, Garching, Germany

J. Lara-Riegos Laboratorio de Bioquímica y Genética Molecular, Facultad de Química de la Universidad Autónoma de Yucatán, Mérida, Yucatán, Mexico

Octavio A. Lecona Centro de Ciencias de la Complejidad (C3), Universidad Nacional Autónoma de México, Mexico City, Mexico

Maestría en Dinámica No Lineal y Sistemas Complejos, Universidad Autónoma de la Ciudad de México, Mexico City, Mexico

Cesar López-Camarillo Posgrado en Ciencias Genómicas, Universidad Autónoma de la Ciudad de México (UACM), Ciudad de México, Mexico

Karl Lundquist School of Physics, Georgia Institute of Technology, Atlanta, GA, USA

Meztli L. Matadamas-Guzman Human Systems Biology Laboratory, Instituto Nacional de Medicina Genómica (INMEGEN), México City, Mexico

Anna Pavlova School of Physics, Georgia Institute of Technology, Atlanta, GA, USA

Judith Pérez-Velázquez Technical University of Munich, Mathematical Modeling of Biological Systems (M12), Zentrum Mathematik, Garching, Germany

Institute of Computational Biology, Helmholtz Zentrum München, Neuherberg, Germany

M. Ramírez-Camacho Centro de Información de Medicamentos, Facultad de Química de la Universidad Autónoma de Yucatán, Mérida, Yucatán, Mexico

Osbaldo Resendis-Antonio Human Systems Biology Laboratory, Instituto Nacional de Medicina Genómica (INMEGEN), México City, Mexico

Red de Apoyo a la Investigación-Coordinación de la Investigación, Científica-Universidad Nacional Autónoma de México (UNAM), Mexico City, Mexico

Centro de Ciencias de la Complejidad-UNAM, México City, Mexico

Ana Leonor Rivera Instituto de Ciencias Nucleares, Universidad Nacional Autónoma de México, Mexico City, Mexico

Centro de Ciencias de la Complejidad (C3), Universidad Nacional Autónoma de México, Mexico City, Mexico

Adriana Robles-Cabrera Posgrado en Investigación Biomédica, Universidad Nacional Autónoma de México, Mexico City, Mexico

Francisco J. Sevilla Instituto de Fisica, Universidad Nacional Autónoma de México, Mexico City, Mexico

Helena Stage School of Mathematics, The University of Manchester, Manchester, UK

Juan C. Toledo-Roy Centro de Ciencias de la Complejidad (C3), Universidad Nacional Autónoma de México, Mexico City, Mexico

J. C. Torres-Romero Laboratorio de Bioquímica y Genética Molecular, Facultad de Química de la Universidad Autónoma de Yucatán, Mérida, Yucatán, Mexico

Diverse Protein-Folding Pathways and Functions of β-Hairpins and β-Sheets

Curtis Balusek, Hyea Hwang, Anthony Hazel, Karl Lundquist, Anna Pavlova, and James C. Gumbart

Abstract One of the most common fundamental secondary-structure elements of proteins is the β-sheet. Folding of β-sheets into various structures, e.g., β-hairpins, β-barrels, and amyloids, is believed to provide the energy required to drive various processes, including membrane-protein insertion into and translocation across the outer membrane of Gram-negative bacteria. The folding of the β-hairpin has also been proposed to function as a conformational switch in some systems. In this chapter, we review the contributions of molecular dynamics simulations to resolving the energetics of β-hairpin folding, the mechanics of β-barrel insertion into the membrane by the BAM complex, the dynamics of β-hairpin conformational switching, and the structures of disease-causing amyloids.

Keywords β-Sheets · β-Barrels · Protein folding · Outer-membrane proteins · Amyloids

1 Introduction

Along with α-helices, β-sheets are one of two common secondary-structure elements. They can take on a variety of shapes and sizes. The simplest element is a single β-hairpin, formed by two adjacent protein strands that make hydrogen bonds between their respective backbones with a short turn between them. A β-sheet contains multiple β-strands, which are not necessarily contiguous. These can further fold into three-dimensional structures such as β-barrels, commonly found in the outer membrane of Gram-negative bacteria as well as the outer membranes

C. Balusek · A. Hazel · K. Lundquist · A. Pavlova · J. C. Gumbart (✉)
School of Physics, Georgia Institute of Technology, Atlanta, GA, USA
e-mail: gumbart@physics.gatech.edu

H. Hwang
School of Materials Science and Engineering, Georgia Institute of Technology, Atlanta, GA, USA

L. Olivares-Quiroz, O. Resendis-Antonio (eds.), *Quantitative Models for Microscopic to Macroscopic Biological Macromolecules and Tissues*,
https://doi.org/10.1007/978-3-319-73975-5_1

of mitochondria and chloroplasts [1], and amyloids, exceedingly large structures implicated in a number of diseases. These structures often possess a high stability, e.g., β-barrels in the outer membrane have folding free energies in the range of -18 to -32 kcal/mol [2]. But when necessary, their structures can be dynamic, such as in the designed conformational switch peptide A [3]. Molecular dynamics (MD) simulations, which integrate Newton's equations of motion for all particles in the system iteratively in time, provide one way to observe these dynamical features of proteins. In the following chapter, we describe a handful of distinct structure-function relationships for β-sheet-containing proteins and the contributions MD simulations have made to our understanding of them.

2 The Gram-Negative Bacterial Outer Membrane

Bacteria are typically subdivided into two distinct groups based upon their cell envelope composition. Gram-positive bacteria have a relatively simpler envelope with an inner membrane surrounded by a thick peptidoglycan cell wall [4]. Gram-negative bacteria are distinguished from their positive counterparts by the presence of an outer membrane (OM) beyond the peptidoglycan cell wall, with a large ($\sim$25-nm) periplasmic space separating the two membranes (Fig. 1a).

The outer membrane is distinct from other lipid bilayers, in both pro- and eukaryotes, due to an asymmetric leaflet composition. It is this intrinsic asymmetry of the OM that prevents most small molecules from diffusing across the membrane spontaneously, as can occur in symmetric bilayers [5–7]. Comparing the two leaflets, the inner leaflet of the OM is primarily composed of phospholipids, such as phosphatidylethanolamine, phosphatidylglycerol, and cardiolipin (approximately 15:3:1) [8, 9], whereas the outer leaflet of the OM is composed of lipopolysaccharides (LPS), which have 5–6 aliphatic tails, a core-oligosaccharide, and in some species O-antigen repeats [10] (Fig. 1b). The hydrophilic core-oligosaccharide of LPS combined with the hydrophobic tails prevents almost all molecules from easily traversing the OM. This is due in part to divalent cations cross-linking the core-oligosaccharide phosphates, reducing the lateral mobility of LPS and inhibiting the permeation of small molecules [9, 11]. Computational simulations have also shown that the core-oligosaccharide plays a critical role in the function of OM proteins [12–14].

The OM is believed to comprise approximately 50% protein by mass [8], most of which are transmembrane spanning β-barrel porins (Fig. 1c), which permit the passive diffusion of small molecules ($<$600 Da) into and out of the periplasm. The existence and abundance of porins prohibit OM proteins from utilizing typical cellular energy sources, such as ATP and ionic gradients. These limitations have been studied extensively using computational simulations to quantify dynamical properties and functions of OM porins, such as exclusion limitation, ion specificity, enzymatic activity, etc. [8, 15–17]. Furthermore, in vitro experiments have shown at least some β-barrel proteins can spontaneously insert into the OM, albeit

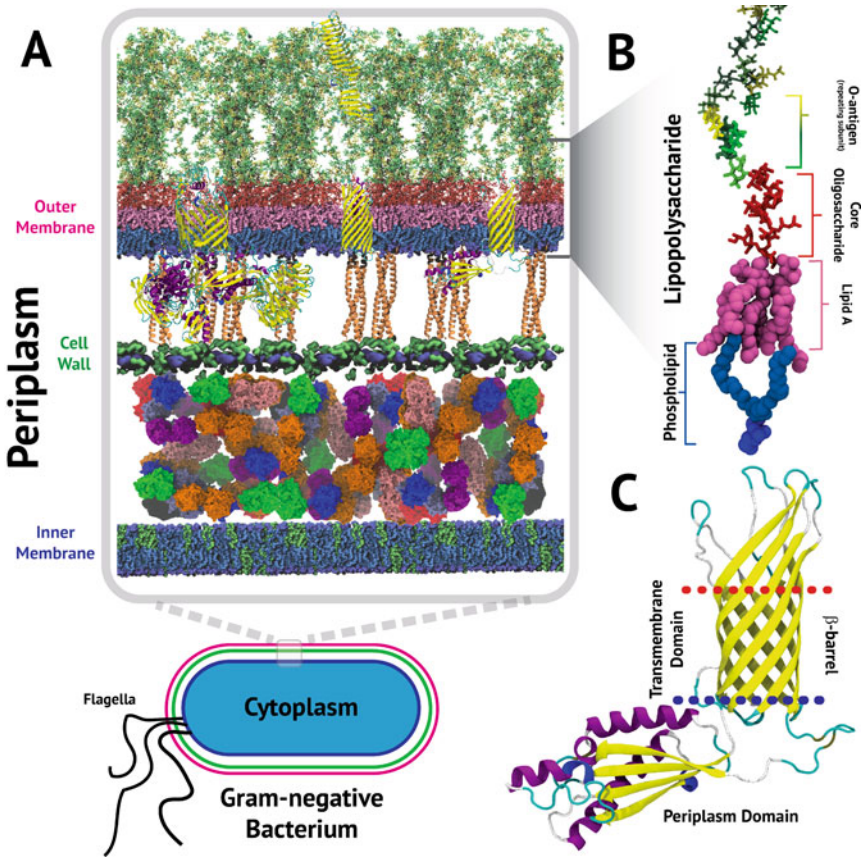

Fig. 1 Gram-negative cell envelope. (**a**) Gram-negative bacteria are characterized by their cell envelope, which contains two membranes and a cell wall, shown atomistically in the enlarged region. The inner and outer membrane are separated by the periplasm, which contains the cell wall and a diverse set of proteins, including chaperones, assembly machineries, and degradases. OM proteins (yellow and purple) shown left to right are β-barrel assembly machinery (BAM) complex, autotransporter pertactin, and OmpA porin. (**b**) An enlarged representation of LPS with lipid A in magenta, core-oligosaccharide in red, and the O-antigen subunit in green hues, above a typical inner leaflet phospholipid (blue). (**c**) OmpA, an OM porin, shown with its periplasmic domain

slowly [18]. Therefore, it has been hypothesized that OM proteins can utilize the energy from β-sheet folding to drive various other processes, e.g., folding OM proteins (see Sect. 4) and importing/exporting substrates [19].

While small molecules can diffuse across porins, large, scarce substrates still require active transport across the OM. One such uptake pathway is through TonB-dependent transporters (TBDTs), which import metal-containing complexes such as siderophores, chelates, and cobalamins across the OM. TBDTs are characterized by a 22-stranded β-barrel motif and a moderately conserved plug domain that occludes the barrel [20, 21]. This plug contains a highly conserved N-terminus, the so-called

Ton-box, which binds to TonB, an inner-membrane anchored, periplasm-spanning protein. TonB utilizes energy generated by the inner-membrane proton motive force to drive substrate transport at the OM [20–22].

β-sheet interactions play a critical role in TonB-mediated substrate transport. The plug domain contains a four-stranded β-sheet with the strands oriented roughly parallel to the membrane plane [20]. Alternatively, when bound, TonB and the Ton-box, which form their own β-strand/strand interaction, are oriented perpendicular to the membrane plane. Simulations on the cobalamin transporter BtuB and the iron-pirate TbpA tested a hypothetical force transduction model, demonstrating that the TonB/Ton-box interaction is stable under the application of force whereas the plug domain unfolds readily [23, 24]. The distinct behavior is due to the fact that breaking the TonB/Ton-box interaction would require shearing, i.e., breaking all hydrogen bonds in the β-sheet simultaneously, whereas unfolding the plug domain requires only unzipping, i.e., breaking one hydrogen bond at a time [20, 23]. Recent atomic force microscopy studies have all but confirmed this force transduction model and, furthermore, suggested that each TBDT has a plug domain that unfolds only as much as necessary to create a pathway for its substrate [25].

3 GB1 as a Model Peptide for Studying the Folding of β-Sheets

In order for most proteins to function, they must first acquire a specific three-dimensional "native" structure, that is encoded within the sequence of amino acids [26]. Proteins typically "fold" into their native structure starting from some unstructured, disordered state after being extruded from the ribosome during mRNA translation. Understanding the mechanism by which proteins find their native structure is important in elucidating how structure is encoded within the amino acid sequence. Model peptides—small sequences with one or a few secondary structural motifs—are often used to study folding mechanisms. Because widely different sequences can give rise to surprisingly similar structures, results from model peptides are broadly applicable to many sequences containing similar structures. The B1 domain of streptococcal protein G (GB1) has often been used to study the folding of β-sheets. The full-length GB1 has 56 residues and contains four β-sheets and one α-helix (see Fig. 2a). The C-terminal β-hairpin (residues 41–56, i.e., β3 and β4 in Fig. 2a) is also used to study a single, isolated β-hairpin (see Fig. 2b).

While NMR experiments were successful in finding natively folded, isolated β-hairpin peptides [27–32], which had been elusive to researchers due to either their instability or tendency to aggregate in solution, they were unable to determine the folding kinetics or folding mechanisms of these peptides. Muñoz et al. performed the first experiments to investigate the folding mechanisms of a β-hairpin peptide in 1997 [33]. Using nanosecond laser temperature-jump experiments for the single tryptophan residue, W43, in the hydrophobic core, they observed that the C-terminal

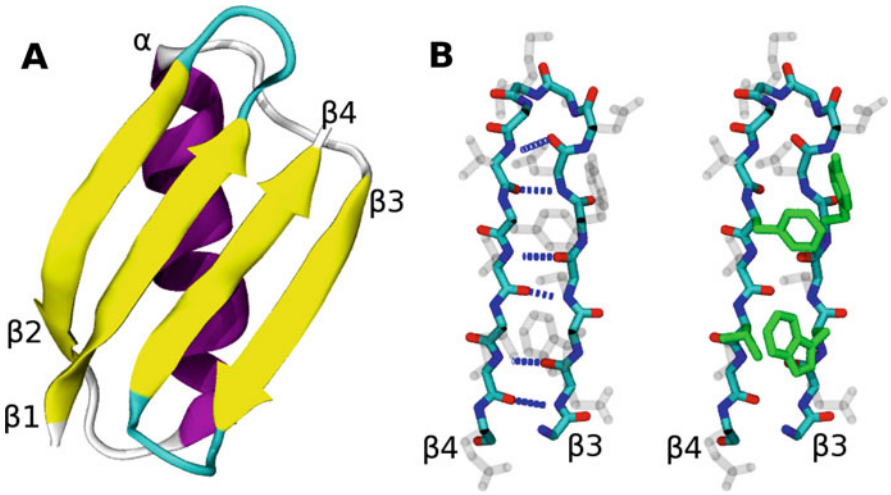

Fig. 2 Structure of GB1 (PDB: 1GB1). (**a**) Full structure of B1 domain of protein G. Protein backbone shown in cartoon representation and colored by secondary structure: (yellow) β-sheet, (cyan) β-turn, (magenta) α-helix, and (white) random coil. (**b**) GB1 residues 41–56 (β3 and β4 in **a**) shown in licorice representation. Backbone atoms colored by atom name and side chain atoms transparent. Left: native backbone hydrogen bonds between residue pairs 42–55, 44–53, and 46–51. Right: hydrophobic core residues 43, 45, 52, and 54 shown in green

β-hairpin of GB1 folds in $\sim$6 μs and is about 50% folded at room temperature. In addition, they observed that GB1 obeys many of the physical mechanisms believed to be involved in protein folding: it's a two-state folder, has a funnel-like free-energy landscape, and is stabilized by both hydrogen bonding and hydrophobic interactions. The turn region containing residues 45–52 is in its native conformation in the transition state, and a simple statistical model where each residue flips between a random coil and β-sheet conformation [33] suggests this may be the main reason for β-hairpins folding about 30 times slower than α-helices [34, 35]. Lastly, Muñoz et al. calculated the enthalpic and entropic contributions of GB1 folding to be $\Delta H = -11.6\,\text{kcal mol}^{-1}$ and $\Delta S = -39\,\text{cal mol}^{-1}\,\text{K}^{-1}$, respectively.

Since the GB1 β-hairpin is such a small molecular system, amenable to MD simulations, the Muñoz et al. study [33] inspired a deluge of computational studies between 1998 and 2002. Some of these studies challenged the turn-first folding mechanism of Muñoz et al. Dinner et al. were the first to use an MD simulation to calculate a free-energy landscape of GB1 [36]. Using collective variables defined by the native hydrogen bonds and hydrophobic core residues shown in Fig. 2b, an L-shaped free-energy landscape suggested that the hydrophobic core collapses first before any native hydrogen bonds form. Formation of hydrogen bonds then propagates outwards from the hydrophobic core, with central hydrogen bonds formed most often. Although these results used an implicit solvent model, two other studies utilizing high-temperature simulations found similar results for explicit solvents [37, 38]. The latter two studies by Pande et al. and Garcia et al.

additionally observed that some structural elements are present in the hydrophobic collapsed state, while native hydrogen bonds had yet to form. Interestingly, short simulations (5 ns) of GB1 at low temperatures found the native structure to still be stable after replacing the nitrogen atoms involved in native hydrogen bonding with fluorines [39]. The hydrophobic core was stable enough to keep the structure intact, suggesting that the hydrophobic core may be the stabilizing element for the β-hairpin. Very long trajectories (38 μs in total) of GB1 in implicit solvent showed kinetic traps along the extended→collapsed pathway due to non-specific hydrogen bonding [40]. By comparing explicit and implicit solvent models with the same force field, Zhou and Berne found that β-hairpin folding may be entropically driven, given that the higher energy hydrophobically collapsed state is the global free energy minimum in implicit solvent, whereas the native state is the global minimum in explicit solvent [41]. The same effect was not observed for helices, where local interactions are the driving force for folding. Therefore, implicit solvents are probably underestimating the total entropy of the water, particularly for the folded state. The implicit solvent model, GB^{OBC}, however, appears to work well enough in this regard with the AMBER96 force field to reproduce the correct two-state behavior for GB1 [42]. While most of these early studies found the folding mechanism to involve either hydrophobic collapse or turn formation proceeded by hydrogen bond formation, one study found an alternative, "reptation" mechanism where an offset β-hairpin with non-native contacts is formed first, which then slides into the correct conformation with native contacts [43]. A later study, however, found that the non-native hairpin must first completely unfold before forming the native hairpin [44], rejecting reptation as a possible mechanism.

After a rush of molecular simulation studies in the 5–6 years following the Muñoz et al. paper, a consensus began to form for the folding mechanism of GB1. The β-hairpin exists as a two-state folder, with the unfolded state being a collapsed structure, rather than an extended one. While there was some debate on the precise structure of the collapsed state, it did appear that some structural elements were present in this state before the native hydrogen bonds formed. The central hydrogen bonds are the most stable, usually forming first, whereas those near the turn region or the termini are formed least often, if at all, often resulting in a frayed structure in the native state with a fluctuating number of hydrogen bonds. However, with the nature of the unfolded state still ambiguous, further studies were needed to pinpoint the exact mechanisms and driving forces for folding. Some evidence points to the turn region being the more important factor over the hydrophobic core. For example, Santiveri et al. showed that for a designed β-hairpin peptide, folding is driven primarily by the turn region, although transition states are stabilized by a hydrophobic tyrosine–tryptophan interaction [45]. Smith et al. later found a more direct connection between hydrophobic collapse and turn formation for another designed β-hairpin peptide, TZ2, using isotope-edited 2D IR spectroscopy [46]. Davis and Dyer also recently showed that salt bridges in the turn region can significantly enhance stability of β-sheets [47]. GB1 has a potential salt bridge pairing in the turn region, but experiments showed that although this salt bridge appears in crystal structures, there are no salt bridge interactions in solution [48],

so these interaction don't appear to affect GB1. Simulations by Evans and Wales found that electrostatic forces appear to be driving the hairpin to fold for their system [49], not van der Waals forces, contrasting the results of Ma and Nussinov, which suggested that hydrophobicity was enough to stabilize the structure. However, Evans and Wales utilized an implicit solvent and found folding times that were an order of magnitude longer than experiments. Yoda et al. examined a third reaction coordinate that monitored the turn region, in addition to two coordinates for the number of native hydrogen bonds and the size of the hydrophobic core, and found a large free energy basin containing unfolded, hydrophobically collapsed, and turn-forming structures [50]. For their system, hydrophobic collapse preceded turn formation. De Sancho et al. found that slow dynamics in the unfolded state are due to the formation and melting of helical structures [51], similar to results from Zagrovic et al. Lastly, although they did not investigate the unfolded state directly, Best et al. observed distinct differences in the free-energy landscape of GB1 for different protein force fields and explicit water models [52]. In particular, water models with stronger water–protein interactions can shift the stability away from the native state towards a more extended, unfolded state.

In conclusion, while GB1 displays typical two-state folding behavior, MD simulations disagree somewhat on the unfolded structure and how the folded structure arises from that unfolded state. While there is strong evidence that the turn region may ultimately play the more important role over the hydrophobic interactions, its relative importance for GB1 specifically is not so clear. Hydrophobic collapse does appear before hydrogen bond formation, but some studies have found turn structure arising either before or during collapse. Additionally, dynamics in the unfolded regime are complicated by short-lived, non-native helical segments. As force fields are better optimized to reproduce experimental data, and protein–water interactions are better characterized, molecular simulations should be able to resolve this discrepancy.

4 Assembly of β-Barrel Proteins

As noted in a previous section, the outer membrane (OM) in Gram-negative bacteria is asymmetric and populated by a number of outer-membrane proteins (OMPs) with β-barrel transmembrane domains [53]. The primary machinery responsible for insertion and assembly of OMPs in Gram-negative bacteria has been identified as a five-protein complex called the β-barrel assembly machinery (BAM) [53] (Fig. 3).

While the exact number of BAM-complex components depends on bacterial species [54, 55], in *E. coli*, the BAM complex is a five-protein assembly. The BAM complex consists of BamA, the central and essential transmembrane unit, along with four accessory lipoproteins, BamB, BamC, BamD, and BamE [53, 56]. An understanding of how this system accomplishes its task has been advanced significantly by the steady release of structures for all its components over the last 10 years. The structures of BamB, BamC, and BamD were first published in

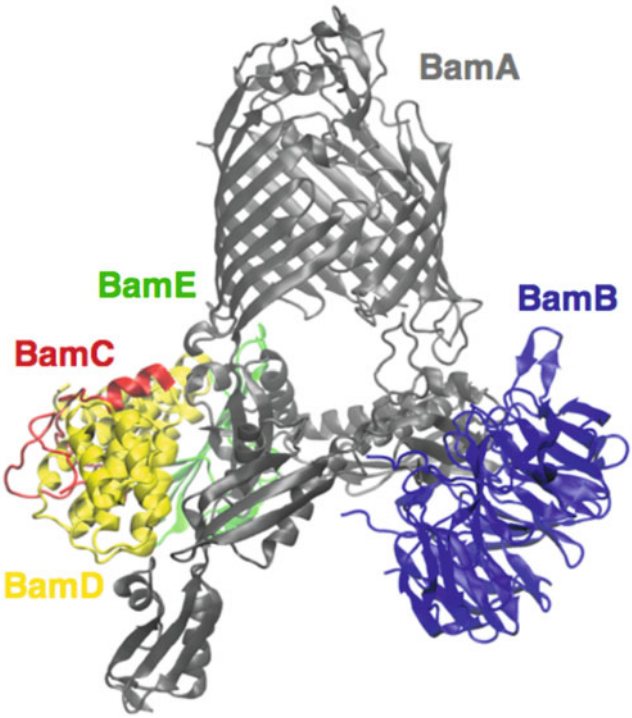

Fig. 3 The *E. coli* BAM complex from Gu et al. (PDB entry 5D0O). BamA is shown in grey, BamB in blue, BamC in red, BamD in yellow, and BamE in green. The helix grip domains are missing from BamC. BamB and BamD interact directly with BamA, while BamC and BamE interact primarily with BamD

2011 [57], while the structure of BamE was published in 2008 [58]. The structure of BamB revealed a β-propeller motif with eight blades and a central pore in what has been called a "doughnut" shape [59]. The structure of BamC consists of an unstructured N-terminal domain (75–100 residues) and two structurally similar helix-grip domains, each of which includes six β-strands and three α-helices [57, 60, 61]. BamD contains five tetratricopeptide (TPR) domains, each of which consists of two α helices of varying lengths [57, 62, 63]. Crystal structures for BamA periplasmic domains were first released in 2007 [64], but did not exist for the β-barrel domain until 2013 [65]. At its N-terminus, BamA was determined to possess five periplasmic domains called polypeptide transport-associated (POTRA) domains, which have a conserved $\beta\alpha\alpha\beta\beta$ fold and a 16-stranded β-barrel at its C-terminus [65–67]. In 2016, the first high-resolution structures for the BAM complex, with and without BamB, were released [68–71].

Fueled by a number of crystal structures for BAM-complex components released over the course of the last 10 years, molecular dynamics simulations have played a critical role in revealing a mechanistic understanding of OMP assembly [65,

69, 72, 73]. Beginning with the release of structures for the β-barrel domain for BamA, simulations revealed several key features of the dynamics of BAM-complex components. The first of these features was a spontaneous separation between the first and last β-strands (β1 and β16, respectively) on the μs timescale, forming a putative "lateral gate" [65]. To verify the existence and relevance of this gate, cross-linking was performed with disulfide mutagenesis to prevent the gate from opening [72]. This mutation was lethal to bacterial cultures, giving support to the biological existence and importance of the separation event. A second feature revealed in BamA simulations was a destabilized region of the membrane near the strand interface caused by an abnormally thin hydrophobic section of the barrel exterior. Together, these features have targeted the gate region as functionally relevant for OMP insertion, although they do not unambiguously establish the actual insertion mechanism. Following the initial simulations of BamA, later MD simulations demonstrated the existence of an exit pore in the extracellular loops above the lateral gate, with cross-linking experiments showing that its opening is required for proper function [72]. It was proposed that this exit pore is necessary to allow the passage of large extracellular loops of nascent OMPs during assembly.

More recently, simulations were used to carry out a systematic study of the POTRA domains of BamA. In this study, Fleming et al. showed that the periplasmic OM surface can bind to the POTRA domains and modulate their conformational flexibility [73]. Based on their findings, they propose that binding to lipoproteins and to the membrane helps the POTRA domains to maintain functionally relevant conformations of the BAM complex. Moreover, due to their amphiphilic nature, β-strand segments of nascent OMPs may find a favorable environment at the interface of the OM inner leaflet and adsorb to the surface. The binding of POTRA domains to this interface may help to arrange these segments into hairpins or β-sheets along the assembly pathway.

Simulations of the full-complex structures released in 2016 have served to broaden an understanding of dynamic features of the complex [69]. The two C-terminal helix-grip domains of BamC were previously suggested to be cell-surface exposed in vivo, likely indicating that they are not closely associated with the complex [74]. In all simulations of BAM complex structures, the C-terminal domains of BamC were observed to be the most mobile of all the domains [69]. Likewise, in one of the BamACDE complexes, electron density was only visible for the N-terminal loop of BamC, indicating that the C-terminal region was highly dynamic [69]. The BamACDE and BamABCDE systems were otherwise shown to be stable in simulations [69]. Removal of BamB or BamD caused an increase in mobility, while the removal of BamC had a minimal effect. Gu et al. conclude, based on their simulations and functional studies, that the entire periplasmic part of the complex rotates about the β-barrel domain of BamA, cycling between conformations to somehow assist in OMP assembly.

Inspired in part by the recent structures and simulation results, three prominent models now exist to explain the role of BamA in substrate insertion [75, 76]. The passive model posits that the substrate is inserted directly into the disordered membrane region created by BamA, and otherwise the BamA barrel plays practically no

functional role. The lumenal folding model asserts that nascent proteins fold entirely inside the lumen of the barrel before exiting through the lateral gate opening. Finally, the hybrid barrel model supposes that the strand separation at the lateral gate creates a β-strand-folding template upon which the strands of the nascent barrel are constructed. The BamA β-barrel grows as each nascent strand is added until the newly formed barrel buds off and is released into the membrane.

A number of questions and possible shortcomings exist with each of the aforementioned models. The passive model appears to have almost no role for the BamA β-barrel, other than to create a membrane defect. The lumenal folding model would require BamA to accommodate and fold proteins in its lumen, some of which are much larger than BamA itself. In addition, lumenal folding without gate opening would fail to provide an amphiphilic interface to stabilize both the hydrophobic exterior and hydrophilic interior of nascent OMP strands. The hybrid barrel model would provide this amphiphilic interface as well as a template to assist β-sheet formation, but the enormous degree of structural reorganization required to accommodate some OMPs (up to 26-strands [77]) appears untenable on its face [75, 76].

5 Amyloid Fibrils

Misfolding of proteins can have very serious consequences. For humans, the formation of amyloid fibers, or amyloids, which are insoluble and resistant to degradation, is particularly problematic [78–80]. These fibers are formed by normally soluble proteins or peptides that misfold and aggregate into long cross β-sheet structures (see Fig. 4). The fibers are typically 10 nm wide and 0.1–10 μm long and their formation is believed to be responsible for many serious and incurable conditions such as Alzheimer's, Parkinson's, Type II diabetes, and others [78–80].

There is a lot of interest in understanding the formation of amyloid fibers and in developing drugs that can inhibit their formation. Experimental studies have

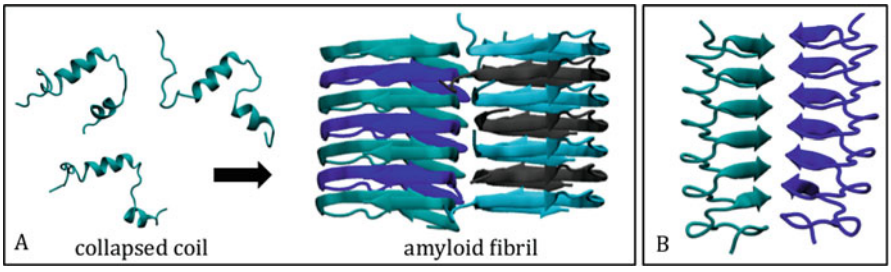

Fig. 4 (**a**) Structures of a β-peptide as collapsed coil in solution [83] (P DB code 1AML) and assembled into amyloid fibril [90] (pdb code 5KK3). (**b**) Structure of a β-helix [91] (PDB code 1EZG)

shown that the aggregation process requires a nucleation step and that several intermediate structures that differ from the final form of the fibers are formed during the assembly [80–82]. After nucleation, the protein monomers are added through a "dock and lock" model, where the monomer first associates with the growing fiber and then locks into the fiber structure by adapting the correct fiber-like conformation [80]. In many cases, the intermediate protein oligomer structures are more toxic to humans than the final amyloid fibers [79].

To date, the most studied case of amyloid formation is the aggregation of amyloid β-peptides (β-peptides), which leads to development of Alzheimer's disease [79]. These 39–43 amino-acids-long peptides are created from cleavage of the amyloid precursor protein; their normal function is not known. NMR studies have shown that the peptide in solution cannot be described by one single structure, and that it mainly adopts collapsed coil structures [83]. Therefore, transition from solution to amyloid would require a large conformational change.

Atomistic MD simulations have been used to study the solution conformations of the Aβ-peptide monomer, oligomerization of small peptide models and fiber elongation [81]. The first MD simulations of an Aβ-peptide were done by Strauss and co-workers [84–86]. It was shown that the WT peptide is disordered in solution and that mutants can enhance the aggregation process by making the peptide more flexible, potentially enabling a faster transition into the nucleation state. Other simulations [87, 88] confirmed that peptide flexibility correlates with aggregation by showing that factors contributing to aggregation, such as longer peptide length, lower pH and high temperature, also increase peptide flexibility. Simulations by Daidone et al. also observed formation of β-hairpin and strand-loop-strand (SLS) conformations [88], similar to the ones found for the monomers in aggregates, suggesting that these conformations are important intermediates in the aggregation and fibril growth processes. Application of replica-exchange molecular dynamics (REMD) by Garcia and coworkers showed that much larger structural ensembles could be generated for the Aβ-peptide compared to conventional MD [89].

Atomistic MD simulations have also been used to look into the structures of early aggregates of amyloid peptides. Although simulations of fiber nucleation and elongation for the full peptide are too computationally demanding due to the system size, several shorter segments of Aβ-peptide, taken from residues 16–42, are able to form fibers by themselves. Simulations of these shorter peptides are much more feasible; for example, models consisting of a few (6–8) residues long amyloid peptides have been used to better understand aggregation [92, 93]. It was found that the peptides could organize into both parallel and anti-parallel β-sheets. Smaller peptides preferred anti-parallel structures, while longer peptides preferred parallel or anti-parallel structures, depending on the sequence. Aromatic residues were found to contribute to the stability of parallel β-sheets. Buchete et al. have simulated Aβ-dimers in their preferred parallel β-sheet conformation [94]. The simulated structures were very compact and rigid; additionally, it was found that interior hydration of the β sheets could contribute to the stability of the structures by stabilizing the interior salt bridges. These bridges are believed to be important for the high stability of amyloid fibers. Baftizadeh et al. studied polyvaline peptides as a

model of general peptide aggregation into amyloids [95]. They found that structures of less than six smaller peptide chains are unstable on time scales of 100 ns, while clusters of eight or more chains are stable. Bias exchange metadynamics was used to create a free energy profile of aggregation based on the number of parallel and anti-parallel β-sheets as well as the number of steric zippers. Formation of anti-parallel β-sheet structures is more favorable initially, until a large nucleus is created. After that, introduction of more parallel β-sheets into the structure was observed. The final free-energy-minimum structures consist mostly of parallel β-sheets. Their later study of Aβ-peptide aggregation [96] showed very similar trends, suggesting that there is a common mechanism for peptide aggregation into fibrils. The main difference compared to the polyvaline peptide was that the barrier for the nucleation was much lower.

The process of fibril elongation has been studied by Han et al. by using replica-exchange MD and a hybrid PACE model, consisting of a united-atom model of the proteins and a coarse-grained model of water, to decrease computational costs and accelerate sampling [97]. The simulations showed that Aβ-monomers can associate with the growing fiber in a wide range of different conformations, both disordered or fiber-like, in agreement with experimental kinetic studies. In most cases, the association started from the N-terminal of the monomer and then proceeded to other parts of the peptide. Formation of the SLS structures was often observed after the initial contact with the fiber, confirming their role in fibril growth.

6 The β-Hairpin as a Conformational Switch

The coupling between electrons and protons plays a vital role in a wide range of biological processes, enzyme reactions, solar cells, chemical sensors, and electrochemical devices. Therefore, the mechanism of the electron transfer (ET) reactions and proton-coupled electron transfer (PCET) reactions, involving the transfer of an electron and a proton, has been a subject of great interest. Using both MD simulations and spectroscopy experiments, Hwang et al. studied the potential contribution of the underlying protein's motions in ET and PCET reactions, by observing redox-induced conformational changes in tyrosine-containing β-hairpin maquettes and their variants [3]. In this study, they used a synthetic 18 amino-acid β-hairpin, which contains a tyrosine or a radical-state tyrosine, and a cross-strand amino acid (histidine or cyclohexylalanine), where a kinetically significant PCET reaction is carried out. Their simulations and analysis, which were focused on the stability and dynamics of the β-hairpin, showed that the redox-driven conformational change is associated with a loss of inter-strand backbone hydrogen bonding, as well as π-π stacking between aromatic and cross-strand amino acids due to the rearrangement of charge on the aromatic side chain in the radical state (see Fig. 5).

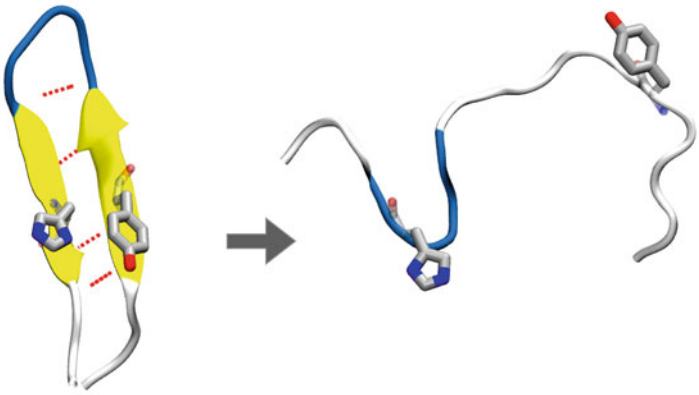

Fig. 5 A conformational transition (folded to unfolded state) of a β-hairpin maquette. Hydrogen bonds are in red. The two aromatic residues involved, tyrosine and histidine, are shown as sticks

A protein's structure is influenced and malleable by several external and environmental factors, such as mechanical force, light, reducing/oxidizing agents, ions, small molecules, and temperature. Resolving the unique influences of each of these factors on protein folding often requires detailed, atomistic investigations. For example, several all-atom MD simulations have been used to illustrate the role of external forces on protein folding/unfolding. The binding of glycoprotein Ib (GPIbα) to von Willebrand factor (vWF) is triggered by flow-induced shear, and it initiates blood clotting. It is suggested that β-hairpin folding of the b-switch region of glycoprotein Iba (GPIbα) increases the affinity of GPIbα binding to vWF. Simulation studies have investigated how readily proteins transitioned from an unstructured to a structured conformation in the presence of a water flow. Chen et al. [98] identified that the entropy of the protein is a dominant factor in transition; the existence of a free-energy barrier prevents spontaneous transition from a loop state, which is entropically more favorable, to a β-hairpin state. This conformational transition can be accomplished in two major steps: flow-induced backbone dihedral rotation followed by a side-group packing. Zou et al. [99] simulated the b-switch with different flow velocities, demonstrating that the mechanism of the flow-induced folding is initiated by hydrophobic collapse, followed by inter-strand hydrogen-bond formation and turn formation.

In another example of investigating controlled conformational change, MD simulations have been applied to a photo-switchable β-hairpin [100, 101]. The β-turn-like structure can be synthesized by replacing the central amino acid pair of a β-turn with a diazobenzene-containing linker. This synthesized peptide is then photo-switchable thanks to the characteristics of diazobenzene, which can undergo a conformational change from *trans* to *cis* when exposed to light of appropriate wavelength. Moreover, the fact that diazobenzene can revert back to *trans* from *cis* enables the peptide's conformation to be reversibly controlled in solution.

7 Methodological Challenges

Practically all examples cited in the preceding sections involved classical atomistic MD simulations. This class of simulations has proven utility demonstrated over more than three decades of applications, but will that utility continue into the future? Limitations abound, including an inability to model processes involving charge transfer, covalent bond formation or breaking, or even ones that just take place over long (millisecond and above) time scales. However, all of these are being addressed. For example, polarizable force fields, e.g., Drude [102], allow for the charge on a given atom to separate in response to electric fields created by its environments. Such separation could be critically important to capture the fine-grained details of the folding of β-sheets just as it has for α-helices [103].

Reactive force fields, which permit covalent bonds to form and break [104], are not routinely utilized for biomolecular simulations. A more common alternative is some variant of hybrid quantum-mechanical/molecular-mechanical (QM/MM) simulations [105]. These simulations maintain a small QM region, usually focused on the active site where bond formation/breaking is occurring, with the rest of system simulated using classical MD. However, this approach brings a new set of challenges, including the appropriate level of theory for the QM region, how to communicate forces between the two regions, and optimizing the overall computational speed between the two disparate types of calculations. Addressing these challenges will increase the range of QM/MM applications, e.g., studying enzymatic reactions such as those mediated by β-hairpin switches.

Finally, reaching appropriate time scales is an omnipresent problem for MD simulations. Typical MD simulations, such as those described in this chapter, range from nanoseconds to microseconds. However, many of the processes of interest take place over milliseconds to seconds or even more. Faster computers can certainly alleviate this problem momentarily, although the gains in time scales have begun to plateau. One recently successful alternative is the development of specialized hardware, namely the Anton supercomputer, which has permitted classical atomistic simulations to reach into the millisecond range [106, 107]. Novel sampling algorithms have also made an impact, e.g., accelerated MD [108], Markov-state models [109], and simulated tempering [110]. Both approaches, namely longer simulations and enhanced sampling, will be required to study, e.g., outer-membrane-protein folding, as well as many other processes, especially those that occur far from equilibrium.

8 Conclusion

While it is clear that MD simulations have made significant contributions to our understanding of β-sheet structures, folding, dynamics, and mechanics, the aforementioned examples are merely a beginning. Improved force fields [102],

simulations extending to milliseconds [106], and creative new approaches [109] will almost certainly provide an accelerating number of breakthroughs in the coming years.

Acknowledgements This work was supported by the National Science Foundation through a CAREER award to JCG (MCB-1452464) and by the National Institutes of Health (R01-GM123169). Computational resources were provided through the Extreme Science and Engineering Discovery Environment (XSEDE), which is supported by NSF grant number OCI-1053575.

References

1. Pavlova A, Hwang H, Lundquist K, Balusek C, Gumbart JC (2016) Living on the edge: simulations of bacterial outer-membrane proteins. Biochim Biophys Acta 1858:1753–1759
2. Moon CP, Zaccai NR, Fleming PJ, Gessmann D, Fleming KG (2013) Membrane protein thermodynamic stability may serve as the energy sink for sorting in the periplasm. Proc Natl Acad Sci USA 110:4285–4290
3. Hwang H, McCaslin TG, Hazel A, Pagba CV, Nevin CM, Pavlova A, Barry BA, Gumbart JC (2017) Redox-driven conformational dynamics in a photosystem-II-inspired β-hairpin maquette determined through spectroscopy and simulation. J Phys Chem B 121:3536–3545
4. Nikaido H, Vaara M (1985) Molecular basis of bacterial outer membrane permeability. Microbiol Rev 49:1–32
5. Marrink SJ, Berendsen, HJC (1994) Simulation of water transport through a lipid membrane. J Phys Chem 98:4155–4168
6. Marrink SJ, Berendsen, HJC (1996) Permeation process of small molecules across lipid membranes studied by molecular dynamics simulations. J Phys Chem 100:16729–16738
7. Bemporad D, Luttmann C, Essex, JW (2004) Computer simulation of small molecule permeation across a lipid bilayer: dependence on bilayer properties and solute volume, size, and cross-sectional area. Biophys J 87:1–13
8. Koebnik R, Locher KP, Van Gelder, P (2000) Structure and function of bacterial outer membrane proteins: barrels in a nutshell. Mol Microbiol 37:239–253
9. Wu E, Engstrom O, Jo S, Stuhlsatz D, Yeom MS, Klauda JB, Widmalm G, Im W (2013) Molecular dynamics simulation and NMR spectroscopy studies of *E. coli* lipopolysaccharide structure and dynamics. Biophys J 105:1444–1455
10. Nikaido H (2003) Molecular basis of bacterial outer membrane permeability revisited. Microbiol Mol Biol Rev 67:593–656
11. Clifton LA, Skoda MW, Le Brun AP, Ciesielski F, Kuzmenko I, Holt SA, Lakey JH (2015) Effect of divalent cation removal on the structure of gram-negative bacterial outer membrane models. Langmuir 31:404–412
12. Wu EL, Cheng X, Jo S, Rui H, Song KC, Davila-Contreras EM, Qi Y, Lee J, Monje-Galvan V, Venable RM, Klauda JB, Im W (2014) CHARMM-GUI Membrane Builder toward realistic biological membrane simulations. J Comput Chem 35:1997–2004
13. Wu E, Fleming PJ, Yeom MS, Widmalm G, Klauda JB, Fleming KG, Im W (2014) *E. coli* outer membrane interactions with OmpLA. Biophys J 106:10174–10177
14. Balusek C, Gumbart JC (2016) Role of the native outer-membrane environment on the transporter BtuB. Biophys J 111:1409–1417
15. Baaden M, Sansom MSP (2004) OmpT: molecular dynamics simulations of an outer membrane enzyme. Biophys J 87:2942–2953
16. Dhakshnamoorthy B, Ziervogel BK, Blachowicz L, Roux B (2013) A structural study of ion permeation in the OmpF porin from anomalous x-ray diffraction and molecular dynamics simulations. J Am Chem Soc 135:1–20

17. Pothula KR, Solano CJ, Kleinekathofer U (2016) Simulations of outer membrane channels and their permeability. Biochim Biophys Acta 1858:1760–1771
18. Tamm LK, Hong H, Liang B (2004) Folding and assembly of β-barrel membrane proteins. Biochim Biophys Acta 1666:250–263
19. Junker M, Schuster CC, McDonnell AV, Sorg KA, Finn MC, Berger PL, Clark B (2006) Pertactin β-helix folding mechanism suggests common themes for the secretion and folding of autotransporter proteins. Proc Natl Acad Sci USA 103:4918–4923
20. Chimento DP, Kadner RJ, Wiener MC (2005) Comparative structural analysis of TonB-dependent outer membrane transporters: implications for the transport cycle. Proteins Struct Funct Bioinf 59:240–251
21. Noinaj N, Guillier M, Barnard TJ, Buchanan SK (2010) TonB-dependent transporters: regulation, structure, and function. Annu Rev Microbiol 64:43–60
22. Chimento DP, Kadner RJ, Wiener MC (2005) Comparative structural analysis of TonB-dependent outer membrane transporters: implications for the transport cycle. Proteins Struct Funct Bioinf 59:240–251
23. Gumbart JC, Wiener MC, Tajkhorshid E (2007) Mechanics of force propagation in TonB-dependent outer membrane transport. Biophys J 93:496–504
24. Noinaj N, Easley NC, Oke M, Mizuno N, Gumbart J, Boura E, Steere AN, Zak O, Aisen P, Tajkhorshid E, Evans RW, Gorringe AR, Mason AB, Steven AC, Buchanan SK (2012) Structural basis for iron piracy by pathogenic Neisseria. Nature 483:53–58
25. Hickman SJ, Cooper REM, Bellucci L, Paci E, Brockwell DJ (2017) Gating of TonB-dependent transporters by substrate-specific forced remodeling. Nat Commun 8:14804
26. Anfinsen CB (1973) Principles that govern the folding of protein chains. Science 181:223–230
27. Blanco FJ, Jiménez MA, Herranz J, Rico M, Santoro J, Nieto JL (1993) NMR evidence of a short linear peptide that folds into a β-hairpin in aqueous solution. J Am Chem Soc 115:5887–5888
28. Blanco FJ, Rivas G, Serrano L (1994) A short linear peptide that folds into a native stable β-hairpin in aqueous solution. Nat Struct Biol 1:584–590
29. Searle MS, Williams DH, Packman LC (1995) A short linear peptide derived from the N-terminal sequence of ubiquitin folds into a water-stable non-native β-hairpin. Nat Struct Biol 2:999–1006
30. de Alba E, Jiménez MA, Rico M, Nieto J (1996) Conformational investigation of designed short linear peptides able to fold into β-hairpin structures in aqueous solution. Fold Des 1:133–144
31. Ramirez-Alvarado M, Blanco FJ, Serrano L (1996) *De novo* design and structural analysis of a model β-hairpin peptide system. Nat Struct Biol 3:604–612
32. Sieber V, Moe GR (1996) Interactions contributing to the formation of a β-hairpin-like structure in a small peptide. Biochemistry 35:181–188
33. Muñoz V, Thompson PA, Hofrichter J, Eaton WA (1997) Folding dynamics and mechanism of β-hairpin formation. Nature 390:196–199
34. Williams S, Causgrove TP, Gilmanshin R, Fang KS, Callender RH, Woodruff WH, Dyer RB (1996) Fast events in protein folding: helix melting and formation in a small peptide. Biochemistry 35:691–697
35. Thompson PA, Eaton WA, Hofrichter J (1997) Laser temperature jump study of the helix-coil kinetics of an alanine peptide interpreted with a 'kinetic zipper' model. Biochemistry 36:9200–9210
36. Dinner AR, Lazaridis T, Karplus M (1999) Understanding β-hairpin formation. Proc Natl Acad Sci USA 96:9068–9073
37. Pande VS, Rokhsar DS (1999) Molecular dynamics simulations of unfolding and refolding of a β-hairpin fragment of protein G. Proc Natl Acad Sci USA 96:9062–9067
38. García AE, Sanbonmatsu KY (2001) Exploring the energy landscape of a β hairpin in explicit solvent. Proteins Struct Funct Gen 42:345–354

39. Ma B, Nussinov R (2000) Molecular dynamics simulations of a β-hairpin fragment of protein G: balance between side-chain and backbone forces. J Mol Biol 296:1091–1104
40. Zagrovic B, Sorin EJ, Pande V (2001) β-Hairpin folding simulations in atomistic detail using an implicit solvent model. J Mol Biol 313:151–169
41. Zhou R, Berne BJ (2002) Can a continuum solvent model reproduce the free energy landscape of a β-hairpin folding in water? Proc Natl Acad Sci USA 99:12777–12782
42. Shao Q, Yang L, Gao YQ (2009) A test of implicit solvent models on the folding simulation of the GB1 peptide. J Chem Phys 130:195104
43. Wei G, Derreumaux P, Mousseau N (2003) Sampling the complex energy landscape of a simple β-hairpin. J Chem Phys 119:6403–6406
44. Bonomi M, Branduardi D, Gervasio FL, Parrinello M (2008) The unfolded ensemble and folding mechanism of the C-terminal GB1 β-hairpin. J Am Chem Soc 130:13938–13944
45. Santiveri CM, Jiménez MÁ, Rico M, van Gunsteren WR, Daura X (2004) β-Hairpin folding and stability: molecular dynamics simulations of designed peptides in aqueous solution. J Pept Sci 10:546–565
46. Smith AW, Lessing J, Ganim Z, Peng CS, Tokmakoff A, Roy S, Jansen TLC, Knoester J (2010) Melting of a β-hairpin using isotope-edited 2D IR spectroscopy and simulations. J Phys Chem B 114:10913–10924
47. Davis CM, Dyer RB (2016) The role of electrostatic interactions in folding of β-proteins. J Am Chem Soc 138:1456–1464
48. Tomlinson JH, Ullah S, Hansen PE, Williamson MP (2009) Characterization of salt bridges to lysines in the protein G B1 domain. J Am Chem Soc 131:4674–4684
49. Evans DA, Wales DJ (2004) Folding of the GB1 hairpin peptide from discrete path sampling. J Chem Phys 121:1080–1090
50. Yoda T, Sugita Y, Okamoto Y (2007) Cooperative folding mechanism of a β-hairpin peptide studied by a multicanonical replica-exchange molecular dynamics simulation. Proteins Struct Funct Bioinf 66:846–859
51. Sancho DD, Mittal J, Best RB (2013) Folding kinetics and unfolded state dynamics of the GB1 hairpin from molecular simulation. J Chem Theory Comput 9:1743–1753
52. Best RB, Mittal J (2011) Free-energy landscape of the GB1 hairpin in all-atom explicit solvent simulations with different force fields: similarities and differences. Proteins Struct Funct Bioinf 79:1318–1328
53. Hagan CL, Silhavy TJ, Kahne D (2011) β-Barrel membrane protein assembly by the Bam complex. Annu Rev Biochem 80:189–210
54. Paramasivam N, Habeck M, Linke D (2012) Is the C-terminal insertional signal in Gram-negative bacterial outer membrane proteins species-specific or not? BMC Genomics 13:510
55. Anwari K, Poggio S, Perry A, Gatsos X, Ramarathinam SH, Williamson NA, Noinaj N, Buchanan S, Gabriel K, Purcell AW, Jacobs-Wagner C, Lithgow T (2010) A modular BAM complex in the outer membrane of the alpha-proteobacterium Caulobacter crescentus. PLoS One 5:e8619
56. Knowles TJ, Scott-Tucker A, Overduin M, Henderson IR (2009) Membrane protein architects: the role of the BAM complex in outer membrane protein assembly. Nat Rev Microbiol 7:206–214
57. Albrecht R, Zeth K (2011) Structural basis of outer membrane protein biogenesis in bacteria. J Biol Chem 286:27792–27803
58. Kim KH, Paetzel M (2011) Crystal structure of Escherichia coli BamB, a lipoprotein component of the β-barrel assembly machinery complex. J Mol Biol 406:667–678
59. Noinaj N, Fairman JW, Buchanan SK (2011) The crystal structure of BamB suggests interactions with BamA and its role within the BAM complex. J Mol Biol 407:248–260
60. Kim KH, Aulakh S, Tan W, Paetzel M (2011) Crystallographic analysis of the C-terminal domain of the Escherichia coli lipoprotein BamC. Acta Crystallogr Sect F Struct Biol Cryst Commun 67:1350–1358
61. Warner LR, Varga K, Lange OF, Baker SL, Baker D, Sousa MC, Pardi A (2011) Structure of the BamC two-domain protein obtained by Rosetta with a limited NMR data set. J Mol Biol 411:83–95

62. Sandoval CM, Baker SL, Jansen K, Metzner SI, Sousa MC (2011) Crystal structure of BamD: an essential component of the β-Barrel assembly machinery of gram-negative bacteria. J Mol Biol 409:348–357
63. Dong C, Hou HF, Yang X, Shen YQ, Dong YH (2012) Structure of Escherichia coli BamD and its functional implications in outer membrane protein assembly. Acta Crystallogr D Biol Crystallogr 68:95–101
64. Kim S, Malinverni JC, Sliz P, Silhavy TJ, Harrison SC, Kahne D (2007) Structure and function of an essential component of the outer membrane protein assembly machine. Science 317:961–964
65. Noinaj N, Kuszak AJ, Gumbart JC, Lukacik P, Chang H, Easley NC, Lithgow T, Buchanan SK (2013) Structural insight into the biogenesis of β-barrel membrane proteins. Nature 501:385–390
66. Noinaj N, Rollauer SE, Buchanan SK (2015) The β-barrel membrane protein insertase machinery from Gram-negative bacteria. Curr Opin Struct Biol 31:35–42
67. O'Neil PK, Rollauer SE, Noinaj N, Buchanan SK (2015) Fitting the Pieces of the β-Barrel Assembly Machinery Complex. Biochemistry 54:6303–6311
68. Bakelar J, Buchanan SK, Noinaj N (2016) The structure of the β-barrel assembly machinery complex. Science 351:180–186
69. Gu Y, Li H, Dong H, Zeng Y, Zhang Z, Paterson NG, Stansfeld PJ, Wang Z, Zhang Y, Wang W, Dong C (2016) Structural basis of outer membrane protein insertion by the BAM complex. Nature 531:64–69
70. Han L, Zheng J, Wang Y, Yang X, Liu Y, Sun C, Cao B, Zhou H, Ni D, Lou J, Zhao Y, Huang Y (2016) Structure of the BAM complex and its implications for biogenesis of outer-membrane proteins. Nat Struct Mol Biol 23:192–196
71. Iadanza MG, Higgins AJ, Schiffrin B, Calabrese AN, Brockwell DJ, Ashcroft AE, Radford SE, Ranson NA (2016) Lateral opening in the intact β-barrel assembly machinery captured by cryo-EM. Nat Commun 7:12865
72. Noinaj N, Kuszak AJ, Balusek C, Gumbart JC, Buchanan SK (2014) Lateral opening and exit pore formation are required for BamA function. Structure 22:1055–1062
73. Fleming PJ, Patel DS, Wu EL, Qi Y, Yeom MS, Sousa MC, Fleming KG, Im W (2016) BamA POTRA domain interacts with a native lipid membrane surface. Biophys J 110:2698–2709
74. Webb CT, Selkrig J, Perry AJ, Noinaj N, Buchanan SK, Lithgow T (2012) Dynamic association of BAM complex modules includes surface exposure of the lipoprotein BamC. J Mol Biol 422:545–555
75. van den Berg B (2013) Lateral gates: β-barrels get in on the act. Nat Struct Mol Biol 20:1237–1239
76. Kim KH, Aulakh S, Paetzel M (2012) The bacterial outer membrane β-barrel assembly machinery. Protein Sci 21:751–768
77. Dong H, Xiang Q, Gu Y, Wang Z, Paterson NG, Stansfeld PJ, He C, Zhang Y, Wang W, Dong C (2014) Structural basis for outer membrane lipopolysaccharide insertion. Nature 511:52–56
78. Chiti F, Taddei N, Baroni F, Capanni C, Stefani M, Ramponi G, Dobson CM (2002) Kinetic partitioning of protein folding and aggregation. Nat Struct Biol 9:137–143
79. Ross CA, Poirier MA (2004) Protein aggregation and neurodegenerative disease. Nat Med 10:S10–S17
80. Nguyen PH, Li MS, Stock G, Straub JE, Thirumalai D (2007) Monomer adds to preformed structured oligomers of Aβ-peptides by a two-stage dock–lock mechanism. Proc Natl Acad Sci USA 104:111–116
81. Nguyen P, Derreumaux P (2014) Understanding amyloid fibril nucleation and Aβ oligomer/drug interactions from computer simulations. Acc Chem Res 47:603–611
82. Riek R, Eisenberg DS (2016) The activities of amyloids from a structural perspective. Nature 539:227–235
83. Sticht H, Bayer P, Willbold D, Dames S, Hilbich C, Beyreuther K, Frank RW, Rösch P (1995) Structure of amyloid A4-(1–40)-peptide of Alzheimer's disease. Eur J Biochem 233:293–298

84. Massi F, Straub JE (2001) Probing the origins of increased activity of the E22Q Dutch mutant Alzheimer's β-amyloid peptide. Biophys J 81:697–709
85. Massi F, Peng JW, Lee JP, Straub JE (2001) Simulation study of the structure and dynamics of the Alzheimer's amyloid peptide congener in solution. Biophys J 80:31–44
86. Massi F, Klimov D, Thirumalai D, Straub JE (2002) Charge states rather than propensity for β-structure determine enhanced fibrillogenesis in wild-type Alzheimer's β-amyloid peptide compared to E22Q dutch mutant. Protein Sci 11:1639–1647
87. Valerio M, Colosimo A, Conti F, Giuliani A, Grottesi A, Manetti C, Zbilut JP (2005) Early events in protein aggregation: molecular flexibility and hydrophobicity/charge interaction in amyloid peptides as studied by molecular dynamics simulations. Proteins Struct Funct Bioinf 58:110–118
88. Daidone I, Simona F, Roccatano D, Broglia RA, Tiana G, Colombo G, Di Nola A (2004) β-Hairpin conformation of fibrillogenic peptides: structure and α-β transition mechanism revealed by molecular dynamics simulations. Proteins Struct Funct Bioinf 57:198–204
89. Rosenman DJ, Connors C, Chen W, Wang C, García AE (2013) Aβ monomers transiently sample oligomer and fibril-like configurations: ensemble characterization using a combined MD/NMR approach. J Mol Biol 425:3338–3359
90. Colvin MT, Silvers R, Ni QZ, Can TV, Sergeyev I, Rosay M, Donovan KJ, Michael B, Wall J, Linse S, Griffin RG (2016) Atomic resolution structure of monomorphic Aβ42 amyloid fibrils. J Am Chem Soc 138:9663–9674
91. Liou YC, Tocilj A, Davies PL, Jia Z (2000) Mimicry of ice structure by surface hydroxyls and water of a β-helix antifreeze protein. Nature 406:322–324
92. Gsponer J, Haberthür U, Caflisch A (2003) The role of side-chain interactions in the early steps of aggregation: molecular dynamics simulations of an amyloid-forming peptide from the yeast prion Sup35. Proc Natl Acad Sci USA 100:5154–5159
93. Ma B, Nussinov R (2002) Stabilities and conformations of Alzheimer's β-amyloid peptide oligomers (Aβ16–22, Aβ16–35, and Aβ10–35): sequence effects. Proc Natl Acad Sci USA 99:14126–14131
94. Buchete N-V, Tycko R, Hummer G (2005) Molecular dynamics simulations of Alzheimer's β-amyloid protofilaments. J Mol Biol 353:804–821
95. Baftizadeh F, Biarnes X, Pietrucci F, Affinito F, Laio A (2012) Multidimensional view of amyloid fibril nucleation in atomistic detail. J Am Chem Soc 134:3886–3894
96. Baftizadeh F, Pietrucci F, Biarnés X, Laio A (2013) Nucleation process of a fibril precursor in the C-terminal segment of amyloid-β. Phys Rev Lett 110:168103
97. Han W, Schulten K (2014) Fibril elongation by Aβ(17–42): kinetic network analysis of hybrid-resolution molecular dynamics simulations. J Am Chem Soc 136:12450–12460
98. Chen Z, Lou J, Zhu C, Schulten K (2008) Flow-induced structural transition in the β-switch region of glycoprotein Ib. Biophys J 95:1303–1313
99. Zou X, Liu Y, Chen Z, Cárdenas-Jirón GI, Schulten K (2010) Flow-induced β-hairpin folding of the Glycoprotein Ibα β-switch. Biophys J 99:1182–1191
100. Kräutler V, Aemissegger A, Hünenberger PH, Hilvert D, Hansson T, van Gunsteren WF (2005) Use of molecular dynamics in the design and structure determination of a photoinducible β-hairpin. J Am Chem Soc 127:4935–4942
101. Aemissegger A, Kräutler V, van Gunsteren WF, Hilvert D (2005) A photoinducible β-hairpin. J Am Chem Soc 127:2929–2936
102. Lemkul JA, Huang J, Roux B, MacKerell AD (2016) An empirical polarizable force field based on the classical Drude oscillator model: development history and recent applications. Chem Rev 116:4983–5013
103. Huang J, MacKerell Jr AD (2014) Induction of peptide bond dipoles drives cooperative helix formation in the (AAQAA)3 peptide. Biophys J 107:991–997
104. Senftle TP, Hong S, Islam MM, Kylasa SB, Zheng Y, Shin YK, Junkermeier C, Engel-Herbert R, Janik MJ, Aktulga HM, Verstraelen T, Grama A, van Duin ACT (2016) The ReaxFF reactive force-field: development, applications and future directions. NPJ Comput Mater 2:15011

105. van der Kamp MW, Mulholland AJ (2013) Combined quantum mechanics/molecular mechanics (QM/MM) methods in computational enzymology. Biochemistry. 52:2708–2728
106. Shaw DE, Maragakis P, Lindorff-Larsen K, Piana S, Dror RO, Eastwood MP, Bank JA, Jumper JM, Salmon JK, Shan Y, Wriggers W (2010) Atomic-level characterization of the structural dynamics of proteins. Science 330:341–346
107. Lindorff-Larsen K, Maragakis P, Piana S, Shaw DE (2016) Picosecond to millisecond structural dynamics in human ubiquitin. J Phys Chem B 120:8313–8320
108. Pierce LC, Salomon-Ferrer R, Augusto C, de Oliveira F, McCammon JA, Walker RC (2012) Routine access to millisecond time scale events with accelerated molecular dynamics. J Chem Theory Comput 8:2997–3002
109. Harrigan MP, Sultan MM, Hernandez CX, Husic BE, Eastman P, Schwantes CR, Beauchamp KA, McGibbon RT, Pande VS (2017) MSMBuilder: statistical models for biomolecular dynamics. Biophys J 112:10–15
110. Pan AC, Weinreich TM, Piana S, Shaw DE (2016) Demonstrating an order-of-magnitude sampling enhancement in molecular dynamics simulations of complex protein systems. J Chem Theory Comput 12:1360–1367

MicroRNAs, Gene's Regulator in Prostate Cancer

David Alejandro de la Rosa Pérez, Carlos Omar Germán-Garrido, Raúl Aragón-Franco, Jose Gadú Campos-Saucedo, Cesar López-Camarillo, Minerva Camacho-Nuez, and María Elizbeth Alvarez-Sánchez

Abstract Since the discovery of microRNAs (miRNAS) in 1993, findings in gene regulation have increased in the biological scenery. miRNAs have shown an important role in the modulation of a wide collection of physiological and pathological processes, starting on embryonic evolution with carcinomas development. Nowadays, the high availability of gene expression data and the development of computational approaches that predicts miRNA targets are continuously increasing the knowledge about miRNA functions, as well as the sources and consequences of miRNA deregulation within a wide interaction network. In this chapter, knowledge of miRNA expression and its function on prostate cancer is presented.

Keywords MicroRNA · Circulating miRNA · Biomarkers · Cancer · Prostate

1 Introduction

MicroRNAs (miRNAs) are a family of small regulatory RNAs that control the expression of specific genes in a post-transcriptional level by base-pairing typically to the 3′-untranslated regions (3′UTRs) of a target messenger RNAs (mRNAs) to direct a reduction in either translation or stability [1]. They are members of the family of small non-coding RNAs that are endogenous small interfering RNAs (endo-siRNAs), such as PIWI-single-stranded non-coding RNAs ofo 20–23 interacting RNAs (pi-RNAs) [2, 3]. MiRNAs are involved in a broad range

D. A. de la Rosa Pérez · C. López-Camarillo · M. Camacho-Nuez · M. E. Alvarez-Sánchez (✉)
Posgrado en Ciencias Genómicas, Universidad Autónoma de la Ciudad de México (UACM), Ciudad de México, Mexico
e-mail: maria.alvarez@uacm.edu.mx

C. O. Germán-Garrido
Escuela Militar de Graduados de Sanidad, Ciudad de México, Mexico

R. Aragón-Franco · J. G. Campos-Saucedo
Hospital Central Militar, Dirección General de Sanidad SEDENA, Ciudad de México, Mexico

L. Olivares-Quiroz, O. Resendis-Antonio (eds.), *Quantitative Models for Microscopic to Macroscopic Biological Macromolecules and Tissues*,
https://doi.org/10.1007/978-3-319-73975-5_2

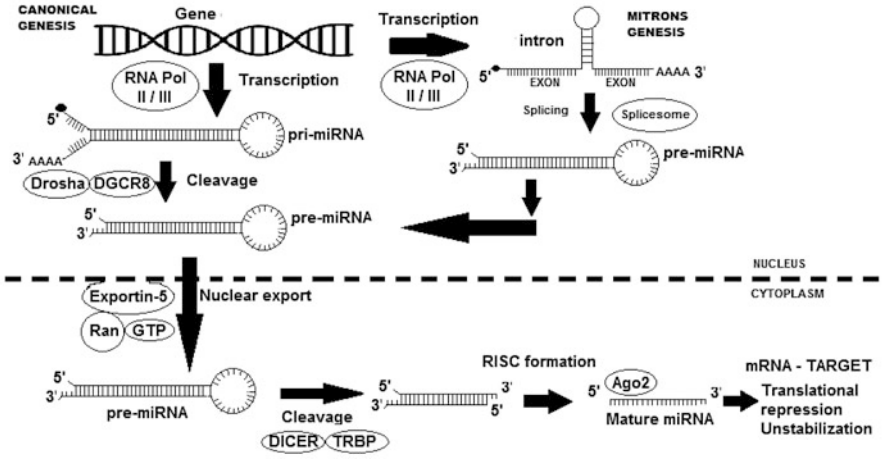

Fig. 1 Canonical and non-canonical (mitrons) microRNA genesis

of cellular functions, as developmental, cell differentiation and cell maintenance functions [4]. MiRNAs are distributed throughout the genome, they can be found as isolated transcript units or clustered and co-transcribed as polycistronic primary transcripts [5] and can either be encoded within protein coding genes in both introns and exons or transcribed from independent genes as intergenic regions. MiRNA transcription can be carried out by RNA polymerase III and II to produce the primary transcripts (primiRNAs) [6, 7], which are thousands nucleotide long capped and polyadenylated hairpin-shaped transcripts. In the canonical miRNA genesis pathway, pri-miRNAs are recognized and cleaved in the nucleus then the mature miRNAs are generated by several processing steps of endonucleolytic cleavages in the cytoplasm. The cleave in the nucleus is carried out by an RNase III enzyme named Drosha, which acts with the microprocessor complex subunit DGCR8 (a molecular anchor necessary for the recognition of pri-miRNA at dsRNA-ssRNA junction) and cleaves 11 bp away from the junction to release hairpin-shaped pre-miRNAs that are subsequently cut by the cytoplasmic RNase III enzyme called DICER to generate mature miRNAs [8–13] (Fig. 1). An alternative miRNAs biogenesis pathway called Mitrons-pathway has been described, miRNAs is embedded in short mRNA introns, then pre-miRNAs are produced unending Drosha cleave, those are completed from splicing and debranching [14, 15]. In both miRNAs pathways, pre-miRNAs are transported into the cytoplasm by exportin 5 and Ran-GTP. In the cytoplasm Dicer joined to TRBP (Trans activated response [TAR] RNA Binding protein) cleaves the terminal loop end of the pre-miRNA producing a short double-stranded RNA duplex that measure around 20–23 bp length. The strand of the duplex with a less thermodynamically stable 5′ end is preferentially conjugated to an Argonaute protein forming the miRNA-induced silencing complex (RISC) [16], however in some cases the complementary strand can be used in the RISC complex [17, 18].

The mature miRNA joined to RISC binds to the mRNA in the 3′ UTR, or in less cases in the coding region, based on complementarity between the miRNA and the mRNA target. Seed sequence, nucleotides 2–8 (counted from the 5′ end) of the mature miRNA [1, 19] is critical for target recognition and hybridizes nearly perfectly with the target mRNA [5].

The understanding of miRNA functions into a network context and the signaling or metabolic pathways with the consequences that their deregulation can produce has been achieved by novelty advances, as the genome-wide identification of miRNA–target, the RNA sequencing.

In the last two decades, several strategies have been used to identify miRNA targets, physical association and/or the correlation of gene expression. Lists of target genes can then be examined collectively in the contexts of KEGG pathways (KEGG PATHWAY is a collection of manually drawn pathway maps representing our knowledge on the molecular interaction, reaction and relation networks for: (1) Metabolism, (2) Genetic information processing, (3) Environmental information processing, (4) Cellular processes, (5) Organismal systems, (6) Human diseases, and (7) Drug development) (http://www.genome.jp/kegg/pathway.html) [20–22], protein–protein interaction networks [23–26] and enrichment analysis for common gene ontology terms [27, 28]. Several computational tools for target enrichment analysis facilitate the identification of hierarchical functions of miRNAs in gene regulatory networks (Table 1). The involvement of miRNAs in signaling pathways and genetic networks provides a challenge to understanding their function. The level of evidence required to establish miRNA–target relationships is set too low that the genuine interactions are eclipsed by noise.

Recently it has been proposed five steps (or levels) to unravel the specific role of miRNA. In the *level 1* the objective is to find or identify a specific microRNA (from the vast list of known microRNAs) and enlist pathways expected to be involved in a disease under study, increasing the probability to associate a miRNA with the disease and create a base to identify the pathway. The condition of a miRNA under a cellular condition can be achieved by the micro-array/transcriptome technique; *level 2* The next step is to identify the status of the miRNA and the key pathway specific genes expression in the selected disease. This is achieved through a database search. Alternatively, the absence of enough published information, conducting a case-control or a pair (tumor and normal tissue) study in cancer could help to establish the status of the microRNA and the key genes, preferably representing the pathway specific markers; *level 3* the predicted miRNA targets need to be experimentally validated. Many human miRNAs are released in the latest version of miRBase (Release 20), but yet many remain to be identified. In the last ten years several algorithms have been developed to identify targets for miRNAs, those are based on the conservation of seed region and binding energy, however, recently some of the algorithms (TargetScan, miRanda, RNA22, PICTAR, PITA, RNAhybrid, DIANA-microT, mirSVR, microInspector, mirTarget2) have incorporated expression profiles in their scoring function [29], helping to increase the accuracy of prediction. It has been observed that the stability of miRNA seed sequences was evolutionarily selected according to the adaptive temperature of each organism, however non-

Table 1 Bioinformatics tools used for miRNA target prediction

Name	Web site	Observations
miTEA (miRNA target enrichment analysis)	http://cbl-gorilla.cs.technion.ac.il/miTEA	miTEA is a tool for identifying and visualizing enriched miRNA targets in ranked lists of genes It searches for enriched miRNA targets that appear densely at the top of a ranked list of genes The search is commanded by a list of genes provided by the user which also select the species and the prediction tool, obtaining a list of miRNAs predicted to target the gene list
DIANA mirPath	http://snf-515788.vm.okeanos.grnet.gr/	DIANA-mirPath is a miRNA pathway analysis web-server, providing accurate statistics, while being able to accommodate advanced pipelines. mirPath can utilize predicted miRNA targets (in CDS or 3′-UTR regions) provided by the DIANA-microT-CDS algorithm or even experimentally validated miRNA interactions derived from DIANA-TarBase. Using this analysis the user will achieve schematics pathways marking the proteins that can be affected by the selected miRNA
miRTrail	http://mirtrail.bioinf.uni-sb.de	miRTrail allows to do an analysis for potential relationships between a set of miRNAs and a set of mRNAs, the miRNA and mRNA information must be uploaded. At the moment, miRTrail supports miRBase identifiers for miRNAs and GeneSymbol identifiers for the mRNAs
CoMeTa	http://cometa.tigem.it/index.php	CoMeTa allows the Co-expression and Meta-analysis of miRNA Targets, based on the assumption that the targets of a given miRNA are likely to be co-expressed and therefore to belong to the same miRNA gene network. The CoMeTa tool aims at the inference of miRNA targets and miRNA-regulated gene networks by integrating expression data from hundreds of cellular and tissue conditions
mirTarVis	http://hcil.snu.ac.kr/~rati/miRTarVis/index	miRTarVIs is a visual analysis tool for miRNA–mRNA expression profile data, the tool is downloadable to a personal computer with all the database, making the analysis available without an internet connection

(continued)

Table 1 (continued)

Name	Web site	Observations
miRNet	http://www.mirnet.ca	miRNet is a tool with comprehensive support for statistical analysis and functional interpretation of data generated in miRNAs studies Able to support several inputs and statistics, comprehensive functional annotations, creating miRNA–Target interaction networks (miRNA-gene, miRNA-disease, miRNA-small molecule, miRNA-lncRNA, miRNA-epigenetic modifier)
Mirin	http://mirin.ym.edu.tw	Mirin is an online tool for identification of microRNA-mediated module which is formed by protein–protein interactions (PPIs). Mirin integrates microRNA regulations and PPIs with microRNA/mRNA expression data to identify the perturbed microRNA regulatory modules and reveals their functional roles in specific biological conditions
MAGIA (miRNA and genes integrated analysis)	http://gencomp.bio.unipd.it/magia	Magia tool is able to do miRNA target predictions and analysis of miRNA and gene expression profiles by a combination of expression profiles and statistical measures
miEAA (miRNA enrichment analysis and annotation)	http://www.ccb.uni-saarland.de/mieaa_tool	This tool (miEAA) facilitates the functional analysis of sets of miRNAs. It is based on GeneTrail, which is an enrichment analysis tool for gene sets
miRSystem	http://mirsystem.cgm.ntu.edu.tw	miRSystem is a database which integrates seven well-known miRNA target gene prediction programs: DIANA, miRanda, miRBridge, PicTar, PITA, rna22, and TargetScan, supporting only *Homo sapiens* and *Mus musculus* miRNAs
CORNA	http://corna.sf.net	CORNA is a tool written in R, which allows users to test for over-representation of microRNA-target associations using one of three separate statistical tests

(continued)

Table 1 (continued)

Name	Web site	Observations
MMIA (miRNA and mRNA integrated analysis)	http://epigenomics.snu.ac.kr/MMIA/mmia_main.html	MMIA integrates microRNA and mRNA expression data with predicted microRNA target information for analyzing microRNA-associated phenotypes and biological functions by Gene Set Enrichment Analysis (GSEA). To assign biological relevance to the integrated microRNA/mRNA profiles, MMIA uses exhaustive human genome coverage (5782 gene sets), including various disease-associated genes as well as conventional canonical pathways and Gene Ontology
FAME (functional assignment of miRNAs by enrichment)	http://acgt.cs.tau.ac.il/fame	FAME is a tool that uses computational target predictions in order to infer the processes affected by human miRNAs. The approach improves upon standard statistical tools by addressing specific characteristics of miRNA regulation
miSEA (miRNA set enrichment analysis)	http://www.baskent.edu.tr/~hogul/misea	miSEA, which evaluates the enrichment of predefined sets in a microRNA expression profiling experiment with two biological conditions, e.g. control vs. treatment. miSEA allows users to select amongst a large set of microRNA grouping categories, such as family classification, disease association, and genome coordinate

conserved binding sites also mediate repression in translation, so new algorithms should incorporate non-conserved binding sites to avoid false negatives predicted results. In the *level 4*, it is needed to co-relate the gene and the miRNA expression data. Those pathways should be regulated directly by the miRNA according to the results obtained in the first three levels. Bioinformatics tools as Central Pathway or Cytoscape could be used for this propose. In the *level 5* it should be proved the association of miRNA with the identified pathway experimentally and preferably in a tissue specific manner in concordance with the settled in level 1 [30].

2 MiRNAs in Cancer

As it has been discussed, miRNAs play a main role in gene expression control at post-transcriptional level, when the miRNAs are deregulated several kinds of pathological diseases can occur, one of the diseases with a main interest in the

study for miRNAs is the cancer. Key processes in cancer biology are related to the "hallmarks of Cancer" (HC). The HC comprise six biological capabilities acquired during the multi-step development of human tumors, and constitute an organizing principle for rationalizing the complexities of neoplastic disease. They include sustaining proliferate signaling, evading growth suppressors, resisting cell death, inducing angiogenesis, and activating invasion and metastasis. Underlying these hallmarks is genome instability, which generates the genetic diversity that expedites their acquisition, evasion of the immune system, deregulation of energy metabolism and inflammation, which fosters multiple hallmark functions [31].

Apoptosis plays a significant role in both animal development and disease, the deregulation of this process has been invariably linked to the progression of various neoplastic processes. miRNAs that regulate apoptosis, termed apoptomiRs, can be either pro- or antiapoptotic [32]. The first miRNA described as a regulator of apoptosis was the Drosophila bantam gene, which directly suppressed the proapoptotic factor hid, thus facilitating proliferation [33, 34]. Several miRNAs that play a role in modulating apoptosis have also been linked to the initiation and progression of various neoplastic processes. Approximately 50% of miRNAs are located at genomic sites that are disrupted or amplified in various cancers [35]. The first evidence of miRNAs playing a role in cancer development came to light in 2002 in a study [36] that attempted to find tumor suppressor genes at chromosome 13q14, which is frequently deleted in chronic lymphocytic leukemia (CLL) [37]. CLL is characterized by the presence of substantial increased numbers of predominantly non-dividing malignant B cells over-expressing the antiapoptotic B-cell lymphoma 2 (Bcl2) protein. In patients with CLL, the tumor suppressor locus on chromosome 13q14 was found to be frequently altered. However, instead of coding for a tumor suppressor protein, this region contained two miRNA genes, miR-15a and miR-16-1, which are overexpressed, regulating negatively the antiapoptotic *bcl2* gene at posttranscriptional level. Later, many miRNAs with tumor suppressor roles were identified. The miR-34 family, for example, has been shown to exert significant tumor suppressor capabilities. Up-regulation of p53 (a potent tumor suppressor/cell cycle regulator) caused increased miR-34 expression that resulted in G1 arrest in a complementary and parallel fashion to mRNAs that are directly activated by P53 [35, 38]. Also, miR-34 was shown to inhibit the silent mating information regulator 1 (SIRT1) gene resulting in the upregulation of P53, P21, and PUMA (P53-upregulated modulator of apoptosis), thus regulating cell cycle and apoptosis and functioning as a tumor suppressor by modulating the SIRT1-P53 pathway [39]. Furthermore, miR-34 has mediated growth arrest via direct regulation of cell cycle regulatory factors, such as cyclin E2 (CCNE2), cyclin-dependent kinase 4 (CDK4), the transcription factor E2F3, and the hepatocyte growth factor receptor (c-MET), ultimately leading to increased caspase-dependent cell death [34]. In a separate study, miR-34 inhibited the proliferation/growth of human pancreatic tumor–initiating cells, and its overexpression in P53-deficient human pancreatic cancer cells partially restored the tumor-suppressing function of P53 [68]. MCL-1, a member of the BCL-2 family, was also demonstrated to be posttranscriptionally

regulated by miR-29a, b, and c [40, 41]. Forced expression of miR-29b to induce tumor cell apoptosis by reducing MCL-1 expression may represent a novel intervention for cancer therapy. Along similar lines, let-7a exerts tumor suppressor functions by directly targeting the expression of *ras* and *hmga2*, 2 widely recognized oncogenes [42, 43]. Other examples of tumor suppressor miRNAs include miR-7, miR-124, miR-137, miR-146b, miR-15b, miR-128, and miR-326. Furthermore, knockdown of mature miRNAs by selectively targeting *dicer1*, *rnasen*, and its cofactor dgcr8 increased the oncogenic potential of transformed cell lines, resulting in the accelerated tumor formation in mouse models of K-RAS-driven lung cancer and Rb-driven retinoblastoma [44–47].

MiRNAs can also promote tumor development (oncomiRs) depending on the functions of the target protein(s) they regulate. These oncogenic miRNAs include miR-155 and the miR-17-92 cluster that accelerates the tumor development in B-cell lymphomas [48, 49]. Ectopic expression of miR-155 in transgenic mice resulted in pre-B-cell expansion, splenomegaly, and lymphopenia that preceded the development of lymphoblastic leukemia and lymphoma [50]. Now it is known that mir-155 plays a critical role in the development of lymphomas, the components of its regulatory pathways upstream and downstream of the targets remain unclear. It is interesting to note that even before the discovery of miRNAs in mammalian cells, Tam et al. [54] had reported that "bic" locus, the common retroviral integration site for the avian leukosis virus, generated a non-coding RNA. Later, after the discovery of miRNAs, it was found that this transcript harbored the mature miR-155 coding sequence, thus offering a potential explanation for the function of bic [55]. Members of the mir-17-92 cluster are potent activators of cell proliferation and are frequently overexpressed in several neoplasms, including lymphoma, multiple myeloma, medulloblastoma, and cancers of the lung, colon, breast, and prostate [44]. miR-21 is another commonly upregulated miRNA in cancers that include glioblastoma, lymphomas, and cancers of the breast, ovary, colon, rectum, pancreas, lung, liver, gallbladder, prostate, stomach, thyroid, and cervix [44, 51]. Increased expression of miR-21 was found in glioblastoma tumors and cell lines, and its inhibition resulted in increased cell death, suggesting that miR-21 could play the role of an oncogene that inhibited cell death in these tumors [85]. For example, in prostate cancer it has been found that miR21 controls the expression of many mRNA targets related to micro-vascular proliferation and tumor invasiveness, correlating with weak biochemical recurrence-free survival having a predictive value for biochemical recurrence risk in prostate cancer patients after radical prostatectomy [68], and also correlating with castration resistance and metastatic disease. Furthermore, in glioblastoma cells, knockdown of miR-21 induced the activation of caspase-3, transforming growth factor-β, P53, and mitochondrial apoptotic pathways mainly through upregulation of its validated targets, heterogeneous nuclear ribonucleoprotein K, P53-related TAP63, and PDCD4, acting in synergy with the aforementioned proteins [51–53].

3 miRNAs in Prostate Cancer

Prostate cancer is the second place occurring cancer in men worldwide and the first place in mortality [54]. Prostate cancer (PCa) occurrence and mortality are up to 20-fold higher in developed countries with respect to emerging ones, diet and lifestyle have been proposed as factors causing this discrepancy, both modify serum factors that slow down the growth and induce apoptosis in androgen-dependent PCa cells, while high body mass index, blood pressure, and several metabolic factors were correlated with high risk of prostate cancer death [54]. Mortality rates are clearly differentiated by ethnicity. Caribbean hold the highest rates in the world (26.3%), following sub-Saharan Africans (10%) and, at last, the Asians show the lowest (2.5%). In the United States of America it was found that the risk of developing prostate cancer is highest in African Americans, in compared to other populations [55].

As it was discussed above miRNAs are deregulated in several disorders also in cancer. Deregulation can increase or decrease their concentration into the affected cell, and according to their function in normal concentrations miRNAs can be classified as oncogenic miRNAs (oncomiR) and tumor suppressor miRNAs. It has been reported several miRNAs with their respective functions in prostate cancer (Table 2).

4 Circulating miRNAs as Possible Biomarkers in Prostate Cancer

Prostate cancer can be clinically diagnosed as local or advanced and different treatments including observation, radiotherapy, radical prostatectomy, and androgen-deprivation treatment are expected [56–59].

The main screening exams to diagnose prostate cancer include digital rectal exam (DRE), serum level of prostate-specific antigen (PSA), and transrectal ultrasound guided biopsy. A suspected DRE alone reveals prostate cancer, regardless of normal PSA level (in about 18% of all patients; moreover, a suspected digital rectal exam has a positive predictive value of 5–30% in patients who have a PSA level up to 2 ng/mL). Nowadays, PSA assessment is the most usual marker able to correlate with prostate cancer risk, aggressiveness, and outcome in order to detect prostate cancer [60]. Nevertheless, it has been found that several patients develop prostate cancer in spite of low PSA levels though a higher PSA level shows the presence of prostate cancer [61, 62]. High PSA levels could be the result of several factors as well as benign prostatic hyperplasia, gland inflammation, prostatitis, infection, and some drugs [63–66]. PSA screening is usually associated with over-diagnosis, although it has decreased the death rate of prostate cancer [67]. For this reason, efforts to find new biomarkers that enhance the accuracy of screening should be continued.

Table 2 List of miRNAs founded in prostate cancer cell lines and prostate cancer tissue

Oncogenic miRNAs	Function	Tumor suppressor miRNAs	Function
miR-221/ miR-222	Enhances cell proliferation, invasion, cell survival, increases clonogenicity and enhances tumorigenicity in vivo	miR-34a	Induces cell–cycle arrest, cell senescence, and apoptosis and inhibits cell proliferation and cell invasion
miR-375	Promotes early diagnosis	miR-145	Inhibits invasion, migration and arrests cell cycle
miR-18a	Promotes cancer progression	miR-224	Inhibits invasion and migration of PCa cells
miR-4534	Induces pro-cancerous characteristics in non-cancer cell line	miR-452	Regulates cell cycle, cellular adhesion, and motility
miR-650	Suppresses the cellular stress response1 (CSR1) expression	miR-200b	Inhibits PCa cell growth and invasion
miR-32	Inhibits apoptosis and enhances proliferation	miR-382	Inhibits PCa cell proliferation, migration, invasion, and metastasis
miR-106/ miR-25	Facilitates the tumor progression	miR-372	Inhibits proliferation, migration, and invasion of DU145 cells
miR-125b	Enhances cell proliferation and inhibits apoptosis	miR-17-92a	Decreases cell cycle regulatory, proteins and the expression of mesenchymal markers
		miR-27a	Suppresses MAP2K4 in PCa cell
		has-miR-135-a-1	Inhibits cell growth, cell cycle progression, migration, invasion, and xenograft tumor formation
		miR-204-5p	Promotes apoptosis by targeting BCL2 in PCa cell
		miR-30a	Reduces expression of cell cycle protein, cyclin E2
		let-7	Regulates cell cycle, cell
		miR-133/miR-146a	Suppresses tumor progression via targeting EGFR

Circulating miRNas in blood were described by Mitchell et al. [70, 71]. miRNAs are released to the blood stream from the tumoral tissue through several ways, as free miRNAs, into exosomes, into microvesicles, into big oncosomes, joined to apoptotic bodies, associated with high density lipoproteic complexes or joined to proteins. The presence of miRNA in the extracellular environment ignited the hypotheses that cells selectively release miRNAs which mediate cell–cell signaling via paracrine

or even endocrine routes [78–80]. Some research groups have demonstrated that extracellular miRNAs entrapped within apoptotic bodies and exosomes can be transferred to recipient cells, alter gene expression, and mediate functional effects [78, 81–85]. Patterns of mRNAs in exosomes and their donor cells correlate poorly, suggesting specific sorting of miRNA "for export" [78, 84–86]. The mechanism behind this sorting needs to be investigated in more detail.

The miRNAs released in the bloodstream are protected against degradation and readily detectable by PCR methods; mainly in cancer specific miRNAs levels have been used to correlate disease status, stage, aggressiveness, and response to therapy performing the miRNA profiling in plasma or serum. In the case of prostate cancer, cell-free miRNAs levels are able to differentiate between localized and metastatic prostate cancer or correlate with the risk score or Gleason grade, associating miRNAs with aggressiveness or indolent disease and may aid in tumor staging and treatment decisions at the time of diagnosis [72–75].

Agalogu et al. [69] assessed serum levels of three miRNAs in 51 patients with prostate cancer (subdivided into localized/locally advanced and metastatic) and 20 healthy controls. They identified increased levels of miR-21 and miR-221 in the prostate cancer group as a whole compared to the controls. miR-141 was not significantly elevated in the group as a whole, but when the metastatic group was considered in isolation, all three miRNAs were significantly elevated, with mir-141 being the most elevated of the three.

Lodes et al. [70] analyzed sera from patients with a number of malignancies using a micro-array hybridization technique, identifying 15 upregulated miRNAs in the sera of prostate cancer patients vs. healthy controls (miR-16, -92a, -103, -107, -197, -34b, -328, -485-3p, -486-5p, -92b, -574-3p, -636, -640, -766, -885-5p). This study did not confirm the finding of increased miR-141 expression; however, the group of prostate cancer patients was small ($n = 6$). Additionally, no qRT-PCR confirmation of the micro-array results was performed.

Several miRNAs have been found over-expressed in plasma/serum of patients with prostate cancer, some of them as miR-21, and miR-141 were validated about the cellular function respect prostate cancer context following the five levels assessment. Some studies [70, 76, 77] have reported an over-expression of the miRNA-107, which is encoded at 10p23.11, this miRNA has a fold change around 10; a study in a court of thirty-eight prostate cancer patients at different clinical stages (from I to IV) revealed that miR-107 is over-expressed at each clinical stage of prostate cancer relative to the control group (Fig. 2), there was not significative difference between media value at each clinical stage of cancer (*t*-test), however there is a shape showing an increasing of relative expression for miR-107 related to the clinical stage of cancer.

It should be necessary to increase the size of the assessed groups to find a clear correlation between the clinical stage of prostate cancer and the relative expression of miR-107.

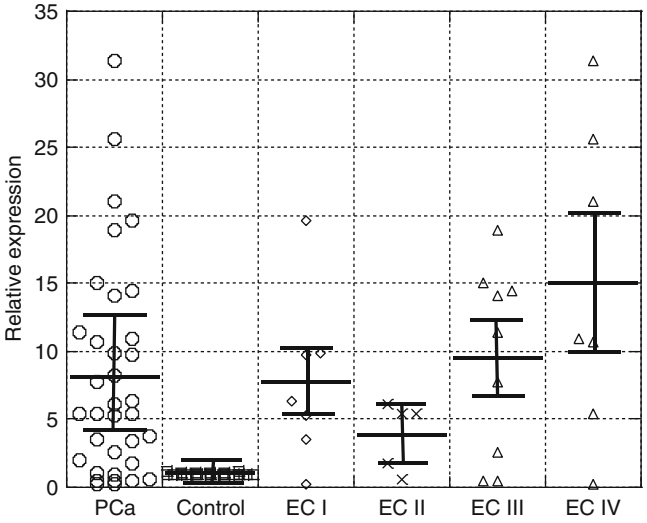

Fig. 2 Relative expression of miRNA-107 in plasma of patients with conformed PCa, diagnosis, PCa column shows the relative expression of all patients that participate in the study, EC I, II, III, and IV are the patients classified by cancer clinical stage

5 Conclusion

MicroRNAs are small biomolecules with a great number of possible targets in the cellular functions, when those are deregulated several diseases can occur, one of the most studied is cancer, miRNAs can be relevant as therapeutic targets or biomarkers, in prostate cancer there are several miRNAs that have been validated as oncogenic miRNAs and tumor suppressor miRNAs, some of the over-expressed miRNAs in plasma/serum of patients with prostate cancer have been proposed as possible biomarkers of the disease as miR-21 and miR-141, recently miR107 has been relevant by their high relative over-expression in plasma/serum, it has been tested in a cohort of patients with prostate cancer at different clinical stages showing that it is possible to find a correlation between their relative expression in plasma and the clinical stage of cancer. It makes necessary to increase the efforts to find either miRNAs functions in prostate cancer or possible new biomarkers to shelter the current prostatic specific antigen test.

References

1. Filipowicz W, Bhattacharyya SN, Sonenberg N (2008) Mechanisms of post-transcriptional regulation by microRNAs: are the answers in sight? Nat Rev Genet 9:102–114
2. Ghildiyal M, Zamore PD (2009) Small silencing RNAs: an expanding universe. Nat Rev Genet 10(2):94–108

3. Pauli A, Rinn JL, Schier AF (2011) Non-coding RNAs as regulators of embryogenesis. Nat Rev Genet 12(2):136–149
4. Bushati N, Cohen SM (2007) microRNA functions. Annu Rev Cell Dev Biol 23:175–205
5. Rodriguez A, Griffiths-Jones S, Ashurst JL, Bradley A (2004) Identification of mammalian microRNA host genes and transcription units. Genome Res 14(10A):1902–1910
6. Borchert GM, Lanier W, Davidson BL (2006) RNA polymerase III transcribes human microRNAs. Nat Struct Mol Biol 13(12):1097–1101
7. Lee Y, Kim M, Han J, Yeom KH et al (2004) MicroRNA genes are transcribed by RNA polymerase II. EMBO J 23(20):4051–4060
8. Carthew RW, Sontheimer EJ (2009) Origins and mechanisms of miRNAs and siRNAs. Cell 136:642–655
9. Kim VN, Han J, Siomi MC (2009) Biogenesis of small RNAs in animals. Nat Rev Mol Cell Biol 10:126–139
10. Siomi H, Siomi MC (2009) On the road to reading the RNA-interference code. Nature 457:396–404
11. Lee Y, Ahn C, Han J, Choi H et al (2003) The nuclear RNase III Drosha initiates microRNA processing. Nature 425(6956):415–419
12. Denli AM, Tops BB, Plasterk RH, Ketting RF et al (2004) Processing of primary microRNAs by the microprocessor complex. Nature 432(7014):231–235
13. Gregory RI, Yan KP, Amuthan G, Chendrimada T et al (2004) The microprocessor complex mediates the genesis of microRNAs. Nature 432(7014):235–240
14. Ruby JG, Jan CH, Bartel DP (2007) Intronic microRNA precursors that bypass Drosha processing. Nature 448(7149):83–86
15. Rasschaert P, Figueroa T, Dambrine G, Rasschaert D, Laurent S (2016) Alternative splicing of a viral mirtron differentially affects the expression of other microRNAs from its cluster and of the host transcript. RNA Biol 13(12):1310–1322
16. Schwarz DS, Hutvagner G, Du T, Xu Z et al (2003) Asymmetry in the assembly of the RNAi enzyme complex. Cell 115(2):199–208
17. Krol J, Loedige I, Filipowicz W (2010) The widespread regulation of microRNA biogenesis, function and decay. Nat Rev Genet 11(9):597–610
18. Cheloufi S, Dos Santos CO, Chong MM, Hannon GJ (2010) A dicer-independent miRNA biogenesis pathway that requires Ago catalysis. Nature 465(7298):584–589
19. Rigoutsos I (2009) New tricks for animal microRNAS: targeting of amino acid coding regions at conserved and nonconserved sites. Cancer Res 69(8):3245–3248
20. Gaidatzis D, van Nimwegen E, Hausser J, Zavolan M (2007) Inference of miRNA targets using evolutionary conservation and pathway analysis. BMC Bioinf 8:69
21. Maragkakis M et al (2009) DIANA-microT web server: elucidating microRNA functions through target prediction. Nucleic Acids Res 37:273–276
22. Shirdel EA, Xie W, Mak TW, Jurisica I (2011) NAViGaTing the micronome using multiple microRNA prediction databases to identify signalling pathwayassociated microRNAs. PLoS ONE 6:e17429
23. Liang H, Li W (2007) MicroRNA regulation of human protein—protein interaction network. RNA 13:1402–1408
24. Hsu CW, Juan HF, Huang HC (2008) Characterization of microRNA-regulated protein-protein interaction network. Proteomics 8:1975–1979
25. Yuan X et al (2009) Clustered microRNAs' coordination in regulating protein-protein interaction network. BMC Syst Biol 3:65
26. Sass S et al (2011) MicroRNAs coordinately regulate protein complexes. BMC Syst Biol 5:136
27. Ashburner M et al (2000) Gene ontology: tool for the unification of biology. Nat Genet 25:25–29
28. Hung JH, Yang TH, Hu Z, Weng Z, DeLisi C (2011) Gene set enrichment analysis: performance evaluation and usage guidelines. Brief Bioinform 13:281–291
29. Betel D, Wilson M, Gabow A, Marks DS, Sander C (2008) The microRNA.org resource: targets and expression. Nucleic Acids Res 36(Database issue):D149–D153

30. Manvatia S, Mangalharab KC, Khana J, Pathaniab GL, Kaulc S, Kaushika M, Aroraa A, Dhara PK (2017) Deciphering the role of microRNA – a step by step guide. Gene Expr Patterns 25–26:59–65
31. Hanahan D et al (2011) Hallmarks of cancer: the next generation. Cell 144(5):646–674
32. Su Z, Yang Z, Xu Y, Chen Y, Yu Q (2015) MicroRNAs in apoptosis, autophagy and necroptosis. Oncotarget 6(11):8474–8490
33. Brennecke J, Hipfner DR, Stark A et al (2003) Bantam encodes a developmentally regulated microRNA that controls cell proliferation and regulates the proapoptotic gene hid in Drosophila. Cell 113:25–36
34. Schickel R, Boyerinas B, Park SM et al (2008) MicroRNAs: key players in the immune system, differentiation, tumorigenesis and cell death. Oncogene 27:5959–5974
35. Calin GA, Sevignani C, Dan Dumitru C et al (2004) Human microRNA genes are frequently located at fragile sites and genomic regions involved in cancers. Proc Natl Acad Sci U S A 101:2999–3004
36. Calin GA, Dumitru CD, Shimizu M et al (2002) Frequent deletions and down-regulation of micro-RNA genes miR15 and miR16 at 13q14 in chronic lymphocytic leukemia. Proc Natl Acad Sci U S A 99:15524–15529
37. Iorio MV, Croce CM (2012) MicroRNA deregulation in cancer: diagnostics, monitoring and therapeutics. A comprehensive review. EMBO Mol Med 4:143–159
38. Bommer GT, Gerin I, Feng Y et al (2007) p53-mediated activation of miRNA34 candidate tumor-suppressor genes. Curr Biol 17:1298–1307
39. Yamakuchi M, Ferlito M, Lowenstein CJ (2008) miR-34a repression of SIRT1 regulates apoptosis. Proc Natl Acad Sci U S A 105:13421–13426
40. Welch C, Chen Y, Stallings RL (2007) MicroRNA-34a functions as a potential tumor suppressor by inducing apoptosis in neuroblastoma cells. Oncogene 26:5017–5022
41. Mott JL, Kobayashi S, Bronk SF et al (2007) mir-29 regulates Mcl-1 protein expression and apoptosis. Oncogene 26:6133–6140
42. Lee YS, Dutta A (2007) (2007) The tumor suppressor microRNA let-7 represses the HMGA2 oncogene. Genes Dev 21:1025–1030
43. Johnson SM, Grosshans H, Shingara J et al (2005) RAS is regulated by the let-7 microRNA family. Cell 120:635–647
44. Farazi TA, Spitzer JI, Morozov P et al (2011) miRNAs in human cancer. J Pathol 223:102–115
45. Kumar MS, Lu J, Mercer KL et al (2007) Impaired microRNA processing enhances cellular transformation and tumorigenesis. Nat Genet 39:673–677
46. Kumar MS, Pester RE, Chen CY et al (2009) Dicer1 functions as a haploinsufficient tumor suppressor. Genes Dev 23:2700–2704
47. Lambertz I, Nittner D, Mestdagh P et al (2010) Monoallelic but not biallelic loss of Dicer1 promotes tumorigenesis in vivo. Cell Death Differ 17:633–641
48. Eis PS, Tam W, Sun L et al (2005) Accumulation of miR-155 and BIC RNA in human B cell lymphomas. Proc Natl Acad Sci U S A 102:3627–3632
49. He L, Thomson JM, Hemann MT et al (2005) A microRNA polycistron as a potential human oncogene. Nature 435:828–833
50. Costinean S, Zanesi N, Pekarsky Y et al (2006) Pre–B cell proliferation and lymphoblastic leukemia/high-grade lymphoma in E mu-miR155 transgenic mice. Proc Natl Acad Sci U S A 103:7024–7029
51. Chan JA, Krichevsky AM, Kosik KS (2005) MicroRNA-21 is an antiapoptotic factor in human glioblastoma cells. Cancer Res 65:6029–6033
52. Chen Y, Liu W, Chao TF et al (2008) MicroRNA-21 down-regulates the expression of tumor suppressor PDCD4 in human glioblastoma cell T98G. Cancer Lett 272:197–205
53. Papagiannakopoulos T, Shapiro A, Kosik KS (2008) MicroRNA-21 targets a network of key tumor-suppressive pathways in glioblastoma cells. Cancer Res 68:8164–8172
54. GLOBOCAN (2012) Estimated cancer incidence, mortality and prevalence Worldwide in 2012: International Agency for Research on Cancer. http://globocan.iarc.fr/Pages/fact_sheets_cancer.aspx [consulted on August 2, 2016]

55. Gronberg H (2003) Prostate cancer epidemiology. Lancet 361:859–864
56. Di Franco R, Borzillo V, Ravo V, Ametrano G, Falivene S, Cammarota F, Rossetti S, D'Aniello C, Cavaliere C, Romano FJ, Malzone MG, Montanari M, Vanacore D et al (2016) Hypofractionated versus conventional radiotherapy in patients with low/intermediate-risk localized prostate cancer: review of rectal and urinary toxicity. WCRJ 3:e751
57. D'Aniello C, Cavaliere C, Fiorica F, Facchini G (2016) Letter to the editor: unenhanced whole-body MRI versus PET-CT for the detection of prostate cancer metastases after primary treatment. Eur Rev Med Pharmacol Sci 20:4626–4627
58. Nardone V, Botta C, Caraglia M, Martino EC, Ambrosio MR, Carfagno T, Tini P, Semeraro L, Misso G, Grimaldi A, Boccellino M, Facchini G, Berretta M et al (2016) Tumor infiltrating T lymphocytes expressing FoxP3, CCR7 or PD-1 predict the outcome of prostate cancer patients subjected to salvage radiotherapy after biochemical relapse. Cancer Biol Ther 17:1213–1220
59. Heidenreich A, Bellmunt J, Bolla M, Joniau S, Mason M, Matveev V et al (2011) EAU guidelines on prostate cancer. Part 1: screening, diagnosis, and treatment of clinically localized disease. Eur Urol 59:61–71
60. Loeb S, Catalona WJ (2007) Prostate-specific antigen in clinical practice. Cancer Lett 249: 30–39
61. Boccellino M, Alaia C, Misso G, Cossu AM, Facchini G, Piscitelli R, Quagliuolo L, Caraglia M (2015) Gene interference strategies as a new tool for the treatment of prostate cancer. Endocrine 49:588–605
62. Facchini, G. Caffo, O. Ortega, C. D'Aniello, C. Di Napoli, M. Cecere, S.C. Pepa, C.D. Crispo, A. Maines, F. Ruatta, F. Iovane, G. Pisconti, S. Montella, M. et al. (2016). Very early PSA response to abiraterone in mCRPC patients: a novel prognostic factor predicting overall survival. Front Pharmacol 7:123.
63. Wang G, Chan ES, Kwan BC, Li PK, Yip SK, Szeto CC, Ng CF (2012) Expression of microRNAs in the urine of patients with bladder cancer. Clin Genitourin Cancer 10:106–113
64. Lolli C, Caffo O, Scarpi E, Aieta M, Conteduca V, Maines F, Bianchi E, Massari F, Veccia A, Chiuri VE, Facchini G, De Giorgi U (2016) Systemic immune-inflammation index predicts the clinical outcome in patients with mCRPC treated with abiraterone. Front Pharmacol 7:376
65. Verzoni E, De Giorgi U, Derosa L, Caffo O, Boccardo F, Facchini G, Porcu L, De Vincenzo F, Zaniboni A, Chiuri VE, Fratino L, Santini D, Adamo V et al (2016) Predictors of longterm response to abiraterone in patients with metastastic castration-resistant prostate cancer: a retrospective cohort study. Oncotarget 7:40085–40094
66. Caffo O, Lo Re G, Sava T, Buti S, Sacco C, Basso U, Zustovich F, Lodde M, Perin A, Facchini G, Veccia A, Maines F, Barile C et al (2015) Intermittent docetaxel chemotherapy as first-line treatment for metastatic castration-resistant prostate cancer patients. Future Oncol 11:965–973
67. Li T, Li RS, Li YH, Zhong S, Chen YY, Zhang CM, MM H, Shen ZJ (2012) miR-21 as an independent biochemical recurrence predictor and potential therapeutic target for prostate cancer. J Urol 187:1466–1472
68. Zhang HL, Qin XJ, Cao DL, Zhu Y, Yao XD, Zhang SL, Dai B, Ye DW (2013) An elevated serum miR-141 level in patients with bone-metastatic prostate cancer is correlated with more bone lesions. Asian J Androl 15:231–235
69. Agaoglu FY, Kovancilar M, Dizdar Y, Darendeliler E, Holdenrieder S, Dalay N, Gezer U (2011) Investigation of miR-21, miR-141, and miR-221 in blood circulation of patients with prostate cancer. Tumor Biol 32(3):583–588
70. Lodes MJ, Caraballo M, Suciu D, Munro S, Kumar A, Anderson B (2009) Detection of cancer with serum miRNAs on an oligonucleotide microarray. PLoS One 4:7
71. Mitchell PS, Parkin RK, Kroh EM, Fritz BR, Wyman SK, Pogosova-Agadjanyan EL et al (2008) Circulating microRNAs as stable blood-based markers for cancer detection. Proc Natl Acad Sci U S A 105:10513–10518
72. D'Amico AV, Whittington R, Malkowicz SB, Cote K, Loffredo M, Schultz D et al (2002) Biochemical outcome after radical prostatectomy or external beam radiation therapy for patients with clinically localized prostate carcinoma in the prostate specific antigen era. Cancer 95:281–286

73. Lian F, Sharma NV, Moran JD, Moreno CS (2015) The biology of castration-resistant prostate cancer. Curr Probl Cancer 39:17–28
74. James ND, Spears MR, Clarke NW, Dearnaley DP, De Bono JS, Gale J et al (2015) Survival with newly diagnosed metastatic prostate cancer in the "Docetaxel Era": data from 917 patients in the control arm of the STAMPEDE Trial (MRCPR08, CRUK/06/019). Eur Urol 67: 1028–1038
75. Sweeney CJ, Chen YH, Carducci M, Liu G, Jarrard DF, Eisenberger M et al (2015) Chemohormonal therapy in metastatic hormone-sensitive prostate cancer. N Engl J Med 373:737–476
76. Bryant RJ, Pawlowski T, Catto JWF, Marsden G, Vessella RL, Rhees B, Kuslich C, Visakorpi T, Hamdy FC (2012) Changes in circulating microRNA levels associated with prostate cancer. Br J Cancer 106(4):768–774
77. Mihelich BL, Maranville JC, Nolley R, Peehl DM, Nonn L (2015) Elevated serum microRNA levels associate with absence of high-grade prostate cancer in a retrospective cohort. PLoS ONE 10(4):e0124245
78. Valadi H, Ekström K, Bossios A, Sjöstrand M, Lee JJ, Lötvall JO (2007) Exosome-mediated transfer of mRNAs and microRNAs is a novel mechanism of genetic exchange between cells. Nat Cell Biol 9(6):654–659
79. Cortez MA, Bueso-Ramos C, Ferdin J, Lopez-Berestein G, Sood AK, Calin GA (2011) MicroRNAs in body fluids–the mix of hormones and biomarkers. Nat Rev Clin Oncol 8(8):467–477
80. Chendrimada TP, Gregory RI, Kumaraswamy E, Norman J, Cooch N, Nishikura K et al (2005) TRBP recruits the Dicer complex to Ago2 for microRNA processing and gene silencing. Nature 436:740–744
81. Skog J, Würdinger T, van Rijn S, Meijer DH, Gainche L, Sena-Esteves M, Curry WT Jr, Carter BS, Krichevsky AM, Breakefield XO (2008) Glioblastoma microvesicles transport RNA and proteins that promote tumour growth and provide diagnostic biomarkers. Nat Cell Biol 10(12):1470–1476
82. Kosaka N, Iguchi H, Yoshioka Y, Takeshita F, Matsuki Y, Ochiya T (2010) Secretory mechanisms and intercellular transfer of microRNAs in living cells. J Biol Chem 285(23): 17442–17452
83. Pegtel DM, Cosmopoulos K, Thorley-Lawson DA, Van Eijndhoven MA, Hopmans ES, Lindenberg JL et al (2010) Functional delivery of viral miRNAs via exosomes. Proc Natl Acad Sci U S A 107:6328–6333
84. Pigati L, Yaddanapudi SC, Iyengar R, Kim DJ, Hearn SA, Danforth D, Hastings ML, Duelli DM (2010) Selective release of microRNA species from normal and malignant mammary epithelial cells. PLoS One 5(10):e13515
85. Mittelbrunn M, Gutiérrez-Vázquez C, Villarroya-Beltri C, González S, Sánchez-Cabo F, González MÁ, Bernad A, Sánchez-Madrid F (2011) Unidirectional transfer of microRNA-loaded exosomes from T cells to antigen-presenting cells. Nat Commun 2:282
86. Skog J, Würdinger T, van Rijn S, Meijer DH, Gainche L, Sena-Esteves M, Curry WT Jr, Carter BS, Krichevsky AM, Breakefield XO (2008) Glioblastoma microvesicles transport RNA and proteins that promote tumour growth and provide diagnostic biomarkers. Nat Cell 10(12):1470–1476

Subdiffusive Transport in Heterogeneous Patchy Environments

Sergei Fedotov and Helena Stage

Abstract Transport across heterogeneous, patchy environments is a ubiquitous phenomenon spanning fields of study including ecological movement, intracellular transport and regions of specialised function in a cell. These regions or patches may be highly heterogeneous in their properties, and often exhibit anomalous behaviour (resulting from e.g. crowding or viscoelastic effects) which necessitates the inclusion of non-Markovian dynamics in their study. However, many such processes are also subject to an internal self-regulating or tempering process due to concurrent competing functions being carried out. In this work we develop a model for anomalous transport across a heterogeneous, patchy environment subject to tempering. We show that in the long-time an equilibrium may be reached with constant effective transport rates between the patches. This result is qualitatively different from untempered systems where subdiffusion results in the long-time accumulation of all particles in the patch with lowest anomalous exponent, $0 < \mu < 1$.

Keywords Anomalous transport · Subdiffusion · Tempering · Patches

1 Introduction

Transport processes in heterogeneous, patchy environments is an active area of research with a multitude of applications (depending on what is meant by a patch, what is being transported and the variables affecting this transport). The notion of patches is particularly prevalent in biophysical and ecological models, describing the movement and competition of animals across different terrains or territories [1], the transport of proteins between cellular organelles with different functions [2], and large scale transport between tissues of different utility in an organism [3, 4].

S. Fedotov · H. Stage (✉)
School of Mathematics, The University of Manchester, Manchester, UK
e-mail: helena.stage@manchester.ac.uk

L. Olivares-Quiroz, O. Resendis-Antonio (eds.), *Quantitative Models for Microscopic to Macroscopic Biological Macromolecules and Tissues*,
https://doi.org/10.1007/978-3-319-73975-5_3

It is of particular importance for cellular transport given the wealth of processes which rely on transport from centrosomes or peripheral organelles to e.g. the cell membrane [5–7]. That is, where the transport taking place is dependent on local changes in function. It has previously been shown that the breakdown of these transport processes is intrinsically linked to certain diseases such as diabetes, Alzheimer's, cancer and cardiovascular problems [6, 8, 9].

It is well-known that cell environments are crowded, leading to the trapping of particles (be they vesicles, enzymes or protein complexes), or subject to significant viscoelastic forces, inhibiting efficient transport, such that the overall transport is observed to be subdiffusive [10–13]. Such transport is understood to occur more slowly than the Brownian equivalent and is often observed via mean square displacement (MSD) measurements of the form $\left\langle X^2(t)\right\rangle \sim t^{\mu}$ where $0 < \mu < 1$ [14]. Models which study transport in these environments often assume that the anomalous exponent μ is constant throughout the environment. However, cells are known to be highly heterogeneous structures such that this assumption is (mostly) not a realistic approximation.

A natural consequence of the cell heterogeneity is switching between passive and active transport. The latter case, e.g. movement aided by motor proteins along microtubules or actin filaments, can lead to superdiffusive behaviour which has an MSD $\left\langle X^2(t)\right\rangle \sim t^{\mu}$ where $1 < \mu < 2$ [14–18]. Both sub- and superdiffusive transport can be regarded as *anomalous*. However, due to the diverging first moment of subdiffusive transport, we shall refer to these patches as being *anomalously trapping*. In the superdiffusive case the transport is faster than what arises from standard Brownian motion. Here also it is usually assumed that μ is constant, which again may be an oversimplification.

We are interested in the effects of allowing for heterogeneities in anomalous transport processes. Previous work on the topic of heterogeneous anomalous exponents can be found in [19–24].

The full morphology (and associated consequences for a transport process) in a cellular region is often analytically intractable, leading to the creation of simplified models which preserve the key features of the transport process in question. This is often done by the introduction of patches (regions of similar properties) and the transport of cargo between these. However, by including additional tempering effects in the patches we feel this assumption is better justified. By this local similarity assumption we shall regard patches as independent of each other.

The aim of this work is to formulate the transport equations for a patchy heterogeneous environment subject to tempering effects. That is, we consider effects such as volume filling, continued transport via other pathways out of the patch, 'leakage' and so on. The main challenges in doing so for a comprehensive model is to account for three different aspects: the heterogeneity of the patches, the tempering effects which may take place in each of them, and the subdiffusive transport resulting from ageing effects in each patch. In the following section we describe the approach employed to treat these effects.

2 Structural Density Approach

Let us consider a system containing η patches with different escape rates. Particles jump from one patch to another according to these rates, such that the location of a particle at a certain point in time is given by $X(t)$. So if $X(0) = 4$, the particle is in fourth patch at $t = 0$. In general, $X(t)$ takes values according to the subscript i with values $i = 1, \ldots \eta$ depending on which patch we are in.

We assume the residence time (or age) since arrival spent by a particle in a patch i at time t is a random quantity given by U_i. Once the particle leaves the patch their age U_i is reset, such that the age of any particle in the patch is independent of previous visits to the patch. Movement between patches happens with rates $\gamma_i(\tau)$, where

$$\gamma_i(\tau) = \lim_{\Delta\tau \to 0^+} \left(\frac{P(\tau \leq U_i < \tau + \Delta\tau | U_i \geq \tau)}{\Delta\tau} \right) \tag{1}$$

[25]. Notice that these rates γ_i depend on the residence time τ the particle has spent so far in the patch. Taking into account the variable ages spent in a patch, we introduce the structural probability densities $\xi_i(t, \tau)$ which obey

$$\xi_i(t, \tau) = \frac{\partial}{\partial \tau} \Pr\{X(t) = i, U_i < \tau\}. \tag{2}$$

That is, $\xi_i(t, \tau)\Delta\tau$ gives the probability of finding particles in patch i at time t with residence times in the interval $(\tau, \tau + \Delta\tau)$. ξ_i will thus give us the distribution of residence times in each patch as desired. The total rate of change of our probability density must balance with the escape rates from the patches, which gives the balance equations for $\xi_i(t, \tau)$:

$$\frac{\partial \xi_i}{\partial t} + \frac{\partial \xi_i}{\partial \tau} = -\gamma_i(\tau)\, \xi_i. \tag{3}$$

Another interpretation of (3) is that changes in the current patch are purely a result of those particles which leave. Whether γ_i increases or decreases depends on the chosen functional form.

If instead of studying each individual particle, we are concerned with the aggregate of all particles, we can assume that the particles are independent of each other and study their mean. In particular, we can consider the transport in terms of the mean density of particles in a patch with a certain residence time. We call this quantity the mean *structural density* $n_i(t, \tau)$ where

$$n_i(t, \tau) = N\xi_i(t, \tau) \tag{4}$$

for a total of N particles in the system. Equation (4) is the statement that the average number of particles in each patch is representative of the probabilities which describe their movement; a mean-field approximation has been applied to the number of particles in each patch. However, this result is independent of the total number of particles, and we may well want to work with the renormalised structural density

$$\rho_i(t,\tau) = \frac{n_i(t,\tau)}{N}, \qquad 0 < \rho_i(t,\tau) < 1 \tag{5}$$

which describes the proportion of the whole number of particles to be found in each patch. Of course, $\rho_i(t,\tau) = \xi_i(t,\tau)$ but ξ_i was introduced as a probability density for a single particle moving between patches, and ρ_i is a renormalised number of particles of certain residence time in a patch resulting from a mean-field approximation. From here on out we shall use the notation $\rho_i(t,\tau)$ to stress that we are working with the mean ensemble of particles, and not just an individual one. In analogy to (3), we can thus write

$$\frac{\partial \rho_i}{\partial t} + \frac{\partial \rho_i}{\partial \tau} = -\gamma_i(\tau)\,\rho_i. \tag{6}$$

This mean structural density is in principle measurable but cumbersome to obtain experimentally for crowded biological systems where particle tracking becomes challenging. A more tractable measurement is $N_i(t)$, the (renormalised) mean number of particles in a certain patch i at time t. Then, $1 = \sum_{i=1}^{\eta} N_i(t)$. Note that $N_i(t)$ is simply the sum of all particles with different residence times in the patch to give

$$N_i(t) = \int_0^t \rho_i(t,\tau)d\tau. \tag{7}$$

Hence, we can decompose the particles such that $1 = \sum_{i=1}^{\eta} \int_0^t \rho_i(t,\tau)d\tau$. Now that we have established the framework for the particles, we must specify the conditions on the system.

The particles that arrive in a patch are accounted for in the boundary conditions of zero residence time. One must also provide some initial conditions regarding the patches at $t = 0$. Here we assume all patches to have initial renormalised particle distributions ρ_i^0 with no age, such that

$$\rho_i(0,\tau) = \rho_i^0 \delta(\tau). \tag{8}$$

Of course, practically one does not expect all particles to simultaneously have zero residence time, but this simplification should not affect the long-term dynamics of the system. Similarly, the boundary conditions consider the effects of new arrivals in each of the patches. We place no limitations on which of the other patches a particle

enters once leaving the current patch. The likelihood of entering another patch j if currently in patch i is governed by the redistribution kernel $\kappa(j|i)$. We thus obtain

$$\rho_i(t,0) = \sum_{j=1}^{\eta} \int_0^t \gamma_j(\tau)\, \rho_j(t,\tau)\, \kappa(i|j) d\tau, \tag{9}$$

which corresponds to the statement that new arrivals ($\tau = 0$) in a patch i are those particles which left the other patches and subsequently entered i. This formulation of the transport has the advantage that it can be generalised to the non-linear case; an easier undertaking than attempting to generalise the linear renewal equations we shall introduce in the following section. By starting from the escape rate we also allow for inclusion of effects starting from a smaller scale.

The results until now are valid for any number of patches. However, there is a wealth of evidence that cellular transport can be understood as a two-patch problem, e.g. in the spreading and proliferation of glioma cancer [26], the interaction of the motor proteins with ATP when moving cargo [27, 28] or the associated conformational changes [13, 29]. These patches can also be considered via their pairwise interactions as discussed in multi-stage cancer growth in [30]. Other examples of the applications of such two-patch models include spiny dendrites [31, 32]. For ease in following the calculations we shall now be concerned with a two-patch system ($\eta = 2$) which we believe retains the essential features of larger patchy systems.

3 Two-Patch Theory

In this section we consider two patches with different escape rates $\gamma_i(\tau)$. We assume there are two different, and independent, processes which affect the escape rate: the residence time since arrival in the patch and the total volume capacity or transportation rate from the patch. This latter effect is assumed constant for each patch; any patch may have a small but non-zero escape constant escape rate. Then,

$$\gamma_i(\tau) = \beta_i(\tau) + \alpha_i, \tag{10}$$

is composed of ageing affects via β_i and tempering effects (such as volume exclusion, depolymerisation rate of protein complexes, etc.) via α_i. Clearly, if a particle leaves one patch it must enter the other with zero residence time. We call this escape process an 'event'. There are thus two types of events corresponding to entry in either patch $i = 1, 2$. We introduce the mean renewal density for event of type i

$$h_i(t) = \rho_i(t,0) \tag{11}$$

to denote each of these possibilities. We can use the method of characteristics to solve (3) where we consider the residence time $\tau(t)$ to be a function of time. That is, the time at any given point t equals the time when the last renewal event happened (and a particle entered the patch) which we denote t_0 and the residence time τ in the patch since then:

$$t = t_0 + \tau \tag{12}$$

such that $t - \tau = t_0 > 0$. It is important to note that this assumes that the residence time is less than the total time that has passed. That is, at the start of our measurements we assume that all particles are newly arrived in their initial patches. The solution is given by

$$\rho_i(t, \tau) = \rho_i(t - \tau, 0) \exp\left(-\alpha_i \tau - \int_0^\tau \beta_i[v] dv\right). \tag{13}$$

We notice that (13) has the form of arrivals at a time $t - \tau$ which then remain for a residence time τ. This is consistent with a survival probability $P(U_i > \tau) = \Psi_i(\tau)$, which is the likelihood of remaining in the ith patch for a duration τ starting from the time t. Then,

$$\Psi_i(\tau) = \exp\left(-\alpha_i \tau - \int_0^\tau \beta_i[v] dv\right), \tag{14}$$

such that, using (11), the solution of (13) becomes

$$\rho_i(t, \tau) = \rho_i(t - \tau, 0)\Psi_i(\tau) = h_i(t - \tau)\Psi_i(\tau). \tag{15}$$

By substitution of this result into (7), we find

$$N_i(t) = \int_0^t \rho_i(t - \tau, 0)\Psi_i(\tau) d\tau. \tag{16}$$

If we consider each component of the escape rate separately, they have associated survival probabilities $\Phi_i^\alpha(\tau) = \exp(-\alpha_i \tau)$ and $\Phi_i^\beta(\tau) = \exp\left(-\int_0^\tau \beta_i(u) du\right)$ which are linear relationships. These individually have probability density functions (PDF) which follow $\phi_i^\alpha(\tau) = \alpha_i \Phi_i^\alpha(\tau)$ and similarly $\phi_i^\beta(\tau) = \beta_i(\tau)\Phi_i^\beta(\tau)$. This is a direct result of the relation $\phi_i(t) = -\partial \Phi_i / \partial t$. Then, one can write the total survival probability as

$$\Psi_i(\tau) = \Phi_i^\beta(\tau) e^{-\alpha_i \tau}. \tag{17}$$

This is simply the standard survival probability one obtains for an age-dependent escape rate, with an additional tempering factor resulting from the constant escape

rate. That is, net survival requires not leaving to due ageing in a certain time interval, and not leaving due to α_i contributions in that same duration. It follows from (17) that the residence time PDF is given by

$$\psi_i(\tau) = \Psi_i(\tau)\left(\alpha_i + \beta_i(\tau)\right) = \gamma_i(\tau)\Psi_i(\tau). \tag{18}$$

So the PDF is the survival probability apportioned by the rate at which particles leave (dependent on current residence time) and the constant small escape rate α. In the two-patch system all particles which leave one patch enter the other, such that the redistribution kernel

$$\kappa(i|j) = 1 - \delta_{ij} = \begin{cases} 0 \text{if} i = j \\ 1 \text{if} i \neq j \end{cases}. \tag{19}$$

That is, all particles leaving patch 1 enter patch 2 and vice versa. We can thus apply (9) by multiplying (15) by γ_i to obtain

$$\gamma_i(\tau)\rho_i(t,\tau) = h_i(t-\tau)\Psi_i(\tau)\gamma_i(\tau) = h_i(t-\tau)\psi_i(\tau), \tag{20}$$

where in the last step we have used (18). By integrating both sides with respect to time and using (8) and (11), we obtain the renewal equations

$$\begin{aligned} h_1(t) =& \rho_2^0\left[\phi_2^\beta(t) + \alpha_2\Phi_2^\beta(t)\right]e^{-\alpha_2\tau} \\ &+ \int_0^t h_2(t-\tau)\left[\phi_2^\beta(\tau) + \alpha_2\Phi_2^\beta(\tau)\right]e^{-\alpha_2\tau}d\tau, \end{aligned} \tag{21}$$

$$\begin{aligned} h_2(t) =& \rho_1^0\left[\phi_1^\beta(t) + \alpha_1\Phi_1^\beta(t)\right]e^{-\alpha_1\tau} \\ &+ \int_0^t h_1(t-\tau)\left[\phi_1^\beta(\tau) + \alpha_1\Phi_1^\beta(\tau)\right]e^{-\alpha_1\tau}d\tau. \end{aligned} \tag{22}$$

Equations (21) and (22) describe an alternating renewal process, and are the classical starting point in the treatment of two-patch transport processes [33, 34]. A standard approach to their solution is to apply a Laplace transformation $\mathcal{L}_t\{f(t)\}(s) = \widehat{f}(s) = \int_0^\infty e^{-st}f(t)dt$ which allows us to simplify the convolution of the two quantities. Since α_i is constant, this leads to

$$\widehat{h}_1(s) = \frac{\rho_2^0\widehat{\psi}_2(s) + \rho_1^0\widehat{\psi}_1(s)\,\widehat{\psi}_2(s)}{1 - \widehat{\psi}_1(s)\,\widehat{\psi}_2(s)}, \tag{23}$$

and

$$\widehat{h}_2(s) = \frac{\rho_1^0 \widehat{\psi}_1(s) + \rho_2^0 \widehat{\psi}_1(s)\,\widehat{\psi}_2(s)}{1 - \widehat{\psi}_1(s)\,\widehat{\psi}_2(s)}, \tag{24}$$

where $\widehat{\psi}_i(s) = \widehat{\phi}_i^{\beta}(s + \alpha_i) + \alpha_i \widehat{\Phi}_i^{\beta}(s + \alpha_i)$. One reason why the renewal density approach is often applied is that since the renewal density corresponds to the density of new arrivals in the patch (see (11)), the integral

$$\int_0^t h_i(t)dt \tag{25}$$

gives the mean number of type i events in the time interval $(0, t)$, which is often a quantity of interest.

An alternative to the renewal density is the introduction of a switching term $I_i(t)$ for each patch defined as

$$I_i(t) = \int_0^t \gamma_i(\tau)\rho_i(t, \tau)d\tau. \tag{26}$$

This switching term can be interpreted as the renormalised flux of particles leaving a patch, where these particles can have any residence time. Hence we integrate over all values of $\tau < t$. From (10) it follows that

$$\begin{aligned} I_i(t) =& \alpha_i N_i(t) + \int_0^t \beta_i(\tau)\Psi_i(\tau)\rho_i(t - \tau, 0)d\tau, \\ =& \int_0^t \psi_i(\tau)\rho_i(t - \tau, 0)d\tau, \end{aligned} \tag{27}$$

where we have used (7), (15) and (18). Taking the Laplace transform of (16), we find that $\widehat{N}_i(s) = \widehat{\rho}_i(s, 0)\widehat{\Psi}_i(s)$. Further, (27) in Laplace space obeys $\widehat{I}_i(s) = \widehat{\psi}_i(s)\widehat{\rho}_i(s, 0)$, such that we can write

$$\widehat{I}_i(s) = \frac{\widehat{\psi}_i(s)}{\widehat{\Psi}_i(s)}\widehat{N}_i(s) \equiv \widehat{K}_i(s)\widehat{N}_i(s). \tag{28}$$

$K_i(t)$ is defined as above in Laplace space, such that we can write $\widehat{K}_i(s) = \alpha_i + \widehat{\phi}_i^{\beta}(s + \alpha_i)/\widehat{\Phi}_i^{\beta}(s + \alpha_i) \equiv \alpha_i + \widehat{K}_i^{\beta}(s + \alpha_i)$. By inversion of (28), we thus find that

$$I_i(t) = \alpha_i N_i(t) + \int_0^t K_i^{\beta}(\tau)e^{-\alpha_i \tau} N_i(t - \tau)d\tau, \tag{29}$$

where it is important that the additional term α_i not only leads to a separate flux, but also affects the flux resulting from the escape rate $\beta(\tau)$ via the term $e^{-\alpha_i \tau}$. So even if these escape rates are assumed to be independent of each other, they still couple in the total switching between the two patches. By differentiating (7) and using (6) and (26) it follows that

$$\begin{aligned}\frac{dN_i}{dt} =& \rho_i(t,t) + \int_0^t \frac{\partial \rho_i(t,\tau)}{\partial t} d\tau \\ =& \rho_i(t,0) - \int_0^t \gamma_i(\tau)\rho_i(t,\tau) d\tau \\ =& \rho_i(t,0) - I_i(t).\end{aligned} \tag{30}$$

For patch 1 we can then use (9) to write

$$\begin{aligned}\frac{dN_1}{dt} =& I_2(t) - I_1(t), \\ =& \alpha_2 N_2(t) + \int_0^t K_2^\beta(\tau) e^{-\alpha_2 \tau} N_2(t-\tau) d\tau \\ & - \alpha_1 N_1(t) - \int_0^t K_1^\beta(\tau) e^{-\alpha_1 \tau} N_1(t-\tau) d\tau,\end{aligned} \tag{31}$$

where we have used (29) in the second step. The number of particles in the other patch can be found by recalling our assumption that $N_1(t) + N_2(t) = 1$. In order to obtain the final equations we must now specify the form of $K_i^\beta(t)$. In the following section we consider the simple case where tempering is not present in the dynamics of the system. These results are already known, but form a good basis of comparison with later results when tempering is included.

4 Transport Between Patches Without Tempering

We shall begin by considering a classical two-patch model where there are no tempering effects on the following movement. This corresponds to large systems wherein volume exclusion effects are negligible, the depolymerisation rate is negligibly small, or arriving particles in the patch are subsequently transported elsewhere in the cell leaving room for new arrivals. In any case, this corresponds to the case where $\gamma_i(\tau) = \beta_i(\tau)$. There may thus still be anomalous trapping or active transport as a result of other components of the patch properties.

We remind the reader that when transport between the two patches is Markovian such that $\gamma_i(\tau) = \lambda_i$ for constant λ_i, we obtain in the long-time limit as $t \to \infty$

the result that $\widehat{\psi}_i(s) = \lambda_i/(s+\lambda_i) \simeq 1 - s/\lambda_i$. This is a direct consequence of the long-time limit corresponding to the case $s \to 0$ in Laplace space. This simple system is governed by the equations

$$\frac{dN_1}{dt} = \lambda_2 N_2(t) - \lambda_1 N_1(t), \tag{32}$$

$$\frac{dN_2}{dt} = \lambda_1 N_1(t) - \lambda_2 N_2(t). \tag{33}$$

A stationary state is thus reached where $N_1^{st} = \lambda_2/(\lambda_1 + \lambda_2)$ and similarly $N_2^{st} = \lambda_1/(\lambda_1+\lambda_2)$. From the definition of the renewal measure, we know that $h_1^{st} = \lambda_2 N_2^{st}$ and $h_2^{st} = \lambda_1 N_1^{st}$. From the above stationary distributions, it follows that both patches have renewal density

$$h_i^{st} = \frac{\lambda_1 \lambda_2}{\lambda_1 + \lambda_2}, \tag{34}$$

which has been the subject of exhaustive research over the years [33].

It is important to note that a small change in these escape rates has no qualitative impact on the long-term distribution of the particles in the patches. If both patches have the same escape rate $\lambda_1 = \lambda_2 = \lambda$, then we expect half of the total number of particles to be found in each patch. If one perturbs this and slightly alters the rates such that $\lambda_1 < \lambda_2$, there will be a proportion of particles $\lambda_2/(\lambda_1 + \lambda_2)$ and $\lambda_1/(\lambda_1 + \lambda_2)$ in patches 1 and 2, respectively. Hence, even a patch with a high escape rate contains a non-zero number of particles. In the following we explore what happens when the transport becomes anomalous.

4.1 Two Anomalous Patches

It is well-established that many intracellular transport processes are not Markovian, and thus are not described by a constant escape rate [16–18]. Instead, a measure of persistence is introduced such that the likelihood of leaving the patch decreases with the residence time of the particle in the patch. This can be modelled via the escape rates

$$\gamma_i(\tau) = \frac{\mu_i}{\tau_0 + \tau}, \qquad 0 < \mu_i < 2, \tag{35}$$

and is characteristic of patches which we shall call *anomalous*. $\tau_0 > 0$ is a parameter for the time scale of the movement between patches and μ_i the constant anomalous exponents. $0 < \mu < 1$ corresponds to subdiffusion (anomalous trapping). If $\mu_1 \neq$

μ_2 the rates at which particles leave either patch differ, and one intuitively expects to find more of the particles in the patch with a smaller escape rate. From (30) we find that

$$\frac{dN_1}{dt} = \int_0^t K_2^\beta(\tau) N_2(t-\tau) d\tau - \int_0^t K_1^\beta(\tau) N_1(t-\tau) d\tau \tag{36}$$

and

$$\frac{dN_2}{dt} = \int_0^t K_1^\beta(\tau) N_1(t-\tau) d\tau - \int_0^t K_2^\beta(\tau) N_2(t-\tau) d\tau. \tag{37}$$

In this case where $\beta_i(\tau) = \mu_i/(\tau+\tau_0)$, $\alpha_i = 0$, we find that $\psi_i(\tau) = \mu_i \tau_0^{\mu_i}/(\tau+\tau_0)^{1+\mu_i}$ and $\Psi_i(\tau) = \tau_0^{\mu_i}/(\tau+\tau_0)^{\mu_i}$. Then, $\widehat{K}_i(s) = \widehat{K}_i^\beta(s) = \widehat{\psi}_i(s)/\widehat{\Psi}_i(s)$ cannot be inverted to obtain an expression of $K_i(t)$ for all times. Instead, we can examine the long-time limit when $t \to \infty$. From (18) and applying a Laplace transformation, we can obtain expressions for $\widehat{\psi}_i(s)$. In the long-time limit we find

$$\widehat{\psi}_i(s) \simeq \begin{cases} 1 - \Gamma(1-\mu_i)(\tau_0 s)^{\mu_i} & 0 < \mu_i < 1 \\ 1 - s\tau_0/(\mu_i - 1) & 1 < \mu_i < 2. \end{cases} \tag{38}$$

Note that the case $1 < \mu_i < 2$ is qualitatively similar at long times to the PDF one obtains from a patch with a constant escape rate. However, instead of a rate we have $\lambda_i \approx (\mu_i - 1)/\tau_0$.

In the case when both patches are anomalous with small escape rates $\mu_1 < \mu_2 < 1$, we are concerned with the very slow transport of particles between two anomalously trapping regions. Substituting the results from (38) into (23)–(24) we find the long-time limits of the renewal densities to be

$$\begin{aligned} \widehat{h}_1(s) \simeq \widehat{h}_2(s) &= \frac{1}{\Gamma(1-\mu_1)(\tau_0 s)^{\mu_1} + \Gamma(1-\mu_2)(\tau_0 s)^{\mu_2}} \\ &\simeq \frac{1}{\Gamma(1-\mu_1)(\tau_0 s)^{\mu_1}}, \end{aligned} \tag{39}$$

where in the second line we have used the result that $\mu_1 < \mu_2$, indicating that this patch is more trapping than patch 2. This leads to the number of switching events between the patches being entirely dictated by the anomalous exponent μ_1; a result in stark contrast with the findings from (34) for the Morkovian case. Naturally, if $\mu_1 = \mu_2$ (39) yields $\widehat{h}_i(s) \simeq [2\Gamma(1-\mu_i)(\tau_0 s)^{\mu_i}]^{-1}$ which is equal for both patches, but as soon as the anomalous exponents change one patch completely dominates the system. All particles will tend to be found in the patch with smallest μ_i, regardless of other μ_i-values. This is an important result as larger systems with more patches can be affected by minor heterogeneities found in the anomalous exponents of each patch.

Note that there is nothing specific about either of these patches and the reverse effect can be obtained by reversing the relation $\mu_2 < \mu_1$. The aim now is to study what occurs when the patches differ and there is only one anomalously trapping patch.

4.2 One Anomalously Trapping Patch

We start by noting that an anomalous patch with $\mu_i > 1$ is equivalent in the long-time limit to a patch with constant escape rate as shown in (38). The result in this limit of having two different anomalous patches (one with $\mu_1 < 1$ and one with $\mu_2 > 1$) is thus the same as that of a comparison between a trapping anomalous patch with $\mu_1 < 1$ and a patch with constant escape rate λ_2. By the same method as before, we find

$$h_1(t) = \frac{t^{\mu_1 - 1}}{\Gamma(1-\mu_1)\Gamma(\mu_1)\tau_0^{\mu_1}} \tag{40}$$

as $t \to \infty$. So in the long-time limit patch 1 is dominant if $\mu_1 < \mu_2$. Note that (40) is independent of the escape process from patch 2: because patch 1 dominates the trapping of particles, even if these temporarily leave the patch before returning, the time spent in patch 2 tends to zero and consequently the renewal between the two patches becomes effectively equivalent to a single patch renewal process. That is, the renewal process effectively describes particles entering and leaving patch 1 with no dependence on patch 2. Heuristically, this corresponds to letting $\lambda_2 \to \infty$.

These results are qualitatively sound: the more trapping patch will aggregate more of the particles. However, a perhaps surprising result is that the long-time results are independent of patch 2. We can write these findings in terms of the renormalised structural density of the number of particles in patch 1, such that

$$\rho_1(t,\tau) = h_1(t-\tau)\Psi_1(\tau) = \frac{\Psi_1(\tau)\, t^{\mu_1 - 1}}{\Gamma(1-\mu_1)\Gamma(\mu_1)\tau_0^{\mu_1}} \tag{41}$$

as $t \to \infty$. So the (mean, renormalised) number of particles in patch 1 at time t with a certain residence time τ tends to the number of particles which entered the patch at a time $t-\tau$ (described by $h_1(t-\tau)$) and which remained there for a time τ (the probability of which is given by the survival probability $\Psi(\tau) = \int_\tau^\infty \psi(u)du$). In what follows we model this aggregation of particles in the anomalously trapping patch.

5 Linear Anomalous Aggregation

When the renewal density follows (40) we know that a non-stationary anomalous aggregation

$$N_1(t) \to 1 \qquad N_2(t) \to 0 \tag{42}$$

occurs in the long-time limit as $t \to \infty$. Heuristically, this should not be surprising: if patch 1 traps more particles and does not contain limiting factors on its size (such as a carrying capacity of the patch or volume exclusion effects) then all particles will accumulate there such that the particles which enter the patch never leave. Consequently, patch 2 will eventually be depleted.

For simplicity, let us assume that the non-trapping patch has a constant escape rate such that

$$\gamma_i = \begin{cases} \frac{\mu_1}{\tau+\tau_0} & (\alpha_1 = 0) \quad i = 1 \\ \lambda_2 & (\mu_2 = 0) \quad i = 2 \end{cases} \tag{43}$$

are our escape rates. This is a reasonable assumption as we have already motivated the aggregation of particles in the anomalously trapping patch. Applying (43) to (6) we obtain

$$\frac{\partial \rho_1}{\partial t} + \frac{\partial \rho_1}{\partial \tau} = -\frac{\mu_1 \rho_1}{\tau_0 + \tau}, \qquad \mu_1 < 1, \tag{44}$$

and

$$\frac{\partial \rho_2}{\partial t} + \frac{\partial \rho_2}{\partial \tau} = -\lambda_2 \rho_2, \qquad \lambda_2 > 0. \tag{45}$$

Solving these equations analogously to (3) via the method of characteristics we find that

$$\rho_1(t, \tau) = \rho_1(t - \tau, 0)\Psi_1(\tau), \tag{46}$$

where $\rho_1(t - \tau, 0)$ is the mean (renormalised) number of newly arrived particles in the patch. These come from patch 2 where from (9) we know that $\rho_1(t, 0) = \int_0^t \gamma_2 \rho_2(t, \tau) d\tau = \lambda_2 N_2(t)$. Similarly, for patch 2 we find that $\rho_2(t, \tau) = \rho_2(t - \tau, 0) e^{-\lambda_2 \tau}$. It follows that

$$\rho_1(t, \tau) = \lambda_2 N_2(t - \tau)\, \Psi_1(\tau), \quad t > \tau \tag{47}$$

where $\Psi_1(\tau) = \int_\tau^\infty \psi_1(u)du$ is the standard power-law survival function

$$\Psi_1(\tau) = \left(\frac{\tau_0}{\tau_0 + \tau}\right)^{\mu_1}. \tag{48}$$

We are further interested in those particles transported to the other patch. To do so, we apply a more formal definition of $h_i(t)$ than what was given in (11). If we define an event as a particle leaving a patch, then in Laplace space the renewal density follows [33]

$$\widehat{h}_i(s) = \frac{\widehat{\psi}_i(s)}{1 - \widehat{\psi}_i(s)} = \frac{\widehat{\psi}_i(s)}{s\widehat{\Psi}_i(s)}, \tag{49}$$

where $\widehat{\psi}_i$, $\widehat{\Psi}_i$ are the Laplace transformations of the residence time PDF and survival probability, respectively. We can thus rewrite (28) as

$$\widehat{I}_i(s) = \widehat{K}_i(s)\widehat{N}_i(s) = s\widehat{h}_i(s)\widehat{N}_i(s). \tag{50}$$

By applying an inverse Laplace transformation we then recover a new equation for the switching term

$$I_1 = \frac{d}{dt}\int_0^t h_1(t-\tau)N_1(\tau)d\tau, \quad I_2(t) = \lambda_2 N_2(t) \tag{51}$$

which can be compared with (29) if desired. The switching is now entirely expressed in terms of the renewal density, and we can thus find the equations for the total number of particles in each patch. From (30) and (31) we can use (51) to find that

$$\frac{dN_1}{dt} = \lambda_2 N_2(t) - \frac{d}{dt}\int_0^t h_1(t-\tau)N_1(\tau)d\tau \tag{52}$$

which is valid for all time. As we have assumed a constant number of particles, $N_1(t) + N_2(t) = 1$. From (38) we know that $\widehat{K}_1(s) = s^{1-\mu_1}/[\tau_0^{\mu_1}\Gamma(1-\mu_1)]$ in the long-time limit. This expression can be interpreted via the fractional derivative imposed by the Riemann-Liouville operator

$${}_0\mathcal{D}_t^{1-\mu_i}[N_i(t)] = \frac{d}{dt}\int_0^t \frac{N_i(t-\tau)d\tau}{\Gamma(\mu_i)\tau^{1-\mu_i}} \tag{53}$$

which in Laplace space obeys $\mathcal{L}_t\{{}_0\mathcal{D}_t^{1-\mu_i}[N_i(t)]\}(s) = s^{1-\mu_i}\widehat{N}_i(s)$ as $s \to 0$ [35]. It follows that we can write

$$\frac{dN_1}{dt} = \lambda_2 N_2(t) - \frac{1}{\tau_0^{\mu_1}\Gamma(1-\mu_1)}\,{}_0\mathcal{D}_t^{1-\mu_1}[N_1(t)]. \tag{54}$$

This does not immediately provide a clearer way of understanding the movement between the two patches, but it illustrates the fractional (slow) nature of escape events from the anomalously trapping patch. However, in the long-time limit we know that aggregation of the particles will occur in patch 1. While there may still be fluctuations in the number of particles occupying said patch, it is not unreasonable to assume it is approximately constant at larger times when the aggregation has occurred. We can then neglect the derivative $dN_1/dt \approx 0$ such that

$$\lambda_2 N_2(t) \simeq \frac{d}{dt}\int_0^t h_1(t-\tau)N_1(\tau)d\tau. \tag{55}$$

This is the statement that the rate at which particles enter patch 1 ($\lambda_2 N_2(t)$) equals the rate at which particles leave the same patch, but which is only valid for large times. By using our assumption that the net number of particles is constant, we find

$$1 = N_1(t) + \frac{1}{\lambda_2}\frac{d}{dt}\int_0^t h_1(t-\tau)N_1(\tau)d\tau. \tag{56}$$

This simple rearrangement patches that the particles are either found in patch 1 or among those which have left patch 1 up until now.

In the long-time limit we can use (49) to determine the behaviour of the renewal density. Using (38) the renewal density follows $\widehat{h}_1(s) = [(s\tau_0)^{\mu_1}\Gamma(1-\mu_1)]^{-1}$as indicated by (39). By applying an inverse Laplace transformation we obtain

$$h_1(t) = \frac{t^{-1+\mu_1}}{\Gamma(1-\mu_1)\Gamma(\mu_1)\tau_0^{\mu_1}} \tag{57}$$

as $t \to \infty$ in analogy with (40). That is, as time goes by, the number of renewal events in the patch decreases and is power law slow. This indicates that there is a slowing down in the number of particles leaving the patch. By substituting this result into (56), we find

$$N_1(t) = 1 - \frac{h_1(t)}{\lambda_2} \qquad N_2(t) = \frac{h_1(t)}{\lambda_2}, \tag{58}$$

which is consistent with the qualitative findings suggested already in (42). However, we now have a greater amount of detail as to how this aggregation occurs. It is important to note that while anomalous aggregation in patch 1 is observed, we do not reach a steady-state distribution of the patch population. Movements can and do still occur between the two patches, albeit very slowly.

We shall now consider what occurs in the case when this aggregation is tempered by an additional escape rate of the system.

6 Anomalous Tempering

Having now detailed the process which occurs in the presence of anomalous patches, we shall now proceed to consider the effects of an additional tempering rate. By adding a constant α_i to the basic description in (35), we obtain

$$\gamma_i(\tau) = \frac{\mu_i}{\tau_0 + \tau} + \alpha_i \qquad 0 < \mu_i < 1, \tag{59}$$

where $\beta_i(\tau) = \mu_i/(\tau + \tau_0)$ is consistent with (10). This could change the effects observed in (58), by e.g., increasing the escape rate so as to maintain a minimum non-zero escape rate from the patch. The value (and sign) of α_i can be chosen according to, e.g., saturation limits in the concentration of ions present in a certain transporter channel [36] or to regulate the presence of enzymes required in protein folding [37]. The details and extent of this tempering are entirely determined by choices in the values of α_i.

An anomalously trapping patch with $\mu_i < 1$ could thus be subject to internal regulation in the form of the tempering term which maintains the escape rate even when a large number of particles are trapped. Another possible interpretation of such a system is one wherein there is a limited binding radius beyond which arriving particles are very weakly bound, thus resulting in a constant associated escape rate. This is the simplest possible form of a self-regulating process [36].

As we now have two escape rates, the switching terms for these patches (defined in (29)) become:

$$I_i(t) = \alpha_i N_i(t) + \int_0^t K_i^{\beta}(\tau) e^{-\alpha_i \tau} N_i(t-\tau) d\tau, \tag{60}$$

where we again must find the long-time limit of the integral term. Since $\widehat{\phi}_i^{\beta}(s) = 1 - \Gamma(1-\mu_i)(\tau_0 s)^{\mu_i}$ and $\widehat{\Phi}_i^{\beta}(s) = \Gamma(1-\mu_i)(\tau_0 s)^{\mu_i}/s$, we find from (28) that $\widehat{K}_i^{\beta}(s) = s^{1-\mu_i}/[\tau_0^{\mu_i}\Gamma(1-\mu_i)]$. The Laplace transformation of (60) yields

$$\widehat{I}_i(s) = \alpha_i \widehat{N}_i(s) + \frac{(s+\alpha_i)^{1-\mu_i}}{\tau_0^{\mu_i}\Gamma(1-\mu_i)} \widehat{N}_i(s) \tag{61}$$

as $s \to 0$. We notice that this expression is analogous to the form of a modified Riemann-Liouville operator (see (53) and [35]), such that we can write

$$I_i(t) = \alpha_i N_i(t) + \frac{e^{-\alpha_i t}}{\tau_0^{\mu_i}\Gamma(1-\mu_i)} {}_0\mathcal{D}_t^{1-\mu_i}[e^{\alpha_i t} N_i(t)]. \tag{62}$$

This is equivalent to a tempered Riemann-Liouville operator (see, e.g., [38]). By the same method as employed for (30)–(31), we obtain equations for the rate of change of particles in each patch:

$$\begin{aligned}\frac{dN_1}{dt} =&\alpha_2 N_2(t) + \frac{e^{-\alpha_2 t}}{\tau_0^{\mu_2}\Gamma(1-\mu_2)}\,{}_0\mathcal{D}_t^{1-\mu_2}[e^{\alpha_2 t}N_2(t)]\\ &-\alpha_1 N_1(t) - \frac{e^{-\alpha_1 t}}{\tau_0^{\mu_1}\Gamma(1-\mu_1)}\,{}_0\mathcal{D}_t^{1-\mu_1}[e^{\alpha_1 t}N_1(t)],\end{aligned} \tag{63}$$

and

$$\begin{aligned}\frac{dN_2}{dt} =&\alpha_1 N_1(t) + \frac{e^{-\alpha_1 t}}{\tau_0^{\mu_1}\Gamma(1-\mu_1)}\,{}_0\mathcal{D}_t^{1-\mu_1}[e^{\alpha_1 t}N_1(t)]\\ &-\alpha_2 N_2(t) - \frac{e^{-\alpha_2 t}}{\tau_0^{\mu_2}\Gamma(1-\mu_2)}\,{}_0\mathcal{D}_t^{1-\mu_2}[e^{\alpha_2 t}N_2(t)],\end{aligned} \tag{64}$$

We thus have two expressions for the number of particles entering and leaving each patch which are analogous to the results of the previous section, but which contain a faster (though still slow) transfer between the patches via the tempered Riemann-Liouville operator. However, for sufficiently large times the tempering effect introduces a cut-off in the operator and we are left with a modified constant escape rate such that

$$\frac{dN_1}{dt} = \lambda_2^* N_2(t) - \lambda_1^* N_1(t), \tag{65}$$

where these escape rates follow

$$\lambda_i^* = \alpha_i + \frac{\alpha_i^{1-\mu_i}}{\tau_0^{\mu_i}\Gamma(1-\mu_i)}. \tag{66}$$

Note that the tempering from α_i is observed in both terms, despite the initial description of γ_i considering two independent processes. This is a result of the non-Markovian behaviour of $\beta_i(\tau)$. If the tempering effects disappear ($\alpha_i = 0$) this rate λ_i^* is no longer valid. However, when there is tempering we find that a non-zero distribution of particles can be expected across both patches. In the stationary case $dN_1/dt = 0$, we find that

$$N_1^{st} = \frac{\lambda_2^*}{\lambda_1^* + \lambda_2^*}, \quad N_2^{st} = \frac{\lambda_1^*}{\lambda_1^* + \lambda_2^*} \tag{67}$$

which mirrors the results obtained in the case with two constant escape rates between the patches. What we conclude from this is that the presence of the tempering in α_i removes the anomalous effects in the long-time limit. However, over shorter time scales the anomalous aggregation effects may still dominate the dynamics. For the simplified case of (65), we obtain an analogous renewal density to (34)

$$h_1^{st} = h_2^{st} = \frac{\lambda_1^* \lambda_2^*}{\lambda_1^* + \lambda_2^*}. \tag{68}$$

If instead of two anomalous tempered patches we consider patch 1 to have an escape rate as given by (59), and patch 2 to have a constant escape rate λ_2, then (63) becomes

$$\begin{aligned} \frac{dN_1}{dt} =& \lambda_2 N_2(t) - \alpha_1 N_1(t) \\ & - \frac{e^{-\alpha_1 t}}{\tau_0^{\mu_1}\Gamma(1-\mu_1)}\, {}_0\mathcal{D}_t^{1-\mu_1}[e^{\alpha_1 t} N_1(t)]. \end{aligned} \tag{69}$$

In this case the mean renormalised structural density from (6) follows

$$\frac{\partial \rho_1}{\partial t} + \frac{\partial \rho_1}{\partial \tau} = -\gamma_1(\tau)\rho_1. \tag{70}$$

Because there is tempering in effect, it is interesting to consider what occurs over longer time scales where the system has presumably equilibrated to a stationary distribution. Then, the particles are still ageing, but there is balance in the number of particles entering and leaving such that $\partial \rho_1^{st}/\partial t = 0$ (note that st refers to any quantity in the stationary patch). Equation (70) thus becomes

$$\frac{\partial \rho_1^{st}}{\partial \tau} = -\left(\frac{\mu_1}{\tau_0 + \tau} + \alpha_1\right)\rho_1^{st}. \tag{71}$$

Using the fact that new arrivals in patch 1 are given by $\rho_1(t,0) = \lambda_2 N_2(t)$, we can solve the above equation to give

$$\rho_1^{st}(\tau) = \lambda_2 N_2^{st}\left(\frac{\tau_0}{\tau_0 + \tau}\right)^{\mu_1} e^{-\tau\alpha_1}, \tag{72}$$

where N_2^{st} is the number of particles in patch 2 when a steady state has been reached. Here we have identified the survival function $\Psi_1(\tau) = \tau_0^{\mu_1} e^{-\tau\alpha_1}/(\tau_0 + \tau)^{\mu_1}$. So the number of particles with lower residence times is still high, but there is a tempering in the number of particles with long residence times. This is seen by

the decaying exponential effectively 'cutting off' the longer power-law tail in $\tau^{-\mu_1}$. By integration over all residence times, the mean renormalised number of particles in patch 1 at equilibrium is given by

$$\begin{aligned} N_1^{st} =& \lambda_2 N_2^{st} \int_0^\infty \left(\frac{\tau_0}{\tau_0+\tau}\right)^{\mu_1} e^{-\tau\alpha_1} d\tau \\ =& \lambda_2 N_2^{st} \tau_0^{\mu_1} e^{\tau_0\alpha_1} \alpha_1^{\mu_1-1} \Gamma(1-\mu_1, \tau_0\alpha_1), \end{aligned} \tag{73}$$

where $\Gamma(a,x) = \int_x^\infty t^{a-1}e^{-t}dt$ is the incomplete Gamma function [35]. By definition, we know that the mean residence time spent in a patch is given by $\langle T_i\rangle = \int_0^\infty \Psi_i(\tau)d\tau$. This is exactly the form we find in the above equation, such that we can write

$$N_1^{st} = \lambda_2 N_2^{st} \langle T_1\rangle , \tag{74}$$

where $\langle T_1\rangle = \tau_0^{\mu_1} e^{\tau_0\alpha_1} \alpha_1^{\mu_1-1}\Gamma(1-\mu_1, \tau_0\alpha_1)$. However, this result is only valid in the case when $\alpha_1 > 0$, as the integral otherwise diverges for $\mu_1 < 1$. Similarly for a constant escape rate we can write $\langle T_2\rangle = 1/\lambda_2$. Since the total number of particles is preserved, we find that

$$N_1^{st} = \frac{\langle T_1\rangle}{\langle T_2\rangle + \langle T_1\rangle}, \quad N_2^{st} = \frac{\langle T_2\rangle}{\langle T_2\rangle + \langle T_1\rangle}. \tag{75}$$

Unsurprisingly, this result also mimics what we obtained when studying two patches both with constant escape rates. If we are in the long-time limit this result is equivalent to that of (65) as one can argue $\langle T_i\rangle \sim 1/\lambda_i$. Both patches here influence the final distribution of the particles, but we also observe that likely the particles will aggregate in the anomalous patch.

The above nicely illustrates the effects of tempering of the anomalous effects: accumulation still occurs with preference for the anomalously trapping patch, but the presence of α_i is such that particles could still be found in either patch. If both patches are tempered, this dominates the long-term dynamics completely (but is still a function of the anomalous exponents μ_i).

7 Discussion and Conclusion

We have formulated the transport of particles in a heterogeneous, patchy environment and illustrated the effects of heterogeneities in the transport via the close study of transport between two patches. It has been shown that in contrast to the Markovian case (where the escape rates from patches or patches are constant), small heterogeneities in the escape rates via the anomalous exponents can lead to

significant and qualitatively different distributions of particles across the system. This result remains true when constructing a larger patchy environment via the pairwise links between different patches.

We have shown that a large number of particles will aggregate in the anomalous nodes (wherein the likelihood of leaving decreases with residence time), but that significant qualitative differences arise depending on whether the patch is anomalously trapping $0 < \mu < 1$ or not $1 < \mu < 2$. We have further demonstrated the effects of tempering terms in the transport processes which lead to a more even distribution of the particles than one obtains for a solely anomalously trapping patch. This is consistent with finite size effects whereupon the trapping can only occur for a binding up to a certain limit—there is thus always a minimum escape rate.

The transport of particles in cell membranes or subcellular structures is known to be subject to both non-Markovian (anomalous) transport effects and the ones introduced in the paper (volume exclusion, finite concentration of reaction components in producing patches, and so on).

In the long-time limit particles are observed to aggregate in the anomalous (more highly trapping) patch at a power law slow rate compared to patches with a constant escape rate. This is summarised in (58). For non-trapping anomalous patches with $1 < \mu < 2$, an equilibrium is reached between the two patches. The combination of these two cases with the effects resulting from tempering can be combined according to the biological system of interest.

It is clear that these effects can have large implications for understanding transport mechanisms in cells. Anomalous and tempering effects are both important and significant contributions to our understanding of cell transport which in combination yield results unseen when modelling these aspects separately.

Aggregation of particles can only occur over time scales shorter than the lifetimes of the particles in question. Naturally, one expects each cell to be subject to birth–death dynamics such that certain particles may ‘perish’ before reaching the attractive patch. One can also consider degradation rates and corruption of certain transcription processes as other inherent limits to the process. These, along with the introduction of carrying capacities in the limitations of the patches, are directions of future work to be explored.

Acknowledgements The authors would like to thank N. Korabel and T. Waigh for fruitful discussions. This work is supported by EPSRC grant EP/N018060/1.

References

1. Petrovskii SV, Morozov AY, Venturino E (2002) Allee effect makes possible patchy invasion in a predator-prey system. Ecol Lett 5(3):345–352
2. Bressloff PC (2014) Stochastic processes in cell biology. Springer, Berlin
3. Méndez V, Fedotov S, Horsthemke W (2010) Reaction-transport systems: mesoscopic foundations, fronts, and spatial instabilities. Springer, Berlin

4. Méndez V, Campos D, Bartumeus F (2014) Stochastic foundations in movement ecology: anomalous diffusion, front propagation and random searches. Springer, Berlin
5. Schewe M, Nematian-Ardestani E, Sun H, Musinszki M et al (2016) A non-canonical voltage-sensing mechanism controls gating in K2P K^+ channels. Cell 164(5):937–949
6. Li N, Wu J-X, Ding D, Cheng J, Gao N, Chen L (2017) Structure of a pancreatic ATP-sensitive potassium channel. Cell 168(1–2):101–110
7. Jahn R, Fasshauer D (2012) Molecular machines governing exocytosis of synaptic vesicles. Nature 490(7419):201–207
8. Hirokawa N, Takemura R (2004) Molecular motors in neuronal development, intracellular transport and diseases. Curr Opin Neurobiol 14(5):564–573
9. Aridor M, Hannan LA (2002) Traffic jams II: an update of diseases of intracellular transport. Traffic 3(11):781–790
10. Saxton MJ (2001) Anomalous subdiffusion in fluorescence photobleaching recovery: a Monte Carlo study. Biophys J 81(4):2226–2240
11. Santamaria F, Wils S, De Schutter E, Augustine GJ (2006) Anomalous diffusion in Purkinje cell dendrites caused by spines. Neuron 52(4):635–648
12. Golding I, Cox EC (2006) Physical nature of bacterial cytoplasm. Phys Rev Lett 96:098102
13. Goychuk I, Kharchenko VO, Metzler R (2014) How molecular motors work in the crowded environment of living cells: coexistence and efficiency of normal and anomalous transport. PLoS ONE 9(3):1–7
14. Klafter J, Sokolov IM (2011) First steps in random walks: from tools to applications. Oxford University Press, Oxford
15. Ariel G, Rabani A, Benisty S, Partridge JD, Harshey RM, Be'er A (2015) Swarming bacteria migrate by Lévy walk. Nat Commun 6(8396)
16. Harris TH, Banigan EJ, Christian DA, Konradt C, Wojno EDT, Norose K, Wilson EH, John B, Weninger W, Luster AD, Liu AJ, Hunter CA (2012) Generalized Lévy walks and the role of chemokines in migration of effector $CD8^+$ T cells. Nature 486(7404):545–548
17. Bruno L, Levi V, Brunstein M, Despósito MA (2009) Transition to superdiffusive behavior in intracellular actin-based transport mediated by molecular motors. Phys Rev E 80:011912
18. Köhler S, Schaller V, Bausch AR (2011) Structure formation in active networks. Nat Mater 10:462–468
19. Chechkin AV, Gorenflo R, Sokolov IM (2005) Fractional diffusion in inhomogeneous media. J Phys A Math Gen 38(42):L679
20. Fedotov S, Falconer S (2012) Subdiffusive master equation with space-dependent anomalous exponent and structural instability. Phys Rev E 85:031132
21. Korabel N, Barkai E (2010) Paradoxes of subdiffusive infiltration in disordered systems. Phys Rev Lett 104:170603
22. Fedotov S, Korabel N (2015) Self-organized anomalous aggregation of particles performing nonlinear and non-Markovian random walks. Phys Rev E 92:062127
23. Fedotov S, Korabel N (2017) Emergence of Lévy walks in systems of interacting individuals. Phys Rev E 95:030107
24. Stickler BA, Schachinger E (2011) Continuous time anomalous diffusion in a composite medium. Phys Rev E 84:021116
25. Lawless JF (2003) Statistical models and methods for lifetime data. Wiley, New York
26. Fedotov S, Iomin A, Ryashko L (2011) Non-Markovian models for migration-proliferation dichotomy of cancer cells: anomalous switching and spreading rate. Phys Rev E 84:061131
27. Goychuk I (2015) Anomalous transport of subdiffusing cargos by single kinesin motors: the role of mechano-chemical coupling and anharmonicity of tether. Phys Biol 12(1):016013
28. Hafner AE, Santen L, Rieger H, Shaebani MR (2016) Run-and-pause dynamics of cytoskeletal motor proteins. Nat Sci Rep 6(37162)
29. Krishnamurthy H, Piscitelli CL, Gouaux E (2009) Unlocking the molecular secrets of sodium-coupled transporters. Nature 459:347–355
30. Guigas G, Weiss M (2008) Sampling the cell with anomalous diffusion – the discovery of slowness. Biophys J 94(1):90–94

31. Fedotov S, Méndez V (2008) Non-Markovian model for transport and reactions of particles in spiny dendrites. Phys Rev Lett 101:218102
32. Fedotov S, Al-Shamsi H, Ivanov A, Zubarev A (2010) Anomalous transport and nonlinear reactions in spiny dendrites. Phys Rev E 82:041103
33. Cox DR, Miller HD (1977) The theory of stochastic processes. CRC Press, Boca Raton
34. Cox DR (1970) Renewal theory. Methuen, London
35. Miller KS, Ross B (1993) An introduction to the fractional calculus and fractional differential equations. Wiley, New York
36. Krapivinsky G, Kirichok Y, Clapham DE (2004) The mitochondrial calcium uniporter is a highly selective ion channel. Nature 427:360–364
37. Boillée S, Velde CV, Cleveland DW (2006) ALS: a disease of motor neurons and their nonneuronal neighbors. Neuron 52(1):39–59
38. Meerschaert MM, Zhang Y, Baeumer B (2008) Tempered anomalous diffusion in heterogeneous systems. Geophys Res Lett 35(17):L17403

The Non-equilibrium Nature of Active Motion

Francisco J. Sevilla

Abstract In this contribution chapter, the non-equilibrium nature of active motion is explored in the framework of the Generalized Langevin Equation. The persistence effects that distinguish active motion, observed in a variety of biological organisms and man-made colloidal particles, from the passive one, are put in correspondence with the memory function that characterizes the retarded dissipative effects in the equation. The non-equilibrium aspects of this approach rely on the relaxation of the fluctuation-dissipation relation, that couples the memory function with the autocorrelation function of the fluctuating force in order to describe the equilibrium. In the case of freely diffusing active particles, the Fokker-Planck equation is derived and an effective temperature can be identified if the total overlap between the deterministic solutions of the Generalized Langevin Equation at two times, weighted by the noise correlation function, exists and is finite. Active motion confined by the harmonic, external potential is analyzed on the same framework leading to analogous conclusions.

Keywords Active motion · Generalized Langevin equation · Confined active particles · Fluctuation-dissipation theorem · Persistent Brownian motion

1 Introduction

The systems in out-of-equilibrium conditions are ubiquitous in nature and have been the subject of intense study in many fields of knowledge during the last two centuries, at least. Among those systems, the biological ones are the most representatives of non-equilibrium situations, which despite the most obvious non-equilibrium feature, *life*, other non-equilibrium aspects of biological organisms have

F. J. Sevilla (✉)
Instituto de Fisica, Universidad Nacional Autónoma de México, Apdo. Postal 20-364, 01000, CD.MX., Mexico City, Mexico
e-mail: fjsevilla@fisica.unam.mx

L. Olivares-Quiroz, O. Resendis-Antonio (eds.), *Quantitative Models for Microscopic to Macroscopic Biological Macromolecules and Tissues*,
https://doi.org/10.1007/978-3-319-73975-5_4

received considerable attention, for instance: biological micromotors or molecular motors, which are able to travel along polymer filaments inside a cell [1]; motile organisms, like bacteria, that employs diverse motility patterns to traverse complex habitats [2, 3], for example *E. coli* which performs the so-called *run-and-tumble* dynamics [4] as pattern of motion. More recent advances have allowed the design of artificial particles that take advantage of different physical and/or chemical mechanisms, to self-induced motion that mimics that of biological organisms [5], as such, the design of artificial micromotors, which use locally supplied fuels, to autonomously deliver and release therapeutic payloads and manipulate cells [6].

All these examples have in common that the mobile entities involved, either biological or man-made, are able to develop their own motion by using the locally available energy from the environment and transform it, by complex internal mechanisms (micromotor or microengine) or by ingeniously self-phoretic mechanisms, into self-locomotion [5, 7, 8]. These particles are called *self-propelled* or *active particles*, in contrast to the motion of a pollen grain in water (effect observed by the botanist Robert Brown) that moves passively due to the myriads of collisions with the molecules of the embedding liquid. Systems composed of a collection of self-propelled or active particles receive nowadays the name of *active matter* and are the subject of intense research, mainly because the non-equilibrium features exhibited in the collective and single particle behavior give the possibility to discover new physics, and as consequence, their potential applications.

The intrinsic non-equilibrium aspects of active matter have attracted the attention on these systems, and a front of intense research in different disciplines, mainly in statistical physics and biology, is still growing [5, 7, 8]. From the point of view of non-equilibrium statistical physics, active matter has become a well-defined class of non-equilibrium systems and a fertile field of research, that has allowed the rapid theoretical advancements in the field. Succinctly, active matter escapes from a description of equilibrium since, at microscopic scales, detailed balance between injection and dissipation of energy is not satisfied, which leads inexorably to the production of entropy.

One aspect to highlight in regard to the motility of active particles is that active motion is persistent, that is to say, the particles approximately retain the state of motion for a characteristic finite time scale, called the persistence time. This feature is indeed observed in the patterns of motion of different biological organisms and in the motility behavior of some artificial particles. For instance, the run-and-tumble pattern of motion alternates periods of time for which *E. coli* moves almost with constant speed and in a straight line along a randomly chosen direction, with short periods of time for which the particle is almost in rest tumbling. On a statistical description of this process, run-and-tumble dynamics can be characterized by finite time scale of persistence, which makes motility behavior strongly correlated in time, making non-equilibrium signatures conspicuously observable.

On the other hand, a finite persistence time scale can be induced on micron silica spheres through a diffusion-phoretic mechanism (Janus particles). Such mechanism confer out-of-equilibrium fluctuations on a region of the particle surface (by coating one of the particle hemispheres with a suitable metal for instance), breaking, locally,

the symmetry of the effects of fluctuations on the particle [9, 10]. This breaking of symmetry causes an overdamped description of the translational degree of freedom (particle usually diffuses in aqueous solutions), and an underdamped description of rotational diffusion that leads to the appearance of persistence effects. The pattern of motion generated by this process is called *active Brownian motion*.

Many of the accomplished advancements in the understanding of active matter partly rely on the intuition built from equilibrium systems [11–13]. In reference [14] the authors provide arguments that show that the transition to *collective motion* in the Vicsek model [15]—a system of active particles under the influence of mutual motion alignment and non-thermal angular noise—can be best explained as a liquid-gas transition rather than an order-disorder one. Indeed, the inhomogeneous phases (smectic arrangements of traveling ordered bands surrounded by particles that form a gaseous-like phase) observed at intermediate noise and density are reminiscent of the coexistence liquid-gas phases in the transition.

Other non-equilibrium aspects exhibited in systems of interacting active particles refer to the observed *motility induced phase separation* (MIPS) [11, 13, 16–19], that corresponds to the coexistence of liquid-gas phases of repulsive self-propelled particles where no collective motion emerges. Attempts to give a description of MIPS in terms of equilibrium concepts have appeared, however these are limited and debated [16]. In some models that exhibit MIPS [19], time-reversal symmetry is preserved if the persistence time is small but finite, this endows such systems with an effective fluctuation-dissipation theorem akin to that of thermal equilibrium systems. In systems of spherical active Brownian particles it has been possible to derive an expression for the equation of state of the mechanical pressure of the system as function of particle density. Previous attempts identified the contribution to the pressure exerted by a suspension of active particles that originates upon the notion that an active body would swim away in space unless confined by boundaries [11]. This observation allowed the authors to find a non-equilibrium equation of state whose phase diagrams resemble a van der Waals loop from equilibrium gas-liquid coexistence.

Another equilibrium concept that has resulted valuable in the description of out-of-equilibrium systems is that one of *effective temperature* [20–22], in particular in systems of active particles [23–30]. In general, the possibility of defining an effective temperature relies on the fulfillment of a non-thermal fluctuation-dissipation relation. This is the case for time scales larger than the persistence one, since in this regime the motion of free active particles is well characterized by an effective diffusion coefficient, and can be interpreted as the motion of a passive Brownian particle diffusing in a *fictitious* environment at the effective temperature.

The out-of-equilibrium nature of systems of active particles is revealed markedly when the system is under confinement. Particularly, in the regime for which the characteristic length scale of confinement is smaller, or of the order, of the persistence length scale. Under such conditions, the zero-current probability distribution of non-interacting active particles deviates conspicuously from the equilibrium distribution of Boltzmann and Gibbs. Such effects have been certainly predicted by theory in

models of active particles under the confinement of an external potential [31, 32] and observed experimentally, for instance, in acoustically confined active Brownian particles [33], in confined worker termites [34], and in passive Brownian particles swimming within an active Bath [35].

The non-Boltzmann-Gibbs distributions that correspond to the stationary distributions of run-and-tumble particles, that move with constant speed under the confinement of an external potential, can be understood as the distributions of passive Brownian particles diffusing under the influence of the external potential and of a fictitious inhomogeneous thermal bath (Sevilla, Vasquez-Arzola, Puga-Cital, 2017, unpublished), where the precise spatial dependence of the effective temperature profile can be put in an exact manner in correspondence with the trapping potential. In contrast, models that consider the case for which particle speed fluctuates can lead to Boltzmann-Gibbs-like distributions at least when the particles are confined by an external harmonic potential, as has been shown in a one-dimensional model of active motion [29]. For this particular model of active particles (also known as active-Ornstein-Uhlenbeck particles), the existence of a uniform effective temperature is shown.

The existence of many different theoretical frameworks that consider persistence in their own formulation makes worthy their study and analysis in relation with concepts of non-equilibrium statistical mechanics, partly because some aspects may well correspond to qualitatively distinct phenomena, as has been described in the last paragraph, but mainly because many of these frameworks incorporate straightforwardly the important effects of correlations that leads, for instance, to a proper description of anomalous diffusion. Among these frameworks, we can cite: the *persistent random walks*, recurrently used in biology [36] and studied intensively in statistical physics towards the last decade of the last century [37, 38]; the *continuous-time random walk* [39] which endows random walk with correlations in continuous time; and the *generalized Langevin Equation* [40], which endows the standard equation of Langevin of Brownian motion with finite time correlations. The generalized Langevin equation usually models systems in equilibrium with a viscoelastic bath, which describe the equilibrium of the retarded effects in the viscous drag term of the equation and correlated noises.

A straightforward way to model the active motion of Brownian-like particles, is to include a non-linear dissipative term in the Langevin equation, i.e., by the introduction of a non-linear friction term that keeps the speed of the particles almost constant in time [41, 42], as approximately occurs in many active systems. The non-equilibrium nature of these systems, when particles move under the influence of an external potential, has been analyzed by the calculation of the entropy production [43]. However, given the non-linear nature of the equations involved, no exact expressions for the stationary distributions of the particle positions exist.

In this contribution, we explore the non-equilibrium nature of confined active motion in an external potential, by making a correspondence of the persistence effects of active motion with the memory function that characterizes the retarded dissipative effects in the linear generalized Langevin equation. The non-equilibrium aspects of this approach rely on the relaxation of the fluctuation-dissipation relation,

which describes equilibrium if and only if the memory function in the retarded friction term is proportional to the autocorrelation function of the fluctuating force in the equation.

1.1 The Generalized Langevin Equation: Diffusion of a Free Particle in an Equilibrium Bath at Temperature T

The Generalized Langevin Equation, that describes the kinematic state of a Brownian particle of mass m in one dimension, are

$$m\frac{d}{dt}v(t) = -\gamma \int_{t_0}^{t} ds\, \phi(t-s)v(s) + \xi(t), \tag{1a}$$

$$\frac{d}{dt}x(t) = v(t), \tag{1b}$$

where $x(t)$ and $v(t)$ denote the position and velocity of the particle, respectively. The retarded effects in the dissipation term are encoded in the memory function $\phi(t)$ which has units of $[\text{time}]^{-1}$, while the coefficient γ, the Stokes dragging coefficient, is used as a scale of the net friction force. In the cases of interest, the memory function vanishes after some characteristic time scale that can well be assumed smaller than t_0, therefore $t - t_0$ is the time span for which the memory effects are important and thus, any effect prior to time t_0 can be neglected. In the of-equilibrium processes where the effects of ageing are not important, of particular physical relevance are those cases for which Eq. (1) describe a stationary process, i.e., a process whose statistical properties are invariant under temporal translations, in such a case, t_0 can be set to zero without loss of generality. For simplicity the *noise* term, $\xi(t)$, is assumed to be stationary and Gaussian with vanishing average $\langle \xi(t) \rangle = 0$ and autocorrelation function

$$\langle \xi(t)\xi(s) \rangle = \langle \xi^2 \rangle_{\text{eq}} \Gamma(|t-s|), \tag{2}$$

with $\langle \xi^2 \rangle_{\text{eq}}$ is the parameter that characterizes the fluctuations of thermal equilibrium at temperature T, and $\Gamma(t)$ is a dimensionless function of time.

If in addition to the physical assumptions framed in Eq. (1), it is supposed that the effects of the correlated thermal fluctuations over the particle—induced by a surrounding thermal bath at equilibrium and characterized by the temperature T—are balanced by the dissipation term, then the stochastic process $v(t)$ reaches a stationary regime for which the distribution of velocities, $P_{\text{eq}}(v)$, corresponds to that of equilibrium. Under these conditions, one can safely assume that equipartition is valid for the kinetic energy of the Brownian particle and an explicit relation among the functions $\phi(t)$ and $\Gamma(t)$ can be obtained. Such relation has been called the fluctuation-dissipation relation [40]. In contrast, since the particle diffuses freely, the stochastic process $x(t)$ will not reach a stationary regime. Indeed, the distribution

width of the particle positions, measured by the distribution variance, is expected to grow with time indefinitely. Thus, in regards to the joint dynamics of both processes, $v(t)$ and $x(t)$, we say that the system equilibrates partially.

Though formal derivations of the fluctuation-dissipation relation are known [44], the following derivation is heuristically straightforward. Consider the solution of Eq. (1a), given explicitly by

$$v(t) = v(0)\Phi(t) + \frac{1}{m}\int_0^t ds\, \Phi(t-s)\xi(s), \tag{3}$$

where $v(0)$ is the initial velocity and $\Phi(t)$ is the function that satisfies the equation

$$m\frac{d\Phi(t)}{dt} + \gamma\int_0^t ds\, \phi(t-s)\Phi(t) = 0, \tag{4}$$

which in the Laplace domain has the explicit dependence on $\widetilde{\phi}(\epsilon)$ through the relation

$$\widetilde{\Phi}(\epsilon) = \left[\epsilon + \frac{\gamma}{m}\widetilde{\phi}(\epsilon)\right]^{-1}. \tag{5}$$

A symbol with tilde, $\widetilde{f}(\epsilon)$, denotes the Laplace transform of $f(t)$ given by

$$\widetilde{f}(\epsilon) = \mathcal{L}\{f(t);\epsilon\} = \int_0^\infty dt\, e^{-\epsilon t} f(t) \tag{6}$$

with ϵ the Laplace variable, a complex number.

The assumption that the distribution of velocities of the Brownian particle reaches a stationary regime characterized by thermal equilibrium implies that an equipartition-like theorem applies for the Brownian particle velocity, i.e.

$$\frac{m}{2}\langle v^2(t)\rangle = \frac{k_B T}{2}, \tag{7}$$

where k_B is the Boltzmann constant. If the square of (3) is taken and then multiplied by $m/2$ we have that the ensemble average over all possible realizations of the random force $\xi(t)$ gives

$$\frac{m}{2}\langle v^2(t)\rangle = \frac{m}{2}v^2(0)\Phi^2(t) + \frac{\langle \xi^2\rangle_{\text{eq}}}{m}\int_0^t ds_1 \int_0^{s_1} ds_2\, \Phi(s_1)\Phi(s_2)\Gamma(s_1 - s_2), \tag{8}$$

where we used the fact that $\langle \xi(t)\rangle = 0$ and the explicit dependence on the initial conditions $v(0)$ is shown. However, if the initial velocities of the Brownian particle were distributed according to thermal equilibrium, we must have that

$$\frac{m}{2}\overline{v^2(0)} = \frac{m}{2}\langle v^2(t)\rangle = \frac{k_B T}{2}, \tag{9}$$

must be satisfied, where the $\overline{v^2(0)}$ denotes the ensemble average over initial velocities. We have straightforwardly that

$$k_B T\left[1-\Phi^2(t)\right]=\frac{\langle\xi^2\rangle_{\mathrm{eq}}}{m}\int_0^t ds_1\int_0^{s_1} ds_2\,\Phi(s_1)\Phi(s_2)\Gamma(s_1-s_2), \tag{10}$$

where use of the relation (2) has been made. Now take the time derivative on both sides of the last expression, and after making some rearrangements we get

$$-\frac{2mk_BT}{\langle\xi^2\rangle_{\mathrm{eq}}}\frac{d\Phi(t)}{dt}=\int_0^t ds_2\,\Phi(s_2)\Gamma(t-s_2), \tag{11}$$

whose Laplace transform is given by

$$\frac{2mk_BT}{\langle\xi^2\rangle_{\mathrm{eq}}}[\Phi(0)-\epsilon\widetilde{\Phi}(\epsilon)]=\widetilde{\Phi}(\epsilon)\widetilde{\Gamma}(\epsilon). \tag{12}$$

We must assume that $\phi(t)$ is such that $\lim_{\epsilon\to\infty}\widetilde{\phi}(\epsilon)/\epsilon$ goes to zero, then, by the *Tauberian* theorems we have that $\Phi(0)=1$ and thus

$$\frac{2mk_BT}{\langle\xi^2\rangle_{\mathrm{eq}}}\left[\frac{1}{\widetilde{\Phi}(\epsilon)}-\epsilon\right]=\widetilde{\Gamma}(\epsilon). \tag{13}$$

After substitution of (5) we finally get

$$\widetilde{\Gamma}(\epsilon)=\frac{2k_BT}{\langle\xi^2\rangle_{\mathrm{eq}}}\gamma\widetilde{\phi}(\epsilon) \tag{14}$$

or by recalling that $\langle\xi^2\rangle_{\mathrm{eq}}\Gamma(t)=\langle\xi(s)\xi(s+t)\rangle$ we get

$$\langle\xi(s)\xi(s+t)\rangle=2k_BT\gamma\phi(t). \tag{15}$$

This is the fluctuation-dissipation relation [40], that establishes the equilibrium temperature T as the proportionality factor between the autocorrelation function of the thermal force (*internal noise* [45–47]) and the function that characterizes the retarded effect of the dragging force. Such a relation guarantees the reach of equilibrium for the process $v(t)$ at the temperature of the bath T, for arbitrary time dependence of the noise autocorrelation function as long as this decays to zero with time.

$P(v,t)$ and Its Associated Fokker-Planck Equation

As a consequence of the fluctuation-dissipation relation (15), the stationary distribution of the particle velocities is given by the Maxwell distribution at the fluid temperature T, but evidently with the mass m of the Brownian particle.

The conditional probability distribution, $P(v,t|v(0))$, of a particle having the velocity v at time t given that had velocity $v(0)$ at time $t=0$ is defined by

$$P(v,t|v(0)) \equiv \langle \delta[v - v(t)] \rangle \,, \tag{16}$$

where $v(t)$ is the solution of Eq. (1a) given by (3), and the ensemble average $\langle\,\rangle$ is made over the noise realizations of $\xi(t)$ with fixed initial conditions. We have then that

$$P(v,t|v(0)) = \frac{1}{2\pi}\int_{-\infty}^{\infty} dk\, e^{ik[v - v(0)\Phi(t)]} \left\langle e^{i\frac{k}{m}\int_0^t ds\,\Phi(t-s)\xi(s)} \right\rangle. \tag{17}$$

The quantity

$$\left\langle e^{i\frac{k}{m}\int_0^t ds\,\Phi(t-s)\xi(s)} \right\rangle \tag{18}$$

is the characteristic functional of the stochastic process variable $\xi(t)$, since it has been assumed to be Gaussian has the explicit expression [48]

$$\exp\left\{ -\frac{k^2\langle \xi^2\rangle_{\rm eq}}{m^2}\int_0^t ds_1 \int_0^{s_1} ds_2\, \Phi(s_1)\Phi(s_2)\Gamma(s_1 - s_2)\right\}$$

and therefore we have that

$$P(v,t|v(0)) = \frac{1}{2\pi}\int_{-\infty}^{\infty} dk\, e^{ik[v - v(0)\Phi(t)]} e^{-k^2\frac{\langle \xi^2\rangle_{\rm eq}}{m^2}\int_0^t ds_1 \int_0^{s_1} ds_2\, \Phi(s_1)\Phi(s_2)\Gamma(s_1 - s_2)}.$$

Last expression can be evaluated explicitly and gives

$$P(v,t|v(0)) = \frac{\exp\left\{ -\dfrac{[v - v(0)\Phi(t)]^2}{2\langle [v - v(0)\Phi(t)]^2\rangle}\right\}}{\sqrt{2\pi\,\langle [v - v(0)\Phi(t)]^2\rangle}}, \tag{19}$$

where we have used (3) and (15) to write explicitly in terms of $\phi(t)$

$$\left\langle [v - v(0)\Phi(t)]^2 \right\rangle = 2\frac{\gamma\, k_B T}{m^2}\int_0^t ds_1 \int_0^{s_1} ds_2\, \Phi(s_1)\Phi(s_2)\phi(s_1 - s_2). \tag{20}$$

In the stationary regime $t \to \infty$, we have $\Phi(t) \to 0$ and $\langle [v - v(0)\Phi(t)]^2\rangle \to \langle v^2(\infty)\rangle = k_B T/m$ and therefore

$$P_{\rm st}(v) = \frac{1}{\sqrt{2\pi k_B T/m}} \exp\left\{ -\frac{mv^2}{2k_B T}\right\}, \tag{21}$$

which corresponds to the Maxwell distribution of velocities at the bath's temperature T.

For the purposes that will be clear in Sect. 2, we present a derivation of the Fokker-Planck equation that corresponds to the linear Generalized Langevin Equation (1) of the process $v(t)$, where $\xi(t)$ is a Gaussian stochastic process with vanishing average and autocorrelation function (2). The derivation of this Fokker-Planck has been considered by several authors before [49–52], here we present a heuristic, yet rigorous, derivation of such equation.

First notice that for the Gaussian white noise, i.e. $\phi(t) = \delta(t)$, and therefore $\Phi(t) = e^{-\gamma t/m}$, the relation (15) turns (1) into the Ornstein-Uhlenbeck process for which the conditional probability distribution, $P(v,t|v(0))$ is given by well-known result

$$P(v,t|v(0)) = \frac{\exp\left\{-\dfrac{m[v - v(0)e^{-\gamma t/m}]^2}{2k_BT(1-e^{-2\gamma t})}\right\}}{\sqrt{2\pi k_BT(1-e^{-2\gamma t})/m}}, \tag{22}$$

which satisfies the Fokker-Planck equation [53]

$$\frac{\partial}{\partial t}P(v,t|v(0)) = \frac{\partial}{\partial v}\left[\frac{\gamma}{m}vP(v,t|v(0))\right] + \frac{\gamma}{m^2}k_BT\frac{\partial^2}{\partial v^2}P(v,t|v(0)). \tag{23}$$

Given the linearity of the Langevin equation (1a), it is tempting to propose as a suitable anzats, the following Fokker-Planck equation

$$\frac{\partial}{\partial t}P(v,t|v(0)) = \frac{\partial}{\partial v}\left[\frac{\gamma}{m}\chi_1(t)vP(v,t|v(0))\right] + \frac{\gamma}{m^2}k_BT\chi_2(t)\frac{\partial^2}{\partial v^2}P(v,t|v(0)), \tag{24}$$

where $\chi_1(t)$ and $\chi_2(t)$ are functions to determine with the initial condition $P(v|v(0)) = \delta[v-v(0)]$. The function $\chi_1(t)$ in the first term in the right-hand side of Eq. (24) accounts for the retarded effects of the friction force in (1a), characterized by $\phi(t)$, while $\chi_2(t)$ in the second term represents the effects of the correlations of the internal noise that arise from the fluctuation-dissipation relation (15). In such a case, a connection between $\chi_1(t)$ and $\chi_2(t)$ is expected.

The solution to (24) can be found by the use of Fourier transform which turns the second order partial differential equation (24) into the first order one

$$\frac{\partial}{\partial t}\hat{P}(k,t|v(0)) = -\frac{\gamma}{m}\chi_1(t)\,k\frac{\partial}{\partial k}\hat{P}(k,t|v(0)) - \frac{\gamma}{m^2}k_BT\,\chi_2(t)\,k^2\,\hat{P}(k,t|v(0)), \tag{25}$$

where a function with hat, $\hat{f}(k)$, denotes its Fourier transform

$$\hat{f}(k) = \int_{-\infty}^{\infty} dx\, e^{ikx} f(x), \tag{26}$$

with Fourier variable k.

By the use of the well-known method of the characteristics, we have to solve the following pair of ordinary differential equations

$$\frac{d}{dt}k(t) = \frac{\gamma}{m}\chi_1(t)\,k(t),$$
$$\frac{d}{dt}\hat{P}(t) = -\frac{\gamma}{m^2}k_BT\chi_2(t)\,k^2\,\hat{P}(t),$$

where $\hat{P}(t) = \hat{P}[k(t), t|v(0)]$ denotes the solution of (25) along the characteristic trajectory $k(t)$. The solutions to the last equations are given, respectively, by

$$k(t) = k(0)e^{(\gamma/m)\int_0^t ds\,\chi_1(s)}, \tag{27a}$$
$$\hat{P}(t) = \hat{P}(0)e^{-(\gamma/m^2)k_BT\int_0^t ds\,\chi_2(s)\,k^2(s)}. \tag{27b}$$

From this, the solution in Fourier space is explicitly written as

$$\hat{P}(k,t|v(0)) = \hat{P}\left(ke^{-(\gamma/m)\int_0^t ds\,\chi_1(s)}|v(0)\right) \exp\left\{-(\gamma/m^2)k_BT\,k^2\int_0^t ds\,\chi_2(s)e^{-2(\gamma/m)\int_s^t ds'\,\chi_1(s')}\right\}, \tag{28}$$

where the first factor corresponds to the Fourier transform of the initial distribution $P(v|v(0)) = \delta[v - v(0)]$. After inversion of the Fourier transform we have that

$$P(v,t|v(0)) = \frac{\exp\left\{-\dfrac{\left[v - v(0)e^{-(\gamma/m)\int_0^t ds\,\chi_1(s)}\right]^2}{4(\gamma/m^2)k_BT\int_0^t ds\,\chi_2(s)e^{-2(\gamma/m)\int_s^t ds'\chi_1(s')}}\right\}}{\sqrt{4\pi(\gamma/m^2)k_BT\int_0^t ds\,\chi_2(s)e^{-2(\gamma/m)\int_s^t ds'\chi_1(s')}}}. \tag{29}$$

The functions $\chi_1(t)$ and $\chi_2(t)$ are determined by comparison of expression (29) with (19), we have, respectively, that

$$e^{-(\gamma/m)\int_0^t ds\,\chi_1(s)} = \Phi(t), \tag{30a}$$
$$2\frac{\gamma}{m^2}k_BT\int_0^t ds\,\chi_2(s)e^{-2(\gamma/m)\int_s^t ds'\chi_1(s')} = \left\langle[v - v(0)\Phi(t)]^2\right\rangle. \tag{30b}$$

The explicit relation of $\chi_1(t)$ with the memory function $\phi(t)$ is indirect via the Laplace transform

$$\mathcal{L}\left\{e^{-(\gamma/m)\int_0^t ds\,\chi_1(s)};\epsilon\right\} = \frac{1}{\epsilon + \frac{\gamma}{m}\widetilde{\phi}(\epsilon)}, \tag{31}$$

where we have used that $\widetilde{\Phi}(\epsilon) = [\epsilon + \frac{\gamma}{m}\widetilde{\phi}(\epsilon)]^{-1}$. In terms of $\Phi(t)$ we have

$$\frac{\gamma}{m}\chi_1(t) = \frac{d}{dt}\ln \Phi(t)^{-1}. \tag{32}$$

To determine $\chi_2(t)$, notice that the integral in left hand side of Eq. (30b) can be written in terms of $\Phi(t)$ as

$$\int_0^t ds\, \chi_2(s)\frac{\Phi^2(t)}{\Phi^2(s)} \tag{33}$$

thus rearranging (30b) we have that

$$\int_0^t ds\, \frac{\chi_2(s)}{\Phi^2(s)} = \frac{1}{\Phi^2(t)}\int_0^t ds_1 \int_0^{s_1} ds_2\, \Phi(s_1)\Phi(s_2)\phi(s_1 - s_2) \tag{34}$$

and therefore, after taking the derivative with respect to time

$$\chi_2(t) = \left[\frac{d}{dt}\ln \Phi^{-2}(t)\right]\int_0^t ds_1 \int_0^{s_1} ds_2\, \Phi(s_1)\Phi(s_2)\phi(s_1 - s_2) + \Phi(t)\int_0^t ds\, \phi(t-s)\Phi(s). \tag{35}$$

With expressions (32) and (35), the Fokker-Planck equation corresponding to the generalized Langevin equation (1a) is determined.

The Mean Square Displacement

As it was commented above, the stochastic process $x(t)$ does not reach a stationary regime in the framework of the generalized Langevin equation (1) and therefore the distribution of the particles positions $P(x, t)$ is not stationary, in fact, it is expected the distribution to become broader as time is passing on. The scaling of how fast the distribution becomes broader depends exclusively on the time dependence of the noise autocorrelation function. This fact has allowed the use of (1) [45, 54] to give an alternative to *fractional diffusion equations* [55] and other mathematical frameworks to describe anomalous diffusion, by properly choosing the time dependence of $\phi(t)$ [or equivalently of $\Gamma(t)$ if (15) holds]. The mean squared displacement (second moment of the probability distribution of positions) is the quantity commonly used to describe anomalous diffusion.

From the explicit expression for $v(t)$, given in Eq. (3), the particle position is

$$x(t) = x(0) + v(0)\Phi_I(t) + \frac{1}{m}\int_0^t ds\, \Phi_I(t-s)\xi(s),$$

where

$$\Phi_I(t) \equiv \int_0^t ds\, \Phi(s). \tag{36}$$

By noting that $\langle x(t)\rangle = x(0) + v(0)\Phi_I(t)$ we have that the variance of the position or mean squared displacement with respect to the average trajectory, namely

$$\sigma_{xx}(t) \equiv \left\langle [x(t) - \langle x(t)\rangle]^2 \right\rangle, \tag{37}$$

can be written as

$$\sigma_{xx}(t) = \frac{4k_B T}{m} \int_0^t ds\, \Phi_I(s)\,[1 - \Phi(s)]\,. \tag{38}$$

The asymptotic behavior of the memory function $\phi(t)$ determines the long-time regime of the mean squared displacement (38), through Eqs. (5) and (36). A sufficient condition for the standard linear dependence on time (the so-called normal diffusion) to emerge is that as ϵ goes asymptotically to zero, then $\epsilon\widetilde{\phi}(\epsilon) \sim \epsilon$, for which the corresponding asymptotic behavior of $\Phi(t)$ and $\Phi_I(t)$ is obtained from $\widetilde{\Phi}(\epsilon) \sim C$ and $\widetilde{\Phi}_I(\epsilon) \sim \tau\epsilon^{-1}$, by the Tauberian theorems respectively, where C is a dimensionless constant and τ a constant with units of time, then we have

$$\sigma_{xx}(t) \sim \frac{4k_B T\tau}{m}\, t. \tag{39}$$

Examples Consider as a simple example the case of a memory that decays exponentially fast with time, i.e., $\phi(t) = \alpha e^{-\alpha t}$.

In the limit of infinitely rapid decay, i.e., $\alpha \to \infty$ we have that $\phi(t) = \delta(t)$ and we recover the standard Langevin equation

$$m\frac{dv(t)}{dt} + \gamma v(t) = \xi(t), \tag{40}$$

for the so-called Ornstein-Uhlenbeck process, which gives the well-known result

$$\langle [x(t) - x_0]^2\rangle = \frac{m}{\gamma}\,\overline{v_0^2}\left[2t - \frac{m}{\gamma}(1 - e^{-2\frac{\gamma}{m}t})\right], \tag{41}$$

from which the ballistic result, $\overline{v_0^2}\,t^2$, is obtained when $\frac{\gamma}{m}t \ll 1$, and the standard diffusion result, $\frac{m}{\gamma}\langle v_0^2\rangle t$, is recovered in the regime $\frac{\gamma}{m}t \gg 1$.

For finite α we have that

$$\widetilde{\phi}(\epsilon) = \frac{\alpha}{\epsilon + \alpha}, \tag{42a}$$

$$\widetilde{\Phi}(\epsilon) = \frac{\epsilon + \alpha}{\epsilon(\epsilon + \alpha) + \alpha\frac{\gamma}{m}}. \tag{42b}$$

Power Law Memory

Let's consider the case $\widetilde{\phi}(\epsilon) = \frac{1}{\epsilon^{\alpha}}$, and therefore $\widetilde{\Phi}(\epsilon) = \frac{\epsilon^{\alpha}}{\epsilon^{\alpha+1}+(\gamma/m)^{\alpha+1}}$ which corresponds, in time-domain, to $E_{\alpha,1}[-(\frac{\gamma}{m}t)^{\alpha}]$, where $E_{\alpha,1}(z)$ is the Mittag-Leffler function. It is straightforward to check that then $\Phi_I(t) = tE_{\alpha,2}[-(\frac{\gamma}{m}t)^{\alpha}]$. By considering the asymptotic behavior of the Mittag-Leffler function we have

$$\sigma_{xx}(t) \sim 2\langle v^2(0)t^{2-\alpha}. \tag{43}$$

1.2 Diffusion of a Free Particle Under External Noise: The Out-of-Equilibrium Case (The Effective Temperature)

In the previous section, the partial equilibration of a freely diffusing Brownian particle was considered in the context of the fluctuation-dissipation relation. The equilibrium distribution of velocities requires the satisfaction of this relation and implies basically that the time scale involved in the persistence effects of the particle motion, taken into account by the memory function of the retarded friction term, is the same as the time scale of the correlations of fluctuation of the random force.

We consider now the case when the fluctuation-dissipation relation (15) does not hold, therefore the time dependence of the memory function $\phi(t)$ in the retarded term in Eq. (1a) is independent of the autocorrelation function of the fluctuating force. Under this circumstance, the fluctuating force $\xi(t)$ is called *external noise* [47] and is assumed a Gaussian process with autocorrelation function

$$\langle \xi(t)\xi(s)\rangle = \langle \xi^2\rangle \Gamma(|t-s|), \tag{44}$$

where $\langle \xi^2\rangle$ is a factor that characterizes the intensity of *non-thermal* fluctuations.

The retarded dissipative force is now decoupled from the fluctuating one, and the effects of the first one, do not necessarily balance those of the other, therefore, in the general case, the system will not reach the equilibrium state [45, 54], not even the equilibrium stationarity of the process $v(t)$, as it does in the case described when the fluctuation-dissipation relation holds. This, however, does not preclude the possibility that the process $v(t)$ reaches a non-equilibrium stationary regime. In consequence, there has been fairly interest in systems out of equilibrium and in the search of quantities that could serve as a measure or indicators of a "distance" from equilibrium [19, 22]. Though it is well-known that the rate of entropy production is a clear indicator of the out-of-equilibrium nature of a system, a more straightforward concept to describe this condition is the *effective temperature*. This is not directly built from the concept of temperature in equilibrium thermodynamics, but on a generalization of the fluctuation-dissipation relation [22].

Last considerations make the conditional probability density, given by (19), still valid, however we must have now that

$$\left\langle [v - v(0)\Phi(t)]^2 \right\rangle = \frac{\langle \xi^2 \rangle}{m^2} \int_0^t ds_1 \int_0^{s_1} ds_2 \, \Phi(s_1)\Phi(s_2)\Gamma(s_1 - s_2), \tag{45}$$

where the left-hand side in the last expression depends implicitly on $\phi(t)$ and $\Gamma(t)$, through $\Phi(t)$ and the ensemble average over noise realizations, respectively. The right-hand side on the other hand makes explicit the appearance of $\Gamma(t)$, and as before, $\phi(t)$ appears implicitly through $\Phi(t)$.

If a non-equilibrium stationarity of the process $v(t)$ is expected, it must happen that

$$\left\langle [v - v(0)\Phi(t)]^2 \right\rangle \underset{t\to\infty}{\longrightarrow} \frac{k_B T_{\text{eff}}}{m}, \tag{46}$$

and an effective temperature T_{eff} can be defined if and only if

$$\kappa \equiv \lim_{t\to\infty} \int_0^t ds_1 \int_0^{s_1} ds_2 \, \Phi(s_1)\Phi(s_2)\Gamma(s_1 - s_2) \tag{47}$$

exists. If that is the case, then T_{eff} can be related to the intensity of noise through

$$T_{\text{eff}} = \frac{\langle \xi^2 \rangle}{k_B m} \kappa. \tag{48}$$

Thus, the existence of an effective temperature requires that the time dependence of $\phi(t)$ and $\Gamma(t)$ be such that κ remains finite and constant.

A plausible physical situation corresponds to the case of external noise exponentially correlated,

$$\langle \xi(t)\xi(s) \rangle = \langle \xi^2 \rangle e^{-(|t-s|)/\tau_{\text{cor}}}, \tag{49}$$

with correlation time τ_{cor} and a memory function that decays exponentially as

$$\phi(t) = \tau_{\text{pers}}^{-1} e^{-t/\tau_{\text{pers}}}, \tag{50}$$

where τ_{pers} denotes the persistence time. In such a case we have, after use of the Tauberian theorem, that

$$\kappa = \tau_{\text{cor}} \frac{m}{\gamma} \tag{51}$$

and therefore, the prescription (48) gives

$$T_{\text{eff}} = \frac{\langle \xi^2 \rangle \tau_{\text{cor}}}{k_B \gamma}, \tag{52}$$

which is independent of the persistence time τ_{pers}.

2 Generalized Langevin Equation for Brownian Motion Confined by an External Potential

We now turn to the case of our interest, which corresponds to that one for which both processes, $v(t)$ and $x(t)$, attain a stationary state under out-of-equilibrium conditions, and we focus on the non-equilibrium nature of the zero-flux stationary distributions of the particle positions $P_{\text{st}}(x)$. Stationary solutions for the process $x(t)$ are expected if the Brownian particle is confined either by hard walls or by the external potential $U(x)$. For this case the generalized Langevin equation is given by [40, 56]

$$m\frac{d}{dt}v(t) = -\frac{\partial}{\partial x}U(x) - \gamma \int_0^t ds\, \phi(t-s)v(s) + \xi(t), \tag{53a}$$

$$\frac{d}{dt}x(t) = v(t). \tag{53b}$$

In the physically plausible cases for which the fluctuation-dissipation relation (15) holds, the stochastic processes $v(t)$ and $x(t)$ can be treated as statistically independent, and the joint equilibrium distribution $P_{\text{eq}}(x, v)$ can be factorized as the product of their corresponding equilibrium distribution of Maxwell $P_{\text{eq}}(v)$, Eq. (21), and

$$P_{\text{eq}}(x) = \mathcal{Z}^{-1} e^{-U(x)/k_B T} \tag{54}$$

of Boltzmann-Gibbs, both characterized by the equilibrium temperature T. Evidently the probability distribution (54) has local maxima at the minima of $U(x)$, i.e., particles accumulate around the stable states of $U(x)$. Such conclusions can be reached from the zero-flux stationary solution of the corresponding Fokker-Planck-Kramers equation associated to Eq. (53).

Even though there is no general solution to (53) for arbitrary $U(x)$—due to the non-linear character of the equation—there are solutions for the case of the harmonic potential $\frac{1}{2}m\omega^2 x^2$ which makes Eq. (53) linear in $v(t)$ and $x(t)$. Due to this simplification, this case has been treated almost exhaustively.

In the following section we revisit the procedure to obtain the equilibrium distribution of a Brownian particle trapped in arbitrary external potential $U(x)$ subject to Gaussian white noise and under the assumption that the fluctuation-dissipation relation (15) holds.

2.1 Fokker-Planck-Kramers Equation for a Trapped Brownian Particle in an External Potential $U(x)$: The Equilibrium Distribution for Gaussian White Noise

In the case when the fluctuation-dissipation relation (15) holds, and the internal noise corresponds to Gaussian white noise, we have that Eq. (53) reduce to the Markovian Langevin equation

$$m\frac{d}{dt}v(t) = -\gamma v(t) - \frac{\partial}{\partial x}U(x) + \xi(t), \tag{55a}$$

$$\frac{d}{dt}x(t) = v(t). \tag{55b}$$

We are interested in the long-time regime where the system reaches the expected equilibrium regime. Thus one may avoid the currents due to the effects of the initial data. The probability distribution $P(x, v, t)$ of finding a Brownian particle at position x, moving with velocity v at time t satisfies the so-called Fokker-Planck-Kramers equation

$$\frac{\partial}{\partial t}P(x,v,t) + \frac{\partial}{\partial x}vP(x,v,t) - \frac{1}{m}\frac{\partial}{\partial v}\left[\frac{\partial}{\partial x}U(x)P(x,v,t)\right] = \frac{\gamma}{m}\frac{\partial}{\partial v}\left[v + \frac{k_BT}{m}\frac{\partial}{\partial v}\right]P(x,v,t). \tag{56}$$

Under the assumption that $P(x, v, t)$ is normalizable, then Eq. (56) can be written as a continuity equation, namely

$$\frac{\partial}{\partial t}P(x,v,t) + \nabla_{x,v}\cdot\boldsymbol{J}(x,v,t) = 0, \tag{57}$$

where

$$\nabla_{x,v} \equiv \left(\frac{\partial}{\partial x}, \frac{\partial}{\partial v}\right) \tag{58}$$

and $\boldsymbol{J}(x, v, t)$ is a two-dimensional vector that denotes the total probability current which can be decomposed as the sum of two contributions [53]: the deterministic one

$$\boldsymbol{J}_{\text{det}}(x,v,t) = \left[vP(x,v,t), -\frac{1}{m}\frac{\partial}{\partial x}U(x)\,P(x,v,t)\right]; \tag{59}$$

and the irreversible one

$$\boldsymbol{J}_{\text{irr}}(x,v,t) = \left[0, -\frac{\gamma}{m}\left(v + \frac{k_BT}{m}\frac{\partial}{\partial v}\right)P(x,v,t)\right]. \tag{60}$$

The stationary solution is obtained as a consequence of imposing the so-called *detailed balance conditions*, namely,

$$\boldsymbol{J}_{\text{irr}} = (0, 0), \tag{61a}$$

$$\nabla_{x,v} \cdot \boldsymbol{J}_{\text{det}} = 0, \tag{61b}$$

which lead to the equilibrium solutions $P_{\text{eq}}(x, v)$. The first condition, which establishes the vanishing of the current due to balance of dissipation and thermal fluctuations, implies that

$$\left[v + \frac{k_B T}{m} \frac{\partial}{\partial v} \right] P_{\text{eq}}(x, v) = 0, \tag{62}$$

whose solution can be obtained straightforwardly as

$$P_{\text{eq}}(x, v) = P_{\text{eq}}(x) e^{-mv^2/2k_B T}, \tag{63}$$

where $P_{\text{eq}}(x)$ is a function that depends only on x and is determined by the other detailed balance condition (61b). After substitution of the last expression into (61b) we have

$$\frac{\partial}{\partial x} P_{\text{eq}}(x) + \frac{1}{k_B T} \left[\frac{\partial}{\partial x} U(x) \right] P_{\text{eq}}(x) = 0, \tag{64}$$

whose solution corresponds exactly to the Boltzmann-Gibbs weight

$$P_{\text{eq}}(x) = \mathcal{Z}^{-1} e^{-U(x)/k_B T}, \tag{65}$$

where the constant $\mathcal{Z}$ is found from the normalization condition for $P_{\text{eq}}(x, v)$, i.e.

$$\mathcal{Z} = \int_{-\infty}^{\infty} dv \int_{-\infty}^{\infty} dx \, P_{\text{eq}}(x, v). \tag{66}$$

Thus, the equilibrium distribution is given by the equilibrium distribution of Maxwell and Boltzmann-Gibbs

$$P_{\text{eq}}(v, x) = \mathcal{Z}^{-1} \, e^{-U(x)/k_B T} e^{-mv^2/2k_B T}. \tag{67}$$

3 Non-Markovian Trapped Brownian Motion in an External Potential: The Harmonic Oscillator

We consider the generalized Langevin equations (53) for a Brownian particle diffusing under the influence of the harmonic potential (non-Markovian Brownian harmonic oscillator)

$$U(x) = \frac{1}{2} m\omega^2 x^2. \tag{68}$$

It has been argued that the stationary distribution that corresponds to equilibrium, which in the particular case considered in this section is given by

$$P_{\rm eq}(v,x) = \mathcal{Z}^{-1}\, e^{-m\omega^2 x^2/2k_BT} e^{-mv^2/2k_BT}, \tag{69}$$

is a consequence of the fluctuation-dissipation relation, independently of the specific time dependence of the noise autocorrelation function. This can be proved explicitly for this particular case as follows in the next section.

Due to its linear character, this linear process has been studied comprehensively in the case of internal and external noise as well [46, 47, 57–60], where attention has been paid mainly to the mean values, variances, and velocity autocorrelation function.

3.1 Fluctuation-Dissipation Relation and the Equilibrium Distribution

Consider the non-Markovian Brownian harmonic oscillator

$$m\frac{d}{dt}v(t) = -\gamma\int_{t_0}^{t} ds\,\phi(t-s)v(s) - m\omega^2 x(t) + \xi(t), \tag{70a}$$

$$\frac{d}{dt}x(t) = v(t), \tag{70b}$$

where we have kept explicitly the characteristic time t_0.

As before, our purpose is to compute the quantity $\langle\xi(t_0+t)\xi(t_0)\rangle$. From (70) we have that $\xi(t_0+t)$, $\xi(t_0)$ are given, respectively, by

$$\begin{aligned}\xi(t_0+t) &= m\dot{v}(t_0+t) + \gamma\int_{t_0}^{t_0+t} ds\phi(t_0+t-s)v(s) + m\omega^2 x(t_0+t),\\ \xi(t_0) &= m\dot{v}(t_0) + m\omega^2 x(t_0),\end{aligned} \tag{71}$$

where the dotted symbols denote the change in time of the corresponding symbols without dot.

Besides the assumptions made in the last case we will also assume that $\langle\xi(t)x(t_0)\rangle = 0$ for $t \geq 0$, and that $x(t)$ is also stationary. Since the Laplace transforms of $x(t)$ and $v(t)$ are required to carry out the calculation, we simply give the corresponding expressions, explicitly

$$\widetilde{x}(\epsilon) = \frac{\widetilde{\xi}(\epsilon) + mv(t_0) + x(t_0)[m\epsilon + \gamma\widetilde{\phi}(\epsilon)]}{\epsilon[m\epsilon + \gamma\widetilde{\phi}(\epsilon)] + m\omega^2}, \tag{72}$$

$$\widetilde{v}(\epsilon) = \frac{\epsilon[\widetilde{\xi}(\epsilon) + mv(t_0)] - x(t_0)m\omega^2}{\epsilon[m\epsilon + \gamma\widetilde{\phi}(\epsilon)] + m\omega^2}. \tag{73}$$

Thus,

$$\int_0^\infty dt\, e^{-\epsilon t}\langle \xi(t_0+t)\xi(t_0)\rangle = \int_0^\infty dt\, e^{-\epsilon t}\Big[m^2\langle \dot{v}(t_0+t)\dot{v}(t_0)\rangle + m^2\omega^4\langle x(t_0+t)x(t_0)\rangle$$
$$+m^2\omega^2[\langle \dot{v}(t_0+t)x(t_0)\rangle + \langle x(t_0+t)\dot{v}(t_0)\rangle]$$
$$+m\omega^2\gamma\int_{t_0}^{t_0+t} ds\phi(t_0+t_s)\langle v(s)x(t_0)\rangle$$
$$+m\gamma\int_{t_0}^{t_0+t} ds\phi(t_0+t_s)\langle v(s)\dot{v}(t_0)\rangle\Big]$$

We compute each term by following the same procedure as before. For the first term we have

$$\int_0^\infty dt\, e^{-\epsilon t}m^2\langle \dot{v}(t_0+t)\dot{v}(t_0)\rangle = m^2\epsilon\int_0^\infty dt\, e^{-\epsilon t}\langle v(t_0+t)\dot{v}(t_0)\rangle - m^2\langle v(t_0)\dot{v}(t_0)\rangle$$
$$= -m^2\epsilon\int_0^\infty dt\, e^{-\epsilon t}\langle \dot{v}(t_0+t)v(t_0)\rangle + m^2\omega^2\langle v(t_0)x(t_0)\rangle,$$

where we have used that $v(t)$ is stationary, therefore $\langle v(t_0+t)\dot{v}(t_0)\rangle = -\langle \dot{v}(t_0+t)v(t_0)\rangle$, and since $\langle v(t_0)\xi(t)\rangle = 0$ that $\langle v(t_0)\dot{v}(t_0)\rangle = -\omega^2\langle v(t_0)x(t_0)\rangle$. To simplify the analysis consider that $\langle v(t_0)x(t_0)\rangle = 0$. With this we get

$$\int_0^\infty dt\, e^{-\epsilon t}m^2\langle \dot{v}(t_0+t)\dot{v}(t_0)\rangle = -m^2\epsilon^2\langle \widetilde{v}(\epsilon)v(t_0)\rangle + m^2\epsilon\langle v^2(t_0)\rangle.$$

The quantity $\langle \widetilde{v}(\epsilon)v(t_0)\rangle$ is computed by using (73), we get

$$\langle \widetilde{v}(\epsilon)v(t_0)\rangle = \frac{\epsilon\langle \widetilde{\xi}(\epsilon)v(t_0)\rangle + m\epsilon\langle v^2(t_0)\rangle - m\omega^2\langle x(t_0)v(t_0)\rangle}{\epsilon[m\epsilon + \gamma\widetilde{\phi}(\epsilon)] + m\omega^2},$$

but since $\langle \xi(t)v(t_0)\rangle = 0$, and the assumption $\langle v(t_0)x(t_0)\rangle = 0$, we simply get that

$$\int_0^\infty dt\, e^{-\epsilon t}m^2\langle \dot{v}(t_0+t)\dot{v}(t_0)\rangle = m^2\epsilon\frac{\epsilon\gamma\widetilde{\phi}(\epsilon) + m\omega^2}{\epsilon[m\epsilon + \gamma\widetilde{\phi}(\epsilon)] + m\omega^2}\langle v^2(t_0)\rangle. \tag{74}$$

Similarly,

$$m^2\omega^2\int_0^\infty dt\, e^{-\epsilon t}\langle \dot{v}(t_0+t)x(t_0)\rangle = m^2\omega^2\epsilon\langle \widetilde{v}(\epsilon)x(t_0)\rangle$$
$$= -\frac{m^3\omega^4\epsilon}{\epsilon[m\epsilon + \gamma\widetilde{\phi}(\epsilon)] + m\omega^2}\langle x^2(t_0)\rangle; \tag{75}$$

$$m\gamma\widetilde{\phi}(\epsilon)\int_0^\infty dt\; e^{-\epsilon t}\langle v(t_0+t)\dot{v}(t_0)\rangle = -m\gamma\widetilde{\phi}(\epsilon)\int_0^\infty dt\; e^{-\epsilon t}\langle \dot{v}(t_0+t)v(t_0)\rangle$$
$$= -m\gamma\widetilde{\phi}(\epsilon)\epsilon\langle\widetilde{v}(\epsilon)v(t_0)\rangle + m\gamma\widetilde{\phi}(\epsilon)\langle v^2(t_0)\rangle$$
$$= m\gamma\widetilde{\phi}(\epsilon)\frac{\epsilon\gamma\widetilde{\phi}(\epsilon)+m\omega^2}{\epsilon[m\epsilon+\gamma\widetilde{\phi}(\epsilon)]+m\omega^2}\langle v^2(t_0)\rangle; \tag{76}$$

$$m\omega^2\gamma\widetilde{\phi}(\epsilon)\int_0^\infty dt\; e^{-\epsilon t}\langle v(t_0+t)x(t_0)\rangle = m\omega^2\gamma\widetilde{\phi}(\epsilon)\langle\widetilde{v}(\epsilon)x(t_0)\rangle$$
$$= -\frac{m^2\omega^4\gamma\widetilde{\phi}(\epsilon)}{\epsilon[m\epsilon+\gamma\widetilde{\phi}(\epsilon)]+m\omega^2}\langle x^2(t_0)\rangle. \tag{77}$$

To compute $m^2\omega^2\int_0^\infty dt\;\; e^{-\epsilon t}\langle x(t_0+t)\dot{v}(t_0)\rangle$ we use that $x(t_0+t) = x(t_0) + \int_{t_0}^{t_0+t} ds\; v(s)$ and since $\langle x(t_0)\xi(t)\rangle = 0$, that $\langle x(t_0)\dot{v}(t_0)\rangle = -\omega^2\langle x^2(t_0)\rangle$, thus

$$m^2\omega^2\int_0^\infty dt\; e^{-\epsilon t}\langle x(t_0+t)\dot{v}(t_0)\rangle$$
$$= -\frac{m^2\omega^4}{\epsilon}\langle x^2(t_0)\rangle + m^2\omega^2\int_0^\infty dt\; e^{-\epsilon t}\int_0^t ds\langle v(t_0+s)\dot{v}(t_0)\rangle$$
$$= -\frac{m^2\omega^4}{\epsilon}\langle x^2(t_0)\rangle + \frac{m^2\omega^2}{\epsilon}\int_0^\infty dt\; e^{-\epsilon t}\langle v(t_0+t)\dot{v}(t_0)\rangle$$
$$= -\frac{m^2\omega^4}{\epsilon}\langle x^2(t_0)\rangle - \frac{m^2\omega^2}{\epsilon}\int_0^\infty dt\; e^{-\epsilon t}\langle \dot{v}(t_0+t)v(t_0)\rangle$$
$$= -\frac{m^2\omega^4}{\epsilon}\langle x^2(t_0)\rangle - \frac{m^2\omega^2}{\epsilon}\left[\epsilon\langle\widetilde{v}(\epsilon)v(t_0)\rangle - \langle v^2(t_0)\rangle\right]$$
$$= -\frac{m^2\omega^4}{\epsilon}\langle x^2(t_0)\rangle + \frac{m^2\omega^2}{\epsilon[m\epsilon+\gamma\widetilde{\phi}(\epsilon)]+m\omega^2}\left[\gamma\widetilde{\phi}(\epsilon)+\frac{m\omega^2}{\epsilon}\right]\langle v^2(t_0)\rangle; \tag{78}$$

$$m^2\omega^4\int_0^\infty dt\; e^{-\epsilon t}\langle x(t_0+t)x(t_0)\rangle = \frac{m^2\omega^4[m\epsilon+\gamma\phi(\epsilon)]}{\epsilon[m\epsilon+\gamma\widetilde{\phi}(\epsilon)]+m\omega^2}\langle x^2(t_0)\rangle. \tag{79}$$

By adding (74) to (79) we get

$$\int_0^\infty dt\; e^{-\epsilon t}\langle\xi(t_0+t)\xi(t_0)\rangle = m\gamma\widetilde{\phi}(\epsilon)\langle v^2(t_0)\rangle + \frac{m^2\omega^2}{\epsilon}\left[\langle v^2(t_0)\rangle - \omega^2\langle x^2(t_0)\rangle\right]. \tag{80}$$

Finally by inverting the expression (80) we get

$$\langle\xi(t_0+t)\xi(t_0)\rangle = m\gamma\phi(t)\langle v^2(t_0)\rangle + m^2\omega^2\left[\langle v^2(t_0)\rangle - \omega^2\langle x^2(t_0)\rangle\right]. \tag{81}$$

This is the *fluctuation-dissipation* theorem for the non-Markovian Brownian harmonic oscillator.

If the initial conditions correspond to those in thermodynamic equilibrium, equipartition theorem assures that $m\langle v^2(t_0)\rangle = k_BT$ and $m\omega^2\langle x^2(t_0)\rangle = k_BT$, therefore (81) reduces to the previous one $\langle \xi(t_0+t)\xi(t_0)\rangle = m\gamma\phi(t)\langle v^2(t_0)\rangle$.

The Mean Squared Displacement for Internal Noise

The formal solution to the generalized Langevin equations (70) can be computed straightforwardly by use of the Laplace transform, and is explicitly given by

$$\widetilde{x}(\epsilon) = x(0)\widetilde{\Phi}_{II}(\epsilon) + v(0)\widetilde{\Phi}_{\rm p}(\epsilon) + \frac{1}{m}\widetilde{\xi}(\epsilon)\widetilde{\Phi}_{\rm p}(\epsilon), \tag{82a}$$

$$\widetilde{v}(\epsilon) = v(0)\widetilde{\Phi}(\epsilon)\left[1-\omega^2\widetilde{\Phi}_{\rm p}(\epsilon)\right] - x(0)\omega^2\widetilde{\Phi}_{\rm p}(\epsilon) + \frac{1}{m}\widetilde{\xi}(\epsilon)\widetilde{\Phi}(\epsilon)\left[1-\omega^2\widetilde{\Phi}_{\rm p}(\epsilon)\right], \tag{82b}$$

where we have assumed without loss of generality that $t_0 = 0$ in Eq. (70). The function $\widetilde{\Phi}(\epsilon)$ is given by expression (5), $\widetilde{\Phi}_{II}(\epsilon)$ explicitly by

$$\widetilde{\Phi}_{II}(\epsilon) = \left[\epsilon + \omega^2\widetilde{\Phi}(\epsilon)\right]^{-1}, \tag{83}$$

and

$$\begin{aligned}\widetilde{\Phi}_{\rm p}(\epsilon) &= \widetilde{\Phi}(\epsilon)\widetilde{\Phi}_{II}(\epsilon)\\ &= \left\{\epsilon\left[\epsilon + \frac{\gamma}{m}\widetilde{\phi}(\epsilon)\right] + \omega^2\right\}^{-1}.\end{aligned} \tag{84}$$

From expressions (82), the mean values $\langle x(t)\rangle$ and $\langle v(t)\rangle$ are

$$\langle x(t)\rangle = x(0)\Phi_{II}(t) + v(0)\Phi_{\rm p}(t), \tag{85a}$$

$$\langle v(t)\rangle = v(0)\left[\Phi(t) - \omega^2\int_0^t ds\,\Phi(t)\Phi_{\rm p}(t-s)\right] - x(0)\omega^2\Phi_{\rm p}(t), \tag{85b}$$

respectively, and the respective mean squared displacement, with respect to the average, is given by

$$\begin{aligned}\langle[x(t)-\langle x(t)\rangle]^2\rangle &= \frac{1}{m^2}\int_0^t ds_1\,\Phi_{\rm p}(t-s_1)\int_0^t ds_2\,\Phi_{\rm p}(t-s_2)\langle\xi(s_1)\xi(s_2)\rangle\\ &= 2\frac{\langle\xi^2\rangle}{m^2}\int_0^t ds_1\,\Phi_{\rm p}(s_1)\int_0^{s_1} ds_2\,\Phi_{\rm p}(s_2)\Gamma(s_1-s_2).\end{aligned} \tag{86}$$

Define $\sigma_{xx}^2(t) \equiv \langle [x(t) - \langle x(t) \rangle]^2 \rangle$, then by differentiating expression (86) with respect to time we get

$$\frac{m^2}{2\langle \xi^2 \rangle} \dot{\sigma}_{xx}^2 = \Phi_{\mathrm{p}}(t) \int_0^t ds\, \Phi_{\mathrm{p}}(s) \Gamma(t-s), \tag{87}$$

and therefore that

$$\mathcal{L}\left\{ \frac{m^2 \dot{\sigma}_{xx}^2}{2\langle \xi^2 \rangle \Phi_{\mathrm{p}}(t)} \right\} = \widetilde{\Phi}_{\mathrm{p}}(\epsilon) \widetilde{\Gamma}(\epsilon). \tag{88}$$

If the fluctuation-dissipation relation (15) holds, we get

$$\mathcal{L}\left\{ \frac{m^2 \dot{\sigma}_{xx}^2}{2\Phi_{\mathrm{p}}(t)} \right\} = 2k_B T \gamma \widetilde{\Phi}_{\mathrm{p}}(\epsilon) \widetilde{\phi}(\epsilon). \tag{89}$$

The product $\widetilde{\Phi}_{\mathrm{p}}(\epsilon)\widetilde{\phi}(\epsilon)$ in the right-hand side of the last expression can be computed straightforwardly from (84) in terms of $\widetilde{\Phi}_{\mathrm{p}}(\epsilon)$ alone as

$$\widetilde{\Phi}_{\mathrm{p}}(\epsilon)\widetilde{\phi}(\epsilon) = \frac{m}{\gamma}\left[\frac{1}{\epsilon} - \frac{\widetilde{\Phi}_{\mathrm{p}}(\epsilon)}{\epsilon} \left(\epsilon^2 + \omega^2 \right) \right], \tag{90}$$

then after inversion of the Laplace transform in (87) and rearranging the resulting terms we get

$$\dot{\sigma}_{xx}^2 = \frac{4k_B T}{m}\left[\Phi_{\mathrm{p}}(t) - \Phi_{\mathrm{p}}(t) \frac{d}{dt} \Phi_{\mathrm{p}}(t) - \omega^2 \Phi_{\mathrm{p}}(t) \int_0^t ds\, \Phi_{\mathrm{p}}(s) \right], \tag{91}$$

where we have used that $\Phi(0) = 0$ as this can be proved by taking the limit $\epsilon \widetilde{\Phi}(\epsilon)$ as ϵ goes to ∞. Therefore after integration of last expression we finally have

$$\langle [x(t) - \langle x(t) \rangle]^2 \rangle = \frac{4k_B T}{m}\left[\int_0^t ds\, \Phi_{\mathrm{p}}(s) - \frac{1}{2}\Phi_{\mathrm{p}}^2(t) - \frac{\omega^2}{2}\left(\int_0^t ds\, \Phi(s) \right)^2 \right]. \tag{92}$$

Let us discuss the case of algebraically correlated noise, specifically the *continuous time fractional Gaussian noise* (ctfGn) $\langle \xi(t)\xi(s) \rangle = \langle v_0^2 \rangle_{\mathrm{eq}} \frac{\gamma^{2H}}{m^{2H-2}} 2H(2H-1)|t-s|^{2H-2}$. The long-time limit may be found with the help of the Tauberian theorem. In this particular case we have

$$\Phi(t) = \frac{1}{m}\mathcal{L}^{-1}\left\{ \frac{1}{\epsilon^2 + \epsilon^{2-2H}\gamma_{2H} + \omega^2} \right\}, \tag{93}$$

where we have defined $\gamma_{2H} \equiv \left(\frac{\gamma}{m}\right)^{2H} \Gamma(2H+1)$. Therefore

$$\begin{aligned}
\langle [x(t) - \langle x(t)\rangle]^2\rangle \xrightarrow[t\to\infty]{} & 2\langle V_0^2\rangle_{\rm eq} m \lim_{\epsilon\to 0} \epsilon \left[\frac{1}{\epsilon m[\epsilon^2 + \epsilon^{2-2H}\gamma_{2H} + \omega^2]}\right] \\
& -2\langle V_0^2\rangle_{\rm eq} m \left[\frac{m}{2}\left(\lim_{t\to\infty}\Phi(t)\right)^2 + \frac{m\omega^2}{2}\left[\lim_{t\to\infty}\int_0^t ds\,\Phi(s)\right]^2\right] \\
= & \ 2\frac{\langle V_0^2\rangle_{\rm eq}}{\omega^2} - 2\langle V_0^2\rangle_{\rm eq} m \left[\frac{m}{2}\left(\lim_{\epsilon\to 0}\frac{\epsilon}{m[\epsilon^2 + \epsilon^{2-2H}\gamma_{2H} + \omega^2]}\right)^2\right. \\
& \left. + \frac{m\omega^2}{2}\left[\lim_{\epsilon\to 0}\frac{\epsilon}{\epsilon m[\epsilon^2 + \epsilon^{2-2H}\gamma_{2H} + \omega^2]}\right]^2\right] \\
= & \ 2\frac{\langle V_0^2\rangle_{\rm eq}}{\omega^2} - 2\langle V_0^2\rangle_{\rm eq} m \left[\frac{m\omega^2}{2}\left[\frac{1}{m\omega^2}\right]^2\right] \\
= & \ 2\frac{\langle V_0^2\rangle_{\rm eq}}{\omega^2} - \frac{\langle V_0^2\rangle_{\rm eq}}{\omega^2} \\
= & \ \frac{\langle V_0^2\rangle_{\rm eq}}{\omega^2} \\
= & \ \frac{k_B T}{m\omega^2}. \qquad (94)
\end{aligned}$$

We used the fact the $1 < 2H < 2$ and that the equilibrium distribution is given by the Maxwell distribution.

3.2 *The Brownian Harmonic Oscillator: The Out-of-Equilibrium Case (The Effective Temperature)*

We discussed in the previous section that the Boltzmann-Gibbs factor,

$$e^{-U(x)/k_B T}, \qquad (95)$$

($e^{-m\omega^2 x^2/2k_B T}$ for the Brownian harmonic oscillator) is an explicit consequence of the balance of the effects of the retarded dragging force and the correlated fluctuating noise, which makes the irreversible component of the probability current to vanish, at least for the case of Gaussian white noise.

Motivated by the observation that the persistent motion is the cause for which the distribution of positions of confined active particles does not correspond to the one of Boltzmann-Gibbs, we explore the consequences of relaxing the fluctuation dissipation relation in Eq. (70), on the stationary distribution of positions $P_{\rm st}(x)$.

That is to say, we ask the question: What are the corresponding effects on $P_{\rm st}(x)$ when the dissipative effects are decoupled from the fluctuating ones?

The method followed in Sect. 2.1 does not apply directly since the Fokker-Planck-Kramers equation corresponding to Eqs. (70) involves time dependent transport coefficients as the ones obtained for Fokker-Planck-Kramers equation that corresponds to the generalized Langevin equation of the free Brownian particle [see Eq. (24)].

Our starting point is, instead, the conditional probability density,

$$P(x,t|x(0),v(0)) = \langle \delta[x - x(t)] \rangle, \tag{96}$$

of finding a particle located at position x at time t, given that it was located at $x(0)$ moving with velocity $v(0)$ at time $t = 0$, where the explicit dependence of $x(t)$ on the external noise $\xi(t)$ is given by the Laplace inversion of (82b), namely

$$x(t) = x(0)\Phi_{II}(t) + v(0)\Phi_{\rm p}(t) + \frac{1}{m}\int_0^t ds\, \Phi_{\rm p}(t-s)\xi(s). \tag{97}$$

The linear nature of Eqs. (70) ensures that $x(t)$ is a Gaussian process. We have then that

$$P(x,t|x(0),v(0)) = \frac{1}{2\pi}\int_{-\infty}^{\infty} dk\, e^{ik[x - x(0)\Phi_{II}(t) - v(0)\Phi_{\rm p}(t)]} \left\langle e^{i\frac{k}{m}\int_0^t ds\, \Phi_{\rm p}(t-s)\xi(s)} \right\rangle, \tag{98}$$

where

$$\left\langle e^{i\frac{k}{m}\int_0^t ds\, \Phi_{\rm p}(t-s)\xi(s)} \right\rangle \tag{99}$$

is the characteristic functional of the stochastic process $\xi(t)$, which now has the explicit expression [48]

$$\exp\left\{ -\frac{k^2\langle \xi^2 \rangle}{m^2}\int_0^t ds_1 \int_0^{s_1} ds_2\, \Phi_{\rm p}(s_1)\Phi_{\rm p}(s_2)\Gamma(s_1 - s_2) \right\}, \tag{100}$$

since the process $\xi(t)$ has been assumed Gaussian. We have that

$$\begin{aligned} P(x,t|x(0),v(0)) = \frac{1}{2\pi}\int_{-\infty}^{\infty} dk\, e^{ik[x - x(0)\Phi_{II}(t) - v(0)\Phi_{\rm p}(t)]} \\ \times e^{-k^2\frac{\langle \xi^2 \rangle}{m^2}\int_0^t ds_1 \int_0^{s_1} ds_2\, \Phi_{\rm p}(s_1)\Phi_{\rm p}(s_2)\Gamma(s_1 - s_2)} \end{aligned} \tag{101}$$

from which, we obtain

$$P(x,t|x(0),v(0)) = \frac{\exp\left\{ -\dfrac{\left[x - x(0)\Phi_{II}(t) - v(0)\Phi_{\rm p}(t)\right]^2}{2\langle [x - x(0)\Phi_{II}(t) - v(0)\Phi_{\rm p}(t)]^2 \rangle} \right\}}{\sqrt{2\pi \langle [x - x(0)\Phi_{II}(t) - v(0)\Phi_{\rm p}(t)]^2 \rangle}}. \tag{102}$$

The quantity $\left\langle \left[x - x(0)\Phi_{II}(t) - v(0)\Phi_{\rm p}(t) \right]^2 \right\rangle$ is given explicitly in (86). In this case, the probability density of positions attains a stationary form, $P_{\rm st}(x)$ if and only if, in the asymptotic regime

$$\bar{\kappa} \equiv \lim_{t\to\infty} \frac{\langle \xi^2 \rangle}{m^2} \int_0^t ds_1\, \Phi_{\rm p}(s_1) \int_0^{s_1} ds_2\, \Phi_{\rm p}(s_2) \Gamma(s_1 - s_2) \tag{103}$$

is finite.

For the exponentially correlated external noise (49), and the exponentially decaying memory function (50), we have that

$$P_{\rm st}(x) = \mathcal{Z}^{-1} \exp\left\{ -\frac{m\omega^2 x^2}{2\langle \xi^2 \rangle (\tau_{\rm cor}/m\omega)} \right\}, \tag{104}$$

from which the effective temperature can be recognized to be

$$T_{\rm eff} = \frac{\langle \xi^2 \rangle\, \tau_{\rm cor}}{k_B\, m\omega}. \tag{105}$$

4 Conclusions and Final Remarks

We have investigated the effects of persistent motion on the stationary distribution of positions of trapped active particles. The persistence of motion has been taken into account within the theoretical framework of the generalized Langevin equation, more precisely, we have assumed that the time dependence of the memory function, that appears in the non-Markovian dissipative force, describes persistent motion. We have shown that the intrinsic non-equilibrium aspects of active motion can be incorporated into such description, when unbinding the dissipative dynamics from the fluctuating one, both binded in equilibrium by the fluctuation-dissipation relation. Thus, no connection between the autocorrelation of noise and the memory function is assumed. We found that the probability density of the particle positions is akin to the Boltzmann distribution, but with an effective temperature, as occurs in some other models of active motion, particularly in the model of Szamel of Ornstein-Uhlenbeck active particles [29].

To the author's knowledge, this is the first time the intrinsic non-equilibrium aspects of active motion have been considered within the framework of the generalized Langevin equation, and certainly, there are general aspects, and particular ones as well, still to be investigated. For instance, a derivation of a Fokker-Planck-Kramers equation for arbitrary trapping external potential is still missing in the literature and the generalization of the present analysis (70) to the case of non-Gaussian noise is worthy to be pursued.

Acknowledgements The author kindly acknowledges the support from grant UNAM-DGAPA-PAPIIT-IN114717.

References

1. Reimann P (2002) Phys Rep 361:57. ISSN 0370-1573. http://www.sciencedirect.com/science/article/pii/S0370157301000813
2. Taktikos J, Stark H, Zaburdaev V (2014) PLoS One 8:1. http://dx.doi.org/10.1371%2Fjournal.pone.0081936
3. Taute KM, Gude S, Tans SJ, Shimizu TS (2015) Nat Commun 6:8776. https://www.nature.com/articles/ncomms9776#supplementary-information
4. Schnitzer MJ (1993) Phys Rev E 48:2553. http://link.aps.org/doi/10.1103/PhysRevE.48.2553
5. Bechinger C, Di Leonardo R, Löwen H, Reichhardt C, Volpe G, Volpe G (2016) Rev Mod Phys 88:045006. https://link.aps.org/doi/10.1103/RevModPhys.88.045006
6. Gao W, Dong R, Thamphiwatana S, Li J, Gao W, Zhang L, Wang J (2015) ACS Nano 9:117. pMID: 25549040, http://dx.doi.org/10.1021/nn507097k
7. Ramaswamy S (2010) Annu Rev Condens Matter Phys 1:323. https://doi.org/10.1146/annurev-conmatphys-070909-104101
8. Marchetti MC, Joanny JF, Ramaswamy S, Liverpool TB, Prost J, Rao M, Simha RA (2013) Rev Mod Phys 85:1143. https://link.aps.org/doi/10.1103/RevModPhys.85.1143
9. Howse JR, Jones RAL, Ryan AJ, Gough T, Vafabakhsh R, Golestanian R (2007) Phys Rev Lett 99:048102
10. Buttinoni I, Volpe G, Kümmel F, Volpe G, Bechinger C (2012) J Phys Condens Matter 24:284129. http://stacks.iop.org/0953-8984/24/i=28/a=284129
11. Takatori SC, Yan W, Brady JF (2014) Phys Rev Lett 113:028103. http://link.aps.org/doi/10.1103/PhysRevLett.113.028103
12. Ginot F, Theurkauff I, Levis D, Ybert C, Bocquet L, Berthier L, Cottin-Bizonne C (2015) Phys Rev X 5:011004. https://link.aps.org/doi/10.1103/PhysRevX.5.011004
13. Takatori SC, Brady JF (2015) Phys Rev E 91:032117. http://link.aps.org/doi/10.1103/PhysRevE.91.032117
14. Solon AP, Chaté H, Tailleur J (2015) Phys Rev Lett 114:068101. http://link.aps.org/doi/10.1103/PhysRevLett.114.068101
15. Vicsek T, Czirók A, Ben-Jacob E, Cohen I, Shochet O (1995) Phys Rev Lett 75:1226
16. Speck T, Bialké J, Menzel AM, Löwen H (2014) Phys Rev Lett 112:218304. https://link.aps.org/doi/10.1103/PhysRevLett.112.218304
17. Solon AP, Stenhammar J, Wittkowski R, Kardar M, Kafri Y, Cates ME, Tailleur J (2015) Phys Rev Lett 114:198301. https://link.aps.org/doi/10.1103/PhysRevLett.114.198301
18. Cates ME Tailleur J (2015) Annu Rev Condens Matter Phys 6:219. https://doi.org/10.1146/annurev-conmatphys-031214-014710
19. Fodor E, Nardini C, Cates ME, Tailleur J, Visco P, van Wijland F (2016) Phys Rev Lett 117:038103. https://link.aps.org/doi/10.1103/PhysRevLett.117.038103
20. Oukris H, Israeloff NE (2010) Nat Phys 6:135. ISSN 1745-2473. https://doi.org/10.1038/nphys1482
21. Colombani J, Petit L, Ybert C, Barentin C (2011) Phys Rev Lett 107:130601. http://link.aps.org/doi/10.1103/PhysRevLett.107.130601
22. Dieterich E, Camunas-Soler J, Ribezzi-Crivellari M, Seifert U, Ritort F (2015) Nat Phys 11:971
23. Loi D, Mossa S, Cugliandolo LF (2008) Phys Rev E 77:051111. http://link.aps.org/doi/10.1103/PhysRevE.77.051111
24. Tailleur J Cates ME (2009) EPL (Europhys Lett) 86:60002. http://stacks.iop.org/0295-5075/86/i=6/a=60002
25. Palacci J, Cottin-Bizonne C, Ybert C, Bocquet L (2010) Phys Rev Lett 105:088304
26. Enculescu M Stark H (2011) Phys Rev Lett 107:058301. http://link.aps.org/doi/10.1103/PhysRevLett.107.058301
27. Ben-Isaac E, Park Y, Popescu G, Brown FLH, Gov NS, Shokef Y (2011) Phys Rev Lett 106:238103. http://link.aps.org/doi/10.1103/PhysRevLett.106.238103

28. Loi D, Mossa S, Cugliandolo LF (2011) Soft Matter 7:3726. http://dx.doi.org/10.1039/C0SM01484B
29. Szamel G (2014) Phys Rev E 90:012111. http://link.aps.org/doi/10.1103/PhysRevE.90.012111.
30. Levis D Berthier L (2015) EPL (Europhys Lett) 111:60006. http://stacks.iop.org/0295-5075/111/i=6/a=60006
31. Pototsky A, Stark H (2012) EPL 98:50004
32. Solon AP, Cates ME, Tailleur J (2015) Eur Phys J Spec Top 224:1231. ISSN 1951-6401. http://dx.doi.org/10.1140/epjst/e2015-02457-0
33. Takatori SC, De Dier R, Vermant J, Brady JF (2016) Nat Commun 7:10694. http://www.nature.com/articles/ncomms10694#supplementary-information
34. Miramontes O, DeSouza O, Paiva LR, Marins A, Orozco S (2014) PLoS One 9:e111183
35. Argun A, Moradi A-R, Pinçe E, Bagci GB, Imparato A, Volpe G (2016) Phys Rev E 94:062150. https://link.aps.org/doi/10.1103/PhysRevE.94.062150
36. Codling EA, Plank MJ, Benhamou S (2008) J R Soc Interface 5:813
37. Masoliver J, Lindenberg K, Weiss GH (1989) Physica A 157:891
38. Weiss GH, Rubin RJ (1983) Adv Chem Phys 52:363
39. Masoliver J, Lindenberg K (2017) Eur Phys J B 90:107. ISSN 1434-6036. https://doi.org/10.1140/epjb/e2017-80123-7
40. Kubo R (1966) Rep Prog Phys 29:255. http://stacks.iop.org/0034-4885/29/i=1/a=306
41. Mikhailov AS, Zanette DH (1999) Phys Rev E 60:4571. https://link.aps.org/doi/10.1103/PhysRevE.60.4571
42. Erdmann U, Ebeling W, Schimansky-Geier L, Schweitzer F (2000) Eur Phys J B 15:105. ISSN 1434-6036. http://dx.doi.org/10.1007/s100510051104
43. Chaudhuri D (2014) Phys Rev E 90:022131. https://link.aps.org/doi/10.1103/PhysRevE.90.022131
44. Marconi UMB, Puglisi A, Rondoni L, Vulpiani A (2008) Phys Rep 461:111. ISSN 0370-1573. http://www.sciencedirect.com/science/article/pii/S0370157308000768
45. Wang K, Tokuyama M (1999) Physica A 265:341. ISSN 0378-4371. http://www.sciencedirect.com/science/article/pii/S037843719800644X
46. Despósito MA, Viñales AD (2008) Phys Rev E 77:031123. https://link.aps.org/doi/10.1103/PhysRevE.77.031123
47. Sandev T, Metzler R, Tomovski Ž (2014) J Math Phys 55:023301. http://dx.doi.org/10.1063/1.4863478
48. Kubo R, Toda M, Hashitsume N (1991) Statistical physics II: nonequilibrium statistical mechanics. Springer series in solid-state sciences, 2nd edn., vol 31. Springer, Berlin. ISBN 978-3-540-53833-2, 978-3-642-58244-8
49. Adelman SA (1976) J Chem Phys 64:124. http://dx.doi.org/10.1063/1.431961
50. Fox RF (1977) J Math Phys 18:2331. http://dx.doi.org/10.1063/1.523242
51. Fox RF (1978) Phys Rep 48:179. ISSN 0370-1573. http://www.sciencedirect.com/science/article/pii/037015737890145X
52. Miguel MS, Sancho JM (1980) J Stat Phys 22:605. ISSN 1572-9613. https://doi.org/10.1007/BF01011341
53. Hannes Risken TF (1996) The Fokker-Planck equation: methods of solution and applications. Springer series in synergetics, 2nd edn. Springer, Berlin. ISBN 9783540504986, 3540504982, 9780387504988, 0387504982
54. Viñales AD, Despósito MA (2007) Phys Rev E 75:042102. https://link.aps.org/doi/10.1103/PhysRevE.75.042102
55. Metzler R, Klafter J (2000) Phys Rep 339:1. ISSN 0370-1573. http://www.sciencedirect.com/science/article/pii/S0370157300000703
56. Zwanzig R (1973) J Stat Phys 9:215. ISSN 1572-9613. https://doi.org/10.1007/BF01008729
57. Viñales AD, Despósito MA (2006) Phys Rev E 73:016111. https://link.aps.org/doi/10.1103/PhysRevE.73.016111

58. Viñales AD, Wang KG, Despósito MA (2009) Phys Rev E 80:011101. https://link.aps.org/doi/10.1103/PhysRevE.80.011101
59. Camargo RF, de Oliveira EC, Vaz J Jr (2009) J Math Phys 50:123518. https://doi.org/10.1063/1.3269587
60. Sandev T, Tomovski Ž (2010) Phys Scr 82:065001. http://stacks.iop.org/1402-4896/82/i=6/a=065001

Homeostasis from a Time-Series Perspective: An Intuitive Interpretation of the Variability of Physiological Variables

Ruben Fossion, Jean Pierre J. Fossion, Ana Leonor Rivera, Octavio A. Lecona, Juan C. Toledo-Roy, Karla P. García-Pelagio, Lorena García-Iglesias, and Bruno Estañol

Abstract Homeostasis implies the approximate constancy of specific *regulated variables*, where the independence of the internal from the external environment is ensured by adaptive physiological responses carried out by other so-called

R. Fossion (✉) · A. L. Rivera
Instituto de Ciencias Nucleares, Universidad Nacional Autónoma de México, Mexico City, Mexico

Centro de Ciencias de la Complejidad (C3), Universidad Nacional Autónoma de México, Mexico City, Mexico
e-mail: ruben.fossion@nucleares.unam.mx

J. P. J. Fossion
Belgian Association of Medical Acupuncture (ABMA-BVGA), Brussels, Belgium

O. A. Lecona
Centro de Ciencias de la Complejidad (C3), Universidad Nacional Autónoma de México, Mexico City, Mexico

Maestría en Dinámica No Lineal y Sistemas Complejos, Universidad Autónoma de la Ciudad de México, Mexico City, Mexico

J. C. Toledo-Roy
Centro de Ciencias de la Complejidad (C3), Universidad Nacional Autónoma de México, Mexico City, Mexico

K. P. García-Pelagio
Facultad de Ciencias, Universidad Nacional Autónoma de México, Mexico City, Mexico

L. García-Iglesias
Posgrado en Ciencias Físicas, Universidad Nacional Autónoma de México, Mexico City, Mexico

B. Estañol
Centro de Ciencias de la Complejidad (C3), Universidad Nacional Autónoma de México, Mexico City, Mexico

Laboratorio de Neurofisiología Clínica, Departamento de Neurología y Psiquiatría, Instituto Nacional de Ciencias Médicas y Nutrición "Salvador Zubirán", Mexico City, Mexico

L. Olivares-Quiroz, O. Resendis-Antonio (eds.), *Quantitative Models for Microscopic to Macroscopic Biological Macromolecules and Tissues*,
https://doi.org/10.1007/978-3-319-73975-5_5

effector variables. The loss of homeostasis is the basis to understand chronic-degenerative disease and age-associated frailty. Technological advances presently allow to monitor a large variety of physiological variables in a non-invasive and continuous way and the statistics of the resulting physiological time series is thought to reflect the dynamics of the underlying control mechanisms. Recent years have seen an increased interest in the variability and/or complexity analysis of physiological time series with possible applications in pathophysiology. However, a general understanding is lacking for which variables variability is an indicator of good health (e.g., heart rate variability) and when on the contrary variability implies a risk factor (e.g., blood pressure variability). In the present contribution, we argue that in optimal conditions of youth and health regulated variables and effector variables necessarily exhibit very different statistics, with small and large variances, respectively, and that under adverse circumstances such as ageing and/or chronic-degenerative disease these statistics degenerate in opposite directions, i.e. towards an increased variability in the case of regulated variables and towards a decreased variability for effector variables. We demonstrate this hypothesis for a simple mathematical model of a thermostat, and for blood pressure and body temperature homeostasis for healthy controls and patients with metabolic disease, and suggest that this scheme may explain the general phenomenology of physiological variables of homeostatic regulatory mechanisms.

Keywords Homeostasis · Physiological regulation · Control theory · Control systems · Continuous monitoring · Time series · Early-warning signals · Complexity · Fractal physiology · Variability · Heart rate variability · HRV · Blood pressure variability · BPV · Body temperature

1 Introduction

Homeostasis is one of the core concepts of physiology [1]. The origins of this concept can be found with the French physiologist Claude Bernard (1813–1878) who observed that living systems possess an internal stability that buffers and protects the organism against a continuously changing external environment [2]. Although Bernard was highly honoured and was the most famous French scientist during his lifetime, his hypothesis of a constant *milieu intérieur*, first proposed in 1854, was largely ignored for the next 50 years, one of the reasons being that the technology necessary to measure the internal environment was not yet available [3]. These ideas were expanded and popularized by the American physiologist, Walter Cannon (1871–1945), who coined the term *homeostasis* from the Greek words όμοιος [omoios] "similar" and στάσις [stasis] "standing still", together to mean "staying similar" (but not to be misunderstood as "staying the same") [4]. Homeostasis thus describes the *self-regulating processes* by which a biological system maintains internal *stability* while *adapting* to changing environmental conditions [1, 4]. Homeostatic ideas are shared by the science of *cybernetics*, from the Greek κυβερνητικός [kybernitikos] "steersman", defined in 1948 by the

Jewish American mathematician Norbert Wiener (1894–1964) in collaboration with the Mexican physiologist Arturo Rosenblueth (1900–1976) as "the entire field of control and communication theory, whether in the machine or in the animal" [5]. *Negative feedback* is a central homeostatic and cybernetic concept, referring to how an organism or system automatically opposes any change imposed upon it that could move it away from a predefined *setpoint* [6]. More recently, it has been proposed that there may be other or additional mechanisms important for physiological regulation, not explicitly contained within the original homeostatic concept, in particular *anticipatory regulation*, *behavioural homeostasis* and *feedforward* or *positive feedback*, such that numerous alternative explanatory models have been suggested in an effort to address these apparent gaps in homeostatic thinking, as listed in Ref. [7]: enantiostasis [8], predictive homeostasis [9], reactive homeostasis [9], homeorhesis [10–13], homeorheusis [14], homeokinetics [15], rheostasis [16], homeodynamics [17–19], teleophoresis [20, 21], poikilostasis [22], heterostasis [23], allodynamic regulation [24, 25] and allostasis [26–28]. Others argue that it is not clear whether these alternative concepts offer anything that was not already apparent, or at least readily derivable, from the original concept of homeostasis, and—on the contrary—criticize that these neologisms may unnecessarily complicate the understanding of the unifying principles of physiological regulation [29, 30].

Recently, technological advances allow to monitor a great variety of physiological variables in a non-invasive and continuous way and it came as a surprise that most—if not all—of these variables spontaneously fluctuate in time, even when the monitored subject is in rest. Often, these fluctuations behave in a stochastic and fractal-like way and without obvious periodic patterns [31]. The *variability* of these time series can be studied with various statistical techniques and is conjectured to correlate with the health status of the organ, process or system under study [32], as found, e.g., for the variability of blood oxygen saturation (SpO_2) [33], blood glucose variability [34], variability of gastro-esophageal acidity [35], brain signal variability [36], gait variability [37], heart rate variability (HRV) [38], blood pressure variability (BPV) [39], variability of breathing dynamics [40], skin temperature variability [41, 42] and variability of core body temperature [43, 44], variability of electrodermal activity (EDA) [45], variability of equilibrium and balance function [46] and variability of physical activity (actigraphy) [47–50]. Measurement devices capable of continuous physiological monitoring have become ubiquitous, not only in the medical world but also in the consumer market with a wide variety of activity trackers, smartphones, smartwatches and dedicated applets for data collection, analysis and visualization [51]. These specialized and commercial devices generate huge amounts of data, which are also continuous in time. It is not always clear how to extract the useful information from this new type of continuous data, which is exactly the quest of *time series* analysis [52] in the so-called *Big Data* problem [53]. Also, the phenomenology of these physiological time series is not always well understood, where curiously, for some variables a high variability is interpreted an indication of good health, as in the case of HRV [38], whereas in other cases—on the contrary—it has been suggested to imply a risk factor, as in the case of BPV [39].

In literature, at least two different theoretical frameworks have been proposed to explain the variability of experimental time series in physiology and other fields of knowledge. The *loss of complexity* hypothesis of Goldberger and Lipsitz proposes that the geometrical patterns of anatomical organ structures and the time series of the dynamics of physiological processes are inherently "complex" with a large variability that is increasingly lost with ageing and/or chronic-degenerative disease [31, 54–57]. In the same context, based on the empirical observation that physiological time series tend to follow long-tailed distributions with rare but large deviations away from the mean as opposed to a gaussian distribution with frequent but small fluctuations around a setpoint, Bruce West suggested that the ideas of homeostasis and normality are obstacles for the progress of medicine and that a new paradigm, *fractal physiology*, is needed [58–60]. On the other hand, the framework of *early-warning signals* of Scheffer, Carpenter and collaborators, particularly popular in complex dynamical systems such as the climate, ecology and finance, states that—on the contrary—variables of a system in a state of stability and equilibrium behave in a gaussian way with low variability and little correlation or memory of past events, whereas when the system approaches a critical threshold at the brink of collapse, statistical parameters such as variability, non-gaussianity, correlations and memory tend to increase, and—if they are detected early enough—offer the opportunity to take countermeasures to avoid a catastrophe [61–65].

Homeostatic thinking divides physiological variables in two broad categories of regulated variables as opposed to effector variables, see Table 1 and Ref. [1]. *Regulated variables*, such as blood pressure (BP) or core body temperature, are variables that are to be controlled and to be maintained within a very restricted homeostatic range to ensure the stability of the *milieu intérieur* and they are anatomically distinguishable because of the presence of specific sensors that measure the value of these variables directly; an alternative name could be that of essential variables [66]. On the other hand, *effector variables* and the corresponding *physiological responses*, such as heart rate (HR) or skin temperature, have an adaptive function, they oppose and thereby buffer against perturbations from the inner and outer environment with an objective to maintain the regulated variables as constant as possible; they do not have their own specific sensors,[1] which may suggest that their absolute values are not of primary importance but matter only because of the effect they have on the regulated variables. In the present contribution, we hypothesize that time series of regulated and effector variables can be expected to exhibit very contrasting statistical properties given their different functions in a homeostatic regulatory mechanism, which may explain the apparent contradictions between the loss of complexity and early-warning paradigms. We test this hypothesis in various systems, in Sect. 2 using a simple mathematical model of a thermostat, in Sect. 3

[1]The skin of course does have its own thermosensors, but they are part of a *reflex loop* and not of a local *homeostatic control loop*: when touching something extremely warm or cold, there will be an automatic reaction to move the fingers away, but not a physiological response to locally cool off or warm up the skin to maintain a constant skin temperature.

Table 1 As a first approximation, different homeostatic mechanisms may be considered to coexist in a more or less independent way. The focus of each homeostatic mechanism is a specific *regulated variable* that is to be maintained within a restricted homeostatic range, and therefore use is made of one or more supporting *effector variables* and corresponding *physiological responses* whose function it is to absorb or adapt to variations of the inner and outer environments, with as an objective to safeguard the constancy of the regulated variable as much as possible, based on Refs. [1, 67]. In the present contribution, we will focus on the first few mechanisms of which the variables can be monitored in a continuous and non-invasive way

Homeostatic regulatory mechanisms	
Regulated variable (specific sensors available for direct measurement)	Effector variable(s) and physiological response(s) (indirect estimation by effect on regulated variable)
Arterial blood pressure (BP)	Cardiac output (heart rate, stroke volume)
(baroreceptors)	Vasomotor (vasodilatation, vasoconstriction)
Core body temperature	Vasomotor and superficial skin temperature
(thermoreceptors)	Metabolism
	Shivering vs. sudomotor
	Behaviour and physical exercise
Blood oxygen saturation (SpO_2)	Respiration dynamics (rate, volume)
(chemosensors)	Erythropoietin (EPO) increasing hematocrit (Ht)
Blood oxygen P_{O_2} and carbon dioxide	Respiration dynamics (rate, volume)
partial pressure P_{CO_2} (chemosensors)	P_{CO_2} closely related to extracellular fluid pH
Extracellular fluid pH	Bicarbonate concentration [HCO_3]
(chemosensors)	Carbonic acid concentration [H_2CO_3]
Blood glucose	Insulin
(chemosensors)	Glucagon
Plasma ionized calcium concentration [Ca^{2+}]	Parathyroid hormone (PTH)
(chemosensors)	Calcitonine
Extracellular sodium concentration [Na]	Renin and related aldosterone
(chemosensors)	
Extracellular potassium concentration [K]	Aldosterone
(chemosensors)	
Volume of body water and electrolyte-water balance	Vasopressin or antidiuretic hormone (ADH)
osmolality or osmolarity	Atrial natriuretic peptide (ANP)
(osmosensors)	Thirst

analysing HR and BP time series of healthy controls and diabetic patients, in Sect. 4 focussing on time series of skin temperature as a function of body weight, while in Sect. 5 we propose an intuitive scheme that may explain the phenomenology of variability of physiological variables in general, and finally, in Sect. 6 we present our conclusions.

2 The Thermostat as a Paradigm for Homeostasis

The term *thermostat* is derived from the Greek words θερμός [thermos] "hot" and στατός [statos] "standing, stationary" and refers to a controlling component which senses a system's temperature and allows for this temperature to be maintained near a desired setpoint. In cybernetics and control theory, a *setpoint* is the desired or target value for a specific regulated variable of a system. A thermostat can often be the main control unit for a heating or cooling system, in applications such as ambient air control and sometimes a thermostat combines both the sensing and control action elements of a controlled system, such as in an automotive thermostat, see Fig. 1. It is an example of a *closed-loop control* device and departure of a variable from its setpoint is the basis for *error-controlled regulation*, that is, the use of negative feedback to return the system to its norm, as in homeostasis. A thermostat is most often an instance of a *bang-bang controller* where the heating system is switched on and off as often as necessary. It works by sensing the air temperature, switching on the heating when the air temperature falls below the thermostat setting,

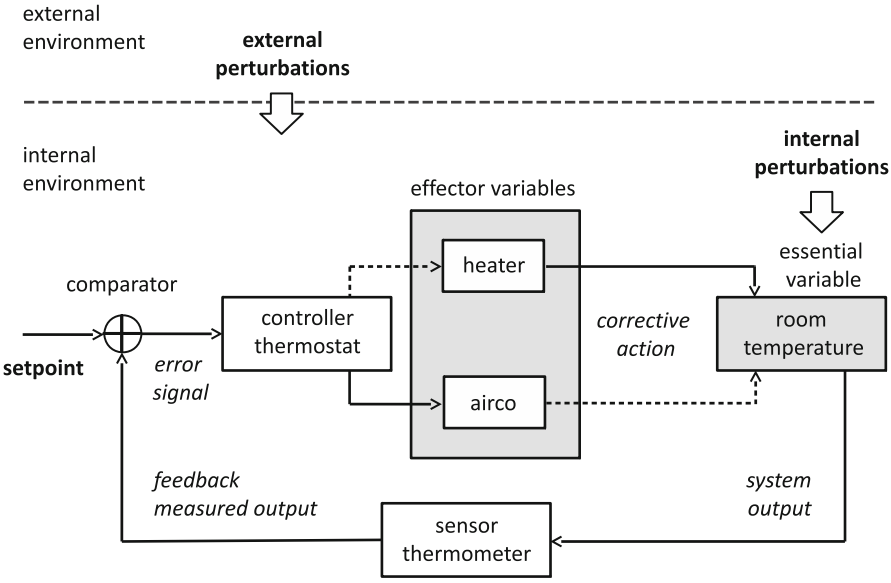

Fig. 1 The control mechanism of a thermostat. The control mechanism is based on a negative feedback loop which acts to maintain the regulated variable of the room temperature within a narrow homeostatic range. The effector variables of the heater and/or the airconditioning allow for the system to adapt to perturbations from the outside and inside environment. A negative feedback loop necessarily consists of an odd number of inhibitory/negative couplings (dashed lines) where connected components are inversely related (an increase in one component induces a decrease in the other component and vice versa) and an arbitrary number of excitatory/positive couplings (continuous lines) where connected components are directly related (an increase in one component induces an increase in the other component and vice versa). Image based on Refs. [1] and [67]

and switching it off once this set temperature has been reached. The heating or cooling equipment runs at full capacity until the set temperature is reached, then shuts off. Other, more advanced controller mechanisms include *proportional controllers*, *proportional–integral–derivative controllers* (or *PID controllers*) and *optimal controllers*. More advanced controllers will be more adaptive, will absorb the perturbations of the inner and outer environment more effectively in the effector variables, or will incorporate a memory of past events, to predict and anticipate future perturbations, with a general objective to minimize more efficiently the error signal between the expected and the obtained values of the regulated variable.

In what follows, in Figs. 2 and 3, we will show the numerical results for a simple mathematical model of the thermostat of Refs. [68, 69], which includes a heater but no airconditioning, to illustrate the statistical differences of time series corresponding to a regulated variable (the inside air temperature) and an effector variable (the heater). The model includes the following variables: outdoor air temperature T_o, indoor air temperature T_i, water temperature of the radiators T_w and a binary function θ_f that indicates whether the furnace of the boiler is active (state 1) or not (state 0). The initial values at $t = 0$ are $T_i(0) = 13\,^{\circ}\mathrm{C}$ and $T_w(0) = 10\,^{\circ}\mathrm{C}$. The thermostat is fixed at the constant setpoint $T_s = 20\,^{\circ}\mathrm{C}$. Heat is transferred between the radiators and the indoor air at a rate $r_1 = 0.03$ proportional to the temperature gradient, heat is lost from the indoor to the outdoor air at a rate $r_2 = 0.01$ due to imperfect insulation, heat is transferred between the indoor air and the water of the boiler at a rate $r_3 = 0.02$, and $r_4 = 1.0$ is the rate at which the water of the boiler heats up when the furnace is switched on. The system is controlled by three coupled difference equations that update the values at time $t + 1$ depending on the values at the previous time step t. We assume that the system updates its values each minute.

$$\theta_f(t+1) = \begin{cases} 1 \text{ if } T_i(t) < T_s(t) \\ 0 \text{ if } T_i(t) \geq T_s(t) \end{cases} \tag{1}$$

$$T_i(t+1) = T_i(t) + r_1\Big(T_w(t) - T_i(t)\Big) + r_2\Big(T_o(t) - T_i(t)\Big) \tag{2}$$

$$T_w(t+1) = T_w(t) + r_3\Big(T_o(t) - T_w(t)\Big) + r_4\theta_f(t) \tag{3}$$

Figure 2 shows results for a numerical simulation of Eqs. (1)–(3) during three successive hypothetical winter days. The variation of the outside air temperature T_o was modelled using a slow linear trend and small random fluctuations superposed on a 24-h periodic cycle, with day temperatures being higher than temperatures during the night, but always lower than the thermostat setpoint $T_o < T_s = 20\,^{\circ}\mathrm{C}$, such that the thermostat control system is always active. The thermostat controller θ_f of Eq. (1) does not include memory of past events, it does not think ahead, and the value for $t + 1$ is updated taking into account only the last known inside air temperature $T_i(t)$. It can be appreciated that the thermostat switches on and off at a faster rate during the night when it is cold outside, and at a slower rate during the day when the outside air temperature is higher. The switching on and

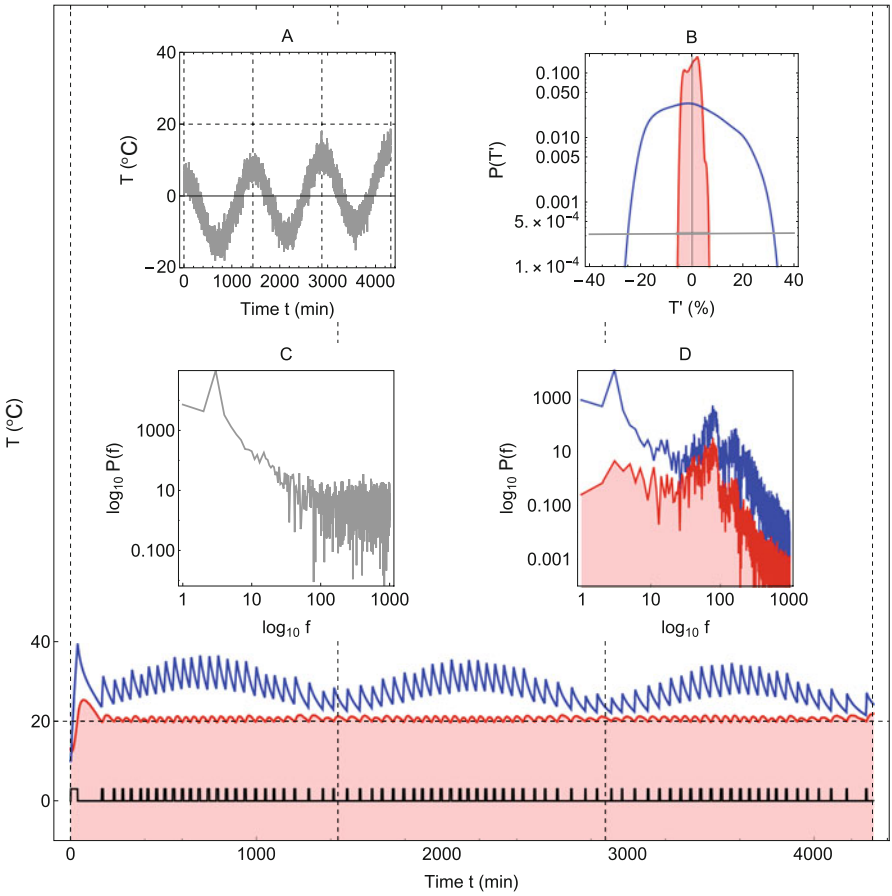

Fig. 2 Mathematical simulation of a simple thermostat based on Refs. [68, 69] for three successive hypothetical winter days. The main figure shows the dynamics of the central heating θ_f switching on and off (black curve, states 1 and 0, respectively), the water temperature in radiators T_w (blue curve) and the inside air temperature T_i (red curve) in response to the outside temperature T_o (grey curve of inset A). Shown are also the probability distributions $P(T')$ of the fluctuations T' of temperature time series T_i, T_w and T_o as a percentage of their respective average values (inset B), the Fourier power spectrum $P(f)$ for T_o (inset C) and for T_w and T_i (inset D). The horizontal gridline indicates the temperature setpoint 20 °C and vertical gridlines indicate midday of the three successive days (main figure and inset A). Frequency f is in units of total number of oscillations for the whole duration of the time series

off rate of the thermostat is reflected in small but rapid fluctuations of the water temperature of the radiators, but also slower and larger periodic oscillations are present because the water of the radiators will be heated up to a higher average temperature during the night than during the day to offset the day-night difference of the outside air temperature. As a result of the heating of the radiators, the inside air temperature always stays very close and within very small rapid fluctuations from

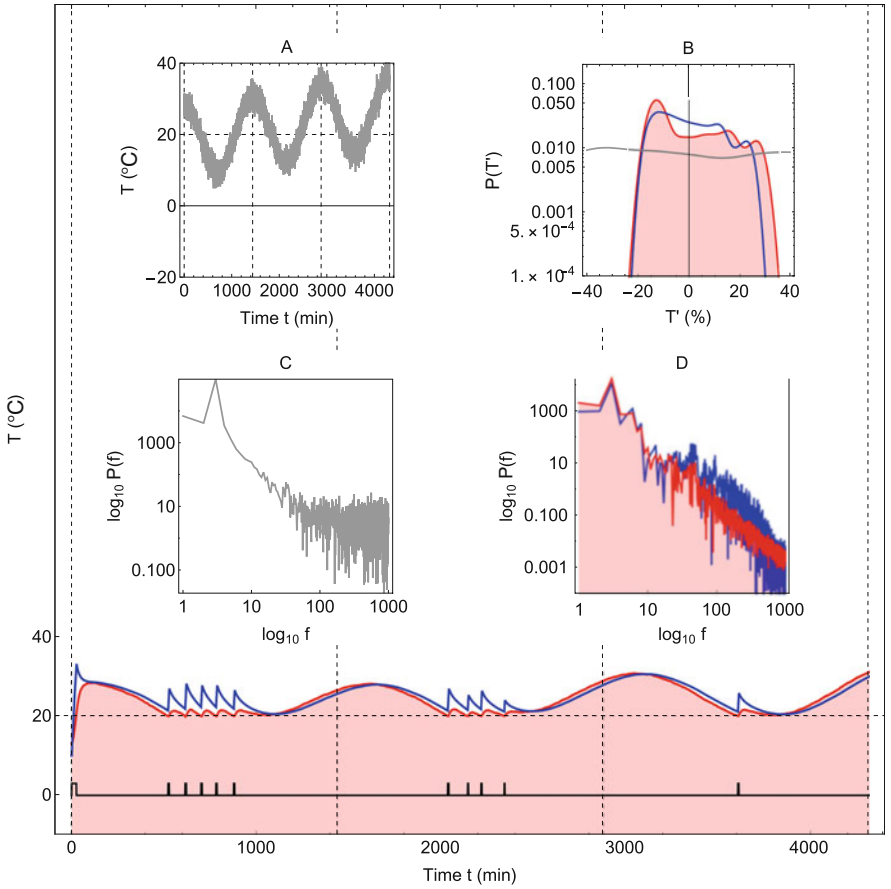

Fig. 3 Similar to Fig. 2 but for three successive hypothetical spring days

the setpoint, $T_i \approx T_s = 20\,^{\circ}\mathrm{C}$. Indeed, when we compare the probability distribution functions $P(X')$ for the fluctuations X' around the average value μ of time series $X(t)$ expressed as a percentage of this average value,

$$X(t)' = 100 \times \frac{X(t) - \mu}{\mu}, \tag{4}$$

for the inside air temperature T_i, the outside air temperature T_o and the water of the radiators T_w, then it is clear that the variability of T_i is well controlled within a restricted range and is much smaller than the variance of T_w and that both are smaller than the variations of T_o. A Fourier spectral analysis of the corresponding time series offers additional insight into how the control mechanism works. The power spectrum $P(f)$ of the time series for T_o shows a dominant peak at $f = 3$, reflecting the periodic day-night cycle over three successive days, and is rather flat

for higher frequencies indicating random white noise. The power spectrum $P(f)$ for T_w shows the same dominant peak at $f = 3$ and an additional broad peak at higher frequencies $50 < f < 100$ corresponding to the rapid cycles of heating and cooling of the water in the radiators at multiple times during the day. On the other hand, the power spectrum $P(f)$ for T_i shows that the outside perturbation at $f = 3$ is successfully suppressed with over 2 orders of magnitude and the dominant feature of $P(f)$ is the peak at $50 < f < 100$ in response to the rapid heating and cooling cycle of the radiators. In other words, it appears that the automatic thermostat system creates its own *intrinsic rhythms*, which have small amplitude but high frequency, and with which the larger but slower outside perturbations are canceled out. For more advanced types of controllers, e.g., capable of incorporating memory about past events, we can expect that more of the outside perturbations will be absorbed in the effector variable T_w to keep the error signal $e(t) = T_i(t) - T_s$ closer to 0; in those cases, the statistical differences between the time series of the effector variable T_w and the regulated variable T_i will be even larger than in the present example.

Figure 3 shows the behaviour of the system during three successive hypothetical days in spring time when the temperature during the night is still below the setpoint, $T_o < T_s$, but the temperature during the day rises above the setpoint, $T_o > T_s$. Therefore, the thermostat will be inactive for most of the daytime, during which the system is incapable to influence neither the water temperature of the radiators T_w nor the inside air temperature T_i, and both are subjected to the perturbations of the outside air temperature T_o. Of course, a heating system can only correct for too-low temperatures, and an extra cooling effector device would be needed to correct also for too-high temperatures, as shown for the full climate control system of Fig. 1, but here, we are interested in studying time series of a control system where the control fails. The probability distributions functions $P(T')$ show that the fluctuations T' of the would-be regulated variable T_i now exhibit a larger variability than the fluctuations of the effector variable T_w. The power spectrum $P(f)$ shows an almost absence of intrinsic rhythms with which the outside perturbations were controlled in Fig. 2 and consequently T_i and T_w follow here the same dynamics as T_o.

3 Arterial Blood Pressure and Heart Rate

Figure 4 shows the control mechanism for blood pressure homeostasis where blood pressure (BP) is the regulated variable and with heart rate (HR), stroke volume (SV) and total peripheral resistance (TPR) as physiological responses of the effector variables, where

$$\text{cardiac output} = \text{heart rate (HR)} \times \text{stroke volume (SV)} \tag{5}$$

$$\text{blood pressure (BP)} = \text{total peripheral resistance (TPR)} \times \text{cardiac output.} \tag{6}$$

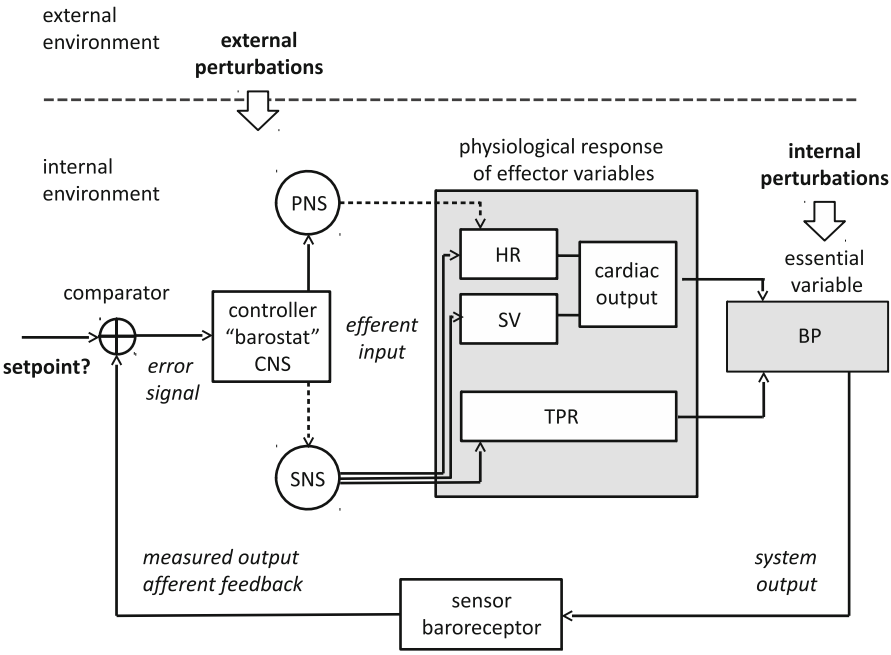

Fig. 4 Similar as for Fig. 1 but for the control loop of arterial blood pressure. The control centrum of the barostat is located in the central nervous system (CNS) which passes commands through the sympathetic (SNS) and parasympathetic (PNS) branches of the autonomous nervous system to the effector variables of heart rate (HR) and stroke volume (SV), whose product is the cardiac output, and the total peripheral resistance (TPR), which together act to maintain blood pressure (BP) in a restricted homeostatic range as measured by the baroreceptor. Image based on Refs. [1] and [67]

Of all the variables mentioned here, HR is easiest to measure on a continuous (beat-to-beat) basis, using, e.g., a common electronic electrocardiographic (ECG) registration. Also BP can be measured continuously, although in this case very specialized (and expensive!) equipment is required, such as a Finapres®, Portapres® or CNAP® device. Using a Portapres®, we collected 5-min HR and BP time series in supine resting position in 30 control subjects, 30 asymptomatic subjects with recently diagnosed type-2 diabetes (DMA) and 15 long-standing patients with type-2 diabetes (DMB), see Refs. [70, 71]. Exclusion criteria included cardiac arrhythmia, hypertension and having taken medication up to 48 h previous to the study. Time series for individual subjects are shown in Fig. 5 (left-hand panels). Average heart rate $\langle HR \rangle$ was similar for controls and the DMA group, but was significantly higher for the DMB group, whereas $\langle SBP \rangle$ was comparable for the three groups, see Fig. 6. Subtle group differences were found between the three populations for the higher-order moments of the distributions of HR and BP, such as standard deviation (SD), the coefficient of variation (CV=SD/mean) skewness

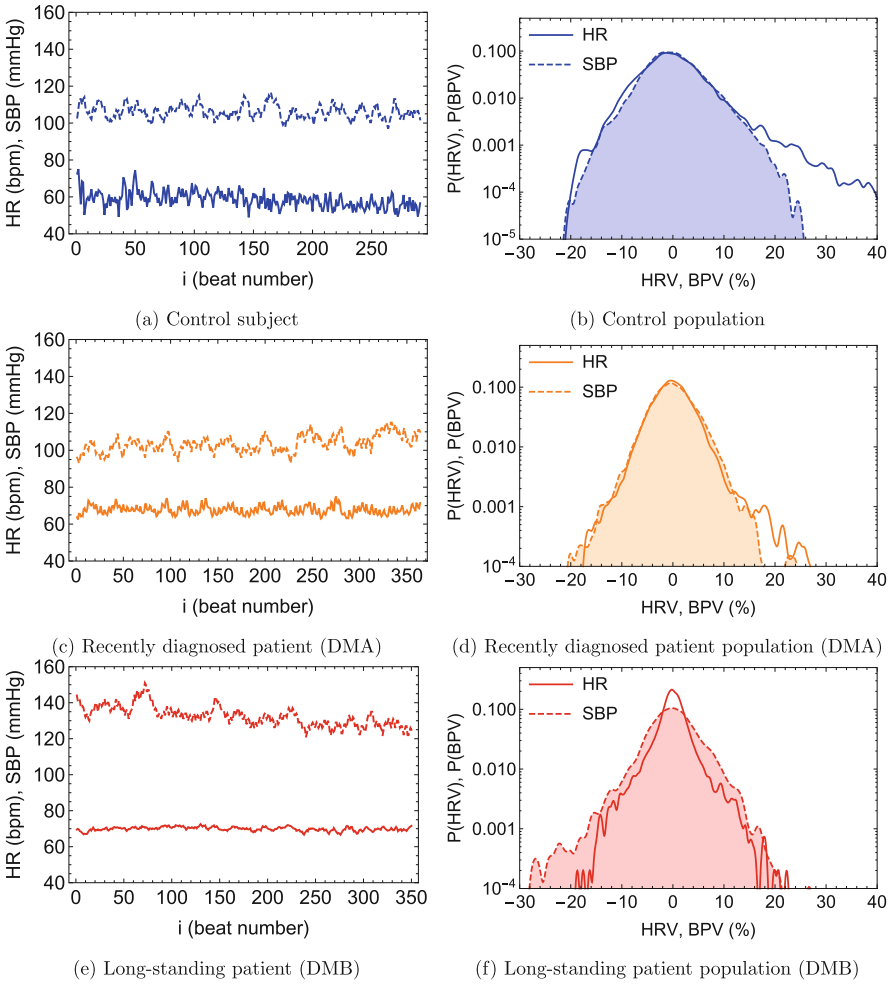

(a) Control subject (b) Control population

(c) Recently diagnosed patient (DMA) (d) Recently diagnosed patient population (DMA)

(e) Long-standing patient (DMB) (f) Long-standing patient population (DMB)

Fig. 5 Time series of individual subjects (left-hand panels) and probability distributions for populations (right-hand panels) for heart rate (HR) and blood pressure (BP) during 5min of supine rest. Shown for (**a**-**b**) healthy control(s), (**c**-**d**) recently diagnosed patient(s) and (**e**-**f**) long-standing patient(s). HR (continuous curves) is measured in beats per minute (bpm), BP (dashed curves) in millimeters of mercury (mmHg) and time in units of beat number. In the case of the probability distributions, in order to show both HR and BP in the same graph, fluctuations of both variables are shown as a percentage of their average value according to Eq. (4). Data from Refs. [70, 71]

(Skew) and kurtosis (Kurt), but statistical significance was obtained only when combining heart rate variability (HRV) and blood pressure variability (BPV) in a single parameter,

$$\alpha = \frac{\text{HRV}}{\text{BPV}}, \tag{7}$$

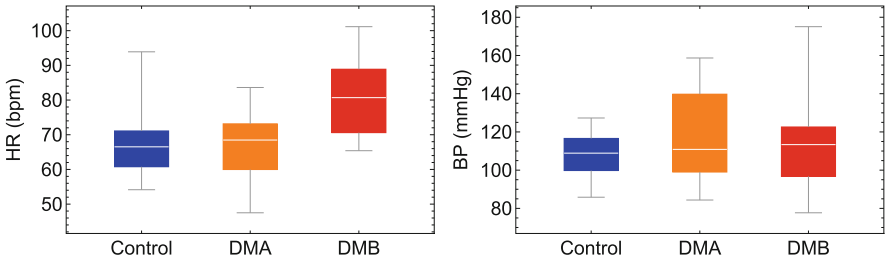

(a) HR population averages (b) BP populations averages

Fig. 6 Box whisker charts of (**a**) average heart rate $\langle \text{HR} \rangle$ and (**b**) average systolic blood pressure $\langle \text{BP} \rangle$, for the control group (blue), recently diagnosed patients DMA (orange) and long-standing patients DMB (red). According to a Kruskal-Wallis nonparametric test, there are significant differences between the control-DMB and DMA-DMB pairs for $\langle \text{HR} \rangle$ at the $p = 10^{-4}$ level, but no significant group differences for $\langle \text{BP} \rangle$. Data from Refs. [70, 71]

where α is large for the control group and is found to decrease as a function of the development of the disease [70]. The interpretation of α is that HRV is a protective factor whereas BPV is a risk factor and that there is a correlation between both. Furthermore, it would seem that more than the absolute values of HRV or BPV separately, it is the relative magnitude of HRV with respect to BPV that appears to correlate with the health status of the populations considered here.

Figure 5 (right-hand panels) shows for each population the probability density functions for the fluctuations of HRV and BPV, where positive values indicate fluctuations above the average and negative values fluctuations below the average. It can be appreciated that for the control group the distribution for HRV is wider than for BPV, in particular, for HRV there is a long tail towards positive fluctuations up to 40% whereas BPV is contained within the range from -20% to $+20\%$. In the case of the DMA group, the width of the HRV probability distribution is greatly reduced and in particular the positive HRV fluctuations have decreased below 30%, whereas now the probability distribution of BPV has become wider than that of HRV towards the negative side. In the case of the DMB group, the probability distribution of BPV has become wider than that of HRV, in particular, the positive HRV fluctuations are now limited to 20%, whereas the negative BPV fluctuations have increased up to 30%. It has been argued that 5-min HR registrations are too short to contain modulations by the sympathetic nervous system (SNS) [72], especially if the registrations are made in supine resting position. Therefore, in the case of the controls, the large positive HRV fluctuations are most probably due to vagal withdrawal (vagolysis) causing temporary HR accelerations, which are probably necessary for the homeostatic control of BP. In the case of DMA, vagolytic capacity is reduced, possibly resulting in a loss of BP control and episodes of hypotension. In the case of DMB, vagolytic capacity is lost completely and BP excursions towards hypotension dominate the probability distribution of BP. It is possible that in the DMB group HR is significantly increased to counter this danger of hypotensive episodes.

4 Body Temperature

The regulation of body temperature depends on the species and the specific body part under study, see Fig. 7. Reptiles, such as lizards, are called *exotherms* and their core temperature adapts to the temperature of the outside environment. Mammals, on the other hand, are *endotherms*, and their core temperature is—over a certain range—approximately independent from the outside temperature. Humans achieve a core temperature near a constant setpoint of about 36.5 °C independent from the outside circumstances by creating a dynamic balance between *thermogenesis* (heat production) and *thermolysis* (heat dissipation), see Fig. 8. In striking this balance, adaptive mechanisms play a very important role, such as cutaneous vasoconstriction when it is cold outside and cutaneous vasodilatation when it is warm, which control the amount of heat radiated from the body towards the outside environment, and consequently skin temperature can be expected to exhibit a large variability in order to keep core temperature constant.

We carried out a pilot study where we monitored skin temperature continuously over seven successive days as a function of the body mass index (weight divided by height squared, BMI $= \mathrm{kg/m^2}$). We considered three groups, a control group with normal weight (ten subjects with $18 < \mathrm{BMI} < 25$), a group of overweight subjects (ten subjects with $25 < \mathrm{BMI} < 30$), and a group with obese subjects (ten subjects with $\mathrm{BMI} > 30$) [42]. Skin temperature can be measured easily and continuously, using, e.g., a thermochron iButton® fixed at the non-dominant wrist using medical tape; core temperature is much more difficult to measure, because a probe should be introduced in a body orifice (mouth, anal, etc.) which is uncomfortable, especially in

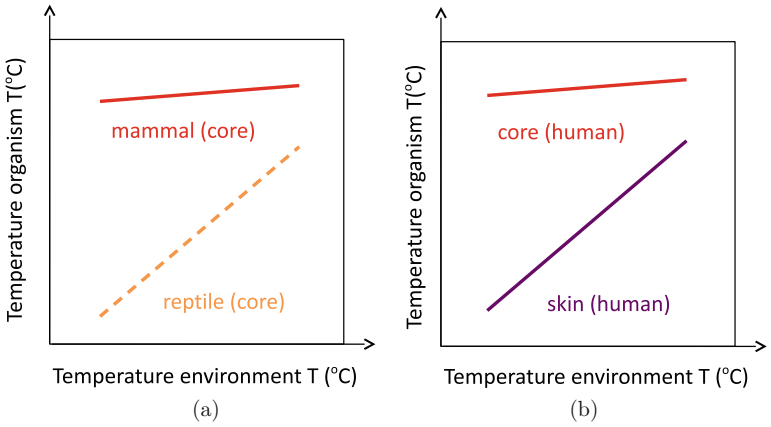

Fig. 7 Schematic representation of body temperature vs. the temperature of the outside environment, (**a**) for endotherms (e.g., humans, continuous red curve) and exotherms (e.g., reptiles, dashed orange curve), based on Ref. [73], and (**b**) for human core temperature (red continuous curve) and human skin temperature (purple continuous curve), based on Ref. [74]

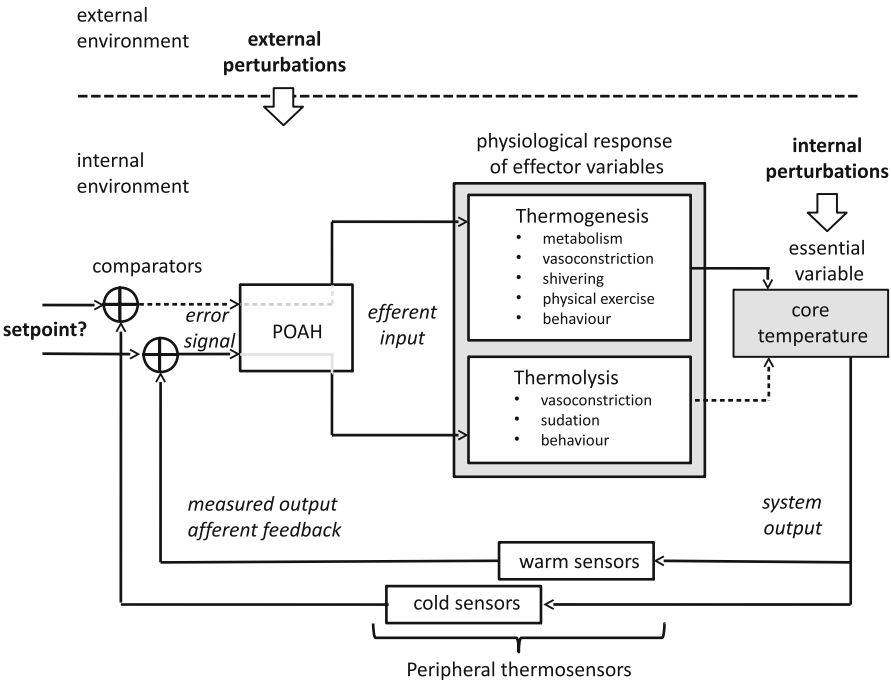

Fig. 8 Similar as for Fig. 1 but for the control loop of core body temperature. The control centrum of core temperature is located in the preoptic anterior hypothalamus (POAH) which activates thermogenetic or thermolytic responses which together act to maintain core temperature in a restricted homeostatic range. Physiological responses include vasomotor effects which determine skin temperature. Behavioural responses include seeking shade when it is hot or putting on a sweater when it is cold. Image based on Refs. [67] and [75]

an ambulatory setting on a long-term basis. In another study, in agreement with our working hypothesis, we have found that skin temperature variability is much larger than core temperature variability [51]. Here, we restrained to the monitoring of skin temperature. Figure 9 shows an example of a continuous 7-day time series of skin temperature in a control subject with normal weight, and the probability distribution of skin temperature for the control group, the overweight group and the obese group. It is clear that the probability distribution is wider for the controls, becomes narrower for the overweight group, and is narrowest for the obese group. The box-whisker plots of Fig. 10 show that there would seem to be a trend for average skin temperature $\langle T \rangle$ to increase with body weight but without statistical significance, possibly because of the small population sizes; on the other hand, variability as measured with the standard deviation (SD) can be seen to decrease with body weight, obtaining statistically significant differences between the control group and the obese group at the $p = 0.022$ level; the skewness of the distribution increases with body weight, but without statistical significance; the kurtosis increases with body weight, from a platykurtic (Kurt < 3) distribution for the controls towards a

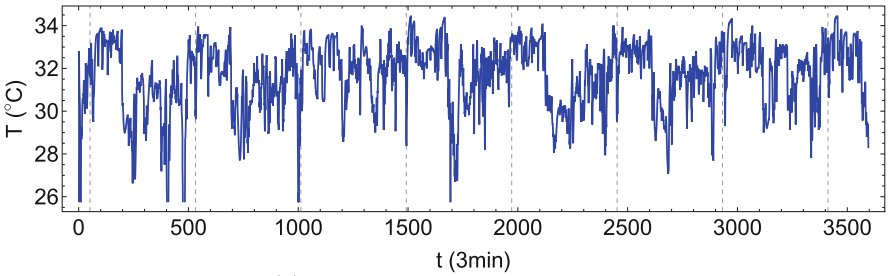

(a) 7-day skin temperature time series

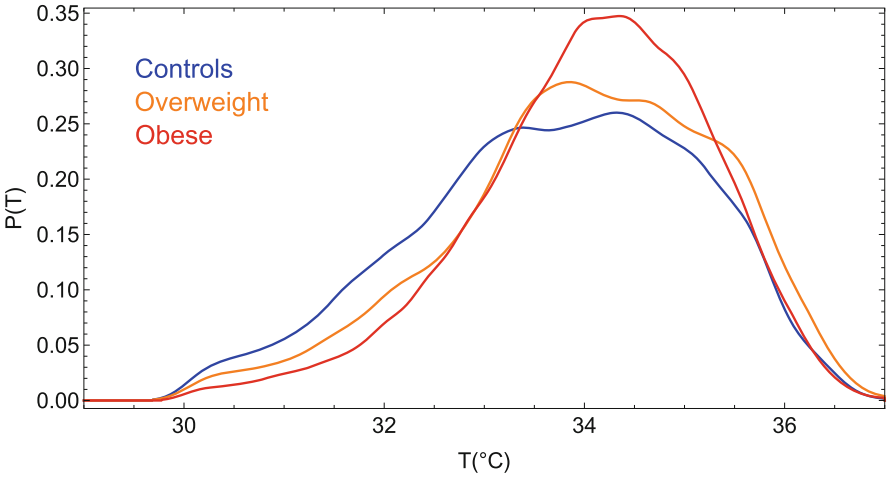

(b) Skin temperature probability density functions

Fig. 9 Continuous monitoring of skin temperature during seven successive days in controls with normal weight, overweight and obese subjects, (**a**) example of a time series of a control subject with vertical gridlines at midnight, and (**b**) probability distribution of the time series of the three groups. Data from Ref. [42]

leptokurtic (Kurt > 3) distribution for the obese population, and in this case there is again statistical significance in the difference between the control group and the obese group at the $p = 0.033$ level.

5 Discussion

When studying a new physiological variable, it is not always clear a priori what type of statistics to expect for the corresponding time series, how this statistics may degenerate under adverse circumstances, and whether any physiological meaning may be contributed to these fluctuations in a clinical context. Although it has been

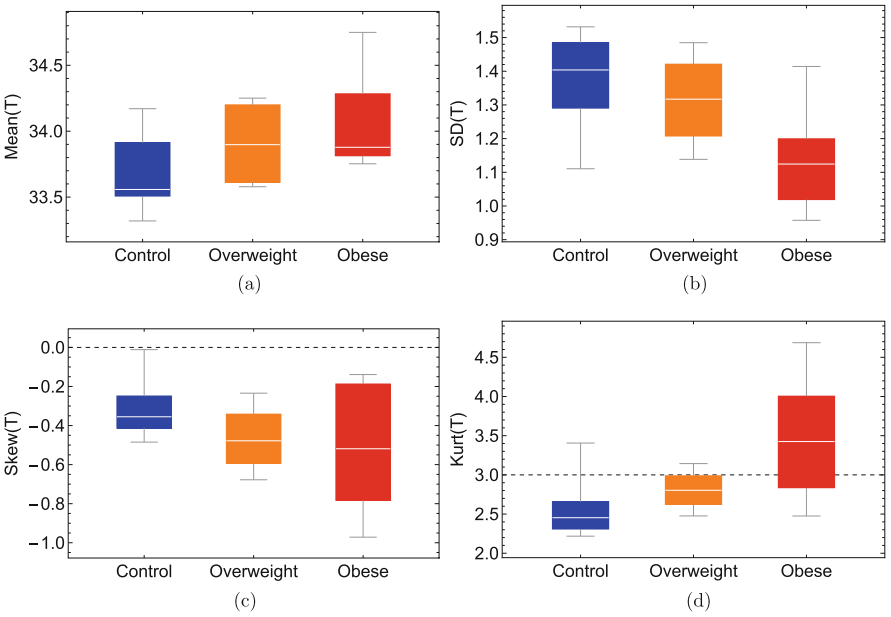

Fig. 10 Box-whisker plots of the moments of the distribution of the skin temperature time series of the control group with normal weight, the overweight group and the obese group, (**a**) mean, (**b**) standard deviation (SD), (**c**) skewness (Skew), and (**d**) kurtosis (Kurt). According to a Kruskal-Wallis nonparametric test, there are significant differences between the control group and the obese group for SD at the $p = 0.022$ level and for Kurt at the $p = 0.033$ level. Horizontal gridlines indicate values for a normal distribution Skew$= 0$ and Kurt $= 3$. Data from Ref. [42]

proposed that blood pressure variability (BPV) is a risk factor [39] and heart rate variability (HRV) an indicator of good health [38], it is not clear whether BPV has diagnostic relevance for specific pathologies such as hypertension [76]. Core body temperature time series have been analysed from the perspective of periodic circadian rhythms, e.g. when studying the effect of body weight and obesity [77–79], but without taking into account the ultradian fluctuations. Fluctuations of skin temperature have been studied, e.g. in intensive care patients [41], but without an interpretation of the physiological implications of the different statistics observed in patients and healthy controls. The research question of the present contribution is whether it is possible to propose a universal guiding principle that helps to explain the statistical behaviour of time series of physiological variables in general, and which can predict how this behaviour degenerates with adverse circumstances such as ageing and/or chronic-degenerative disease.

In the present contribution, we focussed on control theory and the concept of homeostasis, where it is common to distinguish between regulated variables and effector variables, which perform very different functions in the corresponding regulation mechanisms, see Table 1. We studied a variety of different homeo-

static mechanisms: in Sect. 2, we investigated a simple mathematical model of a thermostat, in Sect. 3 we focussed on blood pressure homeostasis in healthy controls and diabetic patients, and in Sect. 4, we analysed time series related to body temperature homeostasis as a function of body weight. Regulated variables are explicitly controlled by the pre-programmed feedback loop, whereas the control of effector variables is implicit and may *self-organize* [80] by interacting with other effector variables and the associated regulated variable. In all the examples that we studied, in optimal conditions, we found that effector variables are more variable than the corresponding regulated variable, reflecting the adaptive function of the former and the narrow homeostatic range to which the latter is confined. In adverse conditions, these variables do not adequately play their distinctive roles in the homeostatic regulation mechanism, i.e. effector variables become less adaptive and the corresponding time series less variable, whereas control over regulated variables is increasingly lost, and consequently the variability of their time series increases. The appropriate framework to describe the degeneration of effector variables would appear to be the *loss of complexity* paradigm [31, 54–57], whereas regulated variables seem to degenerate according to the predictions of the *early-warning signals* paradigm [61–65], see Table 2. This may be a universal principle obeyed by all physiological variables of Table 1 and which may explain the rich phenomenology observed in the statistics of physiological variables.

The field of *fractal physiology* was first proposed after technological advances allowed to monitor physiological variables in a non-invasive and continuous way. We noted that it is more difficult to monitor regulated variables (such as BP and core temperature) than effector variables (such as HR and skin temperature), possibly due to the fact that effector variables mediate between the internal and the external

Table 2 Hypothesis of a general guiding principle to interpret the statistics of experimental time series of physiological variables depending on their role in the homeostatic control mechanism

	Homeostatic regulatory mechanism	
	Regulated variable	Effector variable(s)
	Synonyms: controlled or essential variable	Synonyms: supporting, non-regulated, regulating or self-organized variables
	e.g., *blood pressure (BP)*	e.g., *heart rate (HR)*
Youth health	Properties: controlled, stable, confined	Properties: adaptive, variable
	Framework: gaussian statistics	Framework: fractal physiology
	Small variance	*Large variance*
	Gaussian statistics	*Non-gaussian (fractal and long-tailed) statistics*
	Non-correlated (no memory)	*Correlated (memory)*
Ageing disease	Framework: early-warning signals	Framework: loss of complexity
	Increased variance	*Decreased variance*
	Increased non-gaussianity	*Increased gaussianity*

environment and thus are more readily accessible from outside, whereas regulated variables by definition are related to the *milieu intérieur* which is more difficult to access. Because of these practical reasons, the best studied time series tend to be effector-like variables, which might have introduced the bias that all physiological variables are highly variable and fractal-like, and leading to the impression that gaussian statistics and the concept of homeostasis are obstacles for the advancement of medicine. The main conclusion of the present contribution is that health needs both the fractal (adaptive) properties of effector variables and the gaussian (stability) characteristics of regulated variables to survive.

6 Conclusions

Technological advances allow to monitor an ever larger variety of physiological variables in a non-invasive and continuous way. It is not clear a priori how the time series of newly measured variables should behave statistically, or why a large variability of one variable represents a risk factor (e.g., blood pressure) whereas a large variability of another variable could be an indication of health (e.g., heart rate). In the present contribution, we argue that the role a particular variable plays in the homeostatic control mechanism, a regulated variable vs. an effector variable, determines the way the corresponding time series will behave statistically. With youth and health, a *regulated variable* such as blood pressure is maintained within a restricted homeostatic range with low variability, whereas *effector variables* and the corresponding *physiological responses* that adapt to perturbations from the inner and outer environment are characterized by a large variability. With ageing and/or chronic-degenerative disease, the capacity of these variables to play their respective roles is increasingly lost which is reflected by diminished statistical differences of the corresponding time series, or the regulated variable can become even more variable than the effectors variables. We demonstrated these concepts for a mathematical model of a thermostat, for experimental data of heart rate and blood pressure for healthy controls and diabetic patients, and for experimental data of skin temperature as a function of body weight. We make the prediction that other pairs of homeostatic variables, such as blood oxygen saturation vs. respiration dynamics, or blood glucose vs. insulin and glucagon concentrations, will follow similar patterns.

Acknowledgements We acknowledge the financial support from the Dirección General de Asuntos del Personal Académico (DGAPA) of the Universidad Nacional Autónoma de México (UNAM) grants IN106215, IV100116 and IA105017, from the Consejo Nacional de Ciencia y Tecnología (CONACYT) grants Fronteras 2015-2-1093, Fronteras 2016-01-2277 and CB-2011-01-167441, and the Newton Advanced Fellowship awarded to R.F. by the Academy of Medical Sciences through the UK Government's Newton Fund programme. We are grateful to Alejandro Frank and Christopher Stephens for fruitful discussions.

References

1. Modell H, Cliff W, Michael J, McFarland J, Wenderoth MP, Wright A (2015) A physiologist's view of homeostasis. Adv Physiol Educ 39:259–266
2. Bernard C (1957) Introduction à l'étude de la Médecine Expérimentale. J.B. Baillière et Fils, Paris; 1865 (English Translation by Greene HC, Dover, New York, NY, 1957)
3. Gross CG (2009) Three before their time: neuroscientists whose ideas were ignored by their contemporaries. Exp Brain Res 192:321–34
4. Cannon WB (1963) The wisdom of the body, revised and enlarged edition (first published 1939). W.W. Norton & Co, New York, NY
5. Wiener N (1961) Cybernetics or the control and communication in the animal and the machine, 2nd edn. MIT Press, Cambridge
6. Schneck DJ (1987) Feedback control and the concept of homeostasis. Math Model 9:889–900
7. Ramsay DS, Woods SC (2014) Clarifying the roles of homeostasis and allostasis in physiological regulation. Psychol Rev 121(2):225–247
8. Mangum CP, Towle DW (1977) Physiological adaptation to unstable environments. Am Sci 65:67–75
9. Moore-Ede MC (1986) Physiology of the circadian timing system: predictive versus reactive homeostasis. Am J Physiol 250(5 Pt 2):R737–R752
10. Bauman, DE (2000) Regulation of nutrient partitioning during lactation: homeostasis and homeorhesis revisited. In: Cronjé P, Boomker EA (eds) Ruminant physiology: digestion, metabolism, growth, and reproduction. CABI Pub, Wallingford, Oxon, pp 311–328
11. Bauman DE, Currie WB (1980) Partitioning of nutrients during pregnancy and lactation: a review of mechanisms involving homeostasis and homeorhesis. J Dairy Sci 63(9):1514–1529
12. Waddington CH (1957) The strategy of the genes; a discussion of some aspects of theoretical biology. Allen & Unwin, London
13. Waddington, CH (1968) Towards a theoretical biology; an IUBS symposium (International Union of Biological Sciences), vol. 1. Edinburgh University Press, Edinburgh (prolegomena)
14. Nicolaidis S (2011) Metabolic and humoral mechanisms of feeding and genesis of the ATP/ADP/AMP concept. Physiol Behav 104(1):8–14
15. Soodak H, Iberall A (1978) Homeokinetics: a physical science for complex systems. Science 201(4356):579–582
16. Mrosovsky N (1990) Rheostasis: the physiology of change. Oxford University Press, New York
17. Yates FE (1982) The 10th J. A. F. Stevenson memorial lecture. Outline of a physical theory of physiological systems. Can J Physiol Pharmacol 60(3):217–248
18. Yates FE (1994) Order and complexity in dynamical-systems - homeodynamics as a generalized mechanics for biology. Math Comput Model 19(6–8):49–74
19. Yates FE (2008) Homeokinetics/homeodynamics: a physical heuristic for life and complexity. Ecol Psychol 20(2):148–179
20. Chilliard Y (1986) Bibliographic review: quantitative variations and metabolism of lipids in adipose tissue and the liver during the gestation-lactation cycle. 1. In the rat. Reprod Nutr Dev 26(5A):1057–1103
21. Chilliard Y, Ferlay A, Faulconnier Y, Bonnet M, Rouel J, Bocquier F (2000) Adipose tissue metabolism and its role in adaptations to undernutrition in ruminants. Proc Nutr Soc 59(1):127–134
22. Kuenzel WJ, Beck MM, Teruyama R (1999) Neural sites and pathways regulating food intake in birds: a comparative analysis to mammalian systems. J Exp Zool 283(4–5):348–364
23. Selye H (1973) Homeostasis and heterostasis. Perspect Biol Med 16(3):441–445
24. Berntson GG, Cacioppo JT (2000) From homeostasis to allodynamic regulation. In: Cacioppo JT, Tassinary LG, Berntson GG (eds) Handbook of psychophysiology, vol 2. Cambridge University Press, Cambridge, pp 459–481

25. Berntson GG, Cacioppo JT (2007) Integrative physiology: homeostasis, allostasis, and the orchestration of systemic physiology. In: Cacioppo JT, Tassinary LG, Berntson GG (eds) Handbook of psychophysiology, vol 3. Cambridge University Press, Cambridge, pp 433–452
26. Sterling P (2004) Principles of allostasis: optimal design, predictive regulation, pathophysiology, and rational therapeutics. In: Schulkin J (ed) Allostasis, homeostasis and the costs of physiological adaptation. Cambridge University Press, New York, pp 17–64
27. Sterling P (2012) Allostasis: a model of predictive regulation. Physiol Behav 106(1):5–15
28. Sterling P, Eyer J (1988) Allostasis: a new paradigm to explain arousal pathology. In: Fisher S, Reason JT (eds) Handbook of life stress, cognition, and health. Wiley, Chichester, pp 629–649
29. Carpenter RHS (2004) Homeostasis: a plea for a unified approach. Adv Physiol Educ 28:S180–S187
30. Day TA (2005) Defining stress as a prelude to mapping its neurocircuitry: no help from allostasis. Prog Neuro-Psychopharmacol Biol Psychiatry 29:1195–1200
31. Goldberger AL, Rigney DR, West BJ (1992) Chaos and fractals in human physiology. Sci Am 262:34–41
32. Seely AJE, Macklem PT (2004) Complex systems and the technology of variability analysis. Crit Care 8:R367
33. Chaudhary B, Dasti S, Park Y, Brown T, Davis H, Akhtar B (1998) Hour-to-hour variability of oxygen saturation in sleep apnea. Chest 113(3):719–722
34. Churruca J, Vigil L, Luna E, Ruiz-Galiana J, Varela M (2008) The route to diabetes: loss of complexity in the glycemic profile from health through the metabolic syndrome to type 2 diabetes. Diabetes Metab Syndr Obes 1:3–11
35. Gardner JD, Young W, Sloan S, Robinson M, Miner PB Jr (2005) The fractal nature of human gastro-oesophageal reflux. Aliment Pharmacol Ther 22:823–830
36. Garrett DD, Samanez-Larkin GR, MacDonald SWS, Lindenberger U, McIntosh AR, Gradye CL (2013) Moment-to-moment brain signal variability: a next frontier in human brain mapping? Neurosci Biobehav Rev 37:610–624
37. Hausdorff JM (2005) Gait variability: methods, modeling and meaning. J NeuroEng Rehabil 2:19
38. Malik M et al (1996) Heart rate variability. Standards of measurement, physiological interpretation, and clinical use. Eur Heart J 17:354–381
39. Parati G, Ochoa JE, Lombardi C, Bilo G (2013) Assessment and management of blood-pressure variability. Nat Rev Cardiol 10:143–155
40. Papaioannou V, Pneumatikos I (2012) Fractal physiology, breath-to-breath variability and respiratory diseases: an introduction to complex systems theory application in pulmonary and critical care medicine. In: Andrade AO, Alves Pereira A, Naves ELM, Soares AB (eds) Practical applications in biomedical engineering, Chap 3. ISBN 978-953-51-0924-2, Published: January 9, 2013 under CC BY 3.0 license
41. Varela M, Calvo M, Chana M, Gomez-Mestre I, Asensio R, Galdos P (2005) Clinical implications of temperature curve complexity in critically ill patients. Crit Care Med 33(12):2764–2771
42. Fossion R, Stephens CR, García-Pelagio DP, García-Iglesias L (2017) Data mining and time-series analysis as two complementary approaches to study body temperature in obesity. In: Proceedings of DH'17, London, UK, July 02–05, 2017, p 5
43. Kelly G (2006) Body temperature variability (part 1): a review of the history of body temperature and its variability due to site selection, biological rhythms, fitness, and aging. Altern Med Rev 11(4):278–293
44. Kelly G (2006) Body temperature variability (part 2): masking influences of body temperature variability and a review of body temperature variability in disease. Altern Med Rev 12(1):49–62
45. Visnovcova Z, Mestanika M, Galac M, Mestanikova A, Tonhajzerova I (2016) The complexity of electrodermal activity is altered in mental cognitive stressors. Comput Biol Med 79:123–129

46. Yamagata M, Ikezoe T, Kamiya M, Masaki M, Ichihashi N (2017) Correlation between movement complexity during static standing and balance function in institutionalized older adults. Clin Interv Aging 12:499–503
47. Hu K, Ivanov PCh, Chen Z, Hilton MF, Stanley HE, Shea SA (2009) Non-random fluctuations and multi-scale dynamics regulation of human activity. Proc Natl Acad Sci USA 106(8):2490–2494
48. Ivanov PCh, Hu K, Hilton MF, Shea SA, Stanley HE (2007) Endogenous circadian rhythm in human motor activity uncoupled from circadian influences on cardiac dynamics. Proc Natl Acad Sci USA 104(52):20702–20707
49. Hu K, Van Someren EJW, Shea SA, Scheer FAJL (2009) Reduction of scale invariance of activity fluctuations with aging and Alzheimer's disease: Involvement of the circadian pacemaker. Proc Natl Acad Sci USA 106(8):2490–2494
50. Fossion R, Rivera AL, Toledo-Roy JC, Ellis J, Angelova A (2017) Multiscale adaptive analysis of circadian rhythms and intradaily variability: application to actigraphy time series in acute insomnia subjects. PLoS One 12(7):e0181762. https://doi.org/10.1371/journal.pone.0181762
51. Fossion R, Sáenz A, Zapata-Fonseca L (accepted) On the stability and adaptability of human physiology: Gaussians meet heavy-tailed distributions. INTERdisciplina (CEIICH-UNAM)
52. Hamilton JD (1994) Time series analysis. Princeton University Press, Princeton, NJ
53. Anderson A, Semmelroth D (2015) Statistics for big data for dummies. Wiley, Hoboken
54. Lipsitz LA, Goldberger AL (1992) Loss of complexity and aging: potential applications of fractals and chaos theory to senescence. JAMA 267:1806–1809
55. Goldberger AL (1992) Non-linear dynamics for clinicians: chaos theory, fractals and complexity at the bedside. Lancet 347:1312–1314
56. Goldberger AL, Amaral LAN, Hausdorff JM, Ivanov PCh, Peng C-K, Stanley HE (2002) Fractal dynamics in physiology: alterations with disease and aging. Proc Natl Acad Sci U S A 99(supp.1) 2466–2472
57. Goldberger AL (2006) Complex systems. Proc Am Thorac Soc 3:467–472
58. West BJ (2006) Where medicine went wrong: rediscovering the path to complexity. World Scientific, Singapore
59. West BJ (2010) Homeostasis and Gauss statistics: barriers to understanding natural variability. J Eval Clin Pract 16:403–408
60. West BJ (2013) Fractal physiology and chaos in medicine, 2nd edn. World Scientific, Singapore
61. Scheffer M (2001) Catastrophic shifts in ecosystems. Nature 413:591–596
62. Scheffer M, Bascompte J, Brock WA, Brovkin V, Carpenter SR, Dakos V et al (2009) Early-warning signals for critical transitions. Nature 461:53–59
63. Carpenter SR, Cole JJ, Pace ML, Batt R, Brock WA, Cline T et al (2011) Early warnings of regime shifts: a whole-ecosystem experiment. Science 332:1079–1082
64. Scheffer M, Carpenter SR, Lenton TM, Bascompte J, Brock W, Dakos V et al (2012) Anticipating critical transitions. Science 338:344–348
65. Scheffer M (2009) Critical transitions in nature and society. Princeton University Press, Princeton, NJ
66. Ashby WR (1960) Design for a brain: the origin of adaptive behaviour, 2nd edn. Chapman & Hall, London
67. Billman GE (2013) Homeostasis: the dynamic self-regulatory process that maintains health and buffers against disease. In: Sturmberg JP, Martin CM (eds) Handbook of systems and complexity in health, Chap. 10. Springer, New York, pp 159–170
68. Schelling TC (1978) Thermostats, lemons and other families of models. In: Micromotives and macrobehavior, Chap. 3. W. W. Norton & Company, London
69. Kitts JA (2005) Replication of Schelling's (1978) thermostat model in MatLab and R, webpage on modelling of social dynamics, University of Massachusetts, retrieved from http://socdynamics.org/id4.html on 21 May 2017

70. Rivera AL, Estañol B, Sentíes-Madrid H, Fossion R, Toledo-Roy JC, Mendoza-Temis J et al (2016) Heart rate and systolic blood pressure variability in the time domain in patients with recent and long-standing diabetes mellitus. PLoS One 11(2):e0148378. https://doi.org/10.1371/journal.pone.0148378
71. Rivera AL, Estañol B, Fossion R, Toledo-Roy JC, Callejas-Rojas JA, Gien-López JA et al (2016) Loss of breathing modulation of heart rate variability in patients with recent and long standing diabetes mellitus type II. PLoS One 11(11):e0165904
72. Schaffer F, McCraty R, Zerr CL (2014) A healthy heart is not a metronome: an integrative review of the heart's anatomy and heart rate variability. Front Physiol 5:article number 1040
73. Dawson TJ (1973) Primitive mammals. In: Whittow GC (ed) Comparative physiology of thermoregulation. Special aspects of thermoregulation. Chap. 1, vol III. Academic Press, New York, pp 1–46
74. Gisolfi CV, Mora F (2000) The hot brain. MIT Press, Cambridge
75. Romanovsky AA, Almeida MC, Garami A, Steiner AA, Norman MH, Morrison SF et al (2009) The transient receptor potential vanilloid-1 channel in thermoregulation: a thermosensor it is not. Pharmacol Rev 61:228–261
76. Schillaci G, Pucci G, Parati G (2011) Blood pressure variability: an additional target for antihypertensive treatment? Hypertension 58:133–135
77. Heikens MJ, Gorbach AM, Eden HS, Savastano DM, Chen KY, Skarulis MC et al (2011) Core body temperature in obesity. Am J Clin Nutr 93:963–967
78. Hynd PI, Czerwinski VH, McWhorter TJ (2014) Is propensity to obesity associated with the diurnal pattern of core body temperature? Int J Obes 38:231–235
79. Grimaldi D, Provini F, Pierangeli G, Mazzella N, Zamboni G, Marchesini G et al (2015) Evidence of a diurnal thermogenic handicap in obesity. Chronobiol Int 32:299–302
80. Seeley T (2002) When is self-organization used in biological systems? Biol Bull 202(3):314–318

Looking for Biomarkers in Physiological Time Series

Ana Leonor Rivera, Bruno Estañol, Adriana Robles-Cabrera, Juan C. Toledo-Roy, Ruben Fossion, and Alejandro Frank

Abstract From the point of view of Complexity Sciences, health can be considered as the state of dynamical balance between robustness and adaptability to the changes in the environment. We consider that any human disease can be found in physiological time series by deviations from this point that reflects the loss of this balance. Thus, it is possible to find biomarkers based on non-invasive physiological parameters that characterize the critical healthy state, and could help as early warnings auxiliary for clinical diagnoses of different diseases. In this work, we present a time-domain analysis using the distribution moments, autocorrelation

A. L. Rivera (✉) · R. Fossion
Instituto de Ciencias Nucleares, Universidad Nacional Autónoma de México, Mexico City, Mexico

Centro de Ciencias de la Complejidad (C3), Universidad Nacional Autónoma de México, Mexico City, Mexico

B. Estañol
Centro de Ciencias de la Complejidad (C3), Universidad Nacional Autónoma de México, Mexico City, Mexico

Laboratorio de Neurofisiología Clínica, Departamento de Neurología y Psiquiatría, Instituto Nacional de Ciencias Médicas y Nutrición "Salvador Zubirán", Mexico City, Mexico

A. Robles-Cabrera
Posgrado en Investigación Biomédica, Universidad Nacional Autónoma de México, Mexico City, Mexico

J. C. Toledo-Roy
Centro de Ciencias de la Complejidad (C3), Universidad Nacional Autónoma de México, Mexico City, Mexico

A. Frank
Instituto de Ciencias Nucleares, Universidad Nacional Autónoma de México, Mexico City, Mexico

Centro de Ciencias de la Complejidad, Universidad Nacional Autónoma de México, Mexico City, Mexico

Colegio Nacional, Mexico City, Mexico

L. Olivares-Quiroz, O. Resendis-Antonio (eds.), *Quantitative Models for Microscopic to Macroscopic Biological Macromolecules and Tissues*,
https://doi.org/10.1007/978-3-319-73975-5_6

function, Poincaré diagrams, and the spectral analysis of interbeat intervals and blood pressure time series for control subjects of different age and gender, and diabetic patients. As a preliminary result, a statistical significant difference was found between health and disease in the statistical moments of blood pressure and heart rate variability that can be proposed as biomarkers.

Keywords Physiological time series · Biomarkers · Non-invasive physiological parameters · Heart rate variability · Blood pressure variability

1 Introduction

New technological advances allow to monitor in real time a great variety of physiological observables in inexpensive non-invasive ways. The time series resulting from the continuous monitoring of these physiological observables are characterized by complex fluctuations that reflect the adaptive control mechanisms of the body. In order to understand these mechanisms a careful analysis of these physiological time series is indispensable. Here, we made a short-review of some relevant parameters of these analyses that can be used as biomarkers (characteristics of health).

Human health is determined by the functionality of its various organs and the interaction between them that can be understood from the physical point of view as a complex system [1–4]. Health can be considered as a condition that allows an adequate dynamic balance between its robustness (fixed values of the various parameters that characterize the organism in a deterministic way) and its adaptability (ability to respond to changes in the environment, which are stochastic). In this sense disease can be considered as a deviation from this state. This novel approach to the physics of complex systems is starting to be applied in medicine with the goal to find biomarkers (early warnings) that may aid in the diagnosis of various diseases [5–9].

Blood pressure and heart rate variability played an important role in the search for early warnings of various diseases [10–14]. This is because the cardiovascular system reflects not only the functioning of the heart, arteries, and veins but also the respiratory and central nervous systems. The autonomic nervous system modulates the cardiac cycle through central oscillations (generated by the respiratory and vasomotor centers) and peripheral oscillations (due to respiratory and arterial movements). Parasympathetic modulation decreases the heart rate and its contractility, while sympathetic modulation opposes these effects by regulating peripheral vasoconstriction [15]. The loss of this balance is associated with different diseases and aging. Due to this, there is an interest in the analysis of physiological time series both in the frequency domain and in the time domain to characterize the variability of heart rhythm and blood pressure obtained by non-invasive techniques [9, 11, 16–20]. In this work, we show some biomarkers in the time and frequency domains based on blood pressure and heart rate variability that allow to distinguish control subjects from patients with type 2 diabetes mellitus.

2 Hints for Biomarkers

2.1 Time-Series Analysis

Physiological time-series variability can be seen simply by a plot in the time domain (see Fig. 1a), with histograms (Fig. 1b), in an autocorrelation plot, Fig. 1c [21], and in a Poincaré plot, Fig. 1d [22, 23], a graph of the series with a lag of one point with itself. In the frequency domain, common plots are of the Fourier transform where it is defined a low-frequency region from 0.04 to 0.15 Hz and a high-frequency section that goes from 0.15 to 0.4 Hz (Fig. 1e), and a log-log plot, known as Power Spectral Density, Fig. 1f [20].

Quantitatively, the histograms are centered at the population average μ:

$$\mu = \frac{1}{N}\sum_{i=1}^{N} x_i, \tag{1}$$

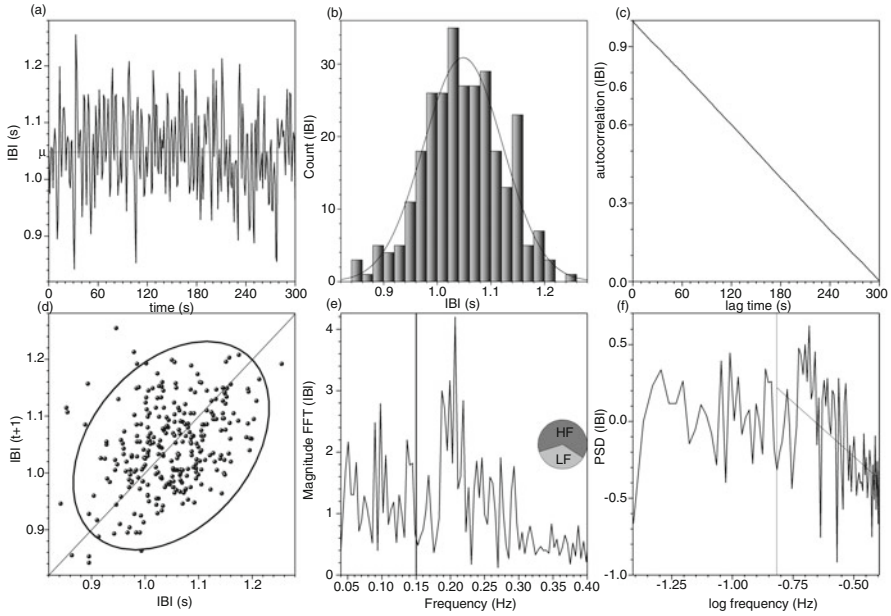

Fig. 1 Typical control Interbeat interval (IBI). IBI of a control male subject, 32 years old, in supine position for 5 min: (**a**) Time-series, vertical line is on the average value. (**b**) Histogram, continuous line corresponds to a normal distribution. (**c**) Autocorrelation function. (**d**) Poincaré plot, ellipse encloses 95% of the data. (**e**) Magnitude of the Fourier transform of the series; the circle shows the proportion between LF and HF areas. (**f**) Power spectral density (log-log of part label **e**). In (**e**) and (**f**), the horizontal line at 0.15 Hz corresponds to the separation between low (LF) and high frequency (HF)

where N is the number of data points recorded, summation is over all data points x_i. Another useful central distribution measure is the median m, a quantity not as strongly affected by outliers or large deviations in the data, which is defined as the central value after the observations have been sorted in increasing order. When the distribution is symmetric all central measures are equal ($\mu = m$). For IBI, m is inversely proportional to the average heart rate. The variability of the time-series is measured by the standard deviation (SD) of the values, that is the square root of the variance [24]:

$$\mathrm{SD} = \sqrt{\frac{1}{N-1}\sum_{i=1}^{N}(x_i - \mu)^2}. \tag{2}$$

SD reflects all the cyclic components responsible for variability in the recording period, gives the total power of spectral analysis, and is a measure of the "rigidity" of the distribution. It is important to be careful with SD, because it is not a well-defined statistical quantity due to its dependence on the length of the recording: SD increases with this length [25].

The symmetry of a distribution can be evaluated by the skewness, sk:

$$sk = \frac{1}{\mathrm{SD}^3}\,\frac{1}{N}\sum_{i=1}^{N}(x_i - m)^3. \tag{3}$$

Because a Gaussian (normal distribution) is a symmetric distribution, it has a null skewness.

Another useful measure of the distribution is the kurtosis, κ, a measure of how concentrated the data is around the mean, reflecting not only the "rigidity" of the time series but also its "planarity" [16]:

$$\kappa = \frac{1}{\mathrm{SD}^4}\,\frac{1}{N}\sum_{i=1}^{N}(x_i - m)^4 - 3. \tag{4}$$

For a Gaussian, the kurtosis is zero, while positive κ corresponds to a leptokurtic distribution (more peaked than a Gaussian) and negative κ describes a platykurtic one (flatter than a Gaussian).

Power spectral density (PSD) evaluates how power distributes as a function of frequency [26]. Three main spectral components are distinguished in a spectrum calculated from short-term recordings of 2–5 min (Fig. 1e) reflecting changes in autonomic modulations of the heart period [20, 27, 28]:

- Very low frequency (VLF), less than 0.04 Hz,
- Low frequency (LF), between 0.04 and 0.15 Hz,
- High frequency (HF), between 0.15 and 0.4 Hz.

VLF is affected by algorithms of baseline or trend removal, so it is common to ignore it in short recordings. It is common to report the quantity LF/HF [20, 29], the frequency radius r_f ($\sqrt{\mathrm{LF}^2 + \mathrm{HF}^2}$) [9] or the exponent in the power-law of the linear interpolation drawn through the log(power)-log(frequency), Fig. 1f [30]. Zero exponent is obtained from the flat spectrum of white noise (all frequencies are present with the same intensity in all the spectrum), non-zero values suggest data correlations, while a value close to 2 suggests there are primarily short-term correlations analogous to a random walk (Brownian motion or brown noise) [31]. One drawback of the power spectrum analysis is that it is highly influenced by non-stationarities in the data, making these exponent estimates sometimes unreliable [32].

Physiological time-series reflect the complex characteristics of the human body; thus, many non-linear aspects can appear on the series. Non-linear measurements of a time series variability can be evaluated through the Poincaré plot, in which each RR interval is plotted against the next RR interval. It is usual to draw in it, an ellipse that contents the 95% of the data and define using the dispersions SD1 (SD of points in the line perpendicular to the identity axis) and SD2 (SD of points in the identity axis), Fig. 1d [22, 23, 33]. The Poincaré plot is probably the most used and studied non-linear diagram for the analysis of the heart rate variability over short time periods because it is a measure of the parasympathetic nervous system activity [22]. It establishes the first-order correlation between the points of the series, and it quantifies the root mean square of successive differences (RMSSD), a traditional heart rate variability metrics [34]. For white noise (stochastic dynamics), SD1 = SD2, thus the 95% of the data is on a circle, in the case of a complete deterministic signal SD1 = 0 (the data is almost on a line). Another non-linear parameter is the approximate entropy that measures the "transmission of information" on the signal, given as [35–38]:

$$S = -\sum_{i=1}^{N} x_i \log x_i. \tag{5}$$

Other parameters that have been used to measure non-linear properties of physiological time-series variability include $1/f$ scaling of Fourier spectra [25, 30, 38, 39], methods derived from chaos theory and fractal analysis, including scaling exponents derived from the power spectrum [31, 40, 41], H scaling exponent, Coarse Graining Spectral Analysis (CGSA) [42], detrended fluctuation analysis DFA [32, 43, 44], empirical mode decomposition [45], and non-linear mode decomposition [46].

2.2 *Ising Model*

One of the most famous physical models that exhibits a phase transition is the Ising model [47], in which the magnetization of a material as a function of temperature is

modeled as a 2D lattice of spin sites that can adopt one of two orientations (which can be thought as up or down). The net magnetization of the lattice, M, is determined by the degree of alignment of the sites: when most sites point the same way, M is high and the material acts as a magnet; when no alignment direction dominates, the material is not magnetized. The value and statistical behavior of M are dictated by a single parameter, the temperature T of the model, which determines the balance between alignment and random orientation of spin sites. What's interesting is that the model exhibits two distinct dynamical phases separated by a phase transition that occurs at a very well-defined critical temperature T_c. This phase transition has been studied extensively both analytically and through numerical simulations of the lattice.

Figure 2 offers an overview of the main characteristics of this paradigmatic model of phase transitions. In the low-temperature regime, that is, at temperatures below Tc (panels in the left column of Fig. 2), the natural tendency of the spin sites to align with their neighbors wins over thermal fluctuations and most of the spins remain aligned in the same orientation (top-left panel). In this ordered phase, the magnetization remains very high, fluctuating in time close to its maximum value of 1 (center-left panel). The power spectrum (bottom-left panel) confirms that these fluctuations are uncorrelated (i.e. random), as indicated by a flat power spectrum. In the high-temperature regime at temperatures above Tc (right-most column of Fig. 2), thermal fluctuations dominate, and the sites can't maintain any large-scale alignment and the lattice has a noise-like appearance (top-right panel). This is the stochastic phase, in which random thermal fluctuations dictate the dynamics. The net magnetization fluctuates very close to zero (center-right panel), and the power spectrum is also consistent with random noise (bottom-right panel). Finally, near the critical temperature T_c (center column of Fig. 2) rich structure appears in the spin lattice, with "islands" of similarly aligned spins forming and disappearing over time, this occurs at many different spatial scales (top-center panel). The magnetization time series is no longer stationary, instead exhibiting temporary trends that result in the magnetization wandering across the whole interval from no net magnetization to almost full magnetization, never remaining near a fixed value for long (center panel). The power spectrum confirms this behavior (bottom-center panel): the fluctuations follow a very clear power-law, as indicated by the straight line in this log-log PSD plot. This means that the time correlation length is maximized: the behavior of the time series exhibits memory to very long timescales.

This phase transition can also be understood by computing several statistical parameters and studying their behavior as a function of temperature. Because their behavior changes as the critical point is approached, these parameters act as early-warnings of the phase transition, and can be used as indicators of the proximity to the critical point. In the case of the Ising model, the moments of the distribution, the lag-1 autocorrelation and the PSD crossover frequency have been shown to be robust early-warnings [47].

Figure 3 shows the net magnetization and several statistical properties of its time series that act as early warnings as a function of temperature. The shaded region indicates the phase transition. As can be quickly glanced, the values of

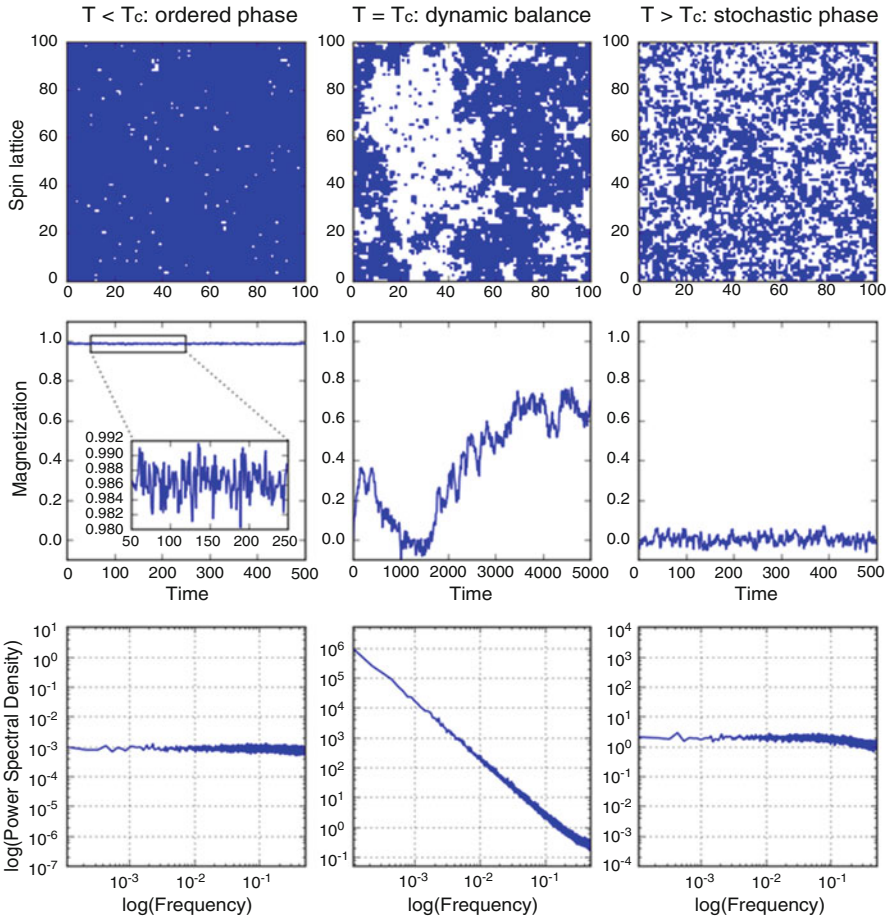

Fig. 2 Ising model. Results for numerical simulations of the model for temperatures below T_c (left-most column), near T_c (center column), and above T_c (right-most column), which show two distinct dynamical phases separated by a critical point. The rows of panels show the 2D state of the lattice (top row), where the colors represent the spin-up and spin-down orientation, the magnetization time series for each case (middle row), and the power spectral density plot obtained through Fourier analysis (bottom row)

these parameters change abruptly as the critical point is approached. The first three statistical moments of the time series, the standard deviation (the square root of the variance; panel b), the skewness (panel c) and the kurtosis (panel d) all show that the distribution is essentially Gaussian (skewness and kurtosis close to zero) with a low variance at low or high temperatures, but changes to a high-variance skewed and leptokurtic (high kurtosis) distribution near the critical point. The lag-1 autocorrelation (panel e), an indicator of the short-term memory of the time series, approaches its maximum value of 1 near the critical point, and tends towards zero

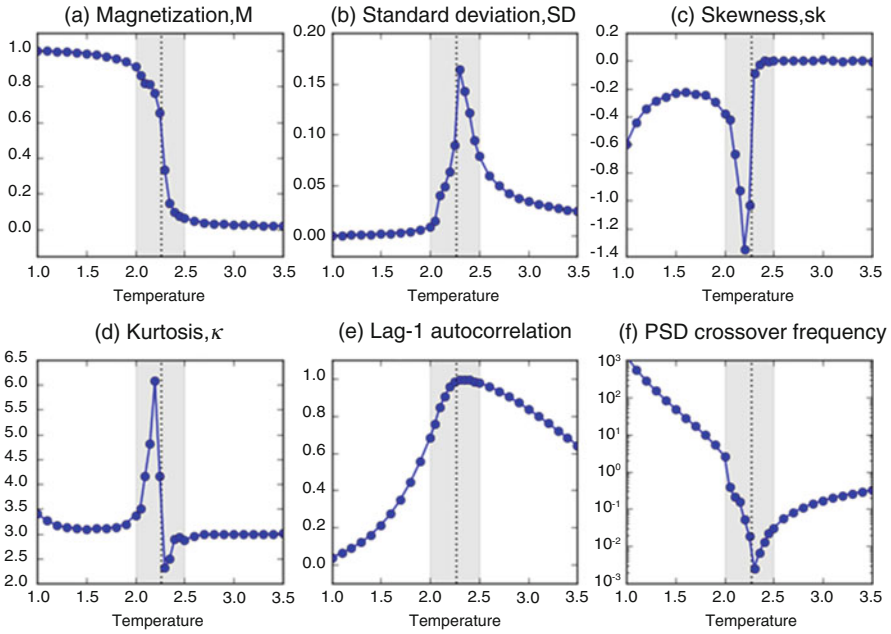

Fig. 3 Early warnings of the Ising model. The net magnetization of the lattice and several associated statistical properties shown as function of temperature. The shaded region indicates the phase transition, while the dotted vertical line is at the theoretical value of T_c. (**a**) Net magnetization of the lattice, (**b**) standard deviation, (**c**) skewness, (**d**) kurtosis, (**e**) lag-1 autocorrelation, and (**f**) PSD crossover frequency

towards low or high temperatures. Finally, the PSD crossover frequency (panel f), which is defined as the frequency in the power spectrum at which the power-law behavior transitions to random noise, and which is an indicator of long-range memory, shows that as the critical point is approached the power-law behavior extends all the way to very short frequencies, indicating that correlations have a very long range.

2.3 Kuramoto Model

Another simple model that exhibits a phase transition and showcases the competition between ordered and stochastic dynamics is the Kuramoto model [48], a model of synchronization that has found successful application in neurosciences [49]. In its original formulation, it consists of N coupled harmonic oscillators, each having a time-dependent phase $\theta_i(t)$, and fixed natural frequency ω_i (chosen randomly from a fixed distribution). The oscillators are coupled, with the interaction strength determined by the *coupling constant* K. From the values of the phases at any given

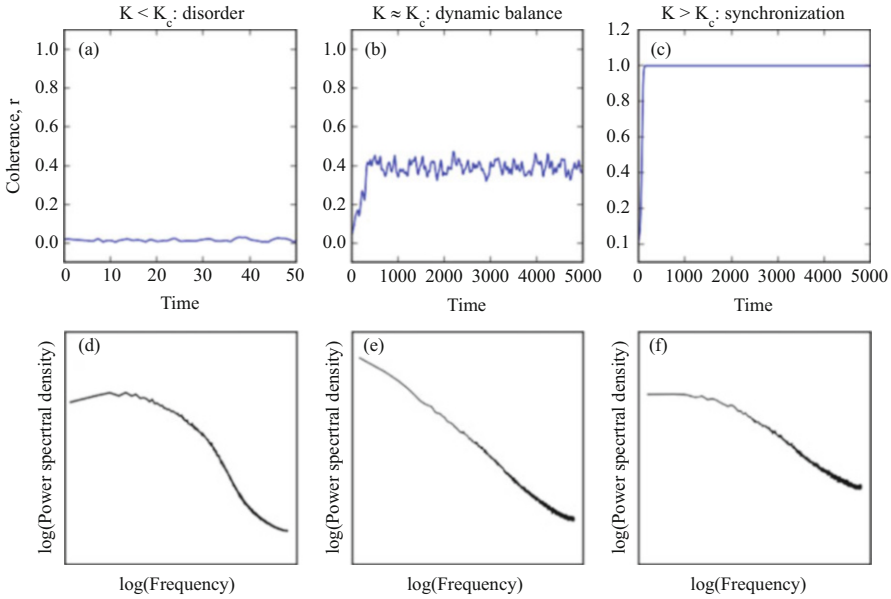

Fig. 4 Kuramoto model. Coherence time series (top row) and power spectra (bottom row) for the Kuramoto model for three different regimes as determined by the value of the coupling constant K: left-hand panels (**a**, **d**) unordered phase, $K < K_c$; middle panels (**b**, **e**) phase transition; $K \approx K_c$; and right-hand panels (**c**, **f**) synchronized phase, $K > K_c$

instant in time one can compute the *coherence* parameter r, which measures the strength of synchronization between the oscillators at that point in time. As with the net magnetization in the Ising model, the coherence r is an order parameter, measuring the degree to which ordered dynamics dominate. When the Kuramoto is simulated for a range of values of the coupling constant K, a phase transition is discovered at a well-defined value K_c. The top row of Fig. 4 shows this transition graphically. When the coupling is weaker than K_c, the oscillators fail to maintain synchronization and each oscillator simply vibrates at its natural frequency, and the global coherence remains low (Fig. 4a). When the coupling is stronger than the critical value, the oscillators very quickly and spontaneously synchronize, vibrating in phase despite having different natural frequencies; thus, coherence remains very near its maximum value of 1, indicating total synchronization (Fig. 4c). Near the critical point K_c, the oscillators vibrate in a dynamic balance between disorder and synchronization, with the coherence r exhibiting large oscillations around a value. The power spectra in the bottom row of Fig. 4 show that near the critical value a power-law is formed, very much like what we saw in the Ising model.

Furthermore, as with the Ising model, it is possible to find computable parameters that provide early warnings of the phase transition. Apart from the apparition of a power-law in the power spectrum, the statistical moments of the distribution and the lag-1 autocorrelation all display notable changes as the phase transition is

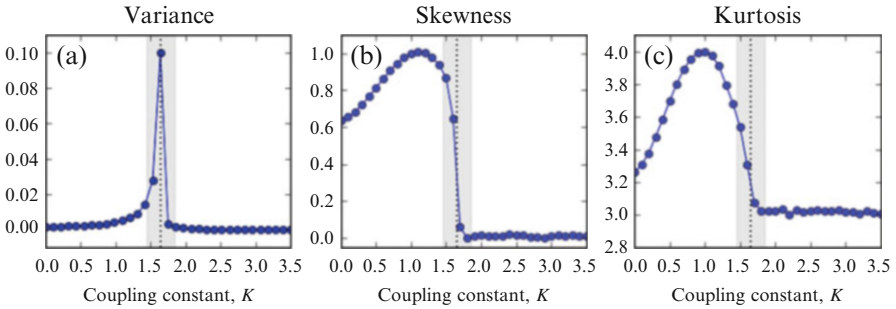

Fig. 5 Early warnings of the Kuramoto model. Statistical moments of the coherence time series as a function of the coupling constant K: (**a**) variance, (**b**) skewness, and (**c**) kurtosis. Shaded region indicates the phase transition, while the dotted vertical line is at the theoretical critical value K_c

approached. In Fig. 5 the variance (square of SD), the skewness and the kurtosis of the time series of the coherence parameter r are shown as a function of the coupling constant K. As before, the shaded regions indicate the region of the phase transition, with the dotted vertical line indicating the theoretical critical value K_c. From this figure, it is clear that the behavior of these statistical moments trace the phase transition.

These two models of phase transitions between ordered and stochastic regimes share many properties, which suggests that some of these properties are universal and should be found in a wide range of systems exhibiting marked shifts in their dynamics. In particular, these models indicate that the proximity to the critical point can be determined by measuring suitable early warnings of the system, such as the statistical moments (mean, standard deviation, skewness, and kurtosis), the autocorrelation function, the lag-1 autocorrelation, and the presence of a power-law in the power spectral density. Our hypothesis is that these parameters can be used as biomarkers of health.

3 Biomarkers of Heart Rate Variability

Heart beat depends on time showing non-linear, non-periodic features due to long-range correlations and fractal aspects that can be destroyed under pathological conditions [50] and with advanced aging [51]. Although cardiac activity is due to various pacemaker tissues, heart rate and rhythm are largely under the control of the autonomous nervous system. The parasympathetic influence on heart rate is mediated via release of acetylcholine by the vague nerve while the sympathetic influence on heart rate is mediated by release of epinephrine and norepinephrine [18]. Efferent sympathetic and vagal activities directed to the sinus node can be modulated by central (e.g., vasomotor and respiratory centers) and peripheral (e.g., oscillation in arterial pressure and respiratory movements) oscillators [28].

These oscillators generate rhythmic fluctuations that allow physicians to infer the state and function of the central oscillators, the sympathetic and vagal efferent activity, humoral factors, and the sinus node. A way to evaluate these fluctuations is analyzing the Heart Rate Variability (HRV) by non-invasive measures as the interbeat interval (IBI) providing a method for understanding cardiac autonomic control [11] and the sympathetic/vagal balance [18]. While efferent vagal activity is a major contributor to the HF component [20, 28, 29], LF is considered by some [28] as a marker of sympathetic modulation and by others as a parameter that includes both sympathetic and vagal influences [20]. Spectral analysis of HRV during controlled breathing test shows the respiratory modulation of the sinus node [9]: parasympathetic modulation decreases the heart rate and cardiac contractility, whereas activity of the sympathetic branch opposes these effects and regulates peripheral vasoconstriction [52].

HRV acquired clinical relevance as a biomarker since Horn and Lee showed that in fetal distress alterations in IBI occur before any other appreciable change happens in the heart rate [53]. Moreover, HRV is a strong and independent predictor of mortality following an acute myocardial infarction [54, 55], and has been used as an early warning sign of diabetic neuropathy [16, 19], cardiovascular disease [56], and aging [57–59]. Recently, a meta-review was published that shows a gender difference in heart rate variability, in particular, women have a statistically significant lower total spectral power than men [60]. Quantification of cardiovascular function can be performed through standard cardiovascular reflex tests [18, 38, 61, 62] or HRV. Cardiovascular reflex test is more difficult to register and it needs the active collaboration of patients (that is not always possible), but there are a set of normal values of the expected responses accepted for clinical assessment [18]. On the other hand, HRV is a simple technique to obtain experimentally, that can be applied to any patient independently of age, gender, and disease, however, there are not range of values completely accepted as the standard of health [11].

Analysis of electrocardiogram registers from Fantasia database of Physionet [39] showsn differences on the HRV between young and old people, moreover male and female young subjects are distinct (Fig. 6). Previous works showed that the standard deviation change between young and elderly subjects [32], but they do not explored other statistical moments (average, median, skewness, and kurtosis) that are also statistically significant different for young and elderly considering the gender of the control subjects (see Fig. 7). We consider that 2 distributions are statistically distinct if the p-value is less than 0.05.

HRV records from female young subjects have less variability and are more rigid compared to the ones from young men, however, elderly controls do not show gender dependence. Young men have distributions with high variability, non-symmetric and platykurtic, young women exhibit less variability and gain symmetry, while older men and women go to more Gaussian distributions. There is a statistically significant difference between young female and male subjects in SD1 from the 95% ellipse of the Poincaré plot. Entropy for young male, female, and elderly women has similar values, but the difference for elderly men is statistically significant. This may be due to hormonal regulation of HRV, that is loss in older

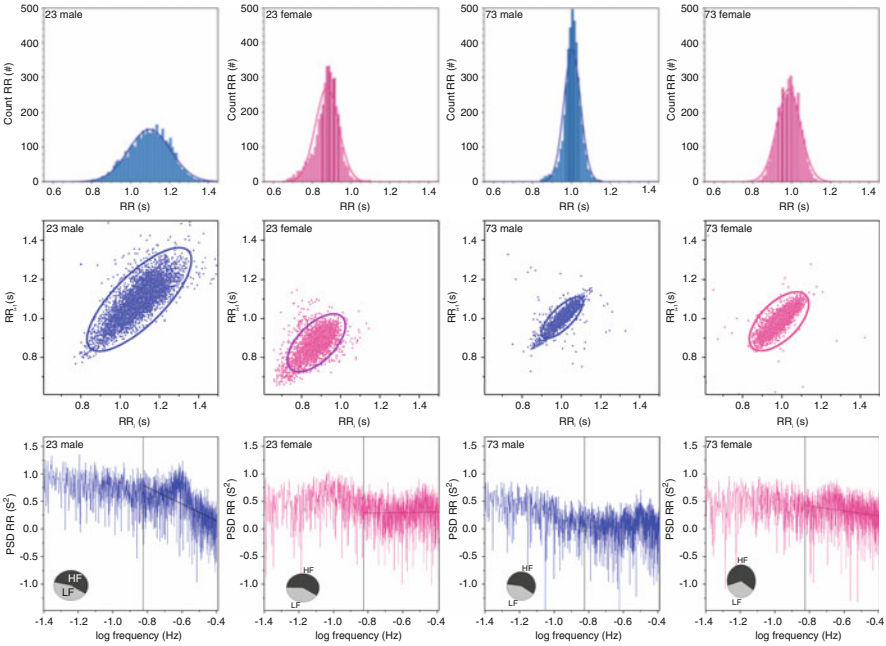

Fig. 6 HRV of control subjects that are watching the movie fantasia in seated position [39]. Histograms with a line that corresponds to a Gaussian distribution (upper panels), Poincaré plots (middle panels) and PSD with a vertical line dividing low from high frequency regions (lower panels). Circular onsets on lower panel correspond to the proportion of LF and HF. From left to right are data from a young man 23 years old, a young female 23 years old, an elderly man 73 years old, and a woman 73 years old

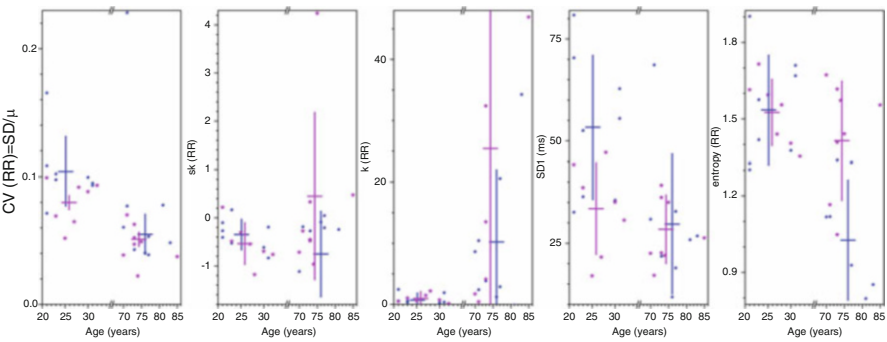

Fig. 7 Analysis of HRV of all the subjects on Fantasia database [39]. Blue dots are data from male and pink stars from female control subjects. From left to right: coefficient of variation, i.e. ratio of standard deviation and average, skewness, kurtosis, SD1 of the Poincaré ellipse and entropy

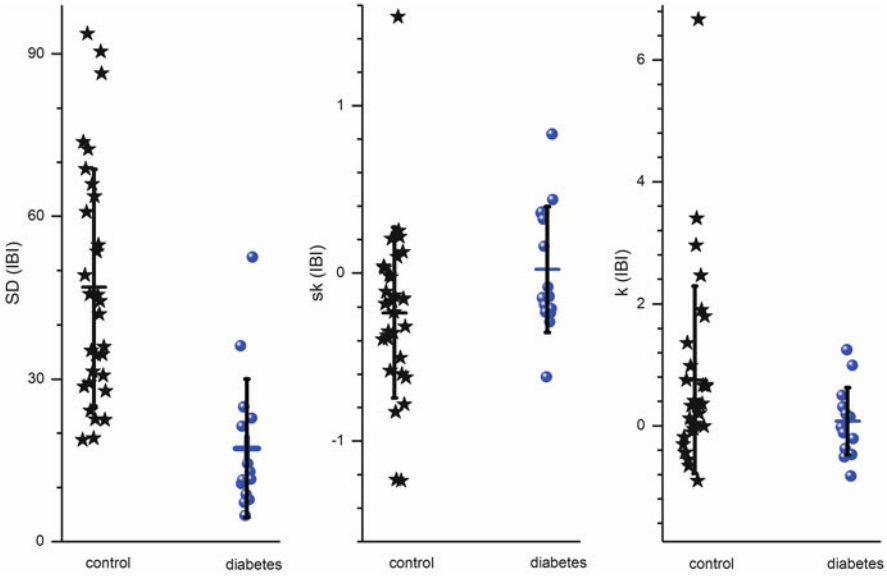

Fig. 8 Analysis of HRV of all the subjects on database from Estañol et al. [65]. Black stars are data from control subjects and blue dots from long-standing diabetes mellitus type 2 patients on supine position for 5 min. Cross-lines correspond to average ± standard deviation of each group. Standard deviation (left hand panel), skewness (middle panel), and kurtosis (right hand panel) are statistically significant different between control and patients with diabetes mellitus type 2 [16]

women and is not present in men. These are signs of a phase transition from control young to elderly subjects.

IBI's histograms for control subjects (Fig. 1b) have a non-Gaussian distribution with a marked asymmetry [63]. It has been proposed that these tails to the left or to the right reflect, respectively, the acceleration or deceleration capacity of the heart rate as an approximate distinction of the vagal and sympathetic effects on the cardiac modulations [64]. Previously we have analyzed also IBI for diabetic patients [9, 16] showing that for long-standing type 2 diabetes mellitus patients, SD of the IBI detrended signal diminishes (heart rate signal becomes more "rigid"), skewness with respect to the median approaches zero (signal fluctuations gain symmetry), and kurtosis goes to zero (fluctuations concentrate around the median); thus, diabetes produces not only a rigid heart rate, but also Gaussian distributions (see Fig. 8).

As we show in Sect. 2, the transition between the two different dynamics (stochastic and deterministic) that govern the Ising and Kuramoto models is characterized by high SD, non-symmetric and leptokurtic distributions. In the case shown in Fig. 8, control records or heart rate variability (IBI) has higher standard deviation, is less symmetric with larger kurtosis than records from diabetic patients. This suggests that control represents balance between robustness (deterministic dynamics) and adaptability (stochastic behavior). Figure 7 shows also this change of regime when the subjects become older.

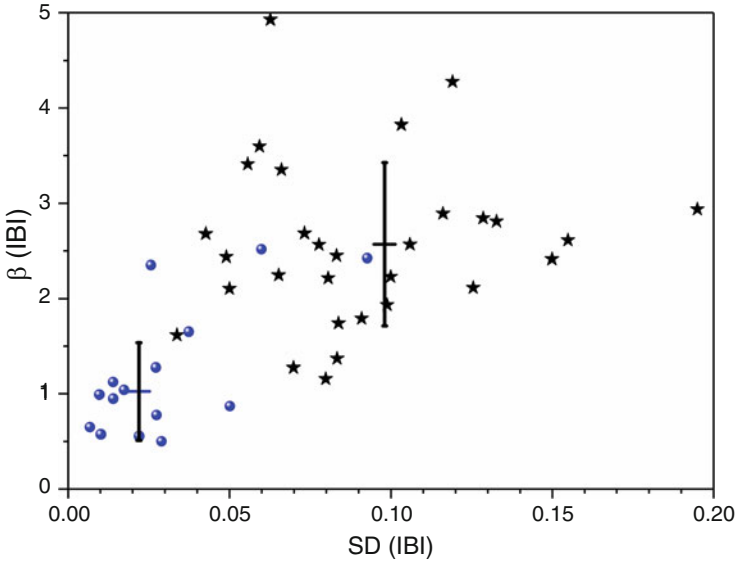

Fig. 9 Biomarker of the respiratory peak as function of the standard deviation for control subjects (black stars) and long-standing diabetes mellitus type 2 patients [9]

If control subjects are breathing in a controlled way at a resonant frequency of 0.1 Hz, periodic modulations are induced due to the baroreceptor reflex in the cardiac rhythm [66]. This produces in the Fourier transform of the IBI signal, a narrow band around 0.1 Hz. To quantify the strength of these effect, it can be used the Respiratory Peak (RP) as the power in the frequency band centered at the peak in the 0.1 Hz region spanning from the starting rising position to the end decreasing point (generally from 0.086 to 0.113 Hz). In order to quantify the relative importance of the cardio-respiratory coupling in a way that is not sensitive to the total power in the spectrum, is defined the biomarker $\beta\left(\frac{\mathrm{RP}}{(\mathrm{LF}+\mathrm{HF})}\right)$ [9]. As seen in Fig. 9 this biomarker allows to distinguish control subjects from long-standing diabetes mellitus type 2 patients.

4 Biomarkers of Blood Pressure Variability

Blood pressure shows less variability than the heart rate (see Fig. 10), and while IBI's histograms are more peaked as DM evolves, SBP's histograms are more peaked for control subjects than for long-standing DM patients. Previously [16] we found that there is no statistically significant difference on SBP's SD and κ, however, skewness goes from positive skew (asymmetric for control subjects) to zero (symmetric for long-standing diabetes mellitus patients).

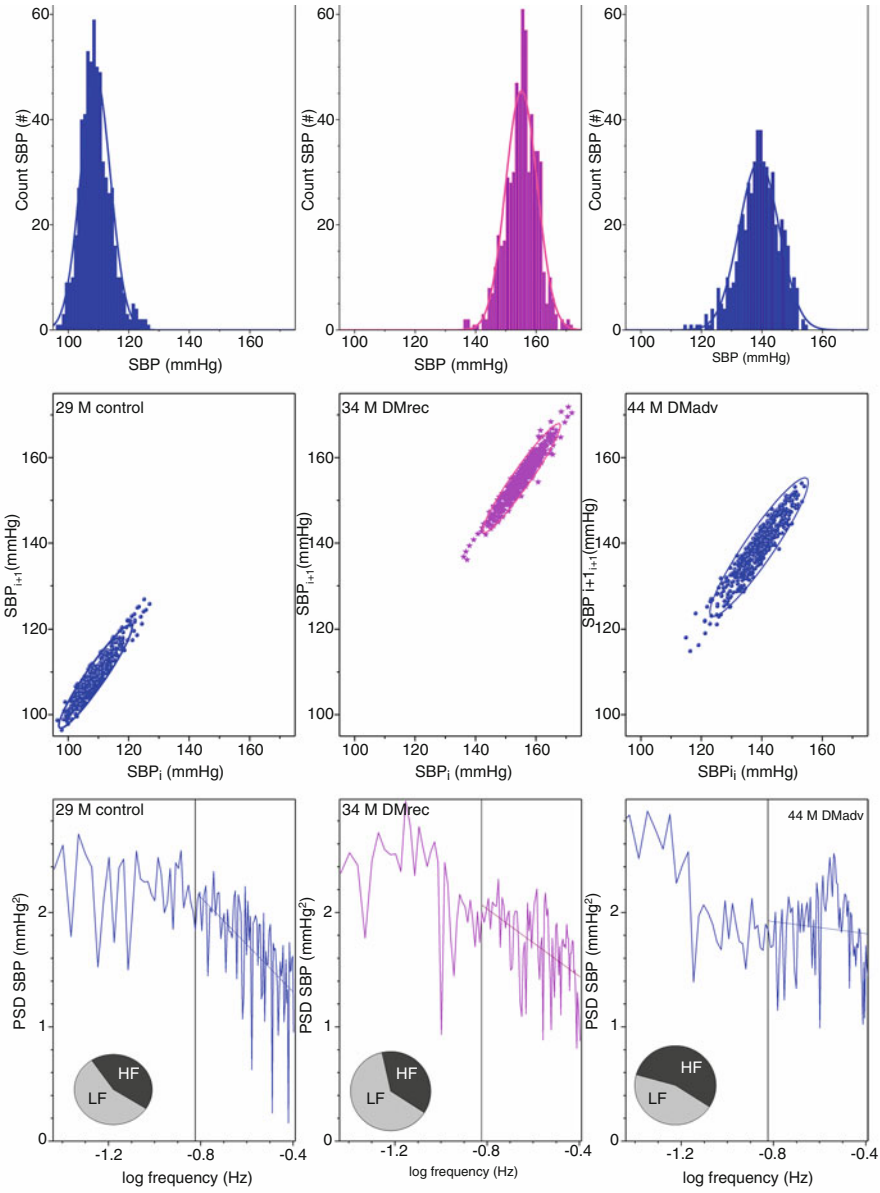

Fig. 10 Systolic blood pressure of subjects standing up during 5 min [16]. Histograms, line corresponds to Gaussian distribution (upper panels) Poincaré plots (middle panels) and PSD with a vertical line dividing low from high frequency regions (lower panels). Circular onsets on lower panel correspond to the proportion of LF and HF. Control subjects (left-hand panel), recently diagnosed type 2 diabetes mellitus patients (middle panel) and long-standing diabetic patient

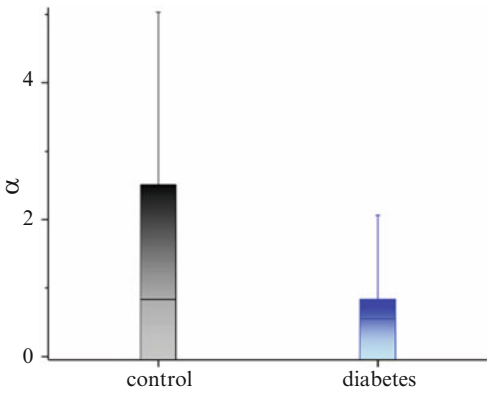

Fig. 11 Biomarker of blood pressure and heart rate variability. Box-plot of the α biomarker for control subjects (black) and long-standing diabetes mellitus type 2 patients (blue) under clinostatism test. Central line is the median, box is one standard deviation and line ends in outliers of the distribution [16]

Under controlled breathing, SBP has symmetric distributions for DM patients, while control subjects have non-zero skewness. Under supine and standing-up positions, SBP's kurtosis goes from leptokurtic (control subjects) to platykurtic for diabetic patients. This result agrees with experiments in dogs with sino-aortic denervation and baroreceptor's damage, where the vagal-sympathetic baroreceptor of the SBP answer is retarded, a platykurtic SBP distribution results [52, 53]. The loss of balance between vagal and sympathetic effects on the baroreceptor is also reflected in the variation of the skewness with respect to the median.

The change of vague and sympathetic modulations of the blood pressure variability as diabetes evolves is also evident on the slope of the PSD in the low frequency region, that changes for a highly correlated behavior (control) to a random one (diabetes), as seen in Fig. 11. This may be due to a progressive decrease of parasympathetic and sympathetic activity to the blood vessels as diabetes evolves.

Interestingly, whereas HRV appears to be a protective health factor, that in health can be considered to be in a "critical point," as we have shown, blood pressure variability is a risk factor [16, 67, 68].

5 Biomarkers Compose from Blood Pressure and Heart Rate Variability

Successive moments of SD, sk and κ are required to describe fine details of variability of a signal so we use $\sqrt{\left(\frac{SD}{m}\right)^2 + sk^2 + \kappa^2}$, which could be interpreted as a sort of "distance" in SD-sk-κ space. As seen in previous sections, this parameter is larger for IBI records of control subjects compared to diabetic patients, while it is smaller for SBP of the same subjects. Thus, a useful biomarker that quantifies simultaneously heart rate and blood pressure variability can be defined as [16]:

$$\alpha = \frac{\left[\sqrt{\left(\frac{\mathrm{SD}}{m}\right)^2 + \mathrm{sk}^2 + \kappa^2}\right]_{\mathrm{IBI}}}{\left[\sqrt{\left(\frac{\mathrm{SD}}{m}\right)^2 + \mathrm{sk}^2 + \kappa^2}\right]_{\mathrm{SBP}}}. \tag{6}$$

This parameter can differentiate control from diabetic patients under clinostatism and controlled breathing test with a statistical significance of $p < 0.05$ (see Fig. 11). It is important to notice that control subjects have a larger variability of α than long-standing diabetes mellitus patients because the last ones have more rigid and symmetric distributions.

6 Conclusion

Reliable non-invasive biomarkers of HRV in the time domain are statistical moments like standard deviation, kurtosis, and skewness with respect to the median. These biomarkers are sign of dysfunction of the vagal and sympathetic modulation of the autonomic nervous system.

As we have seen in the numerical models of Ising (Figs. 2 and 3) and Kuramoto (Figs. 4 and 5) on the critical point, distribution has the higher values of SD (high variability), non-zero sk (asymmetric), and non-zero k (leptokurtic). Here, considering even outliers, we show that for all the young male control subjects, HRV non-invasively measured by IBI records have high SD, not symmetric and leptokurtic distributions (Figs. 6 and 7), going to more Gaussian ones when subjects become older (Fig. 7) or are ill with diabetes (Fig. 8). Moreover, PSD can be adjusted by a line in the LF region of the IBI records of young men (Fig. 6) indicating a scale-invariant behavior, that is loss at elderly subjects (where the PSD is closer to random distributions), or as diabetes evolves (Fig. 8). This indicates that young male control subjects have a HRV characteristic of a state of balance (between rigidity and adaptability) that is loss with aging and illness. In contrast, blood pressure shows less variability than the heart rate (see Fig. 10), showing a change of symmetry from positive skew (for control subjects) to zero (symmetric for long-standing diabetes mellitus patients). This reflects the loss of balance between vagal and sympathetic effects on the baroreceptor, supported by the change of the PSD LF slope from a highly correlated behavior in control to a random one in diabetic patients (Fig. 11).

Acknowledgements Thanks to J. A. López-Rivera for grammatical review. Financial funding for this work was supplied by Dirección General de Asuntos del Personal Académico from Universidad Nacional Autónoma de México (UNAM) grants PAPIIT IN106215, IV100116 and IA105017; grants 2015-02-1093, 2016-01-2277 and CB-2011-01-167441 from Consejo Nacional de Ciencia y Tecnología (CONACyT), and the Newton Advanced Fellowship awarded to RF by the Academy of Medical Sciences through the UK Government's Newton Fund program. The funders had no role in study design, data collection and analysis, decision to publish, or preparation of the manuscript. The authors do not have any conflict of interest.

References

1. Porta A, Bari V, Ranuzzi G et al (2017) Assessing multiscale complexity of short heart rate variability series through a model-based linear approach. Chaos Interdiscip. J Nonlinear Sci 27:093901
2. Valenza G, Citi L, Garcia RG et al (2017) Complexity variability assessment of nonlinear time-varying cardiovascular control. Sci Rep 7:42779. https://doi.org/10.1038/srep42779
3. Alberga D, Mangiatordi GF (2016) Understanding complexity of physiology by combined molecular simulations and experiments: anion channels as a proof of concept. J Physiol 594:2777–2778. https://doi.org/10.1113/JP272001
4. Raoufy MR, Ghafari T, Mani AR (2017) Complexity analysis of respiratory dynamics. Am J Respir Crit Care Med 196:247–248. https://doi.org/10.1164/rccm.201701-0026LE
5. Calvani R, Picca A, Cesari M et al (2017) Biomarkers for sarcopenia: reductionism vs. complexity. Curr Protein Pept Sci. https://doi.org/10.2174/1389203718666170516115422
6. Tippett LJ, Waldvogel HJ, Snell RG et al (2017) The complexity of clinical Huntington's disease: developments in molecular genetics, neuropathology and neuroimaging biomarkers. In: Neurodegenerative diseases. Springer, Cham, pp 129–161
7. de la Torre-Luque A, Bornas X, Balle M, Fiol-Veny A (2016) Complexity and nonlinear biomarkers in emotional disorders: a meta-analytic study. Neurosci Biobehav Rev 68:410–422. https://doi.org/10.1016/j.neubiorev.2016.05.023
8. Dias LM, Thodima V, Friedman J et al (2016) Cross-platform assessment of genomic imbalance confirms the clinical relevance of genomic complexity and reveals loci with potential pathogenic roles in diffuse large B-cell lymphoma. Leuk Lymphoma 57:899–908. https://doi.org/10.3109/10428194.2015.1080364
9. Rivera AL, Estañol B, Fossion R et al (2016) Loss of breathing modulation of heart rate variability in patients with recent and long standing diabetes mellitus type II. PLoS One 11:e0165904. https://doi.org/10.1371/journal.pone.0165904
10. Medenwald D, Swenne CA, Loppnow H et al (2017) Prognostic relevance of the interaction between short-term, metronome-paced heart rate variability, and inflammation: results from the population-based CARLA cohort study. Europace 19:110–118. https://doi.org/10.1093/europace/euv333
11. Berntson GG, Thomas Bigger J, Eckberg DL et al (1997) Heart rate variability: origins, methods, and interpretive caveats. Psychophysiology 34:623–648. https://doi.org/10.1111/j.1469-8986.1997.tb02140.x
12. Malik M (1996) Heart rate variability. Ann Noninvasive Electrocardiol 1:151–181. https://doi.org/10.1111/j.1542-474X.1996.tb00275.x
13. Whittle J (2017) Blood pressure variability predicts clinical outcomes: now what? Hypertension 69:584–586. https://doi.org/10.1161/HYPERTENSIONAHA.116.08806
14. Dolan E, O'Brien E (2010) Blood pressure variability: clarity for clinical practice. Hypertension 56:179–181. https://doi.org/10.1161/HYPERTENSIONAHA.110.154708
15. Levy MN (1971) Sympathetic-Parasympathetic interactions in the heart. Circ Res 29:437–445. https://doi.org/10.1161/01.RES.29.5.437
16. Rivera AL, Estañol B, Sentíes-Madrid H et al (2016) Heart rate and systolic blood pressure variability in the time domain in patients with recent and long-standing diabetes mellitus. PLoS One 11:e0148378. https://doi.org/10.1371/journal.pone.0148378
17. Parati G, Di Rienzo M, Mancia G (2000) How to measure baroreflex sensitivity: from the cardiovascular laboratory to daily life. J Hypertens 18:7–19
18. Task Force of the European Society of Cardiology the North American Society of Pacing Electrophysiology (1996) Heart rate variability. Circulation 93:1043–1065. https://doi.org/10.1161/01.CIR.93.5.1043
19. Pagani M, Lombardi F, Guzzetti S et al (1986) Power spectral analysis of heart rate and arterial pressure variabilities as a marker of sympatho-vagal interaction in man and conscious dog. Circ Res 59:178–193

20. Akselrod S, Gordon D, Ubel FA et al (1981) Power spectrum analysis of heart rate fluctuation: a quantitative probe of beat-to-beat cardiovascular control. Science 213:220–222
21. Acharya UR, Joseph KP, Kannathal N et al (2006) Heart rate variability: a review. Med Biol Eng Comput 44:1031–1051. https://doi.org/10.1007/s11517-006-0119-0
22. Kamen PW, Tonkin AM (1995) Application of the Poincaré plot to heart rate variability: a new measure of functional status in heart failure. Aust NZ J Med 25:18–26. https://doi.org/10.1111/j.1445-5994.1995.tb00573.x
23. Brennan M, Palaniswami M, Kamen P (2001) Do existing measures of Poincare plot geometry reflect nonlinear features of heart rate variability? IEEE Trans Biomed Eng 48:1342–1347. https://doi.org/10.1109/10.959330
24. Ewing DJ, Martyn CN, Young RJ, Clarke BF (1985) The value of cardiovascular autonomic function tests: 10 years experience in diabetes. Diabetes Care 8:491–498. https://doi.org/10.2337/diacare.8.5.491
25. Saul JP, Albrecht P, Berger RD, Cohen RJ (1987) Analysis of long term heart rate variability: methods, 1/f scaling and implications. Comput Cardiol 14:419–422
26. Kay SM, Marple SL (1981) Spectrum analysis—a modern perspective. Proc IEEE 69:1380–1419
27. Saykrs BM (1973) Analysis of heart rate variability. Ergonomics 16:17–32. https://doi.org/10.1080/00140137308924479
28. Malliani A, Pagani M, Lombardi F, Cerutti S (1991) Cardiovascular neural regulation explored in the frequency domain. Circulation 84:482–492
29. Pomeranz B, Macaulay RJ, Caudill MA et al (1985) Assessment of autonomic function in humans by heart rate spectral analysis. Am J Physiol-Heart Circ Physiol 248:H151–H153
30. Kobayashi M, Musha T (1982) 1/f fluctuation of heartbeat period. IEEE Trans Biomed Eng 29:456–457
31. Goldberger AL, West BJ (1987) Fractals in physiology and medicine. Yale J Biol Med 60:421
32. Iyengar N, Peng CK, Morin R et al (1996) Age-related alterations in the fractal scaling of cardiac interbeat interval dynamics. Am J Physiol Regul Integr Comp Physiol 271:R1078–R1084
33. Huikuri HV, Seppänen T, Koistinen MJ et al (1996) Abnormalities in beat-to-beat dynamics of heart rate before the spontaneous onset of life-threatening ventricular tachyarrhythmias in patients with prior myocardial infarction. Circulation 93:1836–1844
34. Ciccone AB, Siedlik JA, Wecht JM et al (2017) Reminder: RMSSD and SD1 are identical heart rate variability metrics. Muscle Nerve 56:674–678. https://doi.org/10.1002/mus.25573
35. Pincus SM, Viscarello RR (1992) Approximate entropy: a regularity measure for fetal heart rate analysis. Obstet Gynecol 79:249–255
36. Pincus SM, Goldberger AL (1994) Physiological time-series analysis: what does regularity quantify? Am J Physiol-Heart Circ Physiol 266:H1643–H1656
37. Mäkikallio TH, Seppänen T, Niemelä M et al (1996) Abnormalities in beat to beat complexity of heart rate dynamics in patients with a previous myocardial infarction. J Am Coll Cardiol 28:1005–1011
38. Goldberger AL (1996) Non-linear dynamics for clinicians: chaos theory, fractals, and complexity at the bedside. Lancet 347:1312–1314
39. Goldberger AL, Amaral LAN, Glass L et al (2000) PhysioBank, PhysioToolkit, and PhysioNet. Circulation 101:e215–e220. https://doi.org/10.1161/01.CIR.101.23.e215
40. Bigger JT, Steinman RC, Rolnitzky LM et al (1996) Power law behavior of RR-interval variability in healthy middle-aged persons, patients with recent acute myocardial infarction, and patients with heart transplants. Circulation 93:2142–2151
41. Huikuri HV, Mäkikallio TH, Airaksinen KJ et al (1998) Power-law relationship of heart rate variability as a predictor of mortality in the elderly. Circulation 97:2031–2036
42. Yamamoto Y, Hughson RL (1991) Coarse-graining spectral analysis: new method for studying heart rate variability. J Appl Physiol 71:1143–1150
43. Peng C-K, Havlin S, Stanley HE, Goldberger AL (1995) Quantification of scaling exponents and crossover phenomena in nonstationary heartbeat time series. Chaos 5:82–87

44. Hausdorff JM, Peng CK, Ladin ZVI et al (1995) Is walking a random walk? Evidence for long-range correlations in stride interval of human gait. J Appl Physiol 78:349–358
45. Shafqat K, Pal SK, Kumari S, Kyriacou PA (2009) Empirical mode decomposition (EMD) analysis of HRV data from locally anesthetized patients. In: 2009 annual international conference of the IEEE engineering in medicine and biology society, pp 2244–2247
46. Iatsenko D, McClintock PV, Stefanovska A (2015) Nonlinear mode decomposition: a noise-robust, adaptive decomposition method. Phys Rev E 92:032916
47. Morales IO, Landa E, Angeles CC et al (2015) Behavior of early warnings near the critical temperature in the two-dimensional Ising model. PLoS One 10:e0130751
48. Acebrón JA, Bonilla LL, Pérez Vicente CJ et al (2005) The Kuramoto model: a simple paradigm for synchronization phenomena. Rev Mod Phys 77:137–185. https://doi.org/10.1103/RevModPhys.77.137
49. Cumin D, Unsworth CP (2007) Generalising the Kuramoto model for the study of neuronal synchronisation in the brain. Phys Nonlinear Phenom 226:181–196. https://doi.org/10.1016/j.physd.2006.12.004
50. Malik M, Camm AJ (1993) Components of heart rate variability—what they really mean and what we really measure. Am J Cardiol 72:821–822
51. O'Brien IA, O'Hare P, Corrall RJ (1986) Heart rate variability in healthy subjects: effect of age and the derivation of normal ranges for tests of autonomic function. Heart 55:348–354. https://doi.org/10.1136/hrt.55.4.348
52. Levy MN (1984) Cardiac sympathetic-parasympathetic interactions. Fed Proc 43:2598–2602
53. Horn EH, Lee ST (1965) Electronic evaluations of the fetal heart rate patterns preceding fetal death: further observation. Am J Obster Gynecol 87:824–826
54. Kleiger RE, Miller JP, Bigger JT, Moss AJ (1987) Decreased heart rate variability and its association with increased mortality after acute myocardial infarction. Am J Cardiol 59:256–262
55. Malik M, Farrell T, Cripps T, Camm AJ (1989) Heart rate variability in relation to prognosis after myocardial infarction: selection of optimal processing techniques. Eur Heart J 10:1060–1074
56. Thayer JF, Yamamoto SS, Brosschot JF (2010) The relationship of autonomic imbalance, heart rate variability and cardiovascular disease risk factors. Int J Cardiol 141:122–131. https://doi.org/10.1016/j.ijcard.2009.09.543
57. Hellman JB, Stacy RW (1976) Variation of respiratory sinus arrhythmia with age. J Appl Physiol 41:734–738
58. Pikkujämsä SM, Mäkikallio TH, Sourander LB et al (1999) Cardiac interbeat interval dynamics from childhood to senescence. Circulation 100:393–399
59. Antelmi I, Paula RSD, Shinzato AR et al (2004) Influence of age, gender, body mass index, and functional capacity on heart rate variability in a cohort of subjects without heart disease. Am J Cardiol 93:381–385. https://doi.org/10.1016/j.amjcard.2003.09.065
60. Koenig J, Thayer JF (2016) Sex differences in healthy human heart rate variability: a meta-analysis. Neurosci Biobehav Rev 64:288–310. https://doi.org/10.1016/j.neubiorev.2016.03.007
61. Malpas SC, Maling TJB (1990) Heart-rate variability and cardiac autonomic function in diabetes. Diabetes 39:1177–1181. https://doi.org/10.2337/diab.39.10.1177
62. Schmitt DT, Ivanov PC (2007) Fractal scale-invariant and nonlinear properties of cardiac dynamics remain stable with advanced age: a new mechanistic picture of cardiac control in healthy elderly. Am J Physiol Regul Integr Comp Physiol 293:R1923–R1937. https://doi.org/10.1152/ajpregu.00372.2007
63. Kovatchev BP, Farhy LS, Cao H et al (2003) Sample asymmetry analysis of heart rate characteristics with application to neonatal sepsis and systemic inflammatory response syndrome. Pediatr Res 54:892–898. https://doi.org/10.1203/01.PDR.0000088074.97781.4F
64. Bauer A, Kantelhardt JW, Barthel P et al (2006) Deceleration capacity of heart rate as a predictor of mortality after myocardial infarction: cohort study. Lancet 367:1674–1681

65. Robles-Cabrera A, Michel-Chavez A, Callejas-Rojas RC et al (2014) The cardiovagal, cardiosympathetic and vasosympathetic arterial baroreflexes and the neural control of short-term blood pressure. Rev Neurol 59:508–516
66. Vaschillo EG, Vaschillo B, Lehrer PM (2006) Characteristics of resonance in heart rate variability stimulated by biofeedback. Appl Psychophysiol Biofeedback 31:129–142
67. Floras JS (2013) Blood pressure variability: a novel and important risk factor. Can J Cardiol 29:557–563
68. Parati G, Ochoa JE, Salvi P et al (2013) Prognostic value of blood pressure variability and average blood pressure levels in patients with hypertension and diabetes. Diabetes Care 36:S312–S324

An Agent-Based Model to Study Selection of *Pseudomonas aeruginosa* Quorum Sensing by Pyocyanin: A Multidisciplinary Perspective on Bacterial Communication

Ammar Jalalimanesh, Christina Kuttler, Rodolfo García-Contreras, and Judith Pérez-Velázquez

Abstract Although bacteria are unicellular organisms, they use a sophisticated mechanism to cooperate with other bacteria which allows them to carry out multicellular-like processes, such as swarming, biofilm formation, induce infections, luminescence, etc. This mechanism is known as quorum sensing (QS) and it functions through the individual release, diffusion and collective sensing of small molecules, called autoinducers, which under their accumulation lead to changes in gene regulation. A range of approaches have been used to study the complex way in which QS works, these tools combine biology, physics, and mathematics. We discuss here how a multidisciplinary perspective is ideal to study QS and present an example of QS in *Pseudomonas aeruginosa*, a human pathogen. In this bacterial species, QS coordinates the expression of virulence factors, that are public goods utilized by the whole population of bacteria regardless if they invested or not in their production. Hence, public good production is a cooperative behavior, susceptible to be exploited by non-public good producers, known as social cheaters. These

A. Jalalimanesh
Technical University of Munich, Zentrum Mathematik, Garching, Germany

Iranian Research Institute for Information Science and Technology (IRANDOC), Tehran, Iran

C. Kuttler
Technical University of Munich, Zentrum Mathematik, Garching, Germany

R. García-Contreras
Department of Microbiology and Parasitology, Faculty of Medicine, UNAM, Mexico City, Mexico

J. Pérez-Velázquez (✉)
Technical University of Munich, Mathematical Modeling of Biological Systems (M12), Zentrum Mathematik, Garching, Germany

Institute of Computational Biology, Helmholtz Zentrum München, Neuherberg, Germany
e-mail: perez-velazquez@helmholtz-muenchen.de

L. Olivares-Quiroz, O. Resendis-Antonio (eds.), *Quantitative Models for Microscopic to Macroscopic Biological Macromolecules and Tissues*,
https://doi.org/10.1007/978-3-319-73975-5_7

individuals, which are QS-deficient, are also less able to tolerate oxidative stress. Our group has shown that pyocyanin (which promotes the generation of reactive oxygen species) produced by the wild-type population may work as a policing mechanism to select functional QS systems in this bacterium. Using an agent-based model (ABM) we are able to confirm that indeed this compound increases the fitness of the cooperative QS proficient individuals. We further explore, with the ABM, how the bacterial environment diffusion properties may be contributing to stabilize QS in certain growth conditions.

Keywords *Pseudomonas aeruginosa* · Pyocyanin · Quorum sensing · Agent-based model · Mathematical models

1 Introduction

Quorum sensing is a cell-to-cell signaling mechanism that enables bacteria to collectively control gene expression. In *Pseudomonas aeruginosa*, it is involved in the expression of cooperative behaviors including the production of costly exoproducts like exoenzymes and siderophores [1]. Individuals that take advantage of such public goods without contributing to their production are considered social cheaters [2] and can potentially invade the population, as they save their resources instead of investing in the production costs of public goods. Furthermore, this allows them to divide slightly faster and to reach higher yields than the wild-type individuals. QS systems regulating public goods are widespread and conserved among several bacterial species. This is allowed by diverse mechanisms counteracting the effects of social cheating, among them are: growth of bacteria in environments that promote the physical separation of cooperators and cheaters [3], decreasing the cheater's fitness [4]—this occurs, e.g., for growth of bacterial populations in highly viscous medium that limits the diffusion of the public goods [5] or a switch between planktonic and colonizing state [20] and growth in the presence of toxic compounds such as H_2O_2 [6, 7] and HCN [8], that preferentially decrease the growth of cheaters over the growth of cooperators.

One of the main QS-controlled virulence factors are the phenazines, which are dibenzo annulated pyrazines with diverse roles in *P. aeruginosa* physiology, from being virulence factors that promote damage to host cells [9], to being terminal QS signal molecules [10]. Among the QS- controlled phenazines produced by *P. aeruginosa*, pyocyanin is produced by several clinical [6, 7, 11] and environmental strains [12] and its concentration in the lung of cystic fibrosis patients is high [13]. Since QS defective mutants are less able to cope against oxidative stress [6, 7] and likely possess less robust membranes than QS proficient individuals [14], we hypothesize that pyocyanin may differentially affect this population, maybe even acting as a policing metabolite. To test this hypothesis, we performed competition experiments [15] and developed mathematical models, our results showed that indeed the production of this metabolite selects the presence of QS systems. The mathematical models were used to confirm the experimental observations and

explore other scenarios. This chapter is dedicated to present the mathematical models in detail. The mathematical modeling also hinted that the bacterial environment diffusion properties may be contributing to stabilize QS in certain growth conditions. Our findings are relevant in many ecological contexts, for example, during lung infections, where the generation of QS deficient mutants (specifically signal blind lasR-mutants) is common, under these conditions pyocyanin production may be an important factor to restrict the selection of QS defective social cheaters, hence increasing the virulence of the strains during the infections.

The chapter is organized in two parts, first we will explain our mathematical model to describe both the QS system of *P. aeruginosa* and the interactions between wild-type and cheaters and then we present the ABM.

2 Pyocyanin Selection

In this section, we will have a look on the dynamics of the competitive, highly interacting QS system of *P. aeruginosa* from a deterministic viewpoint. We do this to later use a deterministic mathematical model to feed some aspects of the discrete (agent-based) model. The most essential components of the whole system—nutrients, bacterial populations, autoinducers, exoenzymes, pyocyanin—are translated into a system of ordinary differential equations (ODE). ODE are common tools to model QS [16]. The notation of the variables can be found in Table 1. We follow the basic approach as introduced in [17] for *P. putida* and focus on a homogeneously distributed situation, i.e., the bacteria are in a well-mixed batch culture.

There are two bacterial types involved: the wild-type, denoted by B_W (behaving in the standard way, i.e. performing QS, being resistant against pyocyanin) and the mutants, denoted B_C (lacking the QS system and being vulnerable to pyocyanin). Both feed on and thus compete for the same nutrient resources, therefore the model approach includes this with a Monod-type saturation term. Correspondingly, the nutrient uptake is included in the model. Please note that there are two types of nutrient considered: digestible nutrients N, and non-digestible nutrients $\tilde{N}$. There are exoenzymes E needed to degrade the non-digestible ones into digestible nutrients. The production of these exoenzymes is under QS-control.

Table 1 ODE model variables, initial values for control case (wild-type only)

Variable	Unit	Initial value	Description
A	nM	70	AHL, QS signal
P	U	0	Pyocyanin
B_w	OD	0.05	PA14 wild-type strain
B_c	OD	0	double mutant *lasR rhlR*
$\tilde{N}$	nM	27.59	Non-digestible nutrients
E	nM	19.1	Exoenzymes
N	nM	2	Digestible nutrients

Table 2 Parameters of the ODE model

Parameter	Description	Parameter	Description
α	Basic AHL production	r_w	Wild-type growth rate
β	Activated AHL production	r_c	Mutant growth rate
γ_A	Abiotic AHL degradation rate	d_w	Wild-type death rate
n	Hill coefficient	d_c	Mutant death rate
C_1	AHL threshold	K_w	Half max. for growth wild-type
β_p	Production of pyocyanin by bacteria	K_c	Half max. for growth mutant
ξ_2	Consumption of pyocyanin by killing bacteria	ξ_1	Max. killing rate by pyocyanin
γ_p	Abiotic pyocyanin degradation	K_P	Pyocyanin concentration for half max killing rate
c_n	Transformation rate into digestible nutrients by exoenzyme E	γ_E	Abiotic decay of exoenzymes
$\gamma_{\tilde{N}}$	Abiotic decay/disappearance of non-digestible nutrients	$K_{\tilde{N}}$	Half max non-digestible nutrients concentration
Y_W	Yield rate for wild-type	γ_n	Abiotic decay/disappearance of digestible nutrients
β_E	Production rate for exoenzymes	Y_C	Yield rate for mutant

Pseudomonas aeruginosa contains at least three different, coupled QS systems. The main ones are called the *las* system and the *rhl* system. Both use AHLs (acyl-homoserine lactones) as autoinducers. We restrict ourselves to the most important system, the *las* system which activates the *rhl* one, producing and sensing 3OC12-HSL molecules. The autoinducer variable is denoted by A. The equation for A is therefore one of the main equations used to model QS dynamics. Note that this equation involves the QS-proficient population, therefore the autoinducer concentration depends on the size of this population. The typical positive feedback loop observed in QS, involving a Hill-function (which contains an autoinducer threshold at which activation occurs), is included, as well as an abiotic degradation.

The pyocyanin (P) production is assumed to be QS-controlled, and therefore involves the A variable, analogously to the exoenzyme production. A detailed list of all parameters used in the model can be found in Table 2. The resulting ODE system reads:

$$\frac{dB_w}{dt} = r_w \frac{N}{K_w + N} B_w - d_w B_w \tag{1a}$$

$$\frac{dB_c}{dt} = r_c \frac{N}{K_c + N} B_c - d_c B_c - \xi_1 \frac{P}{K_p + P} B_c \tag{1b}$$

$$\frac{dA}{dt} = \alpha + \beta \frac{A^n}{C_1^n + A^n} B_w - \gamma_A A \tag{1c}$$

$$\frac{dP}{dt} = \beta_p \frac{A^n}{C_1^n + A^n} B_w - \gamma_p P - \xi_2 \frac{P}{K_p + P} B_c \tag{1d}$$

$$\frac{d\tilde{N}}{dt} = -c_n E \frac{\tilde{N}}{\tilde{N} + K_{\tilde{N}}} - \gamma_{\tilde{N}} \tilde{N} \tag{1e}$$

$$\frac{dN}{dt} = c_n E \frac{\tilde{N}}{\tilde{N} + K_{\tilde{N}}} - \frac{1}{Y_w} r_w \frac{N}{K_w + N} B_w - \frac{1}{Y_c} r_c \frac{N}{K_c + N} B_c - \gamma_n N \tag{1f}$$

$$\frac{dE}{dt} = \beta_E \frac{A^n}{C_1^n + A^n} B_w - \gamma_E E \tag{1g}$$

Obviously, this system preserves the positivity of the solution, as all negative terms contain the respective variable. This means: the solution is positive. Furthermore, due to these degradation terms and limited growth or production terms, the solution stays bounded. The part of the system concerning the QS itself allows for bistability; for more details concerning this, please refer to [18, 19]. An explicit solution cannot be determined due to the complexity of the model, but one can consider numerical solutions. As in our case experimental results are available, one can fit the numerical solution to these experimental data by optimizing the model parameter values. This will be done as a first step for a better quantitative and qualitative understanding, allowing us to validate the processes behind; in a second step, the resulting model with these optimized parameter values can be used for quantitative predictions, e.g. for situations which have not performed experimentally.

Solving the ODE system numerically yields the time course of the involved variables, as it can be seen exemplarily for the total bacterial population and the AHL concentration in Fig. 1.

This first step of the modeling approach served to confirm that the underlying assumptions are valid as the numerical solutions reproduce qualitatively the experimental results. This is useful as it provides us with a very good idea of the order of magnitude of several of the parameters involved, in some case, a good approximation of their values. However, this approach is unable to provide information at the spatial level, reason why, in a second step of the modeling, we will use ABM. We aim to be able to determine whether spatial location or physical properties of the media play a role in the competition. The QS dynamics, however, are expected to be compatible for both, the ODE and the ABM model.

As expected, in the base of only mutant cells (blue curves) being in the system, there is no AHL production at all, but also a very limited bacterial growth since the

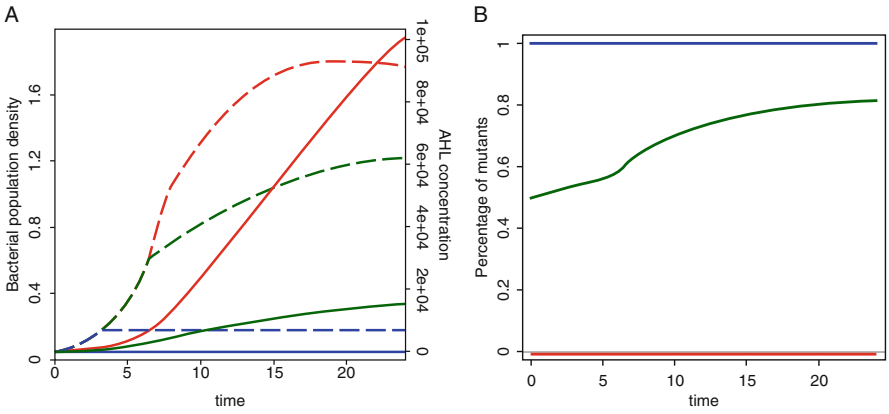

Fig. 1 The curves show the time courses for the situations with only wild-type bacteria (red), an initial mixture of 50% wild-type and 50% mutants (green) and only mutant bacteria (blue). (**a**) Dotted lines correspond to the total bacterial density, solid lines to the AHL concentration. (**b**) Percentage of the mutants within the bacterial population

exoenzymes helping to produce digestible nutrients are completely lacking. The most interesting case concerns the mixture of 50% wild-type and 50% mutants initially, this corresponds to green curves in Fig. 1. Here exoenzymes are available to a certain extent, even though the AHL concentration does reach only lower levels than in the only wild-type case (see Fig. 1a) and pyocyanin is produced by the present wild-type cells, acting against the mutants (see Fig. 1b).

3 An Agent-Based Model

Modeling approaches can be grouped in two large classes: Top-down and bottom-up. In a top-down approach, one models the behavior of a population without considering individual entities. Modeling bacteria using ODE system is an example of top-down approach. Using these methodologies, it would be possible to model a large number of objects. Alternatively, bottom-up approaches model a system considering individuals. In this approach, we consider microscopic level to better mimic a large system. Therefore, the overall system behavior emerges from the interactions of individuals. Here we develop an individual based model (ABM) to simulate bacterial population.

We combine these approaches to obtain a well-rounded understanding of the role of pyocyanin in QS stability. In this way, both approaches complement each other. We use the ODE to feed quantitative and qualitative information to the ABM in terms of the QS dynamics of *P. aeruginosa*, for example we use parameters values estimated from the ODE into the ABM. The main goal of the AB model is to investigate spatially the effects of pyocyanin on competition experiments

between *P. aeruginosa* wild-type and QS deficient *lasR rhlR* mutant. Our ODE model is unable to provide this information. The AB model is spatially two-dimensional and developed using the NetLogo simulation platform. The model is described based on ODD protocol. Using a combined approach, we have a broader perspective, and in some aspects both models intersect. Note for example that, under some conditions, average overall population dynamics of the ABM resemble ODE populations dynamics.

4 Entities, State Variables, and Scales

There are two types of agents in the model, wild-types and QS deficient mutants. All agents have age and energy attributes. Energy is the amount of nutrient which an agent preserves for consumption and reproduction. Agents are located on a matrix consisting of patches. Figure 2 is the graphical representation of our agent-based model. Patches are containing exoenzymes, acylated homoserine lactone (AHL), digestible-nutrient, non-digestible nutrient, and pyocyanin. The exoenzymes degrade non-digestible nutrient into digestible. Limitation of cell division is assumed caused by lack of nutrients only, not by space limitation. The physical interpretation of having the nutrients based on the patch level is fast diffusion due to small nutrient molecules, thus, we assumed a homogeneous distribution of nutrients within the (still small) patches. The attributes of each patch are assigned by appropriate values throughout simulation. The process of assigning the values to the patches' attributes is described in the next section. These substances diffuse from one patch to its neighbors, discretely in time (using Netlogo diffusion function).

We modeled an environment of 100×100 μm. Therefore, we run the simulations in two dimensions using a constant height of 10 μm. The size of bacteria is approximately 1 μm (in diameter). There is no limitation in the number of bacteria per patch. It means that in the presence of nutrient, lack of space is not relevant here. Each time step of simulation is one minute. Time steps are called ticks.

5 Process Overview and Scheduling

Bacteria can move over patches, they consume digestible nutrient and benefit from exoenzymes, the mutants may be affected by pyocyanin. The concentration of substances is updated using Eqs. (1)–(5). Here, we describe the dynamics of the processes recursively, i.e. the next time step $t + 1$ is defined by the current time step t and the state of the system there. These equations are solved every tick for all patches, one by one. The variables are described in Table 3. The other parameters of the equations are described in Table 4.

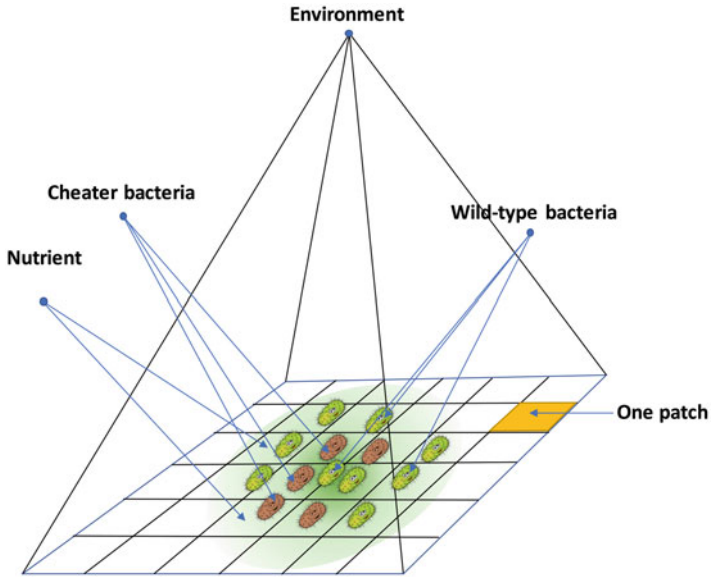

Fig. 2 Schematic view of agent-based model

Table 3 Initial values of substances at the beginning of the simulation

	Variable	Unit	Initial value	Description
1	PG	nM	8	Concentration of digestible nutrient in the patch
2	Exo	nM	2	Concentration of exoenzyme in the patch
3	NDN	nM	204	Concentration of non-digestible nutrient in the patch
4	#Bw	–	10, 50, 90	Number of wild-type bacteria in the patch
5	#Bc	–	10, 50, 90	Number of QS deficient mutant bacteria in the patch
6	AHL	nM	70.3	Concentration of AHL in the patch
7	Pyo	nM	0	Concentration of pyocyanin in the patch
8	BcDR	nM	0	QS deficient mutants' death rate in presence of pyocyanin

$$\mathrm{PG}_{t+1} = \mathrm{PG}_t + \mathrm{cn} \times \mathrm{Exo} \times \mathrm{NDN} \times \frac{1}{\mathrm{Kn} + \mathrm{NDN}_t} - \#\mathrm{Bw} \times cr_w - \#\mathrm{Bc} \times \mathrm{cr}_c - \gamma_n \times \mathrm{PG}_t \tag{1}$$

$$\mathrm{AHL}_{t+1} = \mathrm{AHL}_t + \left(\alpha + \beta \times \mathrm{AHL}_t^2 \times \frac{1}{\left(C_1^2 + \mathrm{AHL}_t^2\right)}\right) \times \#\mathrm{Bw} - \gamma_A \times \mathrm{AHL}_t \tag{2}$$

$$\mathrm{Exo}_{t+1} = \mathrm{Exo}_t + \beta_E \times \#\mathrm{Bw} \times \mathrm{AHL}_t^2 \times \frac{1}{\left(C_1^2 + \mathrm{AHL}_t^2\right)} - \gamma_E \times \mathrm{Exo}_t \tag{3}$$

Table 4 ABM model parameters

	Parameter	Scaled model value	Unit	Description
1	cn	0.06372466	1/min	Transformation rate of non-digestible nutrient (*NDN*) to digestible nutrient
2	kn	0.0667575	nM/patch	Half max non-digestible nutrients concentration
3	cr_w	0.0013333	nM/cell × minute	Digestible nutrients consumption rate of wild-type bacteria
4	cr_c	0.0013333	nM/cell × minute	Digestible nutrients consumption rate of QS deficient mutants
5	γ_n	8.33×10^{-4}	1/min	Decay rate of public goods
6	α	0.914057×10^{-11}	L × nM/(cell × h)	Basic production rate of AHL by wild-types
7	β	17.8324×10^{-10}	L × nM/(cell × h)	Induced production rate of AHL by wild-types
8	C_1	140.249	nM	AHL threshold
9	γ_A	8.33×10^{-4}	1/min	Abiotic AHL degradation
10	β_E	$0.0505132 \times 10^{-12}$	L × nM/(cell × h)	Exoenzyme production rate
11	γ_E	0.00162761	1/min	Abiotic decay rate of exoenzyme
12	γ_{NDN}	1.44631×10^{-4}	1/min	Abiotic decay rate of non-digestible nutrients
13	β_P	0.000082646	1/(cell × minute)	Production of pyocyanin by bacteria
14	γ_P	0.00165423	1/min	Abiotic pyocyanin degradation
15	ξ_2	5.086×10^{-4}	UP/(U × minute)	Consumption of pyocyanin by killing bacteria
16	kp	0.134633	UP	Pyocyanin concentration for half max killing rate
17	ξ_1	0.0054	1/min	Max killing rate by pyocyanin

$$\mathrm{NDN}_{t+1} = \mathrm{NDN}_t + \mathrm{cn} \times \mathrm{Exo}_t \times \mathrm{NDN}_t \times \frac{1}{\mathrm{Kn} + \mathrm{NDN}_t} - \gamma_{\mathrm{NDN}} \times \mathrm{NDN}_t \tag{4}$$

$$\mathrm{Pyo}_{t+1} = \mathrm{Pyo}_t + \beta_P \times \#\mathrm{Bw} \times \mathrm{AHL}_t^2 \times \frac{1}{\left(C_1^2 + \mathrm{AHL}_t^2\right)} - \gamma_P \times \mathrm{Pyo}_t - \xi_2 \times \mathrm{Pyo}_t \times \frac{1}{(\mathrm{kp} + \mathrm{Pyo}_t)} \times \#\mathrm{Bc} \tag{5}$$

There are two criteria for bacteria to divide. First, the bacterium must reach a minimum age to be able to proliferate. Next it should have enough nutrient to divide into two daughter cells. The QS deficient mutants' death rate in presence of pyocyanin is calculated based on Eq. (6)

$$\mathrm{BcDR}_t = \xi_1 \times \mathrm{Pyo}_t \times \frac{1}{(\mathrm{kp} + \mathrm{Pyo}_t)} \tag{6}$$

The initial values of substances at the beginning of the simulation are also presented in Table 3.

6 Design Concepts

In this model, it is assumed that, following the experimental results, that the wild-type indirectly controls the number of mutants as the wild-type bacteria release pyocyanin (toxic to the mutants). The basic design concepts of the model are as follows:

- In case of nutrient availability, each bacterium absorbs a determined amount of nutrient from its host patch reservoir.
- The bacterium gets older when time passes. Bacteria can divide after reaching a certain age.
- When satisfying the mentioned criteria, minimum age and sufficient nutrient, the bacterium divides. After division, the nutrient level for two daughter cells is set to zero. This is a simplifying assumption which basically means that nutrients are needed for proliferation. One of the daughter cells is located on the position of its parent and the other one is in one of the neighbor patches with the lowest cell density.
- There is a rate at which mutants are killed by pyocyanin, which is computed using Eq. (6).

7 Initialization

Table 3 displays the parameter values which are used for running the numerical simulations. As the parameters which are related to the concentration are in liter and the model dimensions are 100×100 μm, these parameters should be multiplied by $10^{-10} \frac{\mathrm{nM}}{L}$. The initial values of substrates are distributed between patches equally. During the numerical simulations, patches allow for a constant diffusion of the substrates at each time step. Equation (7) describes a difference equation for the diffusion process. $c_j^{t+1}$is the concentration of the substrate in the next step of the simulation in patch j. d_c is a diffusion constant between 0 and 1 and denotes the

proportion of patch substrate which is shared by its neighbors. c_k^t is a set of patch neighbors, i.e. 8 patches in our case (two-dimensional world with square patches).

$$c_j^{t+1} = (1 - d_c)\, c_j^t + \left(\frac{1}{8} \sum_{k \in N(j)} d_c c_k^t \right) \tag{7}$$

The time scale of diffusion in water does not allow to solve this equation in one time step (tick), therefore it will be necessary to update the concentration of the substrates by solving Eq. (7) N times per tick, where N is tuned according to the realistic diffusion speed.

We use the following conversion optical density to cells: OD 1 is approximately $1.19 \times 10^{12} \frac{\text{cells}}{L}$, therefore the initial number of cells in our simulation environment regarding its spatial size should be around 1.19×10^2, corresponding to OD 1.

The minimum age for proliferation is set to be two hours for both strains and the minimum saved nutrient for division is set to 0.03 and 0.04 U for QS deficient mutants and wild-type, respectively.

8 Simulation and Results

The model is implemented in NetLogo 6.0 (Fig. 3 is a screen shot of the basic set up.). Figure 4 displays the snapshot of a simulation. The elliptical shapes are bacterial agents where the red ones are wild-type and the blue ones are QS deficient mutants. Nutrient concentration is depicted in a gradient of green to black, where green means available nutrient and black means consumed nutrient.

Our first observation was that the diffusion rate of the substrates highly affects the competition outcome between mutants and wild-type (as mentioned before the diffusion is governed by Eq. (7) and the equation is solved N times per tick). We set $d_c = 1$ which means that the patch shares all its content with its neighbors. Figure 5 shows the effects of N on the competition between the two strains. Time course of the bacteria (in absolute numbers) is shown as well as their proportions (in total one). We hypothesize that the cause of this observation may be the fact that wild-type, as nutrient producers, have access to public goods even under low diffusion rate conditions. However, with increasing diffusion rate, QS deficient mutants gain access to the public goods and will therefore be, under some circumstances, able to invade.

We set up the water diffusion rate to be significantly fast, therefore we set N to be 500. This means an adaptation of the fast time scale of diffusion to the given model for the other processes. We run the simulation by different compositions of bacteria's initial population. Left panel of Fig. 5 shows the simulation results considering pyocyanin dynamics. We run the simulation in three schemes, all started with 100 bacteria. In the first scheme, there were 10 wild-type and 90 QS deficient mutants, in the second one there were 50 wild-type and 50 QS deficient mutants and finally we had 90 wild-type and 10 QS deficient mutants as the initial population.

All the simulations were run for 1750 min.

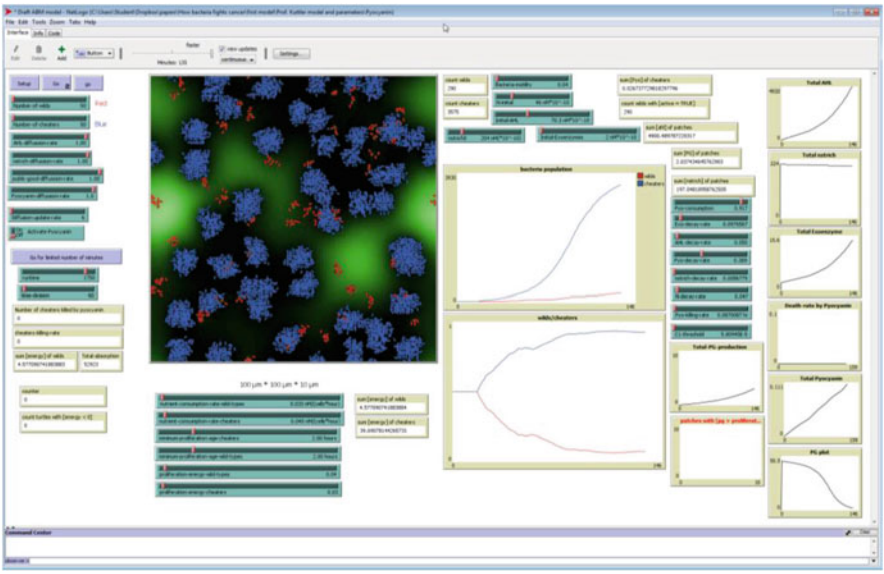

Fig. 3 ABM simulation of bacterial population (NetLogo 6.0)

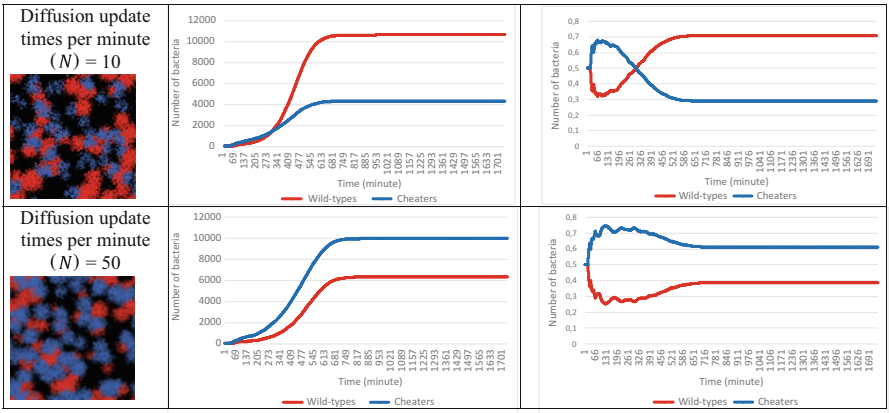

Fig. 4 Simulation of the effects of diffusion update rate on populations growth. For 1750 ticks with N set to 500, it takes 30 min on an Intel 7500 i5 processor with 8 GB of RAM. The model is not running in parallel.

9 Conclusions

The experimental data [15] indicated that QS-regulated pyocyanin production by the wild-type population in *P. aeruginosa* could work as a policing mechanism to select functional QS systems. Following the experiments, we developed two mathematical models to describe how pyocyanin concentration may impact on the evolutionary

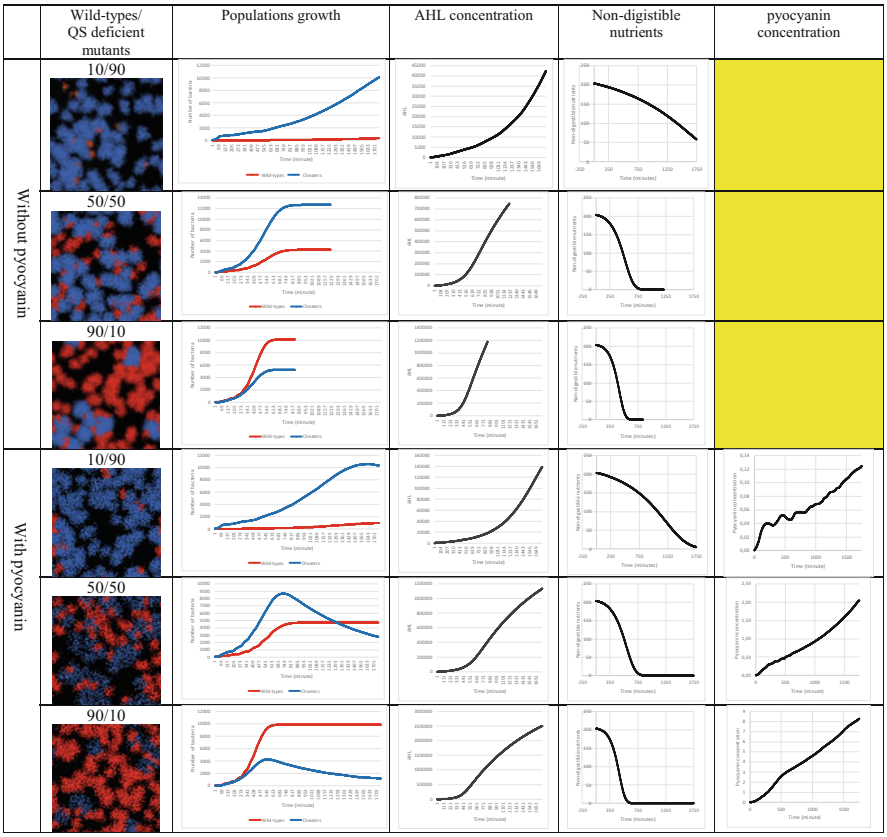

Fig. 5 Simulation results

fitness of mixed bacteria populations of *P. aeruginosa* wild-type (PA14) and its *lasR rhlR* double mutant. Pyocyanin is able to selectively affect mutant growth and survival since it produces oxidative stress (H_2O_2) and the mutants are more sensitive to stress in general and to oxidative stress in particular, since they are unable to induce the expression of antioxidant enzymes like catalase [6, 7] and perhaps since they also may have weaker membranes [14].

The first model is composed of differential equations (deterministic) to describe the QS dynamics, and the second model is an ABM to explore how environment diffusion properties and non-homogeneous distribution of bacteria may play a role in stabilizing QS. Thanks to this multidisciplinary approach we were able to show that a combination of techniques can show that indeed pyocianin acts as a policing mechanism and QS may be affected by physical properties of the environment where bacteria live. This study demonstrates the power of using a combination of methods in complex phenomena such as bacterial QS, these techniques arising from mathematics, physics, chemistry, and biology have helped to uncover findings that otherwise may not be unveiled.

References

1. Popat R, Cornforth DM, Mcnally L, Brown SP (2015) Collective sensing and collective responses in quorum-sensing bacteria. J R Soc Interface 12(103):20140882
2. Diggle SP, Griffin AS, Campbell GS, West SA (2007) Cooperation and conflict in quorum-sensing bacterial populations. Nature 450:411–414
3. Chuang JS, Rivoire O, Leibler S (2009) Simpson's paradox in a synthetic microbial system. Science 323:272–275
4. Hense BA, Schuster M (2015) Core principles of bacterial autoinducer systems. Microbiol Mol Biol Rev 79(1):153–169
5. Kummerli R, Griffin AS, West SA, Buckling A, Harrison F (2009) Viscous medium promotes cooperation in the pathogenic bacterium Pseudomonas aeruginosa. Proc Biol Sci 276:3531–3538
6. García-Contreras R, Nuñez-López L, Jasso-Chávez R, Kwan BW, Belmont JA, Rangel-Vega A, Maeda T, Wood (2015) Quorum sensing enhancement of the stress response promotes resistance to quorum quenching and prevents social cheating. ISME J 9(1):115–125
7. García-Contreras R, Peréz-Eretza B, Jasso-Chávez R, Lira-Silva E, Roldán-Sánchez JA, González-Valdez A, Soberón-Chávez G, Coria-Jiménez R, Martínez-Vázquez M, Alcaraz LD, Maeda T, Wood TK (2015) High variability in quorum quenching and growth inhibition by furanone C-30 in Pseudomonas aeruginosa clinical isolates from cystic fibrosis patients. Pathog Dis 73(6):ftv040
8. Wang M, Schaefer AL, Dandekar AA, Greenberg EP (2015) Quorum sensing and policing of Pseudomonas aeruginosa social cheaters. Proc Natl Acad Sci U S A 112:2187–2191
9. Leto BR, Thomas L (2013) Pyocyanin effects on respiratory epithelium: relevance in *Pseudomonas aeruginosa* airway infections. Trends Microbiol 21(2):73–81
10. Dietrich LE, Price-Whelan A, Petersen A, Whiteley M, Newman DK (2006) The phenazine pyocyanin is a terminal signalling factor in the quorum sensing network of *Pseudomonas aeruginosa*. Mol Microbiol 61(5):1308–1321
11. Schaber JA, Carty NL, McDonald NA, Graham ED, Cheluvappa R, Griswold JA, Hamood AN (2004) Analysis of quorum sensing-deficient clinical isolates of *Pseudomonas aeruginosa*. J Med Microbiol 53:841–853
12. Grosso-Becerra M-V, Santos-Medellín C, González-Valdez A, Méndez J-L, Delgado G, Morales-Espinosa R, Servín-González L, Alcaraz L-D, Soberón-Chávez G (2014) Pseudomonas aeruginosa clinical and environmental isolates constitute a single population with high phenotypic diversity. BMC Genomics 28(5):318
13. Caldwell CC, Chen Y, Goetzmann HS, Hao Y, Borchers MT, Hassett DJ, Young LR, Mavrodi D, Thomashow L, Lau GW (2009) Pseudomonas aeruginosa exotoxin pyocyanin causes cystic fibrosis airway pathogenesis. Am J Pathol 175(6):2473–2488
14. Davenport PW, Griffin JL, Welch M (2015) Quorum sensing is accompanied by global metabolic changes in the opportunistic human pathogen *Pseudomonas aeruginosa*. J Bacteriol 197(12):2072–2082
15. Castañeda-Tamez P, Saucedo-Mora MÁ, Pérez-Velázquez J, Hense BA, Kuttler C, Jalalimanesh A, Maeda T, Pérez-Eretza B, Tomás M, Wood TK, García-Contreras R (2018) Selection of *Pseudomonas aeruginosa* quorum sensing by pyocyanin. In revision.
16. Pérez-Velázquez J, Hense B (2017) Differential equations models to study quorum sensing. In: Leoni L, Rampioni G (eds) Quorum sensing: methods and protocols. Humana Press, New York
17. Fekete A, Kuttler C, Rothballer M, Hense BA, Fischer D, Buddrus-Schiemann K, Lucio M, Müller J, Schmitt-Kopplin P, Hartmann A (2010) Dynamic regulation of n-acyl-homoserine lactone production and degradation in *Pseudomonas putida* ISOF. FEMS Microbiol Ecol 72:22–34
18. Kuttler C, Hense BA (2008) Interplay of two quorum sensing regulation systems of Vibrio fischeri. J Theor Biol 251:167–180

19. Müller J, Kuttler C, Hense BA, Rothballer M, Hartmann A (2006) Cell-cell communication by quorum sensing and dimension-reduction. J Math Biol 53:672–702
20. Mund et al (2016) An age-dependent model to analyse the evolutionary stability of bacterial quorum sensing. J Theor Biol 405:104–115. https://doi.org/10.1016/j.jtbi.2015.12.021

Zinc Efflux in *Trichomonas vaginalis*: In Silico Identification and Expression Analysis of CDF-Like Genes

J. C. Torres-Romero, María Elizbeth Alvarez-Sánchez, K. Fernández-Martín, L. C. Alvarez-Sánchez, V. Arana-Argáez, M. Ramírez-Camacho, and J. Lara-Riegos

Abstract Zinc (Zn) is a common essential component for all organisms because this metal serves as a cofactor or structural element for enzymes and metalloproteins involved in several important biological processes. However, excess levels of Zn can be toxic, as a consequence, the cells have evolved homeostatic mechanisms to regulate intracellular levels of this trace mineral. Zinc efflux and sequestration into internal cellular compartments from cells are mediated, in large part, by the ZNT/SLC30 proteins, which belong to the CDF family of ion transporters. The CDF family has evolved in prokaryotes and has been reported in several organisms, such as fungi, plants, and animals. Zn has been shown to regulate expression of proteins involved in metabolism and pathogenicity mechanisms in the protozoan pathogen *Trichomonas vaginalis*, in contrast high concentrations of this element were also found to be toxic for *T. vaginalis* trophozoites. Until now, Zn homeostasis mechanisms are not yet clear in this parasite. We performed a genome-wide analysis and localized eight members of the CDF gene family in *T. vaginalis* (*TvCDF1-8*).

J. C. Torres-Romero (✉) · K. Fernández-Martín · J. Lara-Riegos
Laboratorio de Bioquímica y Genética Molecular, Facultad de Química de la Universidad Autónoma de Yucatán, Mérida, Yucatán, Mexico
e-mail: julio.torres@correo.uady.mx

M. E. Alvarez-Sánchez
Posgrado en Ciencias Genómicas, Universidad Autónoma de la Ciudad de México (UACM), Ciudad de México, Mexico

L. C. Alvarez-Sánchez
Laboratorio de Virología, Centro de Investigaciones Regionales "Dr. Hideyo Noguchi" de la Universidad Autónoma de Yucatán, Mérida, Yucatán, Mexico

V. Arana-Argáez
Laboratorio de Farmacología, Facultad de Química de la Universidad Autónoma de Yucatán, Mérida, Yucatán, Mexico

M. Ramírez-Camacho
Centro de Información de Medicamentos, Facultad de Química de la Universidad Autónoma de Yucatán, Mérida, Yucatán, Mexico

L. Olivares-Quiroz, O. Resendis-Antonio (eds.), *Quantitative Models for Microscopic to Macroscopic Biological Macromolecules and Tissues*,
https://doi.org/10.1007/978-3-319-73975-5_8

With the use of in silico analyses, the TvCDF protein sequences revealed high conservation and show similar properties to the reported in other CDF orthologs. We analyzed the expression patterns of *TvCDF1-8* transcripts in trophozoites growth under high zinc concentrations, which showed down-regulation in expression. These results indicate that *TvCDF* genes encode membrane transporters and strongly supported their identity as members of CDF-like gene family, and further suggest the function in Zn efflux and sequestration in *T. vaginalis*.

Keywords Zinc · CDF transporters · In silico analysis · Gene expression · *Trichomonas vaginalis*

1 Introduction

The transition metals are necessary for, probably, all organisms as trace elements, which take up the elements they need from their environment. When the metal requirements are satisfied, growth and development of the cells are optimal. If metal uptake is not sufficient, deficiency occurs. On the other hand, when uptake is in excess can lead to toxicity. Each organism has a concentration range for each trace element to maintain an optimal transition metal homeostasis [1, 2].

Following iron, zinc is the second most abundant transition metal cofactor. Zinc plays structural, signaling, and regulatory roles and is found in thousands of proteins, commonly required for the function of more than 300 enzymes spanning all classes. For all these reasons, zinc is an essential micronutrient for all living organisms, from the most complex to the most primitive, including microorganisms. However, excess zinc is toxic to the cell, possibly through inhibition of key enzymes and competition with other relevant metal ions. Thus, a specific concentration range for zinc exists for each living organism [3, 4].

2 Zinc and Pathogenic Microorganisms

In order to grow successfully, microorganisms must have a supply of numerous substances including chemical requirements. Among these chemical requirements for microbial growth include trace elements, such as iron, copper, and zinc. The ability of pathogenic microorganisms to obtain these micronutrients of their host is fundamental to survive and plays a central role in the pathogenesis and the maintenance of a successful infection [5].

Specifically, the zinc is often used for the synthesis of microbial enzymes. Certain microorganisms may also require zinc as cofactors of enzymes and for the proper function of transcription factors [6]. Bioavailable levels of zinc for microbial growth in nature are sufficiently low that most microbes have evolved high-affinity binding and transport systems [7]. The key of the zinc homeostasis in any cell is the

transport. This homeostasis depends on maintaining correct number of transporters in the appropriate location and the concentration of zinc available for transport [8]. Since the excess of zinc is also toxic for the microorganisms, the zinc homeostasis can be envisioned as the equilibrium between metal uptake and efflux from the microbial cells. In many microorganisms, there are several different types of membrane transporters that maintain zinc homeostasis; these include P1B-ATPase family, natural resistance-associated macrophage protein (NRAMP) family, zinc-regulated transporter (ZRT), iron-regulated transporter (IRT)-like protein (ZIP), and cation diffusion facilitator (CDF) family [7, 9, 10]. The CDF family has evolved in prokaryotes and has been reported in several eukaryotic microorganisms, principally in yeasts and parasitic protists [7, 11, 12].

3 CDF Transporters

The CDF family of transporters was first described as a novel family of heavy metal transporters [13]. Although the first identified member of this family was CzcD of *Cupriavidus* (formerly *Ralstonia*) *metallidurans*, it has been reported that this is a ubiquitous family, members of which are found in all three domains of life [14, 15]. Mammalian members have been named "ZnT" and given the systematic name of SLC30 [16].

Although initially the key feature of this family was that they just transport zinc, CDFs have been shown to mediate the transport of other metal ions such as Mn^{2+}, Fe^{2+}, Ni^{2+}, Cd^{2+}, Co^{2+}, and Cu^{2+} [14, 17]. All CDF proteins described in bacteria are involved in resistance to Zn^{2+} and other heavy metal cations. Plant CDFs are called MTPs (metal tolerance proteins) and have primarily been characterized as Mn^{2+} transport proteins. In higher animals, including humans, the ZnT proteins mainly transport Zn^{2+} [14, 18]. For this reason the CDF family is divided into three subfamilies according to the metals they transport: CDF-Zn, CDF-Fe/Zn, and CDF-Mn [15]. Based on phylogenetic analysis, the CDF family is divided into 18 clades, which includes substrate-defined clades for Ni^{2+}, Cd^{2+}, Co^{2+}, and Cu^{2+} transporters. This new grouping of CDFs into defined clades also suggests that Zn^{2+} and Mn^{2+} transport, via CDFs, in eukaryotes and prokaryotes is polyphyletic [19].

The topology of the CDF transporters was predicted based on the prokaryotic proteins belonging to this family. Most members possess six transmembrane domains (TMs) with N- and C-termini on the cytoplasmic side of the membrane (Fig. 1). However, it has been reported that some CDF members, notably the MSC2 protein of *Saccharomyces cerevisiae* and the ZnT5 and ZTL1 in humans, can exhibit from 12 to 15 TMs [20–22]. The function of these additional transmembrane domains has not been clearly demonstrated, but may be related to how these proteins interact with their partners in the heteromeric complexes, while the rest of the CDF transporters functions as a homodimer [17].

The greatest degree of conservation among CDF proteins is found within transmembrane domains I, II, and V. These three TM domains are also highly

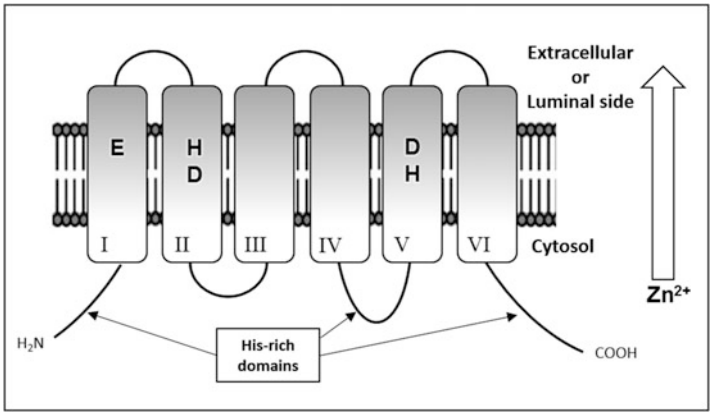

Fig. 1 The predicted topology of CDF/Znt/SLC30 family of metal ion transporter. CDF transporters is predicted to have six transmembrane domains, which are numbered (I–VI). Conserved polar or charged residues that participate in the metal recognition and transport: Glutamate (E) within TM-I and the quartet of Histidine-Aspartate (HD-HD) in the TM-II and -V are indicated. The histidine-rich domains that are implicated in sensing and translocating zinc to the HD-HD site and potentially related in transport activity regulation are also indicated

amphipathic suggesting an important role in substrate transport. This hypothesis is supported by the observation that certain polar or charged amino acids within these domains are among the most highly conserved [23]. Several studies have suggested that the composition of the tetrahedral transport site determines the transport specificity in CDF transporters. This tetrahedral transport site, commonly referred to as metal-binding site A, contains two aspartic acids and two histidines of TM helices II and V referred to as the quartet or HD-HD motif (Fig. 1). The variant DD-HD of the A-site quartet motif has been shown to be responsible for Cd and Zn transport in bacteria. An asparagine is present in human ZnT10 (ND-HD), is other variant which can function as a manganese transporter, while the DD-DD motif is found in plant ZnT homologs that also transport manganese [15, 17, 24, 25].

In yeast and plant ZnT homologs, many amino acids other than HD-HD have been shown to affect metal specificity. Members of the CDF family often contain a histidine-rich region, either between TMs IV and V or at the N- and/or C-termini or at all three locations (Fig. 1). Such regions are predicted to be cytoplasmic, *cis* to metal uptake, and could function as potential metal (Zn^{2+}, Co^{2+}, and/or Cd^{2+}) binding domains. The cytosolic histidine-rich loop, between TMs IV and V, is observed in the Zn^{2+} transporters only and is thought to be implicated in sensing and translocating zinc to the HD-HD site [14, 15, 17]. Although the histidine-rich located in terminus of CDF proteins could not be determinant for the transport, they could have a function as regulators of transport activity of these proteins [18, 26].

4 Zinc in *Trichomonas vaginalis*

The flagellate parasitic protozoan *Trichomonas vaginalis* is the etiologic agent of trichomoniasis, the most common non-viral sexually transmitted infection (STI) in the world. The infection occurs in the female and male urogenital tract and humans are the only natural host for this parasite. The World Health Organization (WHO) estimates an incidence of 276 million new cases each year and prevalence of 187 million of infected individuals. However, the infection is not notifiable [27].

Like other protozoan parasites, *T. vaginalis* requires significant quantities of nutrients, which acquires from their hosts through cell membrane transport and phagocytosis. The pathogenesis of *T. vaginalis* is a multifactorial process which depends, in large part, on the ability of trichomonads to acquire essential micronutrients, which include divalent metal ions such as iron, zinc, calcium, among others [28–30].

Trichomoniasis is asymptomatic in 40–75% of men. It has been postulated that this is due, in part, to high zinc concentration in prostatic fluid (4–7 mM). However, levels <1.6 mM of zinc are well tolerated by *T. vaginalis* trophozoites and could modulate expression of several proteins involved in the pathogenesis by this parasite [31, 32].

4.1 Zinc and Trichomonal Virulence

Zinc concentration can differentially modulate the virulence factors of *T. vaginalis*. The adhesion of *T. vaginalis* trophozoites to host cells involved at least five adhesins: AP23, AP33, AP51, AP65, and AP120. The expression of four of them (exception by AP120) is at least upregulated at the transcriptional level by zinc [29, 33, 34]. Parasite cytoadherence is followed by a cytotoxic effect, where several molecules participate, including proteinases, such as TVCP39 and TVCP65, whose expression is down-regulated in high zinc concentrations [29, 32, 35]. Moreover, the metalloproteinases TvMP50, whose expression is increased in the presence of zinc and TvGP63, which contains a zinc-binding motif (HEXXH), play important roles in parasite proteolytic activity and host cell apoptosis, respectively [32, 36–38].

5 Zinc Homeostasis in *Trichomonas vaginalis*

Despite the evidences that zinc participates in the *T. vaginalis* virulence modulation, little is known regarding their zinc homeostasis-regulating proteins. In eukaryotic cells, zinc homeostasis results from a coordinated regulation by different proteins belonging to the ZIP and CDF transporter families, and zinc-binding proteins (i.e., metallothioneins) involved in uptake, excretion and intracellular storage/trafficking of zinc, respectively.

The information with respect to zinc-binding proteins in *T. vaginalis* is poor. Nevertheless, zinc has been proposed to act as a possible regulator of many proteins that contain "zinc fingers" domains. These proteins have been identified within the *T. vaginalis* genome sequences by in silico analysis and others in an experimental way, as the protein HMP35, a protein from hydrogenosomes, which has a putative RING-like, zinc-binding, cysteine-rich motif [39, 40].

Recently, we identified in *T. vaginalis* eight *ZIP*-like genes (*TvZIP*) with high similarity to the canonical ZIP transporters. At least six *TvZIP* genes are regulated at the transcriptional level by zinc, suggesting that these membranous transporters may be implicated in the Zn uptake in this protozoan parasite [41].

6 Identification of CDF Transporters in *T. vaginalis*

Since the genome sequence of the protozoan parasite *T. vaginalis* was published in 2007 [39], this provided an opportunity to identify target genes by homology analysis using various bioinformatic tools. Three representative CDF protein sequences such as *S. cerevisiae* ZRC1 (NP_013970.1), *C. metallidurans* CzcD (CAA67085.1), and *E. coli* FieF (P69380.1) were used as queries in the *T. vaginalis* genome database (www.trichdb.org) to retrieve the CDF transporter homologous. The genome location of the *T. vaginalis* CDF (*TvCDF*) like genes was analyzed and the complete gene sequences were obtained. Through this genome-wide search strategy, we identified in *T. vaginalis* 8 putative *CDF-like* genes based on similarity to previously characterized CDF proteins in other organisms. Several studies suggested that, due to the large size of the *T. vaginalis* genome (∼160 Mb), a significant portion of the proteome contains paralogous proteins [42, 43]. All *TvCDF* genes identified were found annotated from the whole genome as putative cation diffusion facilitator or cation efflux protein/zinc transporters. All trichomonad *CDF* genes have full-length open reading frames (ORF) ranging from 1038 to 1488 base pairs (bp) (Table 1).

Table 1 List of *CDF* genes identified in *T. vaginalis* genome

Gene name	Gene ID TrichDB	Genome location			ORF (base pairs)	NCBI accession
		Genome sequence	Start	End		
TvCDF1	TVAG_132220	DS113908	7072	8382	1308	XM_001306434
TvCDF2	TVAG_228020	DS114074	14310	12994	1314	XM_001303830
TvCDF3	TVAG_285720	DS114481	11412	12722	1308	XM_001300194
TvCDF4	TVAG_060360	DS113353	61220	59982	1236	XM_001321848
TvCDF5	TVAG_027220	DS113573	40429	41474	1038	XM_001314062
TvCDF6	TVAG_093530	DS113185	108078	109568	1488	XM_001583115
TvCDF7	TVAG_283320	DS113192	194739	196067	1326	XM_001582098
TvCDF8	TVAG_437450	DS113194	264494	265792	1296	XM_001581885

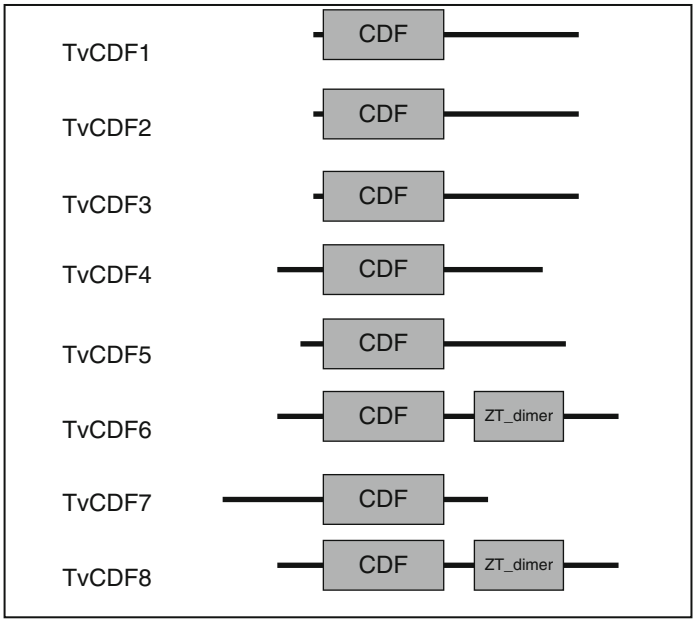

Fig. 2 Schematic representation of the domain architecture of CDF transporters in *T. vaginalis*. The proteins were drawn approximately to scale. The domains are named and located according to the CCD and SMART protein domain databases. *CDF* cation diffusion facilitator, *ZT_dimer Zinc Transport dimerization*

6.1 In silico Analysis of TvCDF Sequences

Several studies have investigated the use of multiple in silico prediction tools to assess the predictive accuracy or the use of consensus programs (metservers) that combine the output from several in silico prediction tools and produce a single consensus outcome, all of which have been reported to offer improved performance over individual tools [44]. Here we analyzed the characteristics of TvCDF sequences by at least two different algorithms. Genomic annotations of the relative positions of the conserved domains within each TvCDF sequence were evaluated through the identification of CDF domains predicted by comparison using the NCBI Conserved Domains Database (https://www.ncbi.nlm.nih.gov/cdd) and the SMART program [45]. The information retrieved by both programs for each gene was used to obtain a graphic representation of the conserved domains found in the selected TvCDF sequences using the SMART database based on CDF domain and had e-values higher than 1^{-10}. As shown in Fig. 2, all TvCDFs possess at least one Cation_efflux domain, of which TvCDF6 and TvCDF8 possess an additional dimerization domain for zinc transporters (ZT_dimer).

It has been demonstrated that most of the CDF family members have six predicted transmembrane (TM) domains, where two aspartic acids and two histidines

in TM-II and TM-V acts as potential metal-binding site [17]. The prediction of the transmembrane regions of the TvCDF-like transporters was constructed based on TMHMM (http://www.cbs.dtu.dk/services/TMHMM) and MEMSAT-SVM (http://bioinf.cs.ucl.ac.uk/psipred/) methods [46, 47]. The predicted topology of TvCDF proteins was illustrated in Fig. 3. TvCDF1, TvCDF2, TvCDF3, TvCDF5, TvCDF7, and TvCDF8 demonstrated the presence of the expected six transmembrane (TM) regions and both the N- and C-terminus located on the intracellular surface of the cell, in agreement with the observed in most of the CDF transporters previously reported. It was found that all TM structures are α-helices consisting of 16-24 amino acid residues. Exceptionally, TvCDF4 and TvCDF6 exhibited the presence of nine and ten TM regions, respectively. However it is consistent with other large CDF members as the ZnT5 reported in humans [17]. This heterogeneity in structure of each TvCDF transporter suggests diversity in functionality.

To find out conserved regions of TvCDF proteins, a multiple alignment with the deduced amino acid sequences of all eight transporter sequences was achieved with the MUSCLE algorithm (http://www.ebi.ac.uk/Tools/msa/muscle/). Alignments were shaded using the program BOXSHADE (https://embnet.vital-it.ch/software/BOX_form.html) at a threshold fraction of 0.3 (no reference sequence). The identical and similar residues were shaded black and gray, respectively. Due to variations between TvCDF predicted sequences, TvCDF1 was used as reference to enumerate potential TM domains. Predicted locations of TM domains were labeled above the sequences as TM I-VI (Fig. 4).

Multiple alignment of these eight sequences showed that TvCDF1, TvCDF2, and TvCDF3 display the same conserved residues found in all members of group I CDF proteins, indicating that these TvCDF transporters are probably responsible for zinc efflux. In addition, locations of the amino acid residues histidine (H) and aspartate (D), which has been suggested to be responsible for zinc binding, are conserved in the TM II and TM V of these three TvCDF. Remarkably, TvCDF7 and TvCDF8 present the conserved motifs: DSXLD and DHRND, which lie in TMs II and V, respectively. The conserved residues (DXXXD) has been implicated to play an important role as a heavy metal-binding site and manganese transport through the membrane, principally in plants [17, 24]. Although conserved metal-binding motif was not found in none of the other three TvCDF (TvCDF4-6) proteins, they specifically present a CDF domain, as mentioned above, indicating the high diversity between TvCDF paralogs.

6.2 Conserved Motif and Primary Sequence Analysis of TvCDFs

To identify the most conserved motif sequences in TvCDF proteins we performed a Motif analysis using MEME tool [48] with the following parameters; maximum number of motifs to find, 5; minimum and maximum motif width set to 6 and 50 amino acids (http://meme.nbcr.net/meme/tools/meme). Five motifs were identified

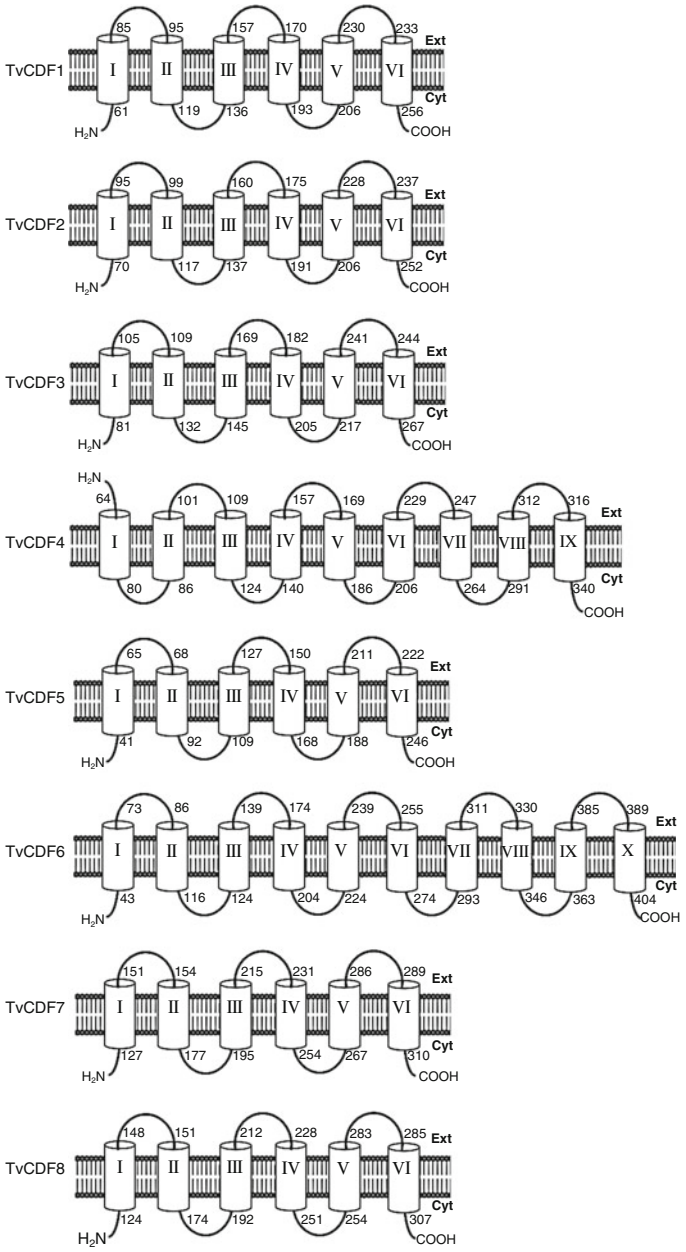

Fig. 3 Putative topology of TvCDF transporters. Prediction of the topology for *T. vaginalis* CDF transporters summarizing the linear coordinates for the helices and indicating the extra- and intracellular regions. Circles with roman numerals represented transmembrane regions. NH_2 and COOH terminal regions were labeled and represented as single lines

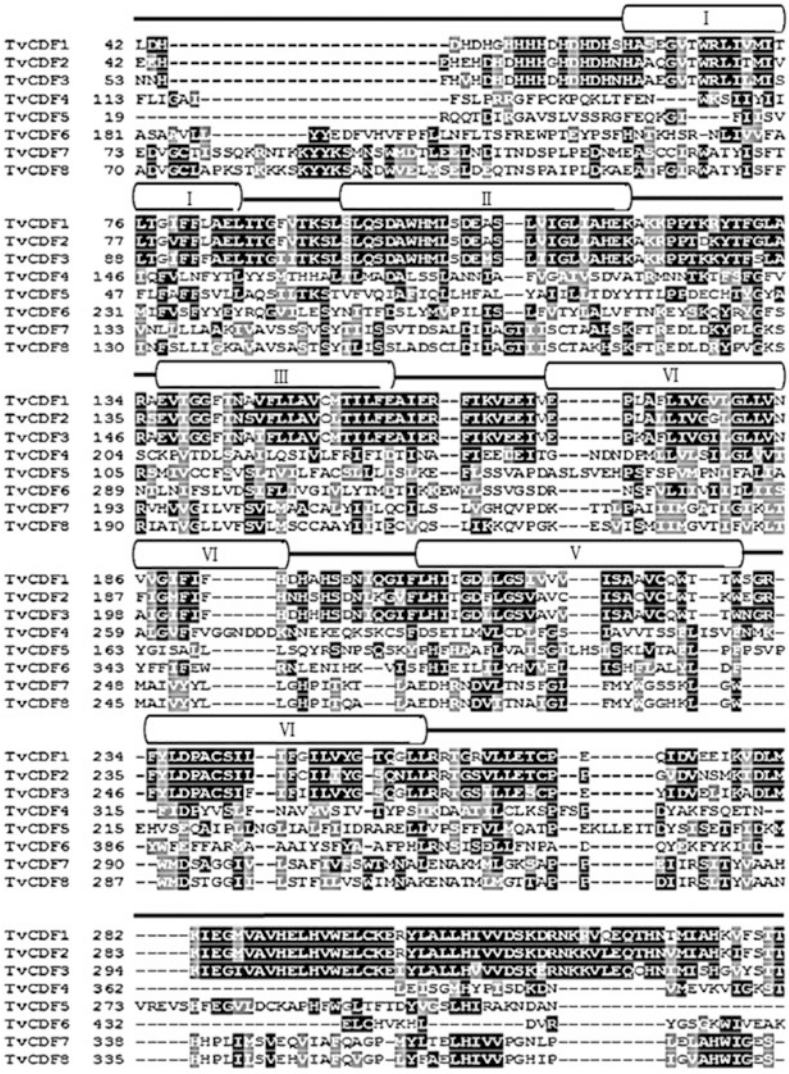

Fig. 4 Alignment of predicted *T. vaginalis* CDF proteins. Sequences alignment was performed by use of the MUSCLE algorithm (http://www.ebi.ac.uk/Tools/msa/muscle/) and identical or similar amino acids were shaded by BOXSHADE (http://www.ch.embnet.org/software/BOX_form.html). Boxes with roman numerals above the sequence indicated the transmembrane spanning domains. Single lines represented the extra- and intracellular regions between TM domains

with an e-value support lower than 1^{-35} and their annotation was searched in Pfam database (http://pfam.xfam.org/). Motifs 1–4 were 50 amino acid residue long, while motif 5 was 41 amino acids. Motifs 3, 4, and 5 were related to CDF protein family and present in all TvCDF sequences. Interestingly all identified motifs correspond to TM domains (Table 2).

The physicochemical parameters of TvCDF sequences were analyzed by using Expasy's ProtParam server [49]. The average protein length ranges from 346 to 496 amino acids. Many studies have reported that the majority of CDF family members consist of 220–650 amino acid residues. Also, were included in the study the molecular weight which ranges from 38,716 to 58,607 Da and the isoelectric point (pI) ranging from 5.30 to 8.08 (Table 3), which are closely related to the characteristics of CDFs from other species. Based on CELLO analysis [50], the subcellular location was predicted (http://cello.life.nctu.edu.tw/). All TvCDF transporters were predicted to be located in the plasma membrane, suggesting that they could be responsible for the zinc efflux in *T. vaginalis*. However, other bioinformatic programs predict the possible location in other membranous organelles (data not shown) that they might be involved in ion detoxification through compartmentalization. For putative functional analysis of the TvCDF proteins, a specialized tool PFP from Kihara Bioinformatics Laboratory (http://kiharalab.org/web/pfp.php), which extracts and scores GO annotations based on their frequency of occurrence in the retrieved sequences, predicted that all TvCDF proteins have the molecular activity as transporter during the biological process of cation transport (Table 3).

6.3 Phylogenetic Analysis of TvCDF Sequences

In order to establish evolutionary relationships between TvCDF proteins and reference CDF proteins, a phylogenetic tree was carried out with sequences from various species using the neighbor-joining method and the JTT correction model. To this purpose, nine sequences from different species were used, including a selection of previously identified mammalian, invertebrate, fungal, and bacterial CDF sequences. The reliability of the phylogenetic tree was estimated using bootstrap values with 1000 replicates using MEGA version 7.0 software (www.megasoftware.net). The phylogenetic tree classified the CDF proteins into three main subfamilies: CDF-Zn, CDF-Zn/Fe, and CDF-Mn (Fig. 5), consistent with published data and sequence similarities between CDF orthologs.

The phylogenetic analysis showed that TvCDF1, 2, and 3 were closely related to members of the subfamily CDF-Zn. It was suggested that the amino acid residues DH-DH is responsible for Zn transport [17], that are conserved in these three first TvCDFs, which indicates that they may be functionally related to Zn efflux in *T. vaginalis*. In addition, TvCDF7 and TvCDF8 formed a cluster with other two members of the subfamily CDF-Mn, since they conserved the quartet DD-DD found in CDF homologs that transport manganese (Figs. 4 and 5). With respect to

Table 2 Conserved motif sequences TvCDF transporters defined by MEME software

Motif	Width	*E* value	Sequence	Protein domain family
1	50	2.3e-065	NTMIAHKVFSTTVQIEFVDDFPQGTDHIGSCFYATSFGSDRIFQT PPVYQHSIGCPHVNLPGHEHDHDH	Not found
2	50	7.7e-050	PGVDVNSMKIDLMKIEGMVAVHELHVWELCKERYLALLH IVVDSKDRNKKVLEQTHNVMIAHKIFSTTVQ	Not found
3	50	1.7e-044	TGIFFLAELITGFVTKSLSLQSDAWHMLSDEASLVIGLIAHEKAKKP PTKRYTFGLARAEVIGGFTNAVF	Cation_efflux
4	50	2.0e-049	GDLLGSIVVVISAAVCQWTTWSGRFYLDPACSILIFGILVYG TQGLLRRTGRVLLETCPEQIDVEEIKVD	Cation_efflux
5	41	9.9e-023	YTFSLARAEVIGGTNAIFLLAVCMTILFEAIERFIKV EEIVEPKAFLIVGILGLLVNAIG	Cation_efflux

Table 3 Predicted physicochemical properties, location and functions of tvCDF proteins

Name	NCBI accession	Theoretical properties			Location subcellular		Molecular function	biological process
		Deduced protein length (aa)	Molecular weight (Da)	Theoretical isoelectric point	CELLO	KHIARA		
TvCDF1	XM_001306434	436	48,446	5.61	Plasma membrane	Membrane	Transporter activity	Cation transport
TvCDF2	XM_001303830	438	49,521	5.68	Plasma membrane	Membrane	Transporter activity	Cation transport
TvCDF3	XM_001300194	436	49,394	5.71	Plasma membrane	Membrane	Transporter activity	Cation transport
TvCDF4	XM_001321848	412	46,440	6.44	Plasma membrane	Membrane	Transporter activity	Cation transport
TvCDF5	XM_001314062	346	38,716	5.74	Plasma membrane	Membrane	Transporter activity	Cation transport
TvCDF6	XM_001583115	496	58,607	8.08	Plasma membrane	Membrane	Transporter activity	Cation transport
TvCDF7	XM_001582098	442	48,812	5.30	Plasma membrane	Membrane	Transporter activity	Cation transport
TvCDF8	XM_001581885	432	47,736	5.63	Plasma membrane	Membrane	Transporter activity	Cation transport

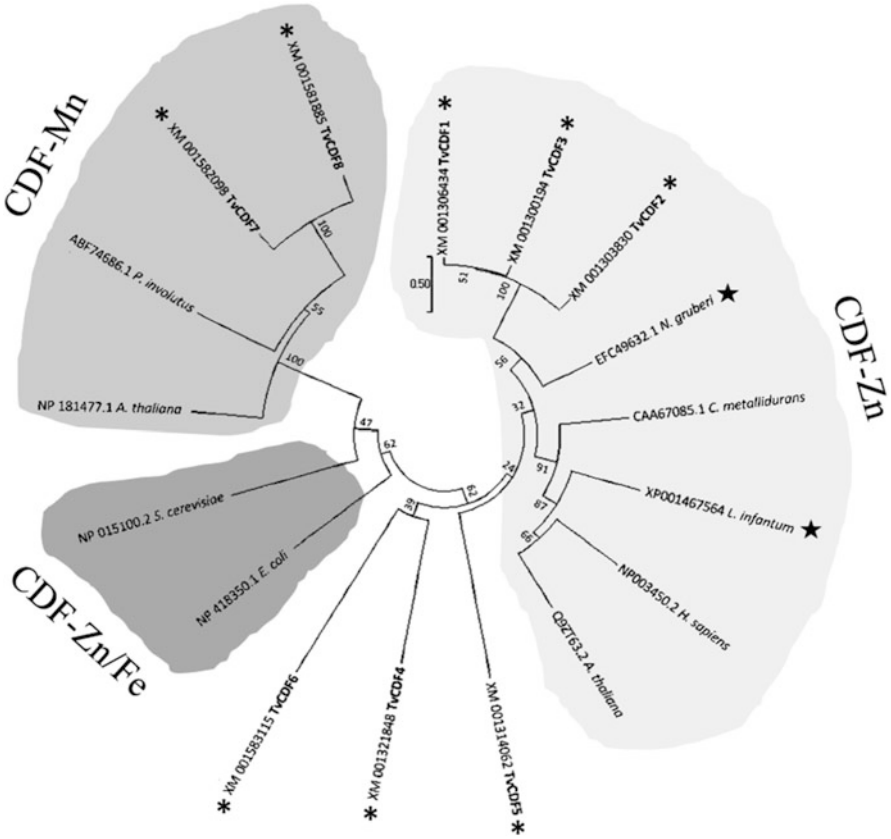

Fig. 5 Phylogenetic relationship of the TvCDF proteins with homologous sequences from selected species. A rooted, neighbor-joining (NJ)-based tree of the CDF proteins was constructed with the deduced sequences of CDF proteins from the three different subfamilies (CDF-Zn, CDF-Zn/Fe, and CDF-Mn). Asterisks indicate the TvCDF sequences. Stars indicate two closely related protozoan CDFs (*Naegleria gruberi* and *Leishmania infantum*)

TvCDF5, 6 and 7, the phylogenetic relationship is not clear, at least with the number of sequences used for this study (Fig. 5).

6.4 Gene Expression Analysis in Response to Zinc

To verify the effect of zinc on the expression of the *TvCDF* genes, the transcriptional profiling was performed on *T. vaginalis* trophozoites grown in Diamond's trypticase-yeast-extract-maltose (TYM medium) supplemented with 12% heat-inactivated horse serum. The zinc-supplemented medium was prepared by adding zinc sulfate at different final concentrations (0.5, 1.0, and 1.5 mM), accord-

ing to previous reports [51]. Total RNA was isolated from normal and treated *T. vaginalis* trophozoites and treated with DNase. First-strand cDNA was synthesized. To examine the expression profiles of target genes, semi-quantitative RT-PCR was employed using 0.2 μL cDNA preparation as a template. All gene-specific primers for *T. vaginalis* target genes were designed using Primer-Blast (http://www.ncbi.nlm.nih.gov/tools/primer-blast/). As an internal control, the constitutively expressed *tubulin* gene from *T. vaginalis* was used. For each primer pair the PCR program was empirically adjusted. PCR products were analyzed using 1% agarose gels stained with ethidium bromide.

We found that under control conditions without zinc salt, all of the analyzed *TvCDF* genes could be detected. Moreover, when *T. vaginalis* cultures were supplemented with zinc, the expression of *TvCDF1, 4,* and *7* was suppressed at the higher concentration of $ZnSO_4$ tested (1.5mM), while the transcript levels of *TvCDF2, 5,* and *8* were not distinct from those observed in the control condition (Fig. 6). Interestingly, the transcript level of *TvCDF3* was increased in the presence of $ZnSO_4$ at 0.5 mM and remains unchanged in the higher zinc concentrations. On the other hand, *TvCDF6* also showed an increase in the level expression but until the 1.0 mM concentration of $ZnSO_4$ and returns to basal levels in higher concentration. These data showed that the expression of some of the *TvCDF* genes is regulated by zinc availability.

7 Discussion and Perspectives

Due to the complexity of the biological processes, the biology and computer science did not seem to have any relationship. This link began when some investigators detailed that nature uses algorithm-like procedures to solve biological problems. By viewing these biological systems as information processing units, bringing together computational, statistical, experimental, and technological methods, they gave rise to the computational molecular biology. Over the last few years, this strategy has been successfully used in the improvement in our ability to study detailed aspects of molecular, cellular, organism-level biological systems, and the analysis of large gene lists within the complete genomes of several organisms, actually recognized as bioinformatic analyses.

T. vaginalis depends on zinc to modulate the expression of several genes and proteins that participate in their metabolism. Although the amount of data on zinc-dependency in trichomonads is available, the mechanisms of zinc homeostasis in this parasite have just started to be elucidated. Recently, we found ZIP-like sequences in the *T. vaginalis* genome demonstrated a zinc-dependent expression at the transcriptional level, which suggests a role for the zinc uptake in this parasitic protist [41]. However, the transporters involved in the zinc efflux to avoid the excess-related toxicity of this metal in this parasite have not been reported, until now.

In this work, using bioinformatic tools, we report eight CDF-like transporters in *T. vaginalis,* which were characterized based on similarity to other CDF family

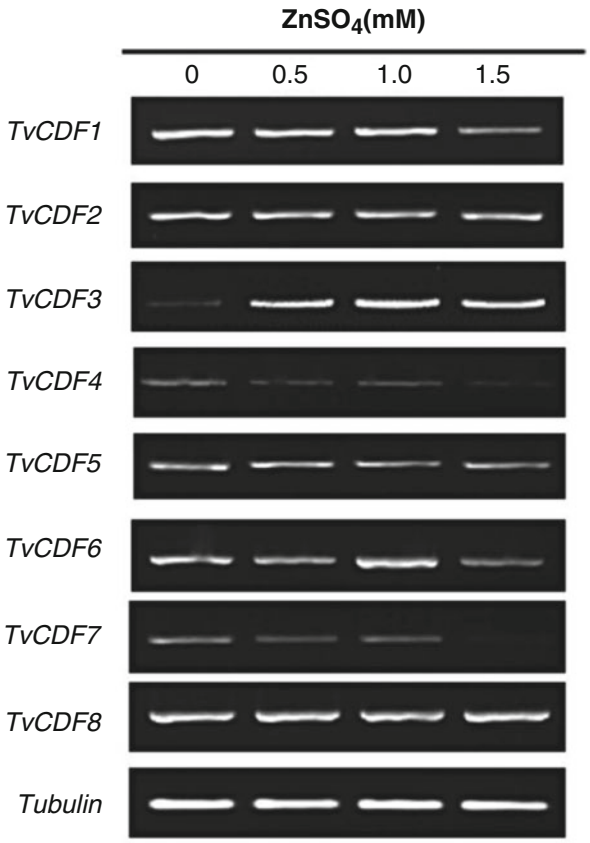

Fig. 6 Expression analysis of *TvCDF* genes in *T. vaginalis* trophozoites cultured under excess zinc concentrations. Expression levels of *TvCDF genes* (TvCDF1-8) were addressed by adding increasing concentrations of ZnSO4 (0, 0.5, 1.0, 1.5 mM) to the culture medium for 24 h. Tubulin gene was used as a constitutively expressed control gene. Analysis was performed by RT-PCR

members. Since the genome sequence of *T. vaginalis* was released, the large size suggested that a significant portion of the proteome contains paralogous proteins [43]. Many studies have reported that the majority of CDF family members consist of 220–650 amino acid residues. ORF analysis of the *TvCDF* genes showed that comprises from a minimum of 1038 (*TvCDF5*) to maximum of 1488 (*TvCDF6*) base pairs (Table 1), which are closely related to the size of *CDF*s from other species [52].

Prediction of TM domains in TvCDF family proteins revealed that the majority presents 6 TM domains (Fig. 3), consistent with the observed in most of the CDF genes in other species. However, TvCDF4 and TvCDF6 exhibit more TM domains, and are more likely to indicate that they belong to the large CDF members [17]. Taken together all bioinformatic and gene expression analyses, we can conclude that

T. vaginalis presents at least three CDF transporters (TvCDF1, 2, and 3) which we found that could be located on the membrane of this protozoan parasite regulating the zinc efflux. Also, this parasite contains other five members of the CDF family that may be capable of transporting other divalent metals in addition to zinc, as manganese.

This study is the first to characterize the CDF gene family and report the expression profile of these types of proteins in this parasite. Although CDF orthologs have been characterized in many eukaryotic cells, to our knowledge, there are no reports concerning the identification and characterization of CDFs in protozoan parasites. Our future works will explore whether the variations in zinc concentrations in the natural environment during infection, principally in male patients, explain the way this anaerobic parasite controls gene expression and their virulence. Nevertheless, these data could bring new insights into the mechanism of zinc transport in *T. vaginalis*.

Acknowledgments This work was undertaken as part of a research project supported by grant 237990 (to J. C. Torres-Romero) from Consejo Nacional de Ciencia y Tecnología (CONACYT), México. K. G. Fernández-Martín is a scholarship recipient from CONACYT.

Conflict of Interest: The authors declare that they have no conflict of interest regarding the publication of this paper.

References

1. Maret W (2013) Zinc and the zinc proteome. In: Banci L (ed) Metallomics and the cell. Springer, Dordrecht, pp 479–501
2. Prashanth L, Kattapagari KK, Chitturi RT, Baddam VRR, Prasad LK (2015) A review on role of essential trace elements in health and disease. J NTR Univ Health Sci 4(2):75
3. Blindauer CA (2015) Advances in the molecular understanding of biological zinc transport. Chem Commun 51(22):4544–4563
4. Wang D, Fierke CA (2013) The BaeSR regulon is involved in defense against zinc toxicity in *E. coli*. Metallomics 5:372–383
5. Abu Kwaik Y, Bumann D (2013) Microbial quest for food in vivo: 'nutritional virulence'as an emerging paradigm. Cell Microbiol 15(6):882–890
6. Cerasi M, Ammendola S, Battistoni A (2013) Competition for zinc binding in the host-pathogen interaction. Front Cell Infect Microbiol 3:108
7. Porcheron G, Garénaux A, Proulx J, Sabri M, Dozois CM (2013) Iron, copper, zinc, and manganese transport and regulation in pathogenic Enterobacteria: correlations between strains, site of infection and the relative importance of the different metal transport systems for virulence. In: Veyrier F, Cellier M (eds) Metal economy in host-microbe interactions. Frontiers Media SA, Lausanne, pp 172–195
8. Nies DH (2007) How cells control zinc homeostasis. Science 317:1695–1696
9. Kambe T, Yamaguchi-Iwai Y, Sasaki R, Nagao M (2004) Overview of mammalian zinc transporters. Cell Mol Life Sci 61:49–68
10. Nadadur SS, Srirama K, Mudipalli A (2008) Iron transport and homeostasis mechanisms: their role in health and disease. Indian J Med Res 128:533–544
11. Dean P, Major P, Nakjang S, Hirt RP, Embley TM (2014) Transport proteins of parasitic protists and their role in nutrient salvage. Front Plant Sci 5:153

12. North M, Steffen J, Loguinov AV, Zimmerman GR, Vulpe CD, Eide DJ (2012) Genome-wide functional profiling identifies genes and processes important for zinc-limited growth of *Saccharomyces cerevisiae*. PLoS Genet 8(6):e1002699
13. Nies DH, Silver S (1995) Ion efflux systems involved in bacterial metal resistances. J Ind Microbiol 14:186–199. https://doi.org/10.1007/BF01569902
14. Kolaj-Robin O, Russell D, Hayes KA, Pembroke JT, Soulimane T (2015) Cation diffusion facilitator family: structure and function. FEBS Lett 589(12):1283–1295
15. Montanini B, Blaudez D, Jeandroz S, Sanders D, Chalot M (2007) Phylogenetic and functional analysis of the cation diffusion facilitator (CDF) family: improved signature and prediction of substrate specificity. BMC Genomics 8(1):107
16. Palmiter RD, Huang L (2004) Efflux and compartmentalization of zinc by members of the SLC30 family of solute carriers. Pflugers Arch 447(5):744–751
17. Kambe T, Tsuji T, Hashimoto A, Itsumura N (2015) The physiological, biochemical, and molecular roles of zinc transporters in zinc homeostasis and metabolism. Physiol Rev 95(3):749–784
18. Nies DH (2003) Efflux-mediated heavy metal resistance in prokaryotes. FEMS Microbiol Rev 27(2-3):313–339
19. Cubillas C, Vinuesa P, Tabche ML, García-de los Santos A (2013) Phylogenomic analysis of cation diffusion facilitator proteins uncovers Ni^{2+}/Co^{2+} transporters. Metallomics 5(12):1634–1643
20. Cragg RA, Christie GR, Phillips SR, Russi RM, Küry S, Mathers JC et al (2002) A novel zinc-regulated human zinc transporter, hZTL1, is localized to the enterocyte apical membrane. J Biol Chem 277(25):22789–22797
21. Kambe T, Narita H, Yamaguchi-Iwai Y, Hirose J, Amano T, Sugiura N et al (2002) Cloning and characterization of a novel mammalian zinc transporter, zinc transporter 5, abundantly expressed in pancreatic β cells. J Biol Chem 277(21):19049–19055
22. Li L, Kaplan J (2001) The yeast gene MSC2, a member of the cation diffusion facilitator family, affects the cellular distribution of zinc. J Biol Chem 276(7):5036–5043
23. Gaither LA, Eide DJ (2001) Eukaryotic zinc transporters and their regulation. In: Zinc biochemistry, physiology, and homeostasis. Springer, Dordrecht, pp 65–84
24. Gustin JL, Zanis MJ, Salt DE (2011) Structure and evolution of the plant cation diffusion facilitator family of ion transporters. BMC Evol Biol 11(1):76
25. Hoch E, Lin W, Chai J, Hershfinkel M, Fu D, Sekler I (2012) Histidine pairing at the metal transport site of mammalian ZnT transporters controls Zn^{2+} over Cd^{2+} selectivity. Proc Natl Acad Sci 109(19):7202–7207
26. Lee SM, Grass G, Haney CJ, Fan B, Rosen BP, Anton A et al (2002) Functional analysis of the *Escherichia coli* zinc transporter ZitB. FEMS Microbiol Lett 215(2):273–278
27. Menezes CB, Frasson AP, Tasca T (2016) Trichomoniasis-are we giving the deserved attention to the most common non-viral sexually transmitted disease worldwide? Microb Cell 3(9):404
28. Crouch ML, Benchimol M, Alderete JF (2001) Binding of fibronectin by *Trichomonas vaginalis* is influenced by iron and calcium. Microb Pathog 31(3):131–144
29. Figueroa-Angulo EE, Rendón-Gandarilla FJ, Puente-Rivera J, Calla-Choque JS, Cárdenas-Guerra RE, Ortega-López J et al (2012) The effects of environmental factors on the virulence of *Trichomonas vaginalis*. Microbes Infect 14:1411–1427
30. Torres-Romero JC, Arroyo R (2009) Responsiveness of *Trichomonas vaginalis* to iron concentrations: evidence for a post-transcriptional iron regulation by an IRE/IRP-like system. Infect Genet Evol 9:1065–1074
31. Krieger JN, Rein MF (1982) Zinc sensitivity of Trichomonas vaginalis: in vitro studies and clinical implications. J Infect Dis 146(3):341–345
32. Vazquez Carrillo LI, Quintas Granados LI, Arroyo R, Mendoza Hernández G, González Robles A, Carvajal Gamez BI, Alvarez Sánchez ME (2011) The effect of Zn2+ on prostatic cell cytotoxicity caused by *Trichomonas vaginalis*. J Integr OMICS 1(2):198–210

33. Garcia AF, Chang TH, Benchimol M, Klumpp DJ, Lehker MW, Alderete JF (2003) Iron and contact with host cells induce expression of adhesins on surface of *Trichomonas vaginalis*. Mol Microbiol 47(5):1207–1224
34. Moreno-Brito V, Yanez-Gomez C, Meza-Cervantez P, Avila-Gonzalez L, Rodriguez MA, Ortega-Lopez J, Gonzalez-Robles A, Arroyo R (2005) A trichomonas vaginalis 120 kDa protein with identity to hydrogenosome pyruvate:ferredoxin oxidoreductase is a surface adhesin induced by iron. Cell Microbiol 7:245–258
35. Hernández-Gutiérrez R, Avila-González L, Ortega-López J, Cruz-Talonia F, Gómez-Gutierrez G, Arroyo R (2004) Trichomonas vaginalis: characterization of a 39-kDa cysteine proteinase found in patient vaginal secretions. Exp Parasitol 107(3):125–135
36. Ma L, Meng Q, Cheng W, Sung Y, Tang P, Hu S, Yu J (2011) Involvement of the GP63 protease in infection of Trichomonas vaginalis. Parasitol Res 109(1):71–79
37. Quan JH, Kang BH, Cha GH, Zhou W, Koh YB, Yang JB et al (2014) Trichonomas vaginalis metalloproteinase induces apoptosis of SiHa cells through disrupting the Mcl-1/Bim and Bcl-xL/Bim complexes. PLoS One 9(10):e110659
38. Quintas-Granados L, Villalpando J, Vázquez-Carrillo L, Arroyo R, Mendoza-Hernández G, Alvarez-Sánchez ME (2013) TvMP50 is an immunogenic metalloproteinase during male trichomoniasis. Mol Cell Proteomics 12:1953–1964
39. Carlton JM, Hirt RP, Silva JC, Delcher AL, Schatz M, Zhao Q et al (2007) Draft genome sequence of the sexually transmitted pathogen *Trichomonas vaginalis*. Science 315(5809): 207–212
40. Dyall SD, Lester DC, Schneider RE, Delgadillo-Correa MG, Plümper E, Martinez A et al (2003) *Trichomonas vaginalis* Hmp35, a putative pore-forming hydrogenosomal membrane protein, can form a complex in yeast mitochondria. J Biol Chem 278(33):30548–30561
41. Fernández-Martín KG, Alvarez-Sánchez ME, Arana-Argáez VE, Alvarez-Sánchez LC, Lara-Riegos JC, Torres-Romero JC (2017) Genome-wide identification, in silico characterization and expression analysis of ZIP-like genes from *Trichomonas vaginalis* in response to zinc and iron. Biometals 30(5):663–675. https://doi.org/10.1007/s10534-017-0034-x
42. Conrad MD, Bradic M, Warring SD, Gorman AW, Carlton JM (2013) Getting trichy: tools and approaches to interrogating *Trichomonas vaginalis* in a post-genome world. Trends Parasitol 29(1):17–25
43. Singh S, Singh G, Singh AK, Gautam G, Farmer R, Lodhi SS, Wadhwa G (2011) Prediction and analysis of paralogous proteins in *Trichomonas vaginalis* genome. Bioinformation 6:31–34
44. Leong IU, Stuckey A, Lai D, Skinner JR, Love DR (2015) Assessment of the predictive accuracy of five in silico prediction tools, alone or in combination, and two metaservers to classify long QT syndrome gene mutations. BMC Med Genet 16:34
45. Schultz J, Milpetz F, Bork P, Ponting CP (1998) SMART, a simple modular architecture research tool: identification of signaling domains. Proc Natl Acad Sci U S A 95(11):5857–5864
46. Krogh A, Larsson B, Heijne G, Sonnhammer E (2001) Predicting transmembrane protein topology with a hidden markov model: application to complete genomes. J Mol Biol 305(3):567–580
47. Buchan DWA, Minneci F, Nugent TCO, Bryson K, Jones DT (2013) Scalable web services for the PSIPRED protein analysis workbench. Nucleic Acids Res 41:W340–W348
48. Bailey TL, Boden M, Buske FA, Frith M, Grant CE, Clementi L, Ren J, Li WW, Noble WS (2009) MEME suite: tools for motif discovery and searching. Nucleic Acids Res 37(Web Server issue):W202–W208
49. Gasteiger E, Hoogland C, Gattiker A, Duvaud S, Wilkins R, Appel RD, Bairoch A (2005) Protein identification and analysis tools on the ExPASy server. In: Walker JM (ed) The proteomics protocols handbook. Humana Press, Totowa, NJ, pp 571–607

50. Yu CS, Chen YC, Lu CH, Hwang JK (2006) Prediction of protein subcellular localization. Proteins 64:643–651
51. Rogers EE, Eide DJ, Guerinot ML (2000) Altered selectivity in an Arabidopsis metal transporter. Proc Natl Acad Sci U S A 97:12356–12360
52. Huang L, Tepaamorndech S (2013) The SLC30 family of zinc transporters - a review of current understanding of their biological and pathophysiological roles. Mol Asp Med 34(2-3):548–560

System Biology, Metabolomics, and Breast Cancer: Where We Are and What Are the Possible Consequences on the Clinical Setting

Alejandra Armengol-Alonso, Meztli L. Matadamas-Guzman, and Osbaldo Resendis-Antonio

Abstract The discovery that the metabolism of cancer cells is different from non-malignant cells is not new, this finding was described more than a century ago by O. Warburg. Nevertheless, in the last decade the technologies such as capillary electrophoresis, mass spectroscopy (MS), and proton nuclear magnetic resonance spectroscopy (H-NMR) have allowed deciphering the complexity and heterogeneity underlying the cancer metabolism. These high-performance technologies are generating a large amount of data that requires conceptual schemes and approaches to efficiently extract and physiologically interpret the dynamic spectrum of the metabolome data in cancer samples. Breast cancer is a disease that highlights the need to develop computational schemes to systematically explore the metabolic alterations that support the malignant phenotype in human cells. Hence, systems biology approaches with capacities to integrate in silico modeling and high-throughput data are very attractive for clinicians to make oncological treatment decisions combined with static parameters such as clinical and histopathological variables. In this chapter we present a cutting-edge review, perspectives and scope of how metabolic approaches in breast cancer studies can be used not only to

A. Armengol-Alonso
Hematology and Oncology Department, Instituto Nacional de Ciencias Médicas y Nutrición Salvador Zubirán, México City, Mexico

M. L. Matadamas-Guzman
Human Systems Biology Laboratory, Instituto Nacional de Medicina Genómica (INMEGEN), México City, Mexico

O. Resendis-Antonio (✉)
Human Systems Biology Laboratory, Instituto Nacional de Medicina Genómica (INMEGEN), México City, Mexico

Red de Apoyo a la Investigación-Coordinación de la Investigación, Científica-Universidad Nacional Autónoma de México (UNAM), Mexico City, Mexico

Centro de Ciencias de la Complejidad-UNAM, México City, Mexico
e-mail: resendis@ccg.unam.mx; oresendis@inmegen.gob.mx

L. Olivares-Quiroz, O. Resendis-Antonio (eds.), *Quantitative Models for Microscopic to Macroscopic Biological Macromolecules and Tissues*,
https://doi.org/10.1007/978-3-319-73975-5_9

integrate the local and systemic response of the host, but also as a technique to look for metabolic biomarkers by non-invasive and simpler sample procedure in biofluids such as serum, saliva, urine, pleural fluid, breath, and ascites. We discuss how the "metabolic phenotype" approach could contribute to developing a personalized medicine by combining metabolome data and computational modeling to evaluate some clinical variables such as detection of relapses, monitoring and response prediction to treatment and toxicity prediction in patients. Even though some advances have been accomplished, in practice there are many challenges and limits that will have to be broken before the metabolomics can be integrated into the day-to-day clinic. Despite this situation, it is evident that the translational multidisciplinary approach combined with the rapid technological development and the correct data interpretation will bring in the future tools for improving outcomes in the clinical area.

Keywords Metabolism in cancer · Systems biology · Genome-scale metabolic reconstructions · Metabolome · Precision medicine

Abbreviations

ABC	Advanced breast cancer
AUC	Area under curve
AUROC	Area under the receiver operating characteristic curve
CE-TOF/MS	Capillary electrophoresis time-of-flight mass spectrometry
CE	Capillary electrophoresis
EBC	Early breast cancer
GC-MS	Gas chromatography-mass spectroscopy
HER2	Human epidermal growth factor receptor 2
H-NMR	Proton nuclear magnetic resonance spectroscopy
HR-MAS	High resolution magic angle spinning magnetic resonance spectrometry
LBC	Localized breast cancer
LC-MS	Liquid chromatography-mass spectroscopy
LTNBC	Localized triple negative breast cancer
LTPBC	Localized triple positive breast cancer
MS	Mass spectroscopy
NMR	Nuclear magnetic resonance spectroscopy
no pCR	No pathologic complete response
OPLS-DA	Orthogonal least-squares discriminant analysis
OS	Overall survival
pCR	Pathologic complete response
PLS-DA	Partial least squares discriminant analysis
TNBC	Triple negative breast cancer
TNMc	Clinical tumor/nodes/metastasis

TNMp	Pathological tumor/nodes/metastasis
TPBC	Triple positive breast cancer
TT	Treatment toxicity
TTP	Time to disease progression

1 Introduction: A Brief Survey of Metabolic Alterations in Cancer

Metabolic alteration is a hallmark in cancer cells whose characterization and understanding have crucial implications to develop optimized drug design and identify feasible biomarkers to improve the diagnosis and prognosis of the disease. The most well-known metabolic alteration in cancer is the Warburg effect, which represents an aerobic glycolysis in cancer cells given by an excessive consumption of glucose and high rates of lactate production even at high concentrations of oxygen available in the microenvironment [1]. Besides glycolysis, glutaminolysis is another main pillar of tumor cells for energy production and an important source of nitrogen for proteins [2]. Glutamine is an abundant metabolite in blood and its consumption and degradation play an essential role to replenish a variety of metabolic functions and consequently, its control has been suggested as a potential metabolic therapeutical strategy again the uncontrolled proliferation in cancer [3]. For instance, glutamine is a fundamental piece in metabolism being responsible for many cellular functions, like nitrogen donor for purines, pyrimidines, and non-essential amino acids necessary for proliferation, also required in the generation of antioxidants to remove reactive oxygen species, as well as carbon donor for fatty acids synthesis [4]. Moreover, it is an indispensable piece in cell signaling, apoptosis, and drug resistance, as well as epithelial-mesenchymal transition, a considerable step in metastasis [5]. Furthermore, glutaminolysis contributes to tumor growth in two distinct but connected ways, by promoting cell proliferation and inhibiting cell death. Overall, both of these metabolic mechanisms, Warburg effect and glutaminolysis, are paired in cancer cells for completing each other the metabolic requirements for biomass production in cancer tissues [6, 7].

Despite these findings have been a milestone in cancer biology, currently there is evidence that these effects can be the tip of the iceberg, and new complex metabolic phenotypes can emerge due at least by two main factors: the genetic heterogeneity in cancer evolution and the specific physiological conditions prevailing in human tissues [8]. Thus, the understanding of how metabolic alterations emerge in different types of cancer and how these can be associated with clinical variables for diagnosis and prognosis is an active field that promises the development of precision medicine based on the personalized description of the genetic background and clinical history of the patients. In order to move toward this last direction, there will be a more close and permanent communication between clinical knowledge in oncology, data obtained from high-throughput technologies and systems biology

schemes to interpret them. Notably, significative advances have been achieved toward the integrative description of metabolome technologies and the development of computational schemes to integrate and interpret data. Thus, recent advances in technologies such as capillary electrophoresis (CE), mass spectroscopy (MS), and proton nuclear magnetic resonance spectroscopy (H-NMR) have allowed to characterize and differentiate the metabolic phenotype between patients with and without cancer by monitoring invasive and non-invasive clinical samples such as biopsies, urine, saliva, and plasma [9]. On the other hand, genome-scale metabolic reconstructions and constraint-based modeling have been a proper paradigm in systems biology to integrate high-throughput data, explore the metabolic phenotype, and predict metabolic targets to reduce proliferation in cancer cells and explore other strategies in human complex diseases. In this chapter, we present a deep discussion of the advances, challenges, and perspectives of how systems biology and metabolome technology is an appealing strategy to understand the metabolic alterations in clinical stages for breast cancer, a disease with a strong impact at worldwide scale. Given the different academic backgrounds between physicians and computational scientists, one of our purposes is to build a line of communication between both areas. To this end we discuss recent clinical applications of metabolome and systems biology in the study of breast cancer. With this idea in mind, we organize the chapter as follows. Section 2 is devoted to present some clinical applications of metabolome data to understand the metabolic alterations in breast cancer. In Sect. 3 we present the main ideas and principles that drive modeling in systems biology, mainly genome scale metabolic reconstructions. Here we highlight the need of mathematical and computational formalisms to get three aims: (1) integrate and interpret high-throughput data from a systemic point of view, (2) construct a framework for systematically building biological hypotheses; and (3) rational design of experiments to reduce the proliferative progress and malignancy of cancer cells. Finally, the last section is focused to analyze and evaluate the current limitations and challenges that we need to face in order to persuade and implement future systems biology schemes in the health-care sector.

2 Clinical Applications of Metabolome: Studies in Breast Cancer

For many years patients with breast cancer were treated with the concept that one treatment would fit to all. Treatment criteria were based only on anatomical and pathologic variables such as tumor, nodes, metastases (TNMc (clinical)/TNMp (pathologic) stage), negative versus positive nodes, and hormone receptors status. However, even though these variables are extremely relevant to determine a patient diagnosis, the overwhelming heterogeneity of cancer has made evident that the drug effectiveness depends on a set of factors such as the genetic context, treatment tolerance, toxicity, HER2 overexpression, and patient metabolism. In the last years

after the omics revolution, the discovery of new biomarkers, receptors, and intracellular mechanisms have allowed to treat in a personalized way and consequently benefiting the patients with the concept of "less is better." The correct selection of the optimal treatment allows to have the most effective and less toxic treatment. Personalized medicine from the therapeutic point of view is defined as a model that uses molecular profiling technologies to tailoring the correct treatment for the right person at the right time [10]. Breast cancer is one of the best cancer examples in which high-throughput technologies have transferred genetic knowledge into clinical practice through the association of different biological subtypes with differentiated prognostic or treatment response [11]. Altered metabolism is a hallmark to sustain the malignancy in cancer given that cancer cells simultaneously rewire their metabolism to increase the production of biomass, and induce genetic profiles that modify the checkpoint mechanism of the cell cycle. Uncovering and understanding the molecular mechanism by which metabolism, cell cycle, and microenvironment link together have important implications to explore the physiological responses that can emerge inside the tumor and design strategies for optimal outcome in the clinical field. The metabolic approach in breast cancer is attractive given that the genomic and transcriptional approach cannot analyze the dynamic metabolites that could be a key determinant of many malignant and non-malignant pivotal cell pathways [12]. Another practical advantage for the clinician and patient is the easier sample taking and the goodness of obtaining multiple samples during the disease evolution. The breast cancer clinical scenarios where the metabolomic approaches have been applied are summarized in Table 1.

2.1 Screening/Early Diagnosis

Despite human life expectancy has increased in the last century, the frequency of chronic diseases, such as cancer, have increased due a variety of factors that include the diet, the environmental and unhealthy lifestyles. Cancer is and will be a common disease that will confront resource-limited health systems; derived from this there is a great interest in screening susceptible population to detect in a preclinical manner which would make the possible cancer cure or reduce treatment costs. Cancer diagnosis in preclinical stages increases the possibilities of cure and evidently has a less expense on health systems. Like any screening maneuver, there is a possibility of damage finding false results (positives or negatives) or giving overtreatment to tumors that do not impact the patient survival. That is why the interest in developing fine diagnostic tools with great accuracy is a constant in cancer screening. The metabolome is theoretically envisaged as a great screening tool because of easiness in obtaining samples and their predictive accuracy. There are several studies in which it has been possible to demonstrate that the metabolic alterations differ markedly between malignant and non-malignant proliferative cells [13].

Table 1 Clinical applications of metabolome: studies in breast cancer

Clinical Scenario	Author/n	Study design	Sample type	Outcome(s)
Screening/early diagnosis	Slupsky et al./$n = 38/67$	Cases/controls	Urine	$R^2 = 0.75 Q^2 = 0.57$
	F-P7 METAcancer consortium/$n = 289/15$	Cases/controls	Breast cancer tissue/breast non-malignant tissue	
Staging	Oatman et al./EBC $n = 44$ ABC $n = 51$	Prospective cohort	Pre- and post-surgery serum	Sensitivity 75% Specificity 69% Accuracy 72%
	Jobard et al./validation cohort EBC $n = 61$ ABC $n = 51$	Prospective cohort	Pre-surgery and pre-chemotherapy serum	AUC 0.91 Sensitivity 78.2–95.6% Specificity 67.3–87.7%
	Memorial Sloan Kettering Cancer Center Biobank LBC $n = 61$ ABC $n = 51$	Prospective cohort	LBC pre-surgery and post-surgery ABC serum	Accuracy 84–87% ER negative Relapse AUC 0.82, sensitivity 82%, specificity 72% Accuracy 75%
	Hadi et al./$n = 152/155$	Cases/controls	Serum Cases pre-surgery	Sensitivity 96% specificity 100%
Classification by biological subtypes	Borgan et al./$n = 46$	Retrospective cohort	Breast cancer tissue	3 luminal subgroups identification ($p = 0.001$)
	Cao et al./$n = 75$ LTNBC LTPBC	Retrospective cohort	Breast cancer tissue	Accuracy 77% ($p = 0.001$)
Predictive markers/neoadjuvant context	Wei et al./$n = 28$ LBC	Prospective cohort	Serum	pCR vs no pCR Discrimination for no pCR 80% AUROC 0.72
Prediction/early detection of toxicity	COMET project (consortium for Metabonomic toxicology)	Murine model	Serum and urine	Sensitivity 41% specificity 77–100%
Measurement of residual disease	Asiago et al./EBC $n = 56$	Prospective cohort	Serum pre-surgery	Relapse prediction 13 months earlier than clinical methods in 55% of relapsed patients
	Oakman et al./$n = 44$ EBC	Prospective cohort	Pre- and post-surgery serum samples	Preoperative LBC Sensitivity 75%, specificity 69% predictive accuracy 72%

(continued)

Table 1 (continued)

Clinical Scenario	Author/n	Study design	Sample type	Outcome(s)
Prognosis/treatment response prediction in ABC	Tenori et al. $n = 579$ ABC	Prospective cohort	Subgroup analysis HER2 positive	TTP accuracy 89.6% OS predictive accuracy 78%

EBC early breast cancer, *LBC* localized breast cancer, *ABC* advanced breast cancer, *LTNBC* localized triple negative breast cancer, *LTPBC* localized triple positive breast cancer, *pCR* pathologic complete response, *no pCR* no pathologic complete response

With the purpose to move toward early diagnosis methods studies have been carried out on gastric, prostate, and pancreatic cancer [14–16]. For instance, Slupsky et al. collected urine samples in breast and ovarian cancer patients at different cTNM stages and in healthy women. They described 67 metabolites from 300 selected, 80% matched in the spectrum and could be dissected to the two study cohorts; women with cancer versus healthy controls [17]. Furthermore, the European FP7 METAcancer consortium analyzed 300 patients with breast tumor and non-malignant breast tissue. As a result of this study, there were identified 600 metabolites as complex lipids, primary metabolites, and unidentified metabolic signals. It was possible to identify significant differences in a heat map between no-malignant breast tissue and breast cancer. Notably, 15 non-malignant breast tissue and 289 breast cancer tissue were compared and the metabolites between the two groups were different with very few outliers [18, 19].

In a recent publication by Zhou et al., H-NMR spectroscopy was performed on urine and serum samples from patients with cancer and healthy controls; using orthogonal least-squares discriminant analysis (OPLS-DA) allowed to discriminate a metabolic profile for cancer. Nine serum metabolites and 3 metabolites in urine were significantly different between the two groups. In OPLS-DA score plots of serum sample there were significant biochemical differences between the two groups ($R^2X = 0.39$ y $Q^2 = 0.75$) [20].

2.2 Staging

The classic canons of the cancer staging are based on anatomical data (tumor size, node infiltration, and distant metastasis); however, it has been proven over time that this classification is not always associated with the prognosis or treatment benefit prediction because there are other variables in the equation. Thus, there are metabolomic studies in renal and bladder cancer which have demonstrated that the metabolomic profiles can differentiate between localized and advanced disease. In breast cancer, Oakman et al. [21] showed significant differences in the metabolic profiles between localized and advanced disease in 44 early breast cancer patients

in whom serum was collected pre- and post-surgery and in serum of 51 advanced breast cancer. The prediction of this metabolic profile for the advanced disease had a sensitivity of 75%, specificity of 69%, and predictive accuracy of 72%. On the other hand, Jobard et al. [22] described a metabolic fingerprint for metastatic disease in women with localized breast cancer and advanced disease, in the training cohort they used 46 preoperative samples in localized disease and 39 samples in advanced disease. In the validation cohort 61 samples in localized disease and 51 in metastatic disease showing a high power of discrimination between both entities. In the Memorial Sloan Kettering Cancer Center (MSK) biobank, the metabolic fingerprint was compared in 90 patients with advanced breast disease and 80 patients with localized breast disease. Patients with localized disease had a basal sample and another post-surgery. Clinical follow-up was 5 years and a training and validation cohort was included in the study. A high predictive accuracy was demonstrated between 84 and 87% to distinguish both entities and in localized disease where a risk score for relapse was generated. This score was compared with conventional clinical risk factors for relapse in ER negative disease and the metabolomic risk score was obtained in the validation cohort AUC 0.82, 82% sensitivity, 72% specificity, and 75% predictive accuracy [23]. Hadi et al. in the serum of 152 pre-surgery breast cancer patients and 155 controls compared by GC-MS (Gas chromatography-mass spectrometry) the metabolic profile followed by chemometric analysis. Partial Least Squares Discriminant Analysis (PLS-DA) model identified significant differences between the groups, sensitivity 96% and specificity of 100% on external validation. An increased lipogenesis and production of volatile organic metabolites indicates key metabolic alteration in breast cancer patients [24].

2.3 Classification by Biological Subtypes

Since the metabolomics approach has the ability to capture the entire picture of host–tumor interaction, it represents an attractive variable for their biological classification. Thus, Borgan et al. analyzed 46 biopsies of breast cancer patients with a combined transcriptomic (RNA extraction and microarray analysis) and metabolomic approach (high resolution magic angle spinning magnetic resonance spectroscopy) [25]. In 31 tumors classified as luminal A using unsupervised hierarchical clustering, three luminal subgroups A1, A2, A3 were identified. The major metabolites differed significantly between each of the profiles ($p = <0.001$) including alpha-glucose, beta-glucose amino acids, myo-inositol, and alanine. In the A2 subgroup were those samples with low glucose levels and high levels of alanine and lactate which results in a greater Warburg effect.

In addition, metabolome studies have contributed to distinguishing different subgroups in same cancer. For instance, the European FP7 METAcancer consortium has reported metabolic heterogeneity in breast cancer biological subtypes (hormone receptor positive and negative tumors) and between histological grade differenti-

ation (grade 1–2 versus grade 3) [11, 12]. Furthermore, Cao et al. characterized the metabolic profiles of triple negative breast cancer (TNBC) and hormonal positive plus HER2 positive breast cancer called triple positive breast cancer (TPBC positive). In order to explore the metabolic activity, high resolution magic angle spinning (HR MAS) magnetic resonance spectroscopy (MRS) was performed in 75 located infiltrating breast cancer tissues. Multivariate partial least squares discriminant analysis (PLS-DA) modeling and relative metabolite quantification were used. The PLS-DA showed high accuracy to separate TNBC and TPBC (77.7%, $p = 0.001$). The concentration of choline was higher in TNBC than TPBC ($p = 0.008$, $q = 0.041$), TNBC lower level of Glutamine ($p = <0.001$, $q = 0.001$) and higher Glutamate ($p = 0.002$, $q = 0.015$) compared to TPBC. In discrimination between HER2 positive and HER2 negative by PLS-DA CV accuracy was 69.1% ($p = <0.001$). High Glycine was found in HER2 positive ($p = 0.002$, $q = 0.012$) [26]. Even though these results represent good news for characterizing the malignant phenotype through some key metabolites, it is needed to study its clinical implications in the prognosis of the disease.

It has been previously described that breast cancer requires glutamine for cell proliferation, in TNBC cell lines has recently been reported that the expression of a Mucin 1 (MUC1). MUC1 is a glycoprotein that causes alterations in metabolic pathways involved in tumor growth. Goode et al. observed a cellular dependence of glutamine with MUC1 expression which facilitates metabolic reprogramming to use glutamine and generate chemoresistance. MUC1 overexpression significantly increased glucose and glutamine uptake in MDA-MB-231 cells and MUC1 knock-down reduced glucose and glutamine uptake in MDA-MB-468 cells [27].

2.4 Predictive Markers/Neoadjuvant Context

The context of neoadjuvant treatment in breast cancer is for the clinician the perfect scenario to test biologically sustainable hypotheses for the search of prognostic or predictive markers that allow treating each patient in a personalized and precise way [28]. Undoubtedly, this enterprise has strong impact in identifying early markers of response to treatment in the understanding of taking better and more dynamic therapeutic decisions. Even though studies evaluating metabolomics in the neoadjuvant context of breast cancer treatment are very scarce, some breakthroughs have been reported. For example, Wei et al. described in serum samples the metabolic profile of 28 patients with non-metastatic breast cancer who received sequential neoadjuvant chemotherapy (Epirubicin 990 mg/m^2 + Cyclophosphamide 600 mg/m^2, 4 three weekly cycles) followed by taxane (Docetaxel 100 mg/m^2, 4 three weekly cycles) [29]. In HER2 positive tumors, trastuzumab was added. They reported a complete pathological response ($n = 8$), partial response ($n = 14$), and no response ($n = 6$) to chemotherapy. A prediction model with LC-MS and NMR was used. Threonine, Isoleucine, Glutamine from NMR and linolenic acid from LC-

MS were significantly different ($p = <0.05$) and ($p = <0.01$), respectively, between the pathological response groups. Combining NMR and LC-MS analysis had the capacity to discriminate up to 80% of the patients who would not have a complete pathological response to neoadjuvant chemotherapy (AUROC = 0.72).

2.5 Prediction or Early Detection of Toxicity

For many years it has been known that the toxicity derived from the oncological treatment varies from patient to patient. Because of this fact, there is a need to identify metabolic biomarkers that help us to select the optimal treatment with the adequade doses for each patient. With this purposes in mind, the COMET project (Consortium for Metabonomic Toxicology) has studied murine models and organ-specific toxicity (liver, kidney) in urine and serum samples with NMR-based technology that has shown that the metabolomic signature can have a sensitivity of 41% and specificity of 77–100%, which is a practical tool for toxicity screening [30].

2.6 Measurement of Residual Disease

Breast cancer, even when clinically appears to be localized to the breast and axillary nodes, is a systemic disease at the time of diagnosis (micrometastatic disease). Notably, the metabolomic profile would allow distinguishing patients with the micrometastatic disease who are at increased risk of relapse. Asiago et al. analyzed serum samples of women with early breast cancer in surveillance following surgical resection to test if metabolomic profile could be used to predict relapse. 257 samples from 56 breast cancer patients, 20 patients relapsed and 36 had no relapse evidence. With a follow-up of at least 2 years Combination NMR (nuclear magnetic resonance spectroscopy) and MS (mass spectroscopy) found a relevant metabolites panel to discriminate relapse versus no relapse; the metabolites predict the relapse 13 months earlier than clinical methods did in 55% of relapsed patients [29].

In another study, Oakman et al. in forty-four early breast cancer patients with pre- and postoperative serum samples analyzed a metabolomic fingerprint by NMR, fifty-one metastatic breast cancer patients were used as control group. This fingerprint was contrasted with the Adjuvantonline calculator for relapse risk measurement. Preoperative localized breast cancer was identified (75% sensitivity, 69% specificity, and 72% predictive accuracy). The comparison with Adjuvantonline was discordant, high risk by Adjuvantonline, pre- and post-metabolomic were 21, 10, and 6 respectively [19].

2.7 *Prognosis/Prediction of Treatment Response in Advanced Breast Cancer*

579 patients with metastatic breast cancer were randomized to receive paclitaxel + lapatinib or placebo. Serum metabolomic profiles were analyzed using NMR spectroscopy. The outcomes were time to progression (TTP), overall survival (OS), and treatment toxicity (TT). In a subgroup analysis in HER2-positive treated with paclitaxel + lapatinib, metabolomic profiles (in the upper and lower thirds of dataset) showed significant differences for TTP ($n = 22$, predictive accuracy = 89.6%) and OS ($n = 16$, predictive accuracy = 78%) [31]. This work illustrates that the metabolomic profile can be used to predict the response and prognosis in a specific type of anti-HER2 target drug (lapatinib) in a specific subgroup of advanced breast cancer.

In summary, metabolome technology applied in cancer clearly opens a window with opportunities to develop new methods of diagnosis and prognosis in breast cancer with potential benefits to improve the outcomes of the treatments applied to patients. However, in order to reach this practice in clinical stages, yet there are challenges that should be overcome such as the proper biochemical interpretation and the biological implications of metabolome measurements. Thus, having obtained the data, a set of practical questions emerge such as what is the activity of the metabolic network associated with the measurements, what are their biological implications, and how this knowledge will be useful in diverse clinical scenarios. These questions define one frontier in personalized medicine and in order to build possible responses one should build computational schemes and methods capable to analyze the data by taking into account the complex nature of the human metabolic networks through a systems biology perspective. Given the inherent complexity of the disease, understanding the mechanisms by which metabolism supports cancer overcomes our intuition and in this context systems biology schemes supply with computational frameworks to integrate the high-throughput data and build testable hypothesis in a systematic and systemic fashion.

The next section is devoted to discussing a paradigm in systems biology that has the capacities to contribute to tackling the previous questions by the simultaneous combination between metabolome data and genome-scale metabolic reconstructions.

3 Systems Biology. Integrative Schemes Between Computational Modeling and High-Throughput Data

With the advent of high-throughput technologies the possibility to extend our molecular knowledge of how human tissues maintain its functional capacities has been significantly extended. Thus "omics" technologies have contributed to uncovering a set of genes, proteins, or metabolites that simultaneously change together for

sustaining the physiological states that we observe in multifactorial diseases such as cancer. Thus, combining these technologies important breakthroughs have been reported to uncover the genetic and epigenetic mechanisms in a variety of cancer and distinguish their metabolic alterations in cancer cell lines and biopsies on human tissues. However, the integrative description and biological interpretation of high-throughput data are not easy and in order to complete this task we should develop computational algorithms that let us to integrate, interpret, and hypothesize the underlying biological mechanisms in the system of study, this latter point being a central aim in Systems Biology [32]. Systems biology deals with the development of computational methods to explore the relationship between the genotype and the phenotype, and old question in biology, but now taking into account that living systems are composed by biological entities such as genes, proteins, and metabolites that interact simultaneously to sustain the phenotype. In the more fundamental essence, the principle in this science is based on the fact that we are a system, it means our body is integrated by a variety of components whose integration and interaction induce states of wellness and disease such as cancer, in other words, seen the physiological states as emergent properties. Thus, in the case of metabolism a variety of breakthroughs have been reported to describe the phenotypic behavior in microorganisms and human tissues in cancer [33]. Even though there is no consensus on defining systems biology, we can highlight three properties in the field: (1) an integrative scheme to integrate and interpret high-throughput data; (2) a mathematical framework to explore and model biological networks, and (3) a computational framework to build testable hypothesis for associating the genotype and phenotype relationship. Thus, systems biology has become a proper description to analyze and explore the biological mechanisms that guide a complex disease such as cancer. An interesting field in this area has been the analysis of the metabolic alterations that guide the phenotype in cancer [6, 34–36]. As we have described in previous sections, metabolic alterations are a hallmark of cancer whose description is currently an active line of research to design new strategies in the therapeutic field [37]. In the next section, we present a mathematical framework to link the metabolome data and the genome-scale metabolic reconstruction, a powerful tool to analyze the metabolic phenotype in cancer [33].

3.1 K-cone: A Mathematical Scheme to Explore the Phenotype from Metabolome Data

Living organisms orchestrate their functions through the constant activity of biochemical reactions, these required to evolve and survive under external environments. With the publication of the human metabolic reconstruction and the high-throughput technologies, the association between the metabolic pathways and the emergence of a disease have been an appealing activity in basic biomedical research and potentially in translational medicine. In this scenery, the development of computational methods for analyzing and interpreting the metabolic activity of a

sample starting from their metabolome profile is one goal in systems biology. In this section, we present one computational scheme that contributes this latter point, how to interpret the different metabolic phenotypes obtained from two or more samples associated with different physiological states. As we will see, the method can be useful to identify the metabolic alterations in cancer studies by taking into account genome-scale metabolic reconstructions and metabolome profile of the samples. The scheme is based on the consideration that we have a metabolic reconstruction defined by a certain number of metabolic reactions, see Fig. 1. Without loss of generality, the dynamical behavior of the metabolites conforming the metabolic network is entirely described by

$$\frac{dx}{dt} = S \cdot v \tag{1}$$

where S is the stoichiometric matrix, x is the vector that contains the concentrations of the metabolites included in the metabolic reconstruction, and v represents the vector with the metabolic fluxes. Then, by considering that the metabolic fluxes for each transformation are ruled by the mass action law, it means the metabolic flux is the rate constant of the reaction multiplied by the concentrations of the substrates

$$v_i = k_i \prod_j^m x^{S_{i,j}} \tag{2}$$

By substituting Eq. (2) into Eq. (1) it is possible to show that Eq. (1) at the steady state condition is written as:

$$S \cdot \Gamma \cdot k = 0 \tag{3}$$

where Γ is a diagonal matrix whose entries contain the mass action terms for the flux of each metabolic reaction (mass action matrix) and k is a vector with all the rate constants.

$$\Gamma = \begin{pmatrix} \prod_j^m x^{S_{i,j}} & 0 & \dots 0 \\ 0 & \prod_j^m x^{S_{i,j}} & \dots 0 \\ 0 & 0 \dots 0 & \prod_j^m x^{S_{i,j}} \end{pmatrix} \quad k = \begin{pmatrix} k_1 \\ \dots \\ k_n \end{pmatrix} \tag{4}$$

This equation now defines a space for all feasible kinetic constants in the steady state, the k-cone. Hence, by assuming that the metabolic reactions follow a mass action law, Eq. (1) at the steady-state condition allows us to write reduced expression. Notably, Eq. (3) is built by three components: the stoichiometric matrix which contains the specific metabolic capacities in the organisms; the matrix Γ which depends only on the concentrations of the metabolites, and the vector k which represents the set of parameters associated with the rate constant for each metabolic reaction. Thus, having measured the metabolome profiles associated with the concentrations of metabolites in a metabolic reconstruction, the solution of

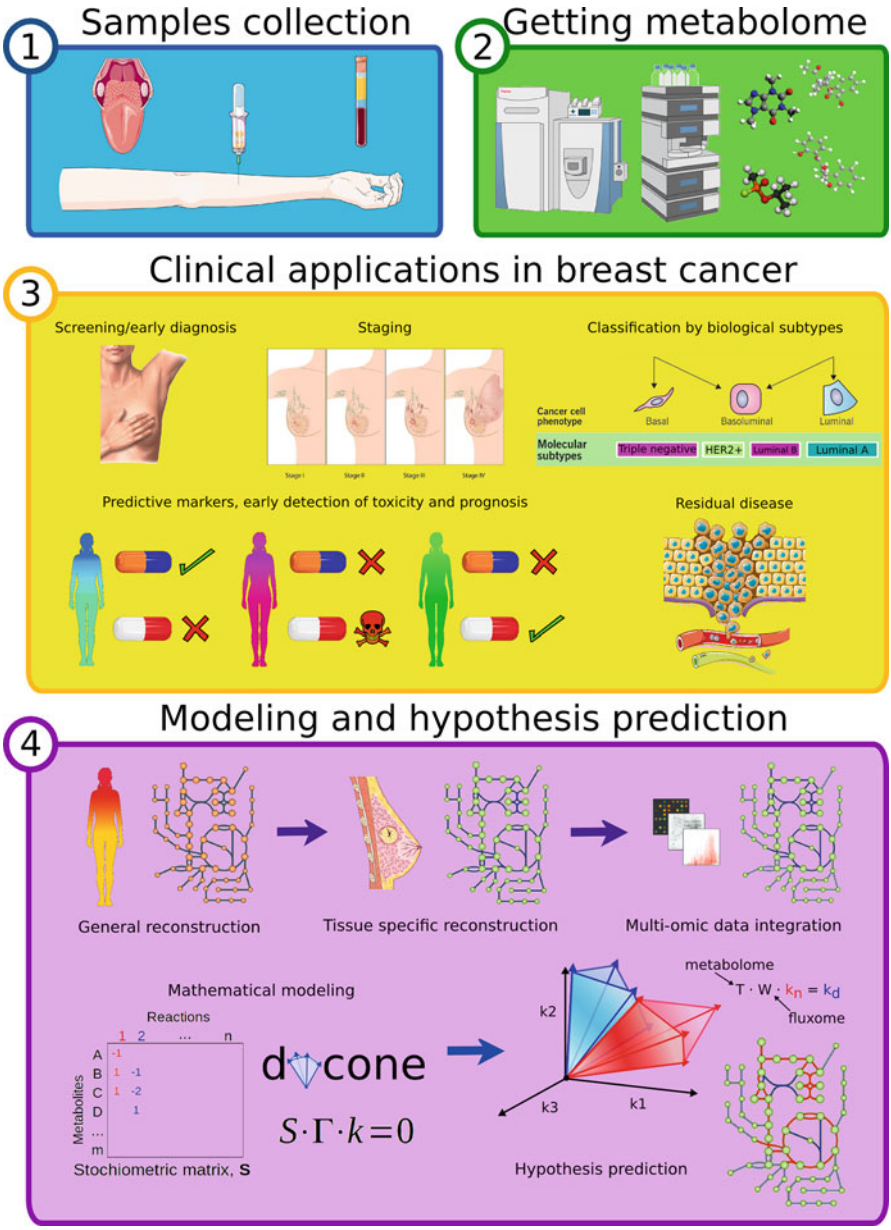

Fig. 1 A possible pipeline to establish the relationship between clinic and metabolome data through the pass of four levels. (**a**) The collection of biofluids (urine, blood, plasma, saliva, etc.) is a central step to obtain the profile of concentrations of metabolites associated with the phenotype among different biological conditions and patients. (**b**) The metaboloma analysis of the samples through different techniques such as NMR and CE-TOF/MS. (**c**) Clinical studies and classification of the samples to store and evaluate metabolome data in prevention, detection, diagnosis, and prognosis. For prediction of a new hypothesis, one of the new approaches is systems biology, specifically mathematical modeling. In this chapter, we describe a specific algorithm called k-cone, developed to analyze differences in metabolic fluxes of metabolic networks in different conditions. Panel (**d**) is depicted the implementation of computational model that contributes to the classification and interpretation of the data at a genome-scale for each patient

Eq. (3) supplies with information about the numerical range of the rate constants that ensure that at steady state the system will reach the metabolic concentrations experimentally measured. These numerical intervals for the kinetic parameters are useful because contribute to define the feasible metabolic space of the reconstructed network. The characterization of the metabolic phenotype is entirely specified by Eq. (3) whose solution, in general, is not unique but it falls into a space of possible solutions, the *k-cone* space [38, 39], given by the null space of the matrix resulted by $S \cdot M$, see Fig. 1. In general, as the metabolic reconstruction increases in number of reactions, the solution of Eq. (3) is not unique and as the feasible space increases, it represents the variety of metabolic mechanisms by which the network can ensure a steady-state condition where the metabolites concentrations are the ones measured experimentally. As shown in Fig. 1, this space of solutions is visually represented as cones in the space of kinetic rate constants. Notably, this method supplies with a pipeline to represent the metabolic capacities of a network based on a set of metabolome measurements, and consequently, a corollary of the method is the study of metabolic alterations that can guide the metabolic phenotype between two or more samples [38, 40]. For instance, we focus our method on the analysis of two physiological samples such as a cancer cell line and control cell line. In this case, the profiles associated with each metabolic phenotype are mathematically specified as follows:

$$\begin{aligned} S \cdot M_n \cdot k_n &= 0 \\ S \cdot M_d \cdot k_d &= 0 \end{aligned} \tag{5}$$

The solutions of the set of equations shown in (5) allow us to tacked a set of questions that uncover the potential metabolic alterations that distinguish each physiological condition. As shown in Fig. 1, the feasible space for each condition has some differences, this indicates the metabolic alteration in kinetic parameters required to ensure each physiological condition. In general terms, both *k-cone* spaces are different and both can be seen as a linear transformation from one to the other. Thus, writing Eq. (1) in vector notation for each set of metabolome data, the kinetic feasible space in each case can be written as follows:

$$k_d = M_d^{-1} \cdot V_d \tag{6}$$

which can be rewritten as follows:

$$\begin{aligned} k_d &= M_d^{-1} \cdot \text{diag}\left(\tfrac{V_d}{V_n}\right) \cdot V_n \\ &= M_d^{-1} \cdot \text{diag}\left(\tfrac{V_d}{V_n}\right) \cdot M_n \cdot M_n^{-1} \cdot V_n \\ &= M_d^{-1} \cdot M_n \cdot \text{diag}\left(\tfrac{V_d}{V_n}\right) \cdot M_n^{-1} \cdot V_n \\ &= M_d^{-1} \cdot M_n \cdot \text{diag}\left(\tfrac{V_d}{V_n}\right) \cdot k_n \end{aligned}$$

Concluding that each point in *k-cone* from disease space can be transformed to the other *k-cone* space:

$$k_d = T \cdot W \cdot k_n \tag{7}$$

with

$$T = M_d^{-1} \cdot M_n$$

$$W = \text{diag}\left(\frac{V_d}{V_n}\right)$$

Equation (7) quantifies the metabolic transformation in the kinetic parameters that guide the metabolic profiles measured experimentally in both conditions, interestingly the difference between the normal and the disease state of the entire space of steady-state kinetic parameters is completely defined by the mass-action terms which can be obtained from metabolome data. The feasible space of kinetic parameters, associated with normal and disease samples, help us to identify differentiated enzymatic activity between both physiological states. This method recently has been applied to explore the metabolic alterations between HaCat and the cancer cell line HeLa, the most studied cell line for cervix cancer [36]. Applying the method to the metabolome data obtained for HeLa cancer cell and HaCat independently, it has been possible to uncover the metabolic differences that guide the malignancy in HeLa with respect to a control system. By selecting the log2-fold between the average of the range for each kinetic parameter, this study concludes that among the enzymes with significative alterations are phosphofructokinase, phosphoglycerate mutase, pyruvate kinase, 6-phosphogluconate dehydrogenase, pyruvate dehydrogenase, and aconitase. More importantly, these findings are in agreement with previous reports [41–45]. In addition to these predictions obtained from our formalism, it has capacities to identify global changes in classical pathways between the comparative analysis of both physiological samples. For instance, the analysis with *k-cone* predicts a strong dysregulation of TCA cycle enzyme activities as well as increased ATP usage and lactate export in HeLa cells, all consistent with the Warburg effect [46]. The set of necessary regulations for proliferation consisted of the up-regulation of four glycolytic enzymes, the up-regulation of ATP synthesis, and the increased export of lactate. Thus, the Warburg effect in HeLa cells seems to be a consequence of maintaining a high proliferation rate. In general, the strongest regulation was observed for phosphofructokinase, which showed an 8-fold increase in enzyme activity in HeLa compared to the HaCaT cell line. Because phosphofructokinase is allosterically regulated by ATP, citrate, and pH, this regulation is consistent with the observed lower concentrations of ATP, citrate, and lactate.

Overall, this first study suggests that *k-cone* analysis can contribute to building hypothesis around the regulatory and metabolic alterations that can support a malignant phenotype such as cancer from metabolome profiles. In the case of cancer cell lines, this method has proven to be a proper description to identify metabolic alterations between control cells and cancer cell lines, this latter point is a valuable goal to design metabolic strategies to control the malignant phenotype in cancer.

Even though this approach represents an important breakthrough in modeling metabolism, an immediate application of the method into samples more complex such biopsies will claim for overcome some challenges such as the heterogeneity of the samples, the physiological interpretation of the metabolome data, and the experimental assessment for the application in precision medicine.

4 Metabolome and Cancer: Critics, Perspectives, and Challenges in the Clinical Application

The advances in breast cancer prognosis and treatment in the last decades have been just to recognize different biological phenotypes and it has allowed in the present and in a near promising future to develop personalized and precision medicine with a great clinical impact. Theoretically, the metabolic approach is a great idea for clinicians who make oncological treatment decisions based on static parameters (clinical and histopathological variables without considering the interaction between tumor and host). However, some challenges should be overcome before metabolome technologies can be utilized in the clinical practice. (Among these challenges we can list the following: small cohorts, number, time and type of sampling, definition lack of a reference standard, complex algorithms to interpret the daunting amount of data, variability and reproducibility, external validation, expensive and sophisticated technology not accessible around the whole world, a clear superiority demonstration with regard to clinical-pathological parameters or complementarity to other approaches like circulating tumor cells or identification of tumor DNA in liquid biopsies, etc.) but the metabolic approach allows to integrate the local and systemic response of the host (interaction between tumor and host). From the clinical perspective, the metabolomic approach is extremely attractive not only for obtaining a non-invasive and simpler sample (serum, saliva, urine, pleural fluid, breath, ascites, etc.) but it allows what other technologies have not been able so far, make possible integrate the local and systemic response of the host. In particular, the characterization of the breast cancer "metabolic phenotype" approach could contribute to an even more personalized and precise treatment which would allow having fewer supra or infra-treated patients and toxicity saving. This aim is not an easy task and will require to evaluate if some fundamental metabolic organizing principles observed in more simple organisms could contribute to understand how cancer acquires robustness under drug action [47–49]. Overall, many challenges and limits will have to be broken before the metabolomics can be integrated into the day-to-day clinic but it is evident that the translational multidisciplinary approach combined with the rapid technological development and the correct dates interpretation will in the future allow the metabolomics applications for precision medicine [50].

Acknowledgments This paper was supported by an internal grant from the Instituto Nacional de Medicina Genomica, Mexico. Meztli L. Matadamas-Guzman is a doctoral student from Programa de Doctorado en Ciencias Biomédicas, Universidad Nacional Autonoma de México (UNAM) and received fellowship 595252 from CONACYT.

References

1. Resendis-Antonio O, González-Torres C, Jaime-Muñoz G, Hernandez-Patiño CE, Salgado-Muñoz CF (2015) Modeling metabolism: a window toward a comprehensive interpretation of networks in cancer. Semin Cancer Biol 30:79–87
2. Rajagopalan KN, DeBerardinis RJ (2011) Role of glutamine in cancer: therapeutic and imaging implications. J Nucl Med 52:1005–1008
3. Wise DR, Thompson CB (2010) Glutamine addiction: a new therapeutic target in cancer. Trends Biochem Sci 35:427–433
4. Deberardinis RJ, Sayed N, Ditsworth D, Thompson CB (2008) Brick by brick: metabolism and tumor cell growth. Curr Opin Genet Dev 18:54–61
5. Yang L, Venneti S, Nagrath D (2017) Glutaminolysis: a hallmark of cancer metabolism. Annu Rev Biomed Eng 19:163–194
6. Resendis-Antonio O, Checa A, Encarnación S (2010) Modeling core metabolism in cancer cells: surveying the topology underlying the Warburg effect. PLoS One 5:e12383
7. Hernández Patiño CE, Jaime-Muñoz G, Resendis-Antonio O (2012) Systems biology of cancer: moving toward the integrative study of the metabolic alterations in cancer cells. Front Physiol 3:481
8. McGranahan N, Swanton C (2017) Clonal heterogeneity and tumor evolution: past, present, and the future. Cell 168:613–628
9. Ishikawa S, Sugimoto M, Kitabatake K, Sugano A, Nakamura M, Kaneko M et al (2016) Identification of salivary metabolomic biomarkers for oral cancer screening. Sci Rep 6:31520
10. Ocana A, Pandiella A (2010) Personalized therapies in the cancer "omics" era. Mol Cancer 9:202
11. Cancer Genome Atlas Network (2012) Comprehensive molecular portraits of human breast tumours. Nature 490:61–70
12. Claudino WM, Goncalves PH, di Leo A, Philip PA, Sarkar FH (2012) Metabolomics in cancer: a bench-to-bedside inter\ion. Crit Rev Oncol Hematol 84:1–7
13. Kroemer G, Pouyssegur J (2008) Tumor cell metabolism: cancer's achilles' heel. Cancer Cell 13:472–482
14. Wu H, Xue R, Tang Z, Deng C, Liu T, Zeng H et al (2010) Metabolomic investigation of gastric cancer tissue using gas chromatography/mass spectrometry. Anal Bioanal Chem 396:1385–1395
15. Sreekumar A, Poisson LM, Rajendiran TM, Khan AP, Cao Q, Yu J et al (2009) Metabolomic profiles delineate potential role for sarcosine in prostate cancer progression. Nature 457:910–914
16. OuYang D, Xu J, Huang H, Chen Z (2011) Metabolomic profiling of serum from human pancreatic cancer patients using 1H NMR spectroscopy and principal component analysis. Appl Biochem Biotechnol 165:148–154
17. Slupsky CM, Steed H, Wells TH, Dabbs K, Schepansky A, Capstick V et al (2010) Urine metabolite analysis offers potential early diagnosis of ovarian and breast cancers. Clin Cancer Res 16:5835–5841
18. Denkert C, Bucher E, Hilvo M, Salek R, Orešič M, Griffin J et al (2012) Metabolomics of human breast cancer: new approaches for tumor typing and biomarker discovery. Genome Med 4:37
19. METAcancer: home [Internet]. [cited 10 Jul 2017]. http://www.METACANCER-fp7.eu

20. Zhou J, Wang Y, Zhang X (2017) Metabonomics studies on serum and urine of patients with breast cancer using ^{1}H-NMR spectroscopy. Oncotarget. https://doi.org/10.18632/oncotarget.16210
21. Oakman C, Tenori L, Claudino WM, Cappadona S, Nepi S, Battaglia A et al (2011) Identification of a serum-detectable metabolomic fingerprint potentially correlated with the presence of micrometastatic disease in early breast cancer patients at varying risks of disease relapse by traditional prognostic methods. Ann Oncol 22:1295–1301
22. Jobard E, Pontoizeau C, Blaise BJ, Bachelot T, Elena-Herrmann B, Trédan OA (2014) Serum nuclear magnetic resonance-based metabolomic signature of advanced metastatic human breast cancer. Cancer Lett 343:33–41
23. Tenori L, Oakman C, Morris PG, Gralka E, Turner N, Cappadona S et al (2015) Serum metabolomic profiles evaluated after surgery may identify patients with oestrogen receptor negative early breast cancer at increased risk of disease recurrence. Results from a retrospective study. Mol Oncol 9:128–139
24. Hadi NI, Jamal Q, Iqbal A, Shaikh F, Somroo S, Musharraf SG (2017) Serum Metabolomic profiles for breast cancer diagnosis, grading and staging by gas chromatography-mass spectrometry. Sci Rep 7(1):1715. https://doi.org/10.1038/s41598-017-01924-9
25. Borgan E, Sitter B, Lingjærde OC, Johnsen H, Lundgren S, Bathen TF et al (2010) Merging transcriptomics and metabolomics–advances in breast cancer profiling. BMC Cancer 10:628
26. Cao MD, Lamichhane S, Lundgren S, Bofin A, Fjøsne H, Giskeødegård GF et al (2014) Metabolic characterization of triple negative breast cancer. BMC Cancer 14:941
27. Goode G, Gunda V, Chaika NV, Purohit V, Yu F, Singh PK (2017) MUC1 facilitates metabolomic reprogramming in triple-negative breast cancer. PLoS One 12:e0176820
28. Damia G, Broggini M, Marsoni S, Venturini S, Generali D (2011) New omics information for clinical trial utility in the primary setting. J Natl Cancer Inst Monogr 2011:128–133
29. Wei S, Liu L, Zhang J, Bowers J, Gowda GAN, Seeger H et al (2013) Metabolomics approach for predicting response to neoadjuvant chemotherapy for breast cancer. Mol Oncol 7:297–307
30. Ebbels TMD, Keun HC, Beckonert OP, Bollard ME, Lindon JC, Holmes E et al (2007) Prediction and classification of drug toxicity using probabilistic modeling of temporal metabolic data: the consortium on metabonomic toxicology screening approach. J Proteome Res 6:4407–4422
31. Tenori L, Oakman C, Claudino WM, Bernini P, Cappadona S, Nepi S et al (2012) Exploration of serum metabolomic profiles and outcomes in women with metastatic breast cancer: a pilot study. Mol Oncol 6:437–444
32. Ebrahim A, Brunk E, Tan J, O'Brien EJ, Kim D, Szubin R et al (2016) Multi-omic data integration enables discovery of hidden biological regularities. Nat Commun 7:13091
33. Zielinski DC, Jamshidi N, Corbett AJ, Bordbar A, Thomas A, Palsson BO (2017) Systems biology analysis of drivers underlying hallmarks of cancer cell metabolism. Sci Rep 7:41241
34. Bordbar A, Yurkovich JT, Paglia G, Rolfsson O, Sigurjónsson ÓE, Palsson BO (2017) Elucidating dynamic metabolic physiology through network integration of quantitative time-course metabolomics. Sci Rep 7:46249
35. Yurkovich JT, Yang L, Palsson BO (2017) Biomarkers are used to predict quantitative metabolite concentration profiles in human red blood cells. PLoS Comput Biol 13:e1005424
36. Diener C, Muñoz-Gonzalez F, Encarnación S, Resendis-Antonio O (2016) The space of enzyme regulation in HeLa cells can be inferred from its intracellular metabolome. Sci Rep 6:28415
37. Locasale JW, Vander Heiden MG, Cantley LC (2010) Rewiring of glycolysis in cancer cell metabolism. Cell Cycle 9:4253–4253
38. Famili I, Mahadevan R, Palsson BO (2005) K-cone analysis: determining all candidate values for kinetic parameters on a network scale. Biophys J 88:1616–1625
39. López-Moyado IF, Resendis-Antonio O (2013) Dynamic metabolic networks, k-cone. In: Encyclopedia of system biology. Springer, New York, pp 624–629
40. Resendis-Antonio O (2009) Filling kinetic gaps: dynamic modeling of metabolism where detailed kinetic information is lacking. PLoS One 4:e4967

41. Yi W, Clark PM, Mason DE, Keenan MC, Hill C, Goddard WA et al (2012) Phosphofructokinase 1 glycosylation regulates cell growth and metabolism. Science 337:975–980
42. Webb BA, Forouhar F, Szu F-E, Seetharaman J, Tong L, Barber DL (2015) Structures of human phosphofructokinase-1 and atomic basis of cancer-associated mutations. Nature 523:111–114
43. Christofk HR, Vander Heiden MG, Harris MH, Ramanathan A, Gerszten RE, Wei R et al (2008) The M2 splice isoform of pyruvate kinase is important for cancer metabolism and tumour growth. Nature 452:230–233
44. Chan B, VanderLaan PA, Sukhatme VP (2013) 6-Phosphogluconate dehydrogenase regulates tumor cell migration in vitro by regulating receptor tyrosine kinase c-met. Biochem Biophys Res Commun 439:247–251
45. Vander Heiden MG, Locasale JW, Swanson KD, Sharfi H, Heffron GJ, Amador-Noguez D et al (2010) Evidence for an alternative glycolytic pathway in rapidly proliferating cells. Science 329:1492–1499
46. Cairns RA, Harris IS, Mak TW (2011) Regulation of cancer cell metabolism. Nat Rev Cancer 11:85–95
47. Zepeda-Mendoza ML, Resendis-Antonio O (2013) Hierarchical agglomerative clustering. In: Encyclopedia of systems biology. Springer, New York, pp 886–887
48. Resendis-Antonio O, Hernández M, Mora Y, Encarnación S (2012) Functional modules, structural topology, and optimal activity in metabolic networks. PLoS Comput Biol 8:e1002720
49. Kitano H (2004) Cancer as a robust system: implications for anticancer therapy. Nat Rev Cancer 4:227–235
50. Diener C, Resendis-Antonio O (2016) Personalized prediction of proliferation rates and metabolic liabilities in cancer biopsies. Front Physiol 7:644

Dynamical Features of a Biochemical Interaction in a Plant Root Hair Cell

A Long Story Short

Víctor F. Breña-Medina

Abstract In this chapter, we briefly discuss key dynamical features of a generalised Schnakenberg model. This model sheds light on the morphogenesis of plant root hair initiation process. Our discussion is focused on the plant called *Arabidopsis thaliana*, which is a prime plant-model for plant researchers as is experimentally well known. Here, relationships between physical attributes and biochemical interactions that occur at a sub-cellular level are revealed. The model consists of a two-component non-homogeneous reaction-diffusion system, which takes into account an on-and-off switching process of small G-protein family members called Rho-of-Plants (ROPs). This interaction however is catalysed by the plant hormone auxin, which is known to play a crucial role in many morphogenetic processes in plants. Upon applying semi-strong theory and performing numerical bifurcation analysis, all together with time-step simulations, we present results from a thorough analysis of the dynamics of spatially localised structures in 1D and 2D spatial domains. These compelling dynamical features are found to give place to a wide variety of patterns. Key features of the full analysis are discussed.

Keywords Plant root hair cell morphogenesis · Reaction-diffusion equations · Localised structure dynamics · Numerical bifurcation analysis · Nonlocal eigenvalue problems

1 Introduction

Morphogenesis is the biological process that organises growth, organisation and differentiation of the structure of an organism or parts of an organism. This process consequently gives rise to new life forms. That being so, a fundamental understanding of morphogenesis is vital for making advances across life sciences

V. F. Breña-Medina (✉)
Department of Mathematics, ITAMRío Hondo 1, Ciudad de México, Mexico
e-mail: victor.brena@itam.mx

L. Olivares-Quiroz, O. Resendis-Antonio (eds.), *Quantitative Models for Microscopic to Macroscopic Biological Macromolecules and Tissues*,
https://doi.org/10.1007/978-3-319-73975-5_10

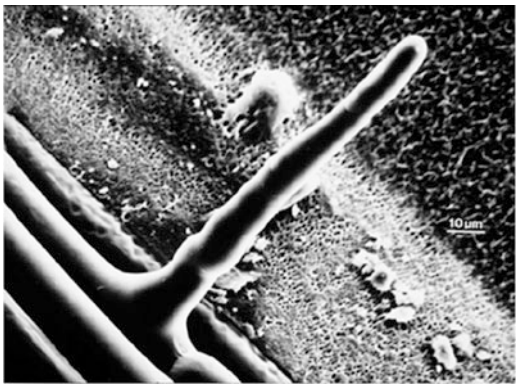

Fig. 1 A RH cell with a hair that is at $1/3$ of its final length. Figure reproduced from [1]

from agriculture up to human health. In agriculture for instance taking cognisance of flowering, self-pollination and nutrient uptake from the soil by plants, or *stem cells* specialisation and *apoptosis* can eventually help with crop yield or reforestation. For this reason, we will focus our discussion on the interplay between certain biochemical interactions in root hair plant cells and physical features as growth.

1.1 A Root-Hair Initiation Process

The majority of the surface area of the root system of a typical flowering plant is provided by its hairy outgrowths. Root hairs (RH)s are protuberances that outgrow from root epidermal surfaces. In *Arabidopsis*, these protuberances can grow up to more than 1 mm in length and approximately 10–20 μm in diameter, see Fig. 1. Thus the study of RHs is agriculturally important for understanding and optimisation of both nutrient uptake and anchorage. For instance, once humid soil is set, mineral salts and water can enter through plant roots. Higher densities of longer RHs are produced in regions where relatively low amounts of less mobile nutrients, such as phosphorus, are available. Roots grow through soil inducing a larger surface area between roots and soil. Consequently, a more advantageous absorption of nutrients is provided.

More widely, RH formation and growth in Arabidopsis has established itself as a key biological model problem within development and cell biology. This is mainly because RHs are found far from the plant body and become visible early in seedlings, so they are particularly amenable to scientific study due to the ease with which they can be imaged. In addition, the formation and growth of a RH represents an important problem in single-cell morphogenesis. Also, Arabidopsis is a model genetic organism for which there is an internationally coordinated project, providing large collections of mutants available for analysis, called *The Multinational Arabidopsis Steering Committee*. RHs grow quickly, at a rate of nearly 1 μm/min, allowing us to analyse efficiently the various phenotypes that

arise under many different genetic mutations. Besides, a detailed analysis of the cellular changes can be experimentally tracked during the RH formation process, because their development is such that cells are organised in a single-file along the developing root epidermis. So young RH cells are found near the root tip and cells of increasing age and stage of growth are found further away in the same longitudinal stripe; see, for instance, [1] and the references therein.

Root hairs develop in predictable and organised files that allow detailed analysis during the whole process. Three different zones can be identified: the *meristematic zone* located in the root tip where new cells are formed in the *meristem*, which is covered by *root cap* cells; the *elongation zone*, where cellular expansion occurs, and the *differentiation zone* where RHs are produced.

Patterning information is provided at an early stage in epidermis development, immature epidermal cells destined to become RH cells are distinguished from their counterpart, non-RH cells, prior to hair outgrowth. The differentiating RH cells present a greater cell division rate, smaller length, greater cytoplasmic density, lower vacuolation rate and distinguishable cell wall epitopes; see, for instance, [2]. In addition, plant hormones known as *auxins* are thought to play a crucial role in almost all aspects of a plant's life. Auxins stimulate growth, and regulate fruit setting, budding, side branching, and the formation of delicate flower parts among many other morphogenic tissue-level responses. In a sense, RH outgrowth is one of the simplest and most easily studied effects that is stimulated by auxin. This hormone flows along the root from the core to the surface; see [3].

After being formed in the meristem, cells that will develop a RH become highly specialised. As the root continues to grow and the meristem moves away, the RH cells get wider, longer and deeper; this is done by diffuse growth, then the RHs form. This process can be divided into two main stages: *initiation*, when a small disc-shaped area of the cell is softened, gives rise to a swelling, and *tip growth*, when a protuberance grows by targeted secretion.

ROPs are examples of *Rho-family small GTPases*, a group of proteins whose role seems to be that of transmitting chemical signals in- and outside a cell in order to effect a number of changes inside the cell. Working as molecular "connectors", these proteins shift between active and inactive states. ROPs control a wide variety of cellular processes, they contribute strongly to crucial cellular level tasks such as morphogenesis, movement, wound healing, division and, of particular interest here, cell polarity generation; see, for example, [4]. These proteins are unique to plants, although are related to *Rac, Cdc42* and Rho-family small GTPases that control morphogenesis of animal and yeast cells, see [5] and the references within. In particular we are interested in the role of ROPs in forming patches that produce local cell outgrowths. That is, in the initiation stage, *small GTP-binding proteins* appear at the growth region. Exchange factor regulators *ARF GTPases* known as *ARF-GEFs* not only are inhibitors preventing ROP localisation, but also are required for the proper polar localisation of *PIN1*, a candidate transporter of the plant hormone auxin, see [6].

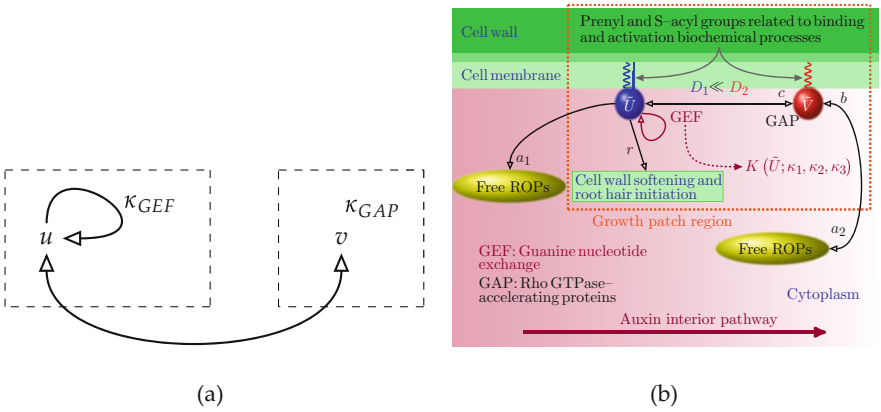

Fig. 2 (**a**) Sketch of the switching fluctuation between active- and inactive-ROP densities. (**b**) Sketch of the model where autocatalytic activation and catalysis effect by auxin are coloured in purple. Figures reproduced from [8]

ROP localisation starts to produce a protuberance, at the same time the pH of the cell wall falls, which leads to softening of the cell wall where a hair is about to be formed. Moreover, plants overexpressing a mutant ROP that is permanently in the active form have balloon-shaped root hairs. On the other hand, protein *ROPGDI1* that can bind to the *GDP-bound* ROP and keep it in that form and in the cytoplasm has been inactivated. This suggests that ROPs are able to cycle from the *GTP-bound* form, which are attached to the cell membrane, to the GDP-bound form, which lie in the *cytoplasm*. In other words, ROPs switch between two states: active when are bound to GTP, and inactive when are bound to GDP, see [7]. The switching fluctuation between both active- and inactive-ROP forms is depicted below in Fig. 2a.

The biochemical process by which the process of RH formation is initiated within an Arabidopsis RH cell is depicted in Fig. 2b; blue and red balloons represent active-GTP ROP and inactive-GDP ROP respectively, ROPs which do not appear in the growth patch region (orange box) are represented by yellow balloons. Active-GTP ROP and Free ROP classes are able to transition to become either inactive-GDP ROP class or get unbound. This is illustrated by a double arrow connecting red and right-hand yellow balloons. A hypothesised autocatalytic process is symbolised by a purple loop-arrow attached to the active-GTP balloon. In addition, the green box encloses active-GTP class members that go to cell wall softening. Cell membrane binding activation processes are generally represented by snaking curves in blue and red accordingly. The interior auxin pathway is indicated by a purple arrow so the auxin gradient is represented by a decreasing purple shade in the same direction. As shall be seen further, we are interested in the binding process in the growth region.

A model of the initiation process was proposed by Payne and Grierson [9] in the form of a Schnakenberg-type reaction-diffusion system for inactive and active

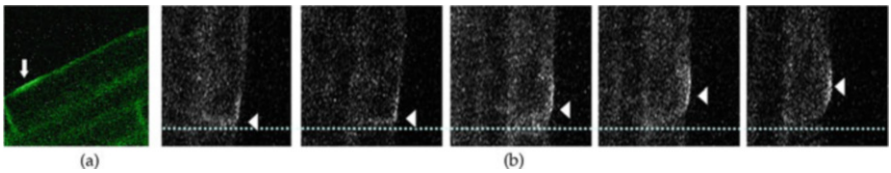

Fig. 3 (**a**) A patch of surface bound ROP imaged using GFP in wild-type just prior to cell wall bulging. Figure reproduced from [9]. (**b**) Time lapse of patch drift within a single cell from end-wall to wild-type location. Figure reproduced from [12]

ROPs. The key feature of the model is that the activation step is postulated to be dependent on the concentration of the plant hormone auxin. Auxin diffuses much faster than ROPs [10] and is too small to be imaged on its own and also very similar to the amino acid *tryptophan*, an essential component in many proteins which makes it impossible to make a sensor that is specific for auxin. However, Jones et al. [3] found a surprising difference between the location of auxin in- and out- pumps in RH and non-RH cells on the root epidermis. From this data, using the auxin flow model introduced by Kramer [11], Jones et al. were able to surmise that there is a decreasing gradient of auxin from the apical end of each RH cell.

Assuming that such a gradient mediates the autocatalytic activation of ROPs, simulations by Payne and Grierson showed that the active-ROP variable tends to form patch-like states towards the apical end, as in Fig. 3a. Moreover, various patch states can be found that show a close qualitative match with observations on the location, width and distribution of multiple hair cells in a variety of mutants.

Grierson et al. [12] presented the new experimental data reproduced in Fig. 3b which sheds light on the dynamic process by which ROP patches form. The process by which a patch of active ROP migrates from the apical cell boundary towards its wild-type position, from where a RH forms, takes place within a timescale of minutes. It appears to be triggered within the growing root as the RH cell reaches a combination of a critical length and a critical overall auxin concentration. In this review we shall present key results from the model derived by Payne and Grierson, which is particularly effective in capturing this dynamical process.

1.2 Fundamental Model

ROPs can become attached to the cell membrane through *prenylation* and *S-acylation*; these chemical modifications determine the steady-state distribution between the cell membrane and cytosol, the membrane interaction dynamics, as well as function [13]. In other words, each ROP protein comes in two states: activate and inactivate. The latter state corresponds to ROPs which may be either bound to the cell membrane or in the cytoplasm. Once bound though, there is a good chance of

phosphorylation, leading to the active form of ROP. In the model here derived we shall not model the binding mechanism per se but shall differentiate only between the active form which can only diffuse within the confines of the cell membrane, and the inactive form, the majority of which is free to diffuse in the cytoplasm. We will also approximate the long-thin RH cell by a domain (either 1D or by a rectangular domain in 2D with high aspect ratio), and shall distinguish between membrane and cytoplasm only through separate diffusion constants, D_1 and D_2 for the active-ROP and inactive-ROP populations, respectively. That is, we model a mathematical domain $(\mathbf{z}, t) \in \Omega^d \times \mathbb{R}^+ \cup \{0\}$, which Ω^d is either the interval $\Omega \equiv [0, L]$ or the rectangle $\Omega^2 \equiv [0, L_x] \times [0, L_y]$ where $L_x > L_y$, and let $u(\mathbf{z}, t)$ represent the concentration of *bound/active* and $v(\mathbf{z}, t)$ the *unbound/inactive* ROP. In the model we shall also reflect the fact that the kinetic processes occur considerably faster than the changes to cell length and auxin concentration levels. Therefore we shall assume that the latter are effective bifurcation parameters that vary quasi-statically.

The active Rho state is assumed to be deactivated at rate κ_{GAP}, and equivalently the inactive Rho state is activated at rate κ_{GEF} depending upon the presence of GEFs or GAPs, respectively; see sketch in Fig. 2b.

To derive a specific form for the activation and deactivation steps we shall take a model that is inspired by similar processes for Rho proteins in mammals and yeast. There, it is widely held that the GEF activation step involves positive feedback (autocatalysis) whereas the GAP step is thought to be passive; see, for example, [7]. Both Jilinke et al. [14] and Otsuji et al. [15] have derived models for active process of cross-talk between the three different mammalian/yeast Rhos—*cdc42, RhoA* and *Rac*—which process is thought to underlie the polarity determination process. Like ROPs, each protein is supposed to come in two states, an activated state (which is bound to the cell membrane) and a deactivated state (either bound or in the cytosol). Similarly the transition between these two states is via GEFs and GAPs. In [14, 15], the GEF-induced activation step of each Rho species is modelled by a Hill function:

$$\kappa_{\text{GEF}}(u) \equiv \kappa_1 + \frac{\kappa_2 u^q}{1 + \kappa_3 u^q}, \tag{1}$$

where κ_1 is the activation rate, κ_2 represents autocatalytic acceleration, κ_3 is a saturation coefficient, and the power q is typically taken to be an integer but need not be. In [14, 15] the typical value $q = 2$ is chosen which preserves the odd power of the nonlinearity in their models. This may be simplified as follows. In plants, although there are several different kinds of ROP, their activation is not thought to involve cross talk. Also, by including a constant production rate of the inactive ROP and a constant probability of recycling or further processing of active ROP, there is no need for an explicit saturation term, which implies that κ_3 can be set to naught; see proposed model in [9].

As we previously referred, Jones et al. [3] found experimental evidence that suggests a longitudinal spatially decaying gradient of auxin which Payne and Grierson postulate modulates the autocatalytic step. That is, we suppose then the parameter κ_2 is spatially dependent: $\kappa_2 = k_{20}\alpha\left(\mathbf{z}; \left|\Omega^d\right|\right)$. Here k_{20} measures an

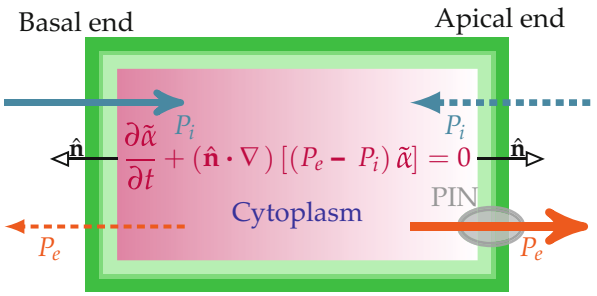

Fig. 4 Sketch of the auxin flux in the RH cell; azimuthal view. The gradient is coloured as a purple shade. Cell wall and cell membrane are coloured as in Fig. 2b. Figure reproduced from [8]

overall concentration of auxin and, as is sketched in Fig. 4, $\alpha\left(\mathbf{z}; \left|\Omega^d\right|\right)$ is a smooth function that represents the spatial distribution of auxin, normalised so that

$$\alpha(0, y) = 1, \qquad \frac{\partial \alpha}{\partial x} < 0, \quad \text{for all } \mathbf{z} \in (0,1) \times (0,1)\,, \text{where} \mathbf{z} = (x, y)\,. \tag{2}$$

In contrast, we suppose that $\kappa_1 = k_1$ a constant. All other processes are supposed to follow the simple law of mass action, with the GEF-induced deactivation/unbinding rate given by a constant $\kappa_{\text{GAP}} = c$. Furthermore, b is assumed to be the constant rate of production of inactive ROP and r the rate at which active ROP is recycled or used up to produce other complexes, including those that go on to produce cell wall softening; see Fig. 2.

On the other hand, for the 2D case, we take into account two different scenarios:

$$\alpha(\mathbf{z}) = e^{-\nu x} \sin(\pi y) \quad \text{and} \quad \alpha(\mathbf{z}) = e^{-\nu x}\,. \tag{3}$$

Under the above assumptions, using the law of mass action allied to Fick's law of diffusion in a standard way, we obtain the reaction-diffusion (RD) system of equations

$$\text{Bound} - \text{activeROP}: \qquad U_t = D_1 \Delta U + k_{20} \alpha\left(\mathbf{z}; \left|\Omega^d\right|\right) U^2 V - (c+r) U + k_1 V\,, \tag{4a}$$

$$\text{Unbound} - \text{inactiveROP}: \qquad V_t = D_2 \Delta V - k_{20} \alpha\left(\mathbf{z}; \left|\Omega^d\right|\right) U^2 V + cU - k_1 V + b\,, \tag{4b}$$

in Ω^d. We also impose the homogeneous Neumann boundary conditions, also known as no-flux boundary conditions,

$$\frac{\partial U}{\partial \hat{\mathbf{n}}} = 0, \quad \frac{\partial V}{\partial \hat{\mathbf{n}}} = 0\,,$$

on $\partial\Omega$, which supposes that the large ROPs do not diffuse through the cell wall.

This system is a generalisation of the Schnakenberg model [16], which is doubtlessly one of the most widely studied models undergoing Turing-like pattern formation schemes. In contrast to other models such as the *Brusselator* [17], which takes into account four chemical reactions, the Schnakenberg one is a simplification where three hypothetical chemical reactions are represented, amongst which one is autocatalytic. As a consequence, it is not only simpler, but also it is already known that the Schnakenberg system can display features that are considered biologically relevant [16]. The usual Schnakenberg system can be obtained from (4) by setting k_1 and c to zero, adding a constant production term to the u-equation, and taking $\alpha \equiv 1$; this transformation can be seen as a homotopy between both systems. Furthermore, both systems are derived from simple reactions where an autocatalytic process is present. In addition, as can be straightforwardly explored, both describe activator-substrate processes. In other words, near activation regions the activator u aggregates so that the substrate v is consumed quickly, as a result substrate valleys occur where activator peaks do; see [18] and the references therein for a review.

From a theoretical point of view there is an extensive range of research on the Schnakenberg model. For instance, Ward and Wei have analysed existence and asymmetry of spikes [19]; stability of symmetric N-spiked steady-states is deeply examined in [20]; self-replication spots and their dynamics in 2D are studied in [21]; and for findings on chemical reactors, see, e.g., [22], where this model plays a central role.

In non-homogenous approach, there has been mathematical analysis in superconductivity (e.g. [23]). Reaction-diffusion equations with spatially dependent coefficients of nonlinear terms are not easy to study analytically, see, e.g., [24]. Nevertheless there have been some previous works both analytical and numerical: for the Schnakenberg system, see, e.g., [25], the Gierer–Meinhardt and Brusselator systems (e.g. [26]), and in models of mitosis in cytokinesis [27]. In this essay we present central results of the Schnakenberg-like system (4) with spatially dependent coefficients which modulate the nonlinear terms.

This chapter is organised as follows: in Sect. 2, the onset of spatially localised structure in RD systems from a Turing perspective is briefly examined; dynamical features observed as auxin is switched on are addressed in Sect. 3; in Sect. 4, a natural transition from a 1D domain to a 2D domain is then briefly presented from a point of view of localised stripe stability analysis; then, geometrical and kinetics characterisation of spot dynamics, along with hybrid patterns consisting of spot and stripes, are reviewed when a two-dimensional spatially dependent gradient is on in Sect. 5. Finally, concluding remarks are found in Sect. 6. All key results on pattern formation dynamics and inherent instabilities on RH-initiation morphogenesis presented here are discussed in [8, 28–31].

2 Spatially Localised Activator Structures

As can be seen in Fig. 3, there are two main features which may be addressed from a viewpoint of the theory of dynamical systems: (1) ROP aggregation and (2) ROP patches drifting. The former seems to occur in such a way that, from an analytical point of view, active-ROP patches have a spatially localised structure. On the other hand, in contrast to patch formation, once formed active-ROP patches slowly shift from the basal end towards interior of the cell. This observation suggests that both mechanisms, aggregation and drifting, arise in two different time scales.

2.1 Turing and Homoclinic Snaking

First of all, U and V components are renamed as u and v, respectively. Without loss of generality, no spatially dependent auxin gradient and a large symmetrical 1D domain are taken into account. In so doing, we set $\alpha \equiv 1$, $k_{20} \equiv k_2$ and $\Omega \equiv [-L/2, L/2]$ for $L \gg 1$, together with homogeneous Neumann boundary conditions.

On the one hand, we first look for Turing patterns, which are known to emerge from pitchfork (breaking-symmetry) bifurcations. As a consequence, upon following a standard approach, necessary conditions to get non-trivial steady-states can be encapsulated by

$$D_1 D_2 \ll \max\left\{D_1^2, D_2^2\right\}, \quad \operatorname{sign}\left\{F_u G_v\right\} < 0\,.$$

Assuming, for instance, that $G_v < 0$, conditions above imply that u-component diffuses much slower than v-component; see [32] for details. As can be seen there, a flat steady-state transits to a non-trivial steady-state as a parameter is slowly varied. In particular, this transition materialises when a double zero of the dispersion relation occurs. In other words, condition

$$(D_2 J_{11} + D_1 J_{22})^2 = 4 D_1 D_2 \det \mathbf{J}\,, \quad (\mathbf{J})_{ij} = J_{ij}\,, \tag{5}$$

is satisfied, where $\mathbf{J}$ is the Jacobian matrix of kinetic terms of system (4) at the steady-state

$$(u_0, v_0)^T = \left(\frac{b}{r}, \frac{br(c+r)}{k_2 b^2 + r^2 k_1}\right)^T. \tag{6}$$

Furthermore, condition (5) corresponds to an accumulation point of Turing bifurcations when $L \gg 1$.

On the other hand, in the limit $L \to \infty$, spatial dynamics can be applied (see, e.g., [33]). Hence, upon setting $u_t = v_t = 0$ we obtain the steady-state system, which is equivalent to an ODE system in $\mathbb{R}^4$,

$$u_x = \frac{p}{D_1}, \qquad p_x = -k_2 u^2 v + (c + r)u - k_1 v, \tag{7a}$$

$$v_x = \frac{q}{D_2}, \qquad q_x = k_2 u^2 v - cu + k_1 v - b. \tag{7b}$$

Notice that this system satisfies two key ingredients: (a) spatial translation invariance and (b) spatial reversibility, which corresponds to the symmetry $(u_x, v_x)^T \to (-u_x, -v_x)^T$ and $x \to -x$. In this context, the steady-state $(u_0, v_0)^T$ of (4) corresponds to an equilibrium $(u_0, 0, v_0, 0)^T$ of (7), which will undergo a transition from being hyperbolic to elliptic equilibrium at a Hamilton–Hopf bifurcation. This bifurcation takes place when eigenvalues of the Jacobian matrix at the equilibrium of (7) collapse into two purely imaginary eigenvalues of multiplicity two for a critical parameter value, which is however found when the same condition (5) is met. In addition, as can be seen in [34], a subcritical Hamilton–Hopf bifurcation is essential to get spatially localised steady-states, which are equivalent to homoclinic orbits for system (7). As a consequence, a subcritical Turing bifurcation plays a key role on the onset of spatially localised structures.

Upon applying the Lyapunov–Schmidt reduction method, we compute the reduced bifurcation equation

$$g(\chi, \mu) = q_1 \mu \chi + q_3 \chi^3 + q_5 \chi^5 + \mathcal{O}(\mu^2 \chi, \mu \chi^3),$$

where $\mu = k_2 - k_{2_c}$ and $\chi \in \mathbb{R}$ parametrises eigenfunctions amplitude of $\mathbf{J}_\kappa$. This matrix is the Jacobian matrix of (4) at the steady-state $(u_0, v_0)^T$, restricted to the eigenspace spanned by cosine Fourier modes; see [8] for details. Bifurcation algebraic structure is provided by equation $g(\chi, \mu) = 0$. From which a criticality transition is predicted as k_2 is slowly varied. That is, criticality parameter $\sigma \equiv q_1 q_3$ predicts a sub- or supercritical pitchfork bifurcation as $\sigma > 0$ or $\sigma < 0$, respectively; see Fig. 5b.

Spatially localised steady-states are then organised in a homoclinic snaking fashion. This form emerges from a subcritical pitchfork bifurcation close to criticality transition. As can be seen in Fig. 5c, stable branches are flanked by fold bifurcations; as a result, stable branches overlap.

Therefore, a subcritical Turing bifurcation is the onset of localised steady-states, which co-exist with spatially extended non-trivial steady-states. Samples of system (4) stable patterns in 1D are displayed in Fig. 5d. On the other hand, stable patterns for a 2D square large domain are shown in Fig. 6. These solutions suggest that a similar mechanism governs such a localised patterns in 2D. See [28, 35] for a detailed discussion.

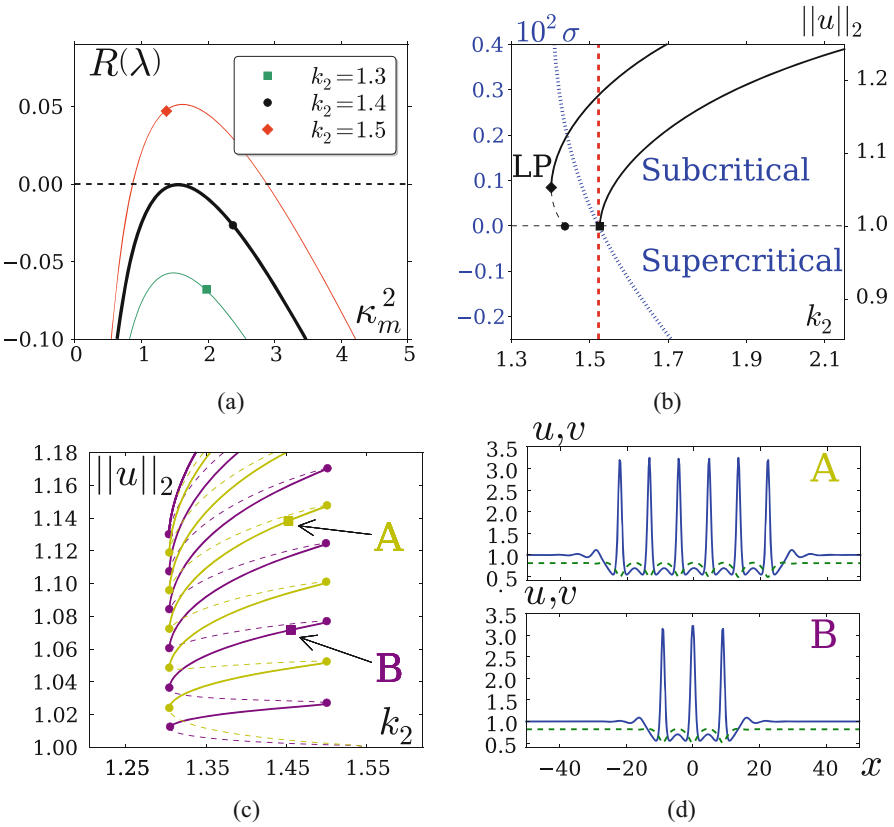

Fig. 5 (**a**) Dispersion relation of $\mathbf{J}_\kappa$; $\kappa_m^2 = m\pi/L$ for $m \in \mathbb{Z}$. The bold solid curve corresponds to where a double root occurs. (**b**) Bifurcation diagram and pitchfork criticality condition; stable branches are shown as solid lines, the filled circle corresponds to a subcritical bifurcation, and the square to a supercritical bifurcation. The subcritical branch undergoes to a fold bifurcation (LP). The pitchfork criticality condition is depicted as a blue heavily dashed line, where the criticality transition is indicated by a red vertical dashed line. (**c**) Homoclinic snaking; even-solutions branch in yellow and odd-solutions branch in purple, and fold bifurcations depicted as filled circles; bold solid lines indicate stable branches. (**d**) Samples of multi-pulse homoclinic stable solutions on the even and odd branch for $k_2 = 1.45$, top and bottom panels, respectively, which correspond to six-spike steady-state (label A) and three-spike steady-state (label B) in panel (**c**). The u-component (blue solid line) and v-component (green dashed line) are plotted. Figures reproduced as well as parameter values from [28]

3 Spatially Dependent Gradient

In order to understand auxin catalyst properties on ROP activation, an auxin gradient as stated in (2) is taken into account. For a 1D domain, this gradient though is as the right-hand scenario in (3) with no transversal component. In addition, as RH cells are still growing at this initiation stage, length seems to also play an important role

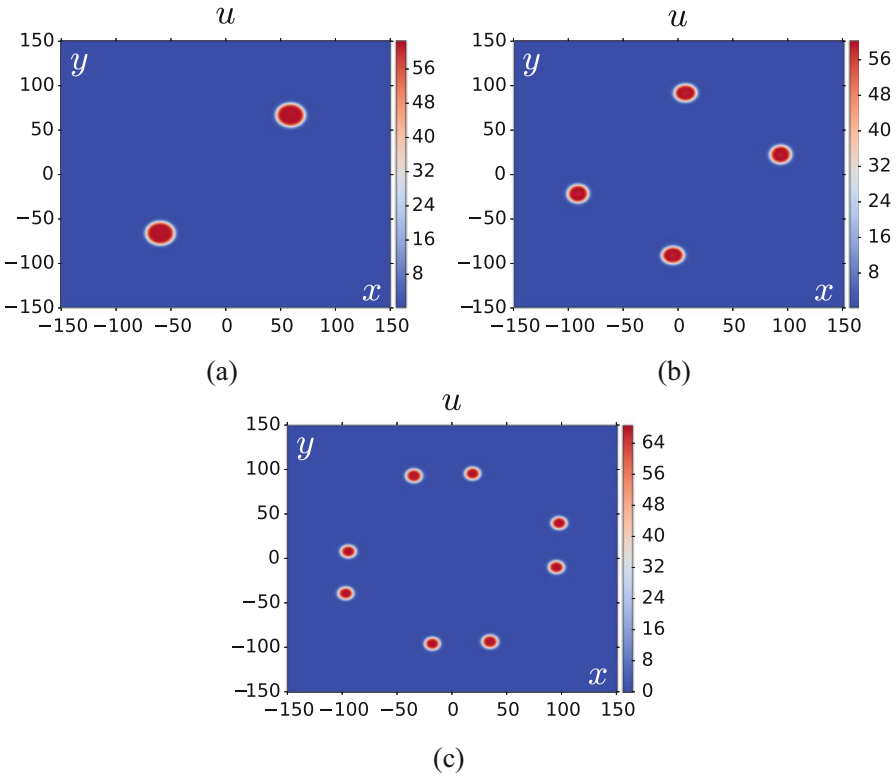

Fig. 6 Stable patterns for a 2D square domain on a cool-warm scale (sidebar). Localised (**a**) two-spot, (**b**) four-spot, (**c**) eight-spot. Figures reproduced as well as parameter values from [28]

in active-ROP pattern formation. Upon taking into account these two ingredients, auxin accelerator rate is $\kappa_2 = k_{20}\alpha(x)$, where k_{20} plays a role as the primary bifurcation parameter, and $\Omega = [0, L]$, where L is a secondary bifurcation parameter.

In so doing, we perform time-step simulations of system (4) for different auxin overall k_{20} values. Initial conditions consist of a random perturbation of order 10^{-4} to steady-state (6). As can be seen in Fig. 7, spikes are quickly formed which then slowly drift towards interior of the domain. In addition, an asymmetrical amplitudes and a travelling-wave-like spikes get pinned closer to left-hand boundary can be observed. These numerical observations suggest: (1) families of stable steady-states arranged in an overlapping bifurcation structure, and (2) two time scales and two spatial scales.

As seen in Sect. 2, upon varying k_{20} a subcritical bifurcation is perturbed and compute the bifurcation diagram shown in Fig. 8a. There, stable branches and unstable branches are flanked by fold bifurcations, which are organised in an overlapping fashion. This is a consequence of a strongly slanted homoclinic-snaking structure previously computed above. Note that as the k_{20} is greater, the more

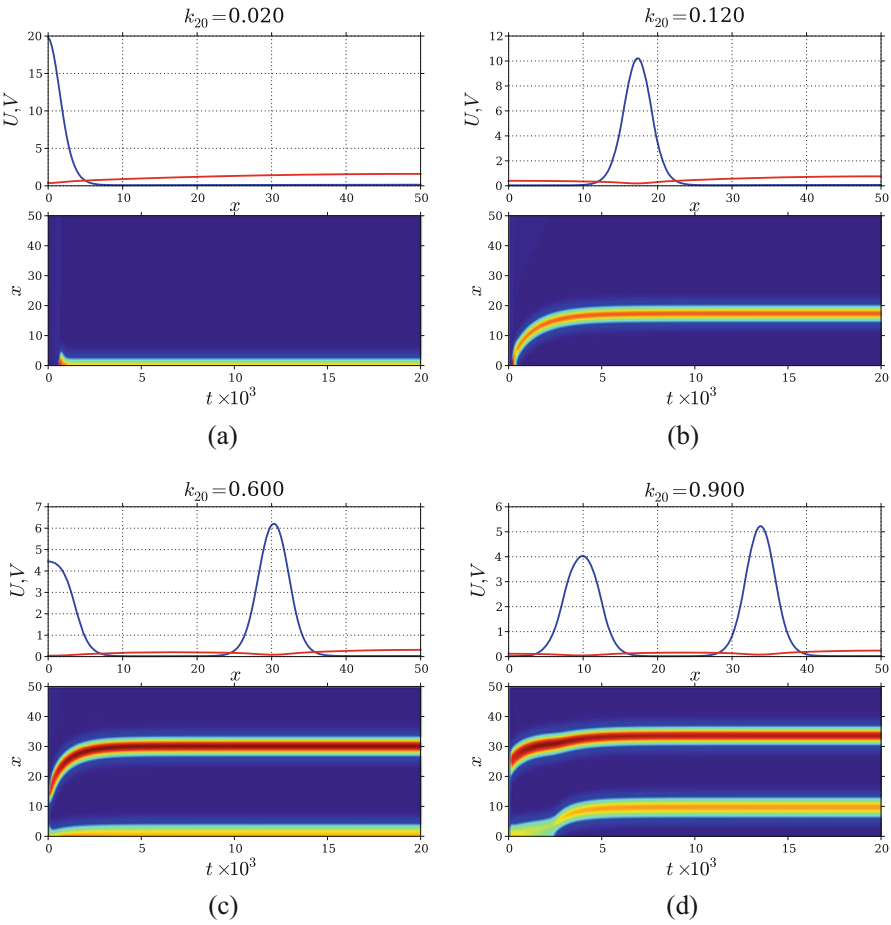

Fig. 7 Final profile and patch dynamics, with no variation of parameters, for (**a**) boundary patch, (**b**) an interior patch, (**c**) double patch, and (**d**) boundary and interior patch. Active- and inactive-ROP density final profiles are plotted in blue and red, respectively (top panels), and u-spike solutions are plotted on a heat bar scale (bottom panels). Figures reproduced as well as parameter values from [29]

spikes arise, which implies that auxin triggers high active-ROP densities in localised regions. Notice that the closer to the left-hand boundary, the smaller amplitude occurs.

Now, spatio-temporal scales are in such way that spikes are formed in a fast time scale to then travel towards a steady location in a slow time scale, and the two spatial scales can be seen as inner and outer scales of each spike. This approach can be seen as a Dirac-delta function works as each spike core. That is, spikes are flat in the outer scale and finite but large in the inner scale; see Fig. 8b.

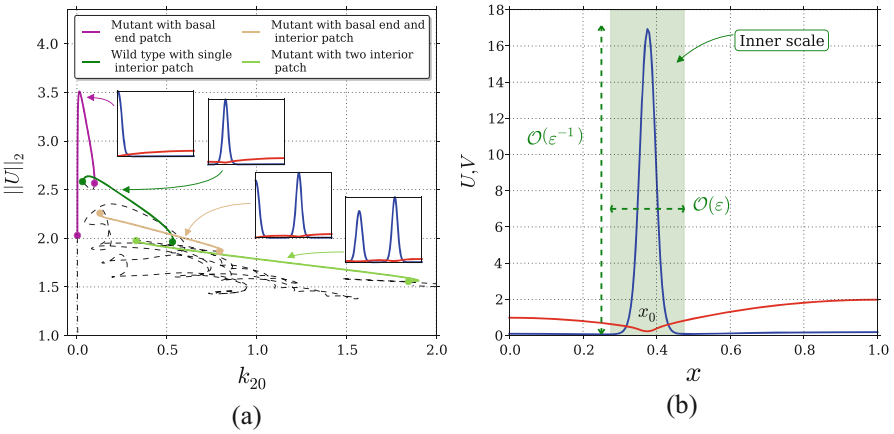

Fig. 8 (**a**) Bifurcation diagram varying k_{20}: boundary-patch, single-interior-patch, boundary-and-interior- patch, and two-interior-patch branches; stable solutions are shown as solid lines, unstable solutions as dashed lines, and points instability points by filled circles. (**b**) Schematic plot of the inner and outer solution for a steady-state solution. The active-component U has a patch, whereas V has a global variation across the domain. Figures reproduced as well as parameter values from [29]

Upon re-scaling $U = \varepsilon^{-1}u$ and $V = \varepsilon v$, where $u, v = \mathcal{O}(1)$, we obtain a singularly perturbed system

$$u_t = \varepsilon^2 u_{xx} + \alpha(x)u^2 v - u + \frac{\varepsilon^2}{\tau\gamma} v\,, \tag{8a}$$

$$\varepsilon\tau v_t = D_0 v_{xx} + 1 - \varepsilon v - \varepsilon^{-1}\left(\tau\gamma\left(\alpha(x)u^2 v - u\right) + \beta\gamma u\right)\,, \tag{8b}$$

in $0 < x < 1$ and $t > 0$, with $u_x = v_x = 0$ at $x = 0, 1$, and $D_0 \equiv \varepsilon D$ which comes from balancing terms in (8b).

Here, the dimensionless parameters are given by

$$\varepsilon^2 \equiv \frac{D_1}{L^2(c+r)}\,, \qquad D \equiv \frac{D_2}{L^2 k_1}\,, \qquad \tau \equiv \frac{c+r}{k_1}\,, \qquad \beta \equiv \frac{r}{k_1}\,, \tag{9}$$

and the primary bifurcation parameter is

$$\gamma \equiv \frac{(c+r)k_1^2}{k_{20}b^2}\,. \tag{10}$$

By applying matched asymptotic method in system (8), we obtain a U and V leading order approximation profiles as stated by

Proposition 3.1 (Modified Version from [29]) *Let $\varepsilon \ll 1$, $D = \mathcal{O}(\varepsilon^{-1})$ with $D = D_0/\varepsilon$ and $\gamma = \mathcal{O}(1)$, and consider an $N+1$ interior patch quasi-steady-*

state solution of (8) *with patches centred at* $x_0, \ldots, x_N$. *Then, a leading order approximation for* U *and* V *is*

$$U \sim \frac{\varepsilon^{-1}}{6\beta\gamma} \sum_{j=0}^{N} w\left(\varepsilon^{-1}(x - x_j)\right) n_j \,, \tag{11a}$$

$$V \sim \varepsilon \left(6\beta\gamma(N+1)\bar{\alpha}_{-1} - \mathbf{n}^T \mathbf{G} \mathbf{n} + \sum_{j=0}^{N} G\left(x; x_j\right) n_j \right) , \tag{11b}$$

where $w(\xi) = 3/2\text{sech}^2\left(\xi/2\right)$, $G(x; x_j)$ *is a Green function, and*

$$\bar{\alpha}_{-1} \equiv \frac{1}{N+1} \left[\frac{1}{\alpha(x_0)} + \cdots + \frac{1}{\alpha(x_N)} \right] .$$

Here $\mathbf{n} = (n_0, \ldots, n_N)^T$ *is the solution to the nonlinear algebraic system*

$$6\beta\gamma \mathbf{B}\mathbf{n}_{-1} = \mathbf{G}\mathbf{n} + 6\beta\gamma(N+1)\bar{\alpha}_{-1}\mathbf{e} - \left(\mathbf{n}^T \mathbf{G}\mathbf{n}\right)\mathbf{e} \,, \quad \mathbf{e} \equiv (1, \ldots, 1)^T \,, \tag{12}$$

where $\mathbf{B} \equiv \text{diag}\left(\alpha\left(x_0\right), \ldots, \alpha\left(x_N\right)\right)$, *and symmetric Green's matrix* $\mathbf{G}$ *is defined by* $(\mathbf{G})_{ij} = G(x_i; x_j)$. *In terms of* n_i, *the leading-order solution for* V *in the vicinity of the i-th patch is* $V^i \sim 6\varepsilon\beta\gamma/\alpha(x_i)n_i$.

As can be seen, each amplitude of active-ROP spike is governed by means of n_j, which depends on auxin gradient as the nonlinear algebraic system (12) indicates; see Figs. 7 and 8a for amplitude asymmetries. Moreover, V approximation consists of the Green's matrix and regulating constants n_j, which implies that boundary conditions and interactions between spikes are mediated by inactive-ROP density. In other words, localised biochemical activation is controlled by auxin; however, geometry and growth factors indirectly determine shape and form of the pattern influence through inactive-ROPs. For full details of other dynamical features not shown here and a complete analysis, see [29].

4 Geometrical Key Role

In the previous section, key features of a two-component RD system in a 1D domain were described to model a RH initiation process catalysed by auxin in a slim and flat RH cell. In so doing, as symplastic auxin flow actively diffuses from RH cell to RH cell, we have only considered a longitudinal spatially dependent gradient. However, non-RH cells are known to flank RH cells. This characteristic has been taken into account by Grieneisen et al. in [36]. From their model, a transversal auxin gradient may be assumed to have impact on active-ROP pattern formation and patches location dynamics. In order to analyse this feature on ROP dynamics,

a 2D domain is now considered. Such a domain provides a setting with an extra degree of freedom. Hence, we address the following questions:

- How would RH width affect ROP pattern formation?
- Would a robust ROP patch formation be able to arise as seen in 1D?
- Which spatial aggregation structure would active-ROPs have in 2D?
- Are there other kind of patterns co-existing with localised patterns?

We first notice that Proposition 3.1 provides a key ingredient. That is, upon denoting spike steady-states (11) as $(u_s(x), v_s(x))^T$, and as the auxin gradient is considered to be y-constant, these states in 1D are also stripe steady-states $(u_s(x;y), v_s(x;y))^T$ in 2D, where transversal direction is parametrised by y. Expressed in a different way, transversal trivial extensions of stationary spike solutions give form to stationary stripe solutions; these stripes are known as *homoclinic stripes* (cf. [37]), see Fig. 9. This homoclinic stripe is constructed by a 1D spike (bold solid curve) pinned at $x_0(\eta;\gamma)$, which gets located in the slow time $\eta = \varepsilon^2 t$ for a fixed γ value. Then, it is transversally extended. As a consequence, a stripe flanked by bold solid curves is obtained.

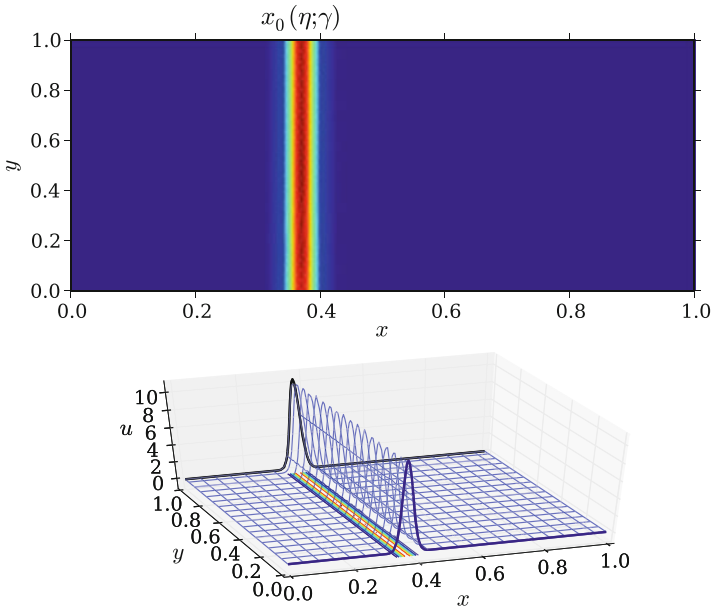

Fig. 9 Homoclinic stripe on a heat scale in the upper panel. In the bottom panel, spikes (bold solid blue curves) at $x_0(\eta;\gamma)$ correspond to stripe ends. This stripe comes from a trivial extension of a 1D spike

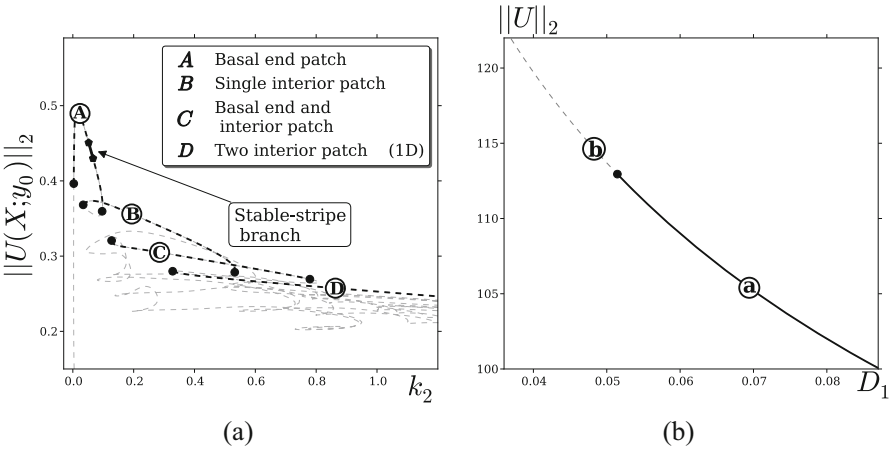

Fig. 10 (**a**) Comparison of bifurcation diagrams between localised stripes and 1D-spike scenarios. Bold dashed portions of the diagram indicate where stable 1D solutions are unstable to transverse instabilities. A narrow stable window is found, given by the solid black curve. (**b**) Bifurcation diagram as D_1 varies from a solution in stable-stripe branch shown in (**a**). An eigenvalue crosses into the right-hand complex semi-plane at the filled black circle. Branch labelled by **a** remains stable as D_1 is increased further (not shown). Figures reproduced as well as parameter values from [30]

In dimensionless form the model is posed on a square $(x, y) \in \Omega^2 \equiv [0, 1]\times[0, 1]$, which has been rescaled from a rectangular domain $\Omega^2 \equiv [0, L_x]\times[0, L_y]$ and aspect ratio $s = (L_x/L_y)^2$, so that in (4) we have allowed for a Laplacian defined as $\Delta \equiv \partial_{xx} + s\partial_{yy}$. As a consequence, we get a bifurcation diagram which has the same structure as bifurcation diagram in Fig. 8a, but stability is drastically changed; see Fig. 10a. We use the L_2-norm of the active component for a fixed value of y as a solution measure. We find patterns with one boundary stripe (A), one interior stripe (B), one boundary and one interior stripe (C), and two interior stripes (D). All the solution branches, apart from a small segment (bold line), are unstable. The stable extended pattern branch (solid black curve ends in Fig. 10a) becomes unstable as D_1 decreases. This gives an insight on the asymptotic limit, i.e. sharper boundary stripes are unstable. To shed light on this, upon selecting a solution from the stable stripe-branch as initial condition, we perform continuation on D_1. As can be seen in Fig. 10b, there is a small critical value at which boundary stripe solutions become unstable.

To rigorously prove that stripes are unstable, semi-strong theory is used to derive a nonlocal eigenvalue problem (NLEP). From Proposition 3.1 for $N = 0$, a stationary stripe solution is substituted into system (8), and upon considering a localised eigenfunction for the active component, we obtain

Proposition 4.1 (Modified Version from [30]) *The stability on an $\mathcal{O}(1)$ time-scale of a quasi steady-state interior stripe solution of (8) is determined by the spectrum of the NLEP*

$$\mathcal{L}_0\Phi_0 - \theta_h(\lambda;m)\, w^2\, \frac{\int_{-\infty}^{\infty} w\Phi_0\, d\xi}{\int_{-\infty}^{\infty} w^2\, d\xi} = \left(\lambda + s\varepsilon^2 m^2\right)\Phi_0\,, \tag{13}$$

$$-\infty < \xi < \infty\,; \quad \Phi_0 \to 0\,, \quad as \quad |\xi| \to \infty\,,$$

where Φ_0 is the localised eigenfunction at the leading order, $\mathcal{L}_0\Phi_0 \equiv \Phi_{0\xi\xi} - \Phi_0 + 2w\Phi_0$, and $\theta_h(\lambda;m)$ is given by

$$\theta_h(\lambda;m) \equiv \mu\left(\frac{\lambda + 1 + s\varepsilon^2 m^2 - 2\kappa}{\lambda + 1 + s\varepsilon^2 m^2 - \mu\kappa}\right), \tag{14}$$

$$\mu \equiv 2\left[1 + \frac{D_0}{6\chi G^0}\right]^{-1}, \qquad \chi \equiv \frac{\tau\alpha\,(x_0)}{36\beta^2\gamma}\,, \qquad G^0 \equiv G\,(x_0;x_0)\,.$$

Here $G\,(x;x_0)$ is defined by

$$G_{xx} - sm^2 G = -\delta\,(x - x_0)\,, \quad 0 < x < 1\,;$$

$$G_x(0;x_0) = G_x(1;x_0) = 0\,; \qquad [G_x]_{x_0} = -1\,,$$

and the wavenumber m in the y-direction is $m = \pi k$ with $k \in \mathbb{Z}^+$.

From (13), a dispersion relation is formally found to be as shown in Fig. 11. This comes from the fact that there exist two roots of $\Re(\lambda)$ at m_{low} and m_{up}, which implies

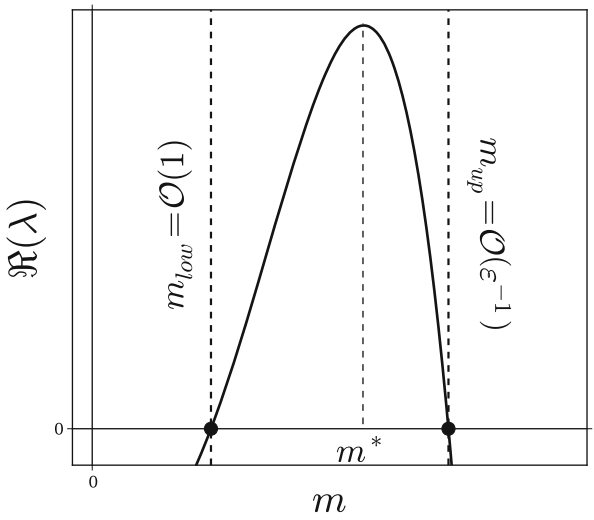

Fig. 11 Sketch of a dispersion relation $\Re(\lambda)$ versus m, showing the unstable band of wavenumbers lying between the vertical dashed lines. The expected number of spots is closely determined by the most unstable mode m^*. Figure reproduced from [30]

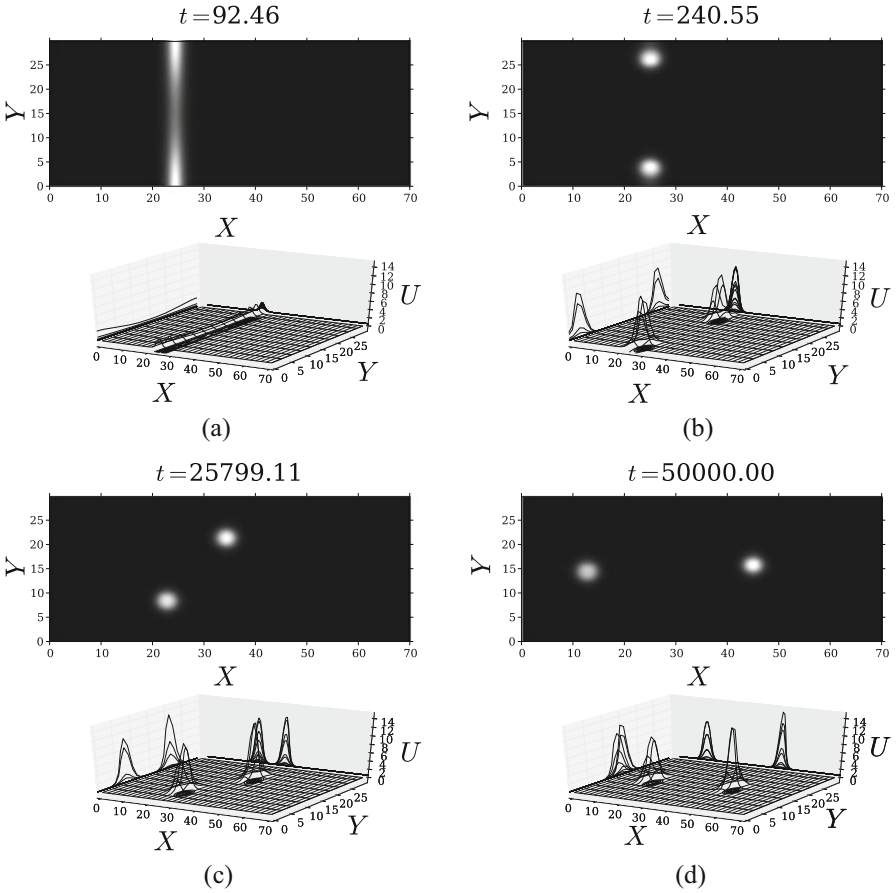

Fig. 12 Breakup instability and secondary $\mathcal{O}(1)$ time-scale instabilities of an interior localised stripe for U. (**a**) The localised stripe initially breaks into two spots; (**b**) once formed, the spots migrate from the boundary towards each other along the x-location line, and (**c**) rotate until they get aligned with the longitudinal direction. (**d**) Finally, they get pinned far from each other. Figures reproduced as well as parameter values from [30] with $k_2 = 0.5$, which corresponds to a stripe location at $x_0 = 24.5$

that there will be always a band of unstable transversal modes m. The most unstable mode m^* determines the number of spots the stripe will break up. For $s = 5.5$ and relative stripe location $x_0 = 0.35$, the dispersion relation (not shown) computed from (13) predicts that an interior stripe break up into either two or three spots. An interior stripe is taken as the initial condition and perform a direct numerical simulation of the full PDE system (4). The results are shown in Fig. 12, where we observe from Fig. 12a and b that the stripe initially breaks into two distinct localised spots. The spatial dynamics of these two newly-created spots is controlled by the auxin gradient. They initially move closer to each other along a vertical line, and

then rotate slowly in a clockwise direction to eventually become aligned with the horizontal direction associated with the auxin gradient $\alpha(x)$ (see Fig. 12c). Finally, in Fig. 12d we show a stable equilibrium configuration of two spots lying along the centre line of the transverse direction. See [30] for full details.

5 ROP Spot Dynamics

Spot location dynamics are depicted in Fig. 12c and d. This location dynamics show attributes governed by the presence of auxin gradient. This characterisation along with instabilities of spot patterns has also been analysed in [31]. To gain further insight, we run a time-step simulation upon taking an unstable boundary stripe solution (labelled by **b** in Fig. 10b) as the initial condition. This computation shows the triggering of a breakup instability, which then gives rise to two spots moving towards domain interior, see Fig. 13. There, the boundary stripe breaks up into two spots (see Fig. 13a) to then slowly drift towards interior (see Fig. 13b). Hence, similarly as in Fig. 12c and d, due to reminiscences of homoclinic snaking, spot formation inherits robusticity traits in 1D addressed in [29].

A wide variety of mixed spot and stripe patterns can be created through breakup instabilities. In order to explore these new types of solution further, we shall perform full numerical continuation of 2D solutions. To do this, we begin with a solution on the stable steady-state branch of Fig. 10. We then continue this solution by varying the main bifurcation auxin overall parameter, both backwards and forwards, to finally obtain the bifurcation diagram depicted in Fig. 14. There, all

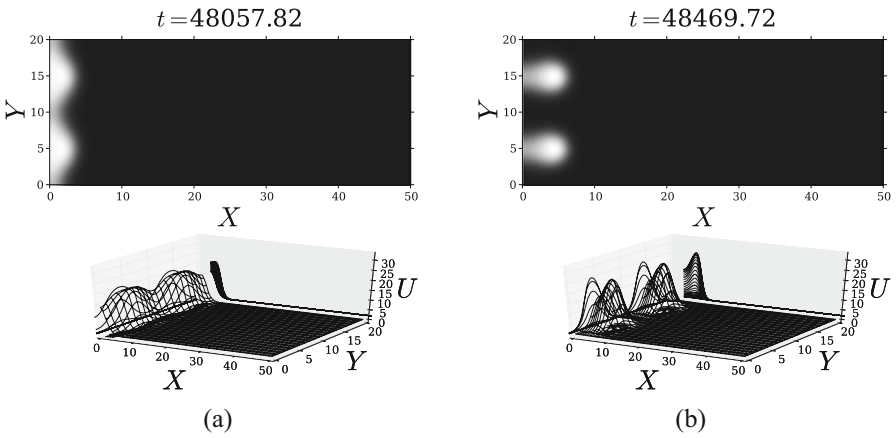

Fig. 13 Relevant snapshots of transversal instability for unstable boundary stripe **b** in Fig. 10b. (**a**) Break up instability and (**b**) two newly formed boundary spots travelling towards interior. Figures reproduced as well as parameter values from [30]

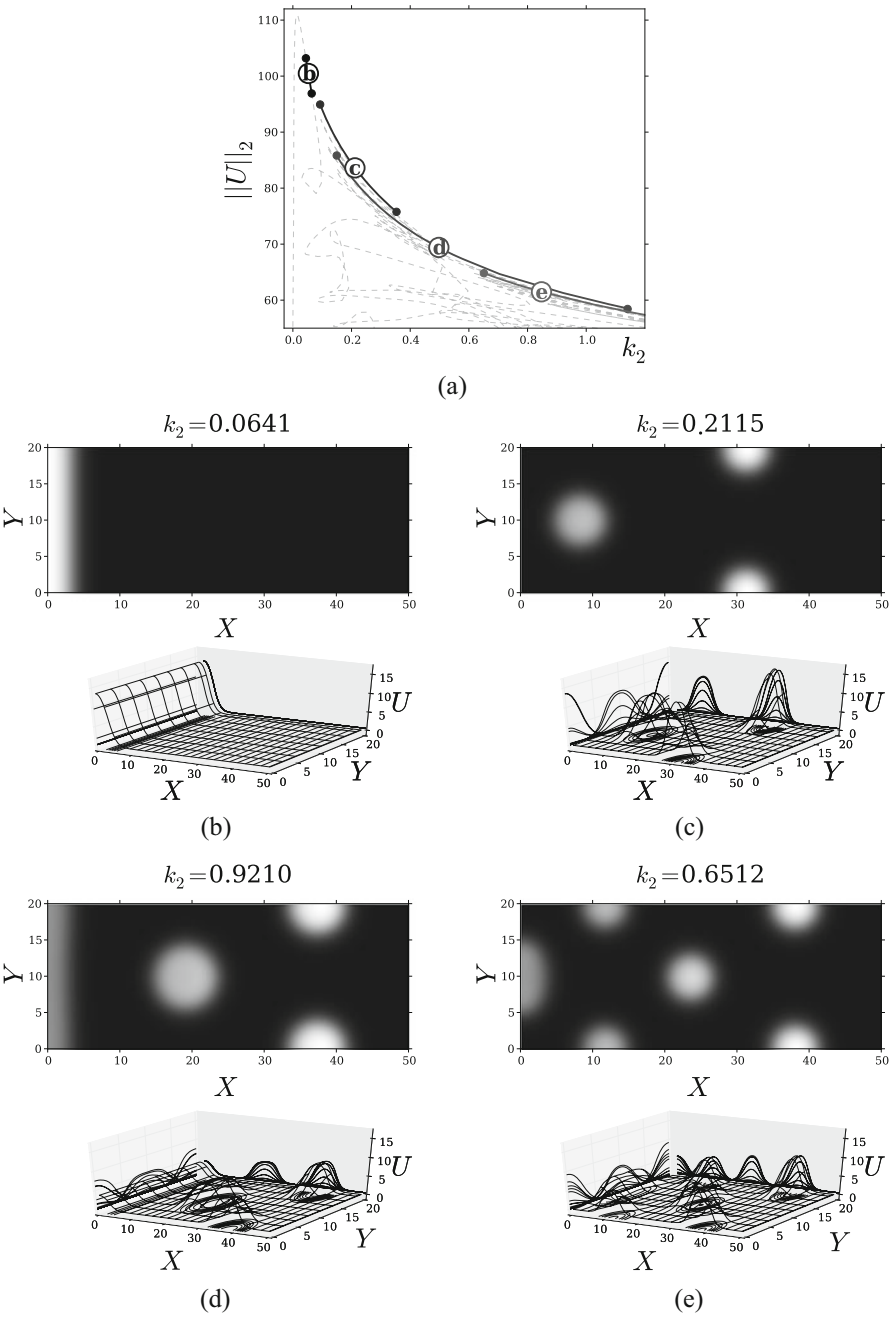

Fig. 14 Bifurcation diagram: spots and a boundary stripe. (**a**) Stable branches are drawn by solid lines and unstable ones by light-grey dashed lines, and filled circles represent fold points. Stable solutions, according to labels (**b**) up to (**e**), are shown in: (**b**) a boundary stripe, (**c**) a spot in the interior and two spots at the boundary, (**d**) a boundary stripe, an interior spot and two spots at the boundary, and (**e**) an interior spot and five spots at the boundary. Figures reproduced as well as parameter values from [30]

unstable branches are plotted as light-grey dashed lines, whereas stable branches are represented as solid lines labelled accordingly as: (b) stable stripes, (c) an interior spot and two spots vertically aligned at the boundary, (d) similar configuration but with an additional stripe, and (e) an interior spot and five spots at the boundary. See Fig. 14b–e for examples of each stable steady-state. In Fig. 14a, as seen before, the bifurcation diagram replicates features studied in the 1D case in [29], such as the overlapping of stable branches of single and multiple localised patches. Stable branches typically become unstable through fold bifurcations. All branches seem to lie on a single connected curve, and no other bifurcations were found except for the pitchfork bifurcations in branch (b). However, branches (c) up to (e) are extremely close to each other and apparently inherit properties from each other.

That is, they seem to undergo a *creation-annihilation cascade* effect similar to that observed in [29]. In other words, take a steady-state which lies on the left-hand end of branch (c) and slide down this branch as auxin overall parameter is increased. It then loses stability at the fold point, and at the other extreme to then fall off in branch (d). Thus a stripe emerges, which pushes the interior spot further in. The same transition follows up to branch (e), more spots arise though as the stripe is destroyed. No further stable branches with steady-states resembling either spots or stripes were found.

Now, in order to derive a 2D solution profiles, we notice that a *conservation principle* is satisfied. Upon assuming radially symmetric N spots, we set evolution operators ∂_t in (4) to zero and find that, in the re-scaled parameter set given in (9)–(10), stationary active-ROP density satisfy that

$$\int_{\Omega} U_0 \, \mathrm{d}\Omega = \frac{d_y}{\beta\gamma}, \quad d_y \equiv \frac{L_y}{L_x},$$

which suggest to re-scale $U = \varepsilon^{-2} U_j$ near each spot, where $j = 1, \ldots, N$. In so doing, we obtain

$$\sum_{j=1}^{N} \int_{\mathbb{R}^2} U_j \, \mathrm{d}\boldsymbol{\xi} \sim \frac{d_y}{\beta\gamma},$$

where $\boldsymbol{\xi} = \varepsilon^{-1} \left(\mathbf{x} - \mathbf{x}_j \right)$. Hence, to properly re-scale system (4) in such a way that a singularly perturbed system is obtained, active- and inactive-ROP densities are re-scaled as follows: $U = \varepsilon^{-2} u$, $V = \varepsilon^2 v$, and consequently $D = \varepsilon^{-2} D_0$, which comes from balancing Eq. (4b). Due to this, we get a system similar to (8) with dimensionless parameters (9)–(10) in a 2D square domain.

We then define a radial variable $\rho \equiv |\boldsymbol{\xi}|$, and asymptotically expand components u and v with respect to ε. This approach yields two main ingredients:

1. A canonical core problem (CCP) is found at leading order, which solutions u_c and v_c give place to spot solution profiles as given by

$$u_{0j} \equiv \sqrt{\frac{D_0}{\beta\gamma\alpha(\mathbf{x}_j)}}\, u_c\,, \quad v_{0j} \equiv \sqrt{\frac{\beta\gamma}{D_0\alpha(\mathbf{x}_j)}}\, v_c\,.$$

2. Spot location dynamics is given from second order term, which is characterised by a source parameter S_j that satisfies the identity

$$S_j = \frac{\beta\gamma}{D_0}\int_0^\infty \left[\frac{\tau}{\beta}\left(\alpha\left(\mathbf{x}_j\right) u_{0j}^2 v_{0j} - u_{0j}\right) + u_{0j}\right]\rho\, d\rho\,, \quad \text{where}$$

$$S_j = \sqrt{\frac{\beta\gamma}{D_0\alpha(\mathbf{x}_j)}}\, S_{cj}\,. \tag{15}$$

From item 1, profile asymmetric amplitudes are observed to be controlled by auxin gradient. On the other hand, identity in item 2 characterises activation by auxin, longitudinal length and on-and-off switching mechanism in regions close where active-ROP density is high. Notice that τ/β modulates nonlinear terms in (15). These parameters suggests that deactivation rate and removal rate play a relevant key role in auxin catalytic process in 2D. As a consequence, it seems to be an indirect influence of geometrical marks near activation regions.

Upon taking into account these two elements together, we derive a differential algebraic equation (DAE) system which characterises slow N spot dynamics,

$$\frac{d\mathbf{x}_j}{d\eta} = n_1\hat{\boldsymbol{\psi}}_j + n_2\frac{\nabla\alpha(\mathbf{x}_j)}{\alpha(\mathbf{x}_j)}, \quad \hat{\boldsymbol{\psi}}_j \equiv -2\pi\left(S_{cj}\nabla_{\mathbf{x}}R_j + \sum_{i\neq j}^{N} S_{ci}\nabla_{\mathbf{x}}G_{ji}\right),$$

$$j = 1,\ldots,N\,, \tag{16}$$

where $\eta = \varepsilon^2 t$ is the slow time-scale, R_j is the regular part of Green's function for a square 2D domain and $G_{ji} = G(\mathbf{x}_j;\mathbf{x}_i)$ regulates spots interaction terms. Notice that system (16) consists of two terms: (1) an interaction vector and (2) a kinetic vector. The later consists of the normalised gradient, and the latter deals with interaction between spots, boundary conditions and shape and form of the domain. In addition, the source parameters S_{cj} in (16) satisfy a nonlinear algebraic system, which depends on the instantaneous spatial configuration of the N spots.

In Fig. 15 we compare our full numerical results for the x and y coordinates for the trajectories of two spots, as computed from the RD system (4), and those computed from the corresponding DAE system. The key distinguishing feature in these results is that the spots become aligned to the longitudinal midline of the domain. We observe that the y-components of the spot trajectories are predicted

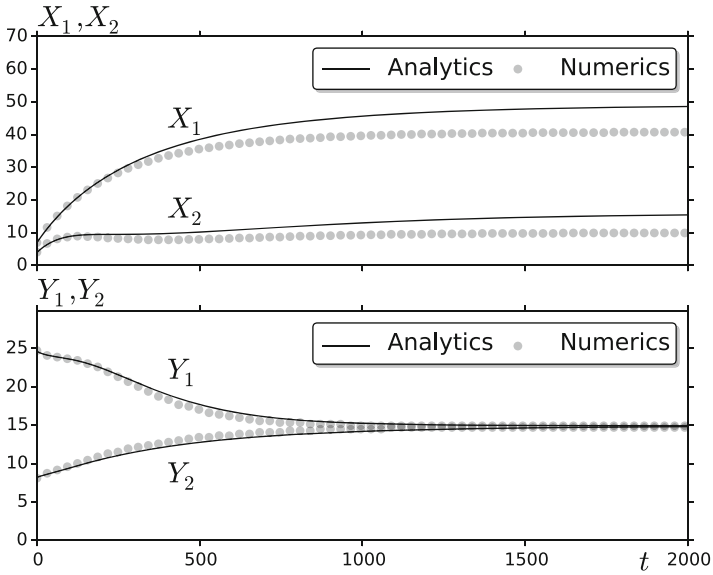

Fig. 15 The time-dependent location of two spots as obtained from system (16) (solid curves). The full numerical results computed from (4) are the filled circles. Observe that the DAE system predicts that the two spots become aligned along the longitudinal midline of the cell. The x-coordinate (upper panel) and the y-coordinate (bottom panel) of the two spots. Figures reproduced as well as parameter values from [31]

rather accurately over long time intervals by the DAE system. The x-components of the trajectories are initially close, but then deviate slightly as t increases.

See [31] for a detailed discussion on spot dynamics and other instabilities characterised by auxin on a 2D domain.

6 Concluding Remarks

Auxin is experimentally known to promote RH cell wall swelling. As a consequence, a RH protuberance is then developed at a critical location along the cell and a specific time. The dynamical ingredients for a biochemical interaction as well as auxin catalyst attributes are captured in a model consisting of a non-homogeneous RD system. This model has been proposed by R. Payne and C. Grierson in [9] and thoroughly analysed in [28–31].

We here present a brief review of the key role dynamical features which give place to pattern formation. Nonetheless, from a modelling point of view, our results also provide a setting which may be suitable for precise further experimental designs. On the other hand, pattern formation theory still remains in darkness; we here depict all essential dynamical components that rigorously characterise localised

solutions, as well as location dynamics controlled by the auxin gradient. Other instabilities arising in 1D and 2D are not here addressed. Nonetheless, features considered can be summarised as follows:

- Turing subcritical bifurcations favours localised solutions; as a consequence, they determine the onset of localised stationary solutions that are organised in a homoclinic snaking fashion.
- Due to reminiscences of homoclinic snaking, as auxin gradient is included as a biochemical accelerator, a strong slanted overlapping of stable branches, which are flaked by fold bifurcations, give rise to hysteretical behaviour.
- Amplitude asymmetry and location are controlled by auxin gradient, where physical features as shape and form are more relevant when a 2D domain is taken into account.
- Although not discussed here, the key instabilities that regulate transitions between family of localised patterns are: (1) competition instability and (2) peanut-splitting instability. The former can be understood as an under-crowding instability which determines whether a pattern consisting of multi-localised structures persists on a $\mathcal{O}(1)$ time scale; on the contrary, the latter works as a over-crowding instability, which promotes nonlinear events yielding spot self-replication. In both cases, a threshold is passed to trigger such an instabilities. These thresholds deal with a strong relationship between auxin and length of the domain.

Notice that there still are physical and biological features not yet considered. These may be other transport processes, geometrical characteristics as torsion and curvature, and a collection of non-RH and RH cells all together with an auxin flux catalysing pattern formation in *Arabidopsis thaliana*.

Acknowledgements I specially thank D. Avitabile, A. Champneys, C. Grierson and M. Ward who have travelled along my side on this dynamical journey. Also, my thanks to the organisers of the Biological Physics Mexico City 2017 Conference for the well-organised meeting. This research has partially been supported by UNAM–PAPIIT grant IA104316–RA104316 (Mexico).

References

1. Grierson C, Nielsen E, Ketelaarc T, Schiefelbein J (2014) Root hairs: the Arabidopsis book 11. American Society of Plant Biologists, Rockville, MD
2. Berger F, Hung C, Dolan L, Schiefelbein J (1998) Control of cell division in the root epidermis of Arabidopsis thaliana. Dev Biol 194:235–245
3. Jones A, Kramer E, Knox K, Swarup R, Bennett M, Lazary C, Leyser HO, Grierson C (2009) Auxin transport through non-hair cells sustains root-hair development. Nat Cell Biol 11:78–84
4. Nagawa S, Xu T, Yang Z (2010) Rho GTPases in plants: conservation and invention of regulators and effectors. Small GTPases 1:78–88
5. Bustelo X, Sauzeau V, Berenjeno I (2007) GTP-binding proteins of the Rho/Rac family: regulation, effectors and functions in vivo. Bioessays 29:356–370

6. Geldner N, Anders N, Wolters H, Keicher J, Kornberger W, Muller P, Delbarre A, Ueda T, Nakano A, Jüngens G (2003) The Arabidopsis GNOM ARF-GEF mediates endosomal recycling, auxin transport, and auxin-dependent plant growth. Cell 112:219–230
7. Mori Y, Jilkine A, Edelstein-Keschet L (2008) Wave-pinning and cell polarity from a bistable reaction-diffusion system. Biophys J 94:3684–3697
8. Breña-Medina VF (2013) Modelling initiation of plant root hairs; a reaction-diffusion system in a non-homogenous environment. PhD thesis, University of Bristol
9. Payne R, Grierson C (2009) A theoretical model for ROP localisation by auxin in Arabidopsis root hair cells. PLoS One 4:e8337. https://doi.org/10.1371/journal.pone.0008337
10. Kramer EM, Rutschow HL, Mabie SS (2011) AuxV: a database of auxin transport velocities. Trends Plant Sci 16:461–463
11. Kramer EM (2004) PIN and AUX/LAX proteins: their role in auxin accumulation. Trends Plant Sci 9:578–582
12. Grierson C et al (2009) Root Development Lab, School of Biological Sciences – University of Bristol
13. Sorek N, Gutman O, Bar E, Abu-Abied M, Feng X, Running M, Lewinsohn E, Ori N, Sadot E, Henis Y, Yalovsky S (2011) Differential effects of prenylation and S-acylation on type I and II ROPs membrane interaction and function. Plant Physiol 155:706–720
14. Jilkine A, Maree A, Edelstein-Keschet L (2007) Mathematical model for spatial segregation of the Rho-family GTPases based on inhibitory crosstalk. Bull Math Biol 69:1943–1978
15. Otsuji M, Ishihara S, Co C, Kaibuchi K, Mochizuki A (2007) A mass conserved reaction-diffusion system captures properties of cell polarity. PLoS Comput Biol 3:e108
16. Schnakenberg J (1979) Simple chemical reaction systems with limit cycle behaviour. J Theor Biol 81:389–400
17. Nicolis G, Prigogine I (1977) Self-organization in nonequilibrium systems. Wiley-Interscience, New York
18. Maini PK, Painter KJ, Phong-Chau HN (1997) Spatial pattern formation in chemical and biological systems. J Chem Soc Faraday Trans 93:3601–3610
19. Ward MJ, Wei J (2002) The existence and stability of asymmetric spike patterns for the Schnakenberg model. Stud Appl Math 109:229–264
20. Iron D, Wei J, Winter M (2004) Stability analysis of Turing patterns generated by the Schnakenberg model. J Math Biol 49:358–390
21. Kolokolnikov T, Ward M, Wei J (2009) Spot self-replication and dynamics for the Schnakenberg model in a two-dimensional domain. J Nonlinear Sci 19:1–56
22. Dufiet V, Boissonade J (1992) Conventional and unconventional Turing patterns. J Chem Phys 96:662–673
23. Lin F, Du Q (1997) Ginzburg-Landau vortices: dynamics, pinning, and hysteresis. SIAM J Math Anal 28:1265–1293
24. Ward M, Mcinerney D, Houston P, Gavaghan D, Maini P (2002) The dynamics and pinning of a spike for a reaction-diffusion system. SIAM J Appl Math 62:1297–1328
25. Maini PK, Benson DL, Sherrat JA (1992) Pattern formation in reaction-diffusion models with spatially inhomogeneous diffusion coefficients. IMA J Math Appl Med Biol 9:197–213
26. Holloway DM, Harrison LG (1995) Order and localization in reaction-diffusion pattern. Phys A Stat Mech Appl 222:210–233
27. Hunding A (1985) Morphogen prepatterns during mitosis and cytokinesis in flattened cells: three dimensional Turing structures of reaction-diffusion systems in cylindrical coordinates. J Theor Biol 114:571–588
28. Breña-Medina V, Champneys AR (2014) Subcritical Turing bifurcation and the morphogenesis of localized structures. Phys Rev E 90:032923
29. Breña-Medina V, Champneys AR, Grierson C, Ward MJ (2014) Mathematical modelling of plant root hair initiation; dynamics of localized patches. SIAM J Appl Dyn Syst 13:210–248
30. Breña-Medina V, Avitabile D, Champneys A, Ward M (2015) Stripe to spot transition in a plant root hair initiation model. SIAM J Appl Math 75:1090–1119

31. Avitabile D, Breña-Medina V, Ward MJ (2017) Spot dynamics in a reaction-diffusion model of plant root hair initiation. arXiv:1703.02608 and bioRxiv:114876
32. Murray J (2002) Mathematical biology II: spatial models and biomedical applications, 3rd edn. Springer, New York
33. Beck M, Knobloch J, Lloyd DJB, Sandstede B, Wagenknecht T (2009) Snakes, Ladders, and Isolas of localized patterns. SIAM J Math Anal 41:936–972
34. Woods PD, Champneys AR (1999) Heteroclinic tangles and homoclinic snaking in the unfolding of a degenerate reversible Hamiltonian-Hopf bifurcation. Physica D 129:147–170
35. Avitabile D, Lloyd D, Burke J, Knobloch E, Sandstede B (2010) To snake or not to snake in the planar Swift-Hohenberg equation. SIAM J Appl Dyn Syst 9:704–733
36. Grieneisen V, Maree A, Hogeweg P, Scheres B (2007) Auxin transport is sufficient to generate a maximum and gradient guiding root growth. Nature 449:1008–1013
37. Doelman A, van der Ploeg H (2002) Homoclinic stripe patterns. SIAM J Appl Dyn Syst 1: 65–104

About the Editors

Luis Olivares-Quiroz is currently full-time physics professor, researcher, and lecturer at Universidad Autonoma de la Ciudad de Mexico (UACM). He obtained his PhD in 2007 with a thesis on the statistical mechanics of protein folding and its connection to the glass transition. After receiving his PhD, he has been involved actively in research at the interface of physics and molecular biology, particularly on the application of statistical physics, stochastic process, complex networks, and genetic algorithms (GAs) to the analysis of protein folding and unfolding, peptide and protein translocation across membranes, identification of active sites in biological macromolecules as well as computer simulations of interacting potentials for protein folding using GAs. He has been invited to different research institutions both in Mexico and abroad: Department of Biochemistry, University of Arizona, Tucson (USA); Forschungszentrum (Germany); Faculté des Sciences, University of Nantes (France); Department of Physics, Georgia Tech at Atlanta (USA); and the Biophysical Sciences Institute at Durham University (UK). In Mexico, he has been an active and intense promoter of research in biological physics. In 2009 he was granted the National Prize for Science Dissemination for the publishing of a book on the quantum physics of ultracold liquids and gases. He has been also editor-in-chief of *Physical Biology of Proteins and Peptides: Theory, Experiment, and Simulation* published by Springer in 2015.

Osbaldo Resendis-Antonio is professor of systems biology at the National Institute of Genome Medicine (INMEGEN) and the Research Support Network (RAI-UNAM) at the National Institute of Medical Sciences and Nutrition Salvador Zubirán, both in México City. After receiving a Ph.D. in physics in 2003, he switched the emphasis of his research to systems biology, first as a postdoctoral fellow in the Institute Henry Poincare (France), the Center for Nitrogen Fixation-UNAM (México); and the Department of Systems Biology at the University of California San Diego (USA); and then as a principal researcher at the Center for Genomic Sciences-UNAM, México, in 2008. He has been visiting professor in the

L. Olivares-Quiroz, O. Resendis-Antonio (eds.), *Quantitative Models for Microscopic to Macroscopic Biological Macromolecules and Tissues*,
https://doi.org/10.1007/978-3-319-73975-5

Systems Biology Department at Harvard Medical School (USA), the group of Bioinformatics and Systems Biology at the University of Rostock (Germany), and the Institute for Systems Biology at Seattle, Washington (USA). His research interest is focused to survey the metabolic pathway alterations associated with multifactorial diseases, such as cancer, through the integrative description among genome-scale metabolic reconstructions, high-throughput data, and the development of constraint-based modeling.

Index

L. Olivares-Quiroz, O. Resendis-Antonio (eds.), *Quantitative Models for Microscopic to Macroscopic Biological Macromolecules and Tissues*,
https://doi.org/10.1007/978-3-319-73975-5